UNIVERSITÄT
DUISBURG
ESSEN

Offen im Denken

Reactivation of Hydrated Cement and Recycled Concrete Powders by Thermal Treatment for Partial Replacement of Virgin Cement

Von der Fakultät für Ingenieurwissenschaften
Abteilung Bauwissenschaften,
Institut für Materialwissenschaft
der Universität Duisburg-Essen

genehmigte Dissertation zur Erlangung des akademischen Grades eines
Doktor der Ingenieurwissenschaften (Dr. -Ing.)

vorgelegt von

M. Eng. Gustave Semugaza
[Rwanda Polytechnic (RP), Integrated Polytechnic Regional Centre (IPRC) Kigali, Rwanda]

Datum der mündlichen Prüfung: 08.02.2024
Hauptreferent: Prof. Dr. rer. nat. habil. Doru C. Lupascu
Korreferent: Prof. Dr.-Ing. Martina Schnellenbach-Held

Essen 2024

To my wife Annoncee Mukasekuru

Declaration

I declare that the contents of this dissertation are original work prepared by myself, except when a particular reference is made to the work of others, including electronic sources. This work has not been submitted entirely or partially for any other degree or qualification in this or any other university. This dissertation is the outcome of my original work, and the work done in collaboration has been duly acknowledged.

Gustave Semugaza

Essen, July 2023

Abstract

Concrete has been used as a leading construction material for many decades. Its increasing demand is associated with the continuous increase of the earth's population leading to the depletion of natural resources. On the other hand, construction modernization requires demolishing old buildings, roads, and bridges, producing a massive amount of Construction and Demolition Wastes (CDW). Much of it is composed of old concrete. The substantial reduction of natural resources and the dumping of these wastes constitute a significant source of environmental problems. Besides, the production of cement, which is the principal binder of concrete, is accountable for considerable CO_2 emissions and is very energy-intensive. Therefore, recycling old concrete for partial replacement of Virgin Cement (VCe) in new concrete or mortar is essential for protecting the environment and reducing CO_2 emissions.

Thermal treatment has been proven to recover the hydration ability of Hydrated Cement Powder (HCeP), which helps as a reference material for evaluating Recycled Concrete Powder (RcCoP). Several techniques separate the components of old concrete. This research considers the Smart Crushing (SC) and Electrodynamic Fragmentation (EF) methods to obtain the RcCoP with as much cementitious content as possible. These two types of materials and the methods used to produce the RcCoP are compared after thermal treatment at temperatures from 200 °C to 1000 °C.

The necessary chemical transformations happen at different temperatures during the thermal treatment process. Subsequently, the strength development phases, specifically the calcium silicate phases, can be reformed depending on the pre-treatment temperature. Thus, the treatment temperature defines the dehydration products that control the rehydration ability. Several laboratory techniques assess the chemical transformations and phase development resulting from the thermal treatment at different temperatures. These techniques include Thermogravimetry (TG), Differential Scanning Calorimetry (DSC), and X-Ray Diffraction (XRD). The microstructure, porosity and pore size distribution, and mechanical strength associated with pre-treatment temperatures were investigated by Scanning Electron Microscopy (SEM), Mercury Intrusion Porosimetry (MIP), and compressive and flexural strength testing, respectively.

The temperature treatment range of 400 °C – 800 °C produces the best content of strength development phases. 600 °C is the optimum thermal treatment temperature. It results in significant content of dicalcium silicate (C_2S_α and C_2S_β) and the highest content of the remaining previously unhydrated tricalcium silicate (C_3S). Nevertheless, the amount of this C_3S phase is little compared to the one in VCe. The C_3S is the primary phase that controls strength development, especially at an early age (first week). It is highly reactive and cannot be recovered, indicating that the total hydration capacity cannot be regained. However, the C_2S_α that forms through thermal treatment is more reactive than C_2S_ β, which benefits strength reformation.

Using 100% thermally treated HCeP and RcCoP indicates that approximately 55% of strength development ability can be recovered for the HCeP, while only <10% can be retrieved for the RcCoP. This massive difference is due to the content of a high amount of quartz and coesite phases (SiO_2), especially quartz, dominating the phase composition. The SiO_2 is not a strength-forming phase. It is thermally stable and not decomposed during thermal treatment. Also, the crystals of the SiO_2 phase dominate the microstructure of all thermally treated RcCoP. In contrast, the microstructure of thermally treated HCeP shows more condensed rehydration products and is much more compact, emphasizing an increased ability for strength

development. The HCeP pre-treated at 600 °C can replace the VCe in mortar for up to 20% without affecting the mechanical strength. The replacement of VCe in mortar by thermally treated RcCoP was not conducted because a minimal strength development ability was recovered in 100% thermally treated RcCoP, regardless of the pre-treatment temperature.

Zusammenfassung

Beton wird seit vielen Jahrzehnten als führender Baustoff verwendet. Seine steigende Nachfrage steht im Zusammenhang mit dem kontinuierlichen Anstieg der Weltbevölkerung, der zur Erschöpfung der natürlichen Ressourcen führt. Auf der anderen Seite erfordert die Modernisierung des Baubestands den Abriss alter Gebäude, Straßen und Brücken, wodurch eine große Menge an Bau- und Abbruchabfällen entsteht, die ingroßen Teilen aus altem Beton bestehen. Die erhebliche Verringerung der natürlichen Ressourcen und die Deponierung dieser Abfälle stellen eine bedeutende Quelle für Umweltprobleme dar. Außerdem ist die Herstellung von Zement, dem Hauptbindemittel von Beton, für erhebliche CO_2-Emissionen verantwortlich und sehr energieintensiv. Daher ist das Recycling von Altbeton zum teilweisen Ersatz von Frischzement (VCe) in neuem Beton oder Mörtel für den Umweltschutz und die Verringerung der CO_2-Emissionen von wesentlicher Bedeutung.

Es ist erwiesen, dass die thermische Behandlung die Hydratationsfähigkeit von hydratisiertem Zementpulver (HCeP) wiederherstellt, das als Referenzmaterial für die Bewertung von recyceltem Betonpulver (RcCoP) dient. Es gibt verschiedene Techniken zur Trennung der Bestandteile von Altbeton. In dieser Untersuchung werden die Verfahren Smart Crushing (SC) und Electrodynamic Fragmentation (EF) angewandt, um RcCoP mit einem möglichst hohen Anteil an zementhaltigem Material zu erhalten. Diese beiden Materialtypen und die zur Herstellung von RcCoP verwendeten Methoden werden nach einer thermischen Behandlung bei Temperaturen von 200 °C bis 1000 °C verglichen.

Die chemischen Umwandlungen finden bei unterschiedlichen Temperaturen während der thermischen Behandlung statt. Anschließend können die festigkeitsgebenden Phasen, insbesondere die Calciumsilikatphasen, in Abhängigkeit von der Vorbehandlungstemperatur wiederhergestellt werden. Somit bestimmt die Behandlungstemperatur die Dehydratationsprodukte, die das Rehydratationspotenzial steuern. Mit verschiedenen Labortechniken wurden die chemischen Umwandlungen und die Phasenentwicklung infolge der thermischen Behandlung bei unterschiedlichen Temperaturen untersucht. Zu diesen Techniken gehören die Thermogravimetrie (TG), die Differentialscanningkalorimetrie (DSC) und die Röntgenbeugung (XRD). Außerdem wurden die Mikrostruktur, die Porosität und die Porengrößenverteilung sowie die mechanische Festigkeit in Abhängigkeit von den Vorbehandlungstemperaturen mit Hilfe der Rasterelektronenmikroskopie (REM), der Quecksilberintrusionsporosimetrie (MIP) und der Druck- und Biegefestigkeitsprüfmaschine untersucht.

Der Temperaturbehandlungsbereich von 400 °C – 800 °C ergibt den besten Gehalt an festigkeitsgebenden Phasen, und 600 °C ist die optimale Temperatur für die thermische Behandlung. Sie führt zu einem signifikanten Gehalt an Dicalciumsilicat (C_2S_α und C_2S_β) und dem höchsten Gehalt an dem verbleibenden unhydratisierten Tricalciumsilicat (C_3S). Die Menge dieser C_3S-Phase ist jedoch gering im Vergleich zu derjenigen in VCe. Die C_3S-Phase ist die primäre Phase, die die Entwicklung der Festigkeit insbesondere in einem frühen Alter (erste Woche) steuert. Sie ist hoch reaktiv und kann nicht wiederhergestellt werden, was bedeutet, dass das gesamte Hydratationspotenzial nicht wiederhergestellt werden kann. Das C_2S-α, das sich durch die thermische Behandlung bildet, ist jedoch reaktiver als das C_2S-β, was der Festigkeitsreformation zugutekommt.

Die Verwendung von 100 % thermisch behandeltem HCeP und RcCoP zeigt, dass etwa 55 % der Festigkeit für das HCeP wiedergewonnen werden kann, während nur <10 % für das RcCoP wiedergewonnen werden kann. Dieser massive Unterschied ist auf den hohen Gehalt an

Quarz- und Coesitphasen (SiO_2), insbesondere Quarz, zurückzuführen, die die Phasenzusammensetzung dominieren. Das SiO_2 ist keine festigkeitsbildende Phase. Es ist thermisch stabil und wird bei der thermischen Behandlung nicht zersetzt. Außerdem dominieren die Kristalle der SiO_2-Phase das Mikrogefüge aller thermisch behandelten RcCoP. Im Gegensatz dazu weist die Mikrostruktur von thermisch behandeltem HCeP mehr kondensierte Rehydratationsprodukte auf und ist wesentlich kompakter, was auf eine erhöhte Fähigkeit zur Festigkeitsentwicklung hinweist. Das bei 600 °C vorbehandelte HCeP kann das VCe im Mörtel bis zu 20 % ersetzen, ohne die mechanische Festigkeit zu beeinträchtigen. Der Ersatz von VCe im Mörtel durch thermisch behandeltes RcCoP wurde nicht durchgeführt, da die Fähigkeit zur Festigkeitsentwicklung bei 100 % thermisch behandeltem RcCoP unabhängig von der Vorbehandlungstemperatur nur minimal wiederhergestellt wurde.

Acknowledgements

I greatly express my heartfelt appreciation to the following persons and institutions who have contributed to the successful completion of this research:

- My supervisor and main adviser, Prof. Dr. rer. nat. Doru C. Lupascu. Without your guidance and support, this research would have never succeeded. Thank you for believing in me and helping me to think outside the box.
- My co-adviser Dr.-Ing. Tommy Mielke. Thank you for your guidance and advice, especially for the experimental laboratory work.
- Dr.-Ing. Hans-Joachim Keck. Your constructive ideas during several meetings and your assistance regarding financial support are highly appreciated.
- Dr. Marianela Escobar Castillo. Your timely inspiring discussions, specifically for the chemical analysis, are greatly acknowledged.
- PD Dr. Vladimir V. Shvartsman. Your continuous advice on making a successful PhD research and scientific insights are exceedingly acknowledged.
- Dr. Miriana Vadala. Your constructive questions and comments, kindness, and social support are deeply appreciated.
- Dr. Juliana Schell. Your scientific insights and kindness are highly appreciated.
- Dr. Kateryna Loza. Your assistance with SEM and EDX material analysis is greatly acknowledged.
- The institute's secretary, Sabine Kriegel, is highly appreciated for her invaluable assistance with administrative documents.
- The laboratory technicians, Stefan Nawrath, Merlin Schmuck, Karl-Heinz Menze, and Andreas Schmidt, are highly acknowledged for their enthusiastic assistance in several ways.
- The members of the UpCement project and PhD students, Anne Z. Gierth, Neshable Noel, and Susanne Helmich, are sincerely appreciated for their challenging discussions and contribution to thesis proofreading. Grammarly tool is also acknowledged for typing assistance.
- The other PhD students. Astita Dubey, Thien Dang, Young Un Jin, Andrei Karabanov, Eva Kröll, Daniil Levin, Sobhan Mohammadi Fathabad, Witchaya Arpavate and Felix Paul. I certainly enjoyed the time we spent together. Your friendship is highly appreciated.
- DAAD and the government of Rwanda for financing my studies through the scholarship awarded to me.
- The Ministry of Economics of the state of North Rhine-Westphalia within the project UpCement (EFO 0126A) for partially financing the research.
- My parents and siblings for their love, prayers and encouragement.
- My beloved wife, for her endless love, care, support, and encouragement.

To the almighty God for keeping me alive and giving me strength.

Table of Contents

Declaration i
Abstract ii
Zusammenfassung iv
Acknowledgements vi
Table of Contents vii
List of Abbreviations x
1. Introduction 1
1.1. Background and problem statement 1
1.2. Research objectives 3
2. State of the Art 4
2.1. A brief history of cement 4
2.2. Cement production and basics 5
2.2.1. Definition 5
2.2.2. Classification of cement types 5
2.2.3. Composition and production of cement clinker 6
2.3. Crystal structure of cement strength development phases 9
2.3.1. Tricalcium silicate 9
2.3.2. Dicalcium silicate 10
2.3.3. Tricalcium aluminate 12
2.3.4. Tetracalcium aluminoferrite 13
2.4. Cement hydration 13
2.4.1. Hydration of clinker phases 14
2.4.2. Cement hydration stages 18
2.4.3. Factors influencing the strength development of cement paste 20
2.4.4. Correlation between the microstructure and strength of cement paste 23
2.5. Reactivation of hydrated cement and recycled concrete powders 25
2.5.1. Dehydration of HCeP and RcCoP 25
2.5.2. Rehydration of HCeP and RcCoP 33
2.6. Concrete recycling and production of RcCoP 41
2.6.1. Concrete recycling 41
2.6.2. Technologies used for the production of RcCoP 43
2.7. Summary 45
3. Experimental Methodology 46
3.1. The preparation process of the research materials 46
3.1.1. Preparation of the Hydrated Cement Powder (HCeP) 46
3.1.2. Preparation of Recycled Concrete Powder (RcCoP) 46
3.1.3. The thermal treatment procedure for reactivation of the HCeP and RcCoP 49

3.2. Investigation of the extent of reactivation of the HCeP and RcCoP 52
3.2.1. X-ray fluorescence (XRF) 52
3.2.2. Differential Scanning Calorimetry (DSC) and Thermogravimetry (TG) 53
3.2.3. X-Ray Diffraction (XRD) 53
3.2.4. Specific surface area 54
3.2.5. Scanning Electron Microscopy (SEM) and Energy Dispersive X-ray Spectroscopy (EDX) 54
3.2.6. Porosity and pore size distribution 55
3.2.7. Determination of strength 57
4. Reactivation of hydrated cement powder through thermal treatment 59
4.1. Experimental results 59
4.1.1. XRD and XRF 59
4.1.2. DSC – TG 66
4.1.3. Specific surface area 69
4.1.4. SEM and EDX 69
4.2. Discussion of the results 71
5. Reactivation of recycled concrete powder through thermal treatment 74
5.1. Experimental results 74
5.1.1. XRD and XRF 74
5.1.2. DSC – TG 82
5.1.3. SEM and EDX 87
5.2. Discussion of the results 90
6. Porosity and strength development 93
6.1. Strength results 93
6.1.1. Strength of HCeS 93
6.1.2. Strength of RcCoS 97
6.2. Porosity results 99
6.2.1. Porosity of HCeS 99
6.2.2. Porosity of RcCoS 101
6.3. Correlation between compressive strength, porosity, and median pore diameter .103
6.4. Discussion of the results 106
6.4.1. Discussion of strength results 106
6.4.2. Discussion of porosity results 107
7. Conclusions and recommendations 110
7.1. Conclusions 110
7.2. Recommendations 113
List of Figures 115
List of Tables 120

References.....121
Appendix.....134

List of Abbreviations

AFm	Monosulfoaluminoferrite
AFt	Trisulfoaluminoferrite
Al_2O_3	Aluminium oxide (alumina)
C_2S (Ca_2SiO_4)	Dicalcium silicate
C_2S_α	Dicalcium silicate alpha
C_2S_β	Dicalcium silicate beta
C_3A ($3CaO \cdot Al_2O_3$)	Tricalcium aluminate (Aluminate)
$C_3A \cdot 3CaSO_4 \cdot 2H_2O$	Ettringite
C_3S (Ca_3SiO_5)	Tricalcium silicate (Hatrurite)
C_4AF ($4CaO \cdot Al_2O_3 \cdot Fe_2O_3$)	Tetracalcium aluminoferrite
$Ca(HCO_2)_2$	Calcium formate
CaBr	Calcium bromide
CaCl	Calcium chloride
$CaCO_3$	Calcium carbonate (calcite)
CaO	Calcium oxide (lime)
$CaSO_4$	Gypsum (Calcium sulfate)
CC	Conventional Crusher
CDW	Construction and Demolition Waste
CH [$Ca(OH)_2$]	Calcium hydroxide
CO_2	Carbon dioxide
C-S-H	Calcium Silicate Hydrate
DhCeP	Dehydrated Cement Powder
DhCoP	Dehydrated Concrete Powder
DSC	Differential Scanning Calorimetry
DTG	Derivative thermogravimetry
EDX	Energy Dispersive X-ray spectroscopy
EF	Electrodynamic Fragmentation
Fe_2O_3	Iron oxide
FRcCoA	Fine Recycled Concrete Aggregates
HCeM	Hydrated Cement Mortar
HCeP	Hydrated Cement Powder
HCeS	Hydrated Cement Specimens
MgCl	Magnesium chloride
MIP	Mercury Intrusion Porosimetry
NA	Natural Aggregates
NaCl	Sodium chloride
OPC	Ordinary Portland Cement
RcCe	Recycled Cement
RcCo	Recycled Concrete
RcCoA	Recycled Concrete Aggregates
RcCoF	Recycled Concrete Fines
RcCoP	Recycled Concrete Powder
RcCoS	Recycled Concrete Specimen
RhCeM	Rehydrated Cement Mortar
RhCeP	Rehydrated Cement Powder
RhCeS	Rehydrated Cement Specimens
RhCoP	Rehydrated Concrete Powder

RhCoS	Rehydrated Concrete Specimens
RwCeP	Rewetted Cement Powder
RwCeS	Rewetted Cement Specimens
SC	Smart Crushing
SEM	Scanning Electron Microscopy
SiO_2	Silicon dioxide (quartz)
TG	Thermogravimetry
VCe	Virgin Cement
w/c	Water/cement ratio
XRD	X-Ray Diffraction

1. Introduction

1.1. Background and problem statement

Concrete is one of the principal construction materials in the world. **Meyer [1]** estimated the global annual concrete production as more than 10 billion tonnes. Subsequently, increasing demand for concrete was indicated by many researchers, specifying that it results in the depletion of the natural resources used to produce this massive amount of concrete needed for construction **[2–5]**. The construction, renovation, and demolition of buildings, roads, and bridges generate massive Construction and Demolition Waste (CDW), of which a considerable quantity is disposed-of. **Matias et al. [6]** stated that only 28% of 450 Mt of CDW produced in Europe every year is recycled and requested a need to increase the quantity of recycled CDW. This recycled CDW has been extensively studied and used as recycled aggregates in producing new concrete. Still, using fine recycled aggregates (< 2 mm) has been prohibited due to inadequate data.

Cement is the major component of concrete that has been magnificently used for decades. However, its production is responsible for about 7% of global CO_2 emissions and is energy-intensive because it is a thermal process at around 1450 °C **[7].** Therefore, reducing the need for cement used in construction is necessary to reduce CO_2 emissions. One of the best ways to achieve this goal is to make the reuse of Recycled Concrete Fines (RcCoF) possible. Previous research has specified that the heat treatment method can be conducted on these fines to replace part of the cement required for the new concrete production **[8, 9]**. This increased significance in the recycling of CDW is beneficial for protecting the environment by reducing the natural resources needed, the disposal of wastes to landfills, and particularly the CO_2 emissions through partial replacement of cement. In this research, the cement produced from the industry without material recycling is named Virgin Cement (VCe), the same as the commonly used term Ordinary Portland Cement (OPC).

Numerous researchers indicated the temperature ranges that explain different chemical processes occurring when Hydrated Cement Powder (HCeP) is subjected to heat treatments **[8, 10–14]**. This laboratory-produced powder results from crushing, grinding and milling the hydrated cement paste. Ultimately, this material is essential for this research, and its heat treatment serves as a basis to provide insights into what happens in the thermally treated recycled concrete fines. The thermal treatment causes the dehydration and decomposition of the hydration products, essentially ettringite ($C_3A{\cdot}3CaSO_4{\cdot}2H_2O$), Calcium Silicate Hydrate (C-S-H), portlandite ($Ca(OH)_2$), and calcite ($CaCO_3$) **[15]**.

The evaporable water from pores or cavities and parts of the physically bound water are initially liberated at around 105 °C. It is believed that water can be eliminated at 120 °C. The decomposition of ettringite occurs between 110 and 170 °C, while the C-S-H also starts to decompose. Portlandite decomposes in the temperature range of 400–550 °C, and calcite decomposition into lime (CaO) happens at high temperatures between 600 and 900 °C. Besides, some authors agree that partial initial anhydrous phases, such as larnite (C_2S_β) and brownmillerite (C_4AF), may remain unaltered during heating **[16, 11]**. Moreover, because alite (C_3S) is highly reactive, only a few authors, such as Wang et al. **[17]**, indicate that its anhydrous part may also remain. Apart from these phases, it is specified by different researchers that alpha quartz (SiO_2_α) converts to beta quartz (SiO_2_β) at around 580 °C only during the thermal treatment of RcCoF **[18, 8]**.

The HCeP exposed to the appropriate temperatures can recover some extent of its hydration capacity by releasing the free water and the water bound to the hydration products and undergoing the required chemical transformations **[10, 19]**. Thus, the above hydration products can be recovered during the rehydration of the dehydrated products. The rehydration of Dehydrated Cement Powder (DhCeP) results from the reactions of water with some phases (dehydrated) in DhCeP to form the new hydration products **[20, 16, 11].** The calcium silicate phases are formed during the thermal treatment in the suitable temperature range. Several researchers **[18, 21, 16, 22, 23, 11, 10]** have revealed that the best heating temperature range is 400 – 800 °C. However, they have also specified that partially dehydrated hydration phases transform when the HCeP is heated at a very high temperature above 800 °C. As a result, the compressive and flexural strengths are maximum with thermal treatment at the optimum temperature and decrease with pre-treatment above the optimum temperature. The latter is much less than the temperature required for VCe production **[16, 8, 10]**. Therefore, the recovered cement strength can estimate the reactivation potential, and there is a connection between the chemical transformations by thermal treatment and the achievable compressive and flexural strengths **[23]**.

The water binding ability regained when rehydrating the DhCeP comes with various properties compared to the hydration of VCe. The core of these differences is the higher water demand for standard consistency associated with the rehydration of DhCeP. A higher surface area causes this increased water demand. Besides, the free CaO produced during dehydration impacts the instantaneous reaction of dehydrated products, amplifying the water demand, decreasing the setting time, and affecting the achievable mechanical strength **[16]**. The same challenges have also been reported for the thermal treatment of Recycled Concrete Powder (RcCoP) **[24, 25]**.

Although an investigation on the thermal treatment of HCeP was previously conducted, **Lim and Mondal [26]** indicated a knowledge gap in a detailed characterization of the transformation changes. Additionally, it is crucial to assess the complete hydration by investigating the reactivation of the RcCoP by thermal treatment. Besides, this is the scenario that reflects the industrial conditions. Furthermore, there is an increased interest in investigating the recycling of old concrete wastes to produce fines that can partially replace the VCe in the concrete mixtures to solve the above-mentioned environmental problems. As for the HCeP, this powder obtained from old concrete recycling needs treatment to increase its binding activity, and thermal treatment can be conducted for this purpose. Nonetheless, the production method significantly impacts the quality of the obtained RcCoP. Different researchers have considered several approaches for the production of the RcCoF **[27–39]**, but this research used the Smart Crushing (SC) and the Electrodynamic Fragmentation (EF) methods to produce the RcCoP. Particularly, the RcCoP used is even finer than the RcCoF considered before.

Thermogravimetry and Differential Scanning Calorimetry (TG/DSC) are essential to determine the decomposition points of the non-heated and pre-heated HCeP and RcCoP. In addition, X-Ray Diffraction (XRD) is a typical technique to investigate the crystalline phase composition, and Scanning Electron Microscopy (SEM) is used to observe the microstructure evolution. Moreover, the strength of rehydrated HCeP and RcCoP is evaluated, and the Mercury Intrusion Porosimetry (MIP) is used for the porosity and pore size distribution assessment. All these methods have been previously successfully applied to these material types and provided reliable results **[16, 40, 11].** This research investigates the pre-treatment optimum temperature

for the reactivation of HCeP and RcCoP as a partial replacement of VCe in new concrete mixtures. Moreover, the process involved in strength development is extensively assessed.

1.2. Research objectives

Most research on recycling old concrete has focused on investigating the reuse of recycled concrete aggregates as a coarse fraction. However, the reuse of fine fraction (< 2 mm) can be more important, as specified in **Section 1.1**.

The main objective of this research is to reactivate the HCeP and RcCoP by thermal treatment for partial replacement of VCe in new mortar or concrete mixtures.

The following specific objectives were identified to achieve this principal objective:

- The production methods of HCeP and RcCoP need to be evaluated in detail to emphasize differences in the procedure and the resulting products.
- The investigation of the optimum thermal treatment temperature for HCeP and RcCoP is needed regarding the workability, setting time, porosity, and particularly the achievable strength.
- A phase formation analysis is required to assess the effect of thermal treatment on the recovery of the HCeP and RcCoP binding ability.
- Examining the rehydrated cement and concrete specimens under the microscope is necessary to evaluate the microstructure resulting from thermal treatment.
- Determining the mechanical strength is essential to evaluate the extent of strength recovery for reactivated HCeP and RcCoP and the degree of replacement of VCe in mortar.

2. State of the Art

This chapter discusses the literature related to the research objectives to the most recent findings and technologies. Three main parts can be differentiated after briefly describing the history of cement **(Section 2.1)**. The first part provides a general understanding of cement, from its production procedure to the hydration process, including the structure of strength development phases **(Sections 2.2 to 2.4)**. The second part **(Section 2.5)** focuses on the chemical transformations involved in the reactivation of hydrated cement. Finally, the third **(Section 2.6)** discusses concrete recycling, emphasizing the methods of producing recycled concrete powder.

2.1. A brief history of cement

The use of cement in construction started many years ago. It is believed that the history of cement dates before 1724, with the Romans as a material made of crushed rock mixed with burnt lime as a binder. The understanding of the material had advanced until 1824 when Joseph Aspdin named it Portland cement **[41]**. After then, several authors discussed the production process, use and characteristics of different cement types. In addition, the chemistry of cement has been extensively investigated, but all the authors agree that it is a very complex subject that needs continuous research. For example, in 1935, Sir Frederick Lea had already published a book on the chemistry of cement and concrete **[42]**.

Several other authors have contributed to the understanding of cement material. These authors include **Locher [41]** in 2006, who focused on describing the principles of production and use of cement. In 2014, **Kurdowski [43]** combined the progress in cement research until then and considerably contributed to an advanced understanding of cement and concrete chemistry from fresh to hardened state. Moreover, the book of Lea has been edited consecutively. The fifth edition in 2019 by **Hewlett and Liska [44]** has considered the relevancy and durability of different types of cement and concretes. Nevertheless, the awareness of high CO_2 emissions and depletion of raw materials requires finding an alternative to the increased need for cement in construction. Recycling and reactivating old concrete fines is one of the best solutions.

According to this brief history of cement, it is clear that the material has been enormously documented. However, there are remaining questions about the hydration of VCe, making it a highly complex material. Besides, its rehydration is as complex, maybe even more. Since the evaluation of reactivated cement relies on the extent of strength it can achieve when mixed with water; this chapter will focus on the properties related to strength development, especially for the first part. Moreover, the second part investigates the rehydration process.

2.2. Cement production and basics

2.2.1. Definition

The DIN EN 197-1 standard defines cement as a hydraulic binder, i.e. a finely ground inorganic substance that produces cement paste when mixed with water. This paste sets and hardens through hydration and, after hardening, remains solid and dimensionally stable even under water. Hydration involves chemical reactions between cement and water, resulting in hydraulic hardening by forming calcium silicate hydrates. However, other compounds like calcium aluminates can contribute to the hardening process. The most important use of cement is to produce mortar and concrete by binding the fine (max. particle size < 4mm) and coarse (max. particle size > 4mm) aggregates together, respectively, to form a strong building material **[41]**.

2.2.2. Classification of cement types

The differences in raw material deposits and climatic conditions contribute to the formation of different construction materials and, therefore, the development of different types of cement **[41]**. The DIN EN 197-1 standard describes the 27 European standard types of cement (CEM I – V). It specifies their compositions, required strength values and other essential criteria. The constituents of the European and German standard cement types include Portland cement clinker (K), granulated blastfurnace slag (S), pozzolanic material (P and Q), fly ash (V and W), burnt shale (T), limestone (L, LL), Silica fume (D), minor additional constituents (filler) (F), calcium sulfate, and cement admixtures (additives). Among these constituents, the Portland cement clinker, or simply clinker, is the most used. It is mainly made of calcium silicates (tricalcium silicate and dicalcium silicate) with a high CaO-bound content. It allows a reaction with the mixing water, resulting in a realistically rapid hardening.

The 27 European standard cement types are divided into five main types. They are principally differentiated according to their cement clinker and additives composition and the strength classes 32.5 N/R, 42.5 N/R and 52.5 N/R. N/R denote normal (standard) and rapid strength gain, respectively. In addition, it is permitted to add up to 5% of secondary components (minor additional constituents) to all cement types. Calcium sulfate (gypsum, anhydrite) is added in small quantities to control the setting time. **Table 2-1** shows a summarized version of the classification of cement types according to DIN EN 197-1 standard.

Table 2-1: Classification of cement types according to DIN EN 197-1 standard.

Designation	Additive	Cement type	Clinker content (%)
Portland cement		CEM I	95 - 100
Portland-composite cement	S, D, P, Q, V, W, T, L, LL, M (mixture)	CEM II/A	80 - 94*
		CEM II/B	65 - 79
Blastfurnace cement	S	CEM III/A	35 - 64
		CEM III/B	20 - 34
		CEM III/C	5 - 19
Pozzolanic cement	D, P, Q, V, W	CEM IV/A	65 - 89
		CEM IV/B	45 - 64
Composite cement	S, P, Q, V	CEM V/A	40 - 64
		CEM V/B	20 - 38

*Exception Portland silica fume cement with 90 - 94% clinker content

2.2.3. Composition and production of cement clinker

Cement clinker is a well-defined material documented by several authors **[45, 46, 43, 47, 44, 48, 41]**. It is obtained by calcining and sintering a mixture of raw materials at a high temperature (~1450°C). These raw materials contain the principal oxides calcium oxide (CaO), silicon dioxide (silica) (SiO_2), aluminium oxide (alumina) (Al_2O_3), and iron oxide (Fe_2O_3) in different proportions. The heating process is conducted in the rotary kiln. The process produces the four principal compounds of clinker: tricalcium silicate, dicalcium silicate, tricalcium aluminate, and tetracalcium aluminoferrite. Cement is obtained after finely grinding the cement clinker. **Table 2-2** indicates the representative oxide composition of general-purpose Portland cement with their weight percentages. These oxides are bound in the cement phases. Essentially, the highest content of CaO (64.67 wt. %) with moderate content of SiO_2 (21.03 wt. %) is identified for strength development. The content of the other oxides is much lower or negligible. **Table 2-3** shows that the C_3S content is considerably high in the typical phase composition of German cement clinker.

Table 2-2: Representative oxide composition of a general-purpose Portland cement © John Wiley & Sons, 2011 [49].

Oxide	Shorthand notation	Common name	Weight percent
CaO	C	lime	64.67
SiO_2	S	silica	21.03
Al_2O_3	A	alumina	6.16
Fe_2O_3	F	ferric oxide	2.58
MgO	M	magnesia	2.62
K_2O	K	alkalis	0.61
Na_2O	N	alkalis	0.34
SO_3	$\overline{S}$	sulfur trioxide	2.03
CO_2	$\overline{C}$	carbon dioxide	—
H_2O	H	water	—

Table 2-3: Typical German cement clinker phase composition © Verlag Bau+ Technik GmbH, 2006 [41].

Clinker phase	Chemical formula	Abbreviated formula	Content in % by mass
Tricalcium silicate (Alite)	$3CaO \cdot SiO_2$	C_3S	52 - 85
Dicalcium silicate (Belite)	$2CaO \cdot SiO_2$	C_2S	0.2 - 27
Calcium aluminoferrite (Aluminoferrite)	$2CaO \cdot (Al_2O_3, Fe_2O_3)$	$C_2(A,F)$	4 - 16
Tricalcium aluminate (Aluminate)	$3CaO \cdot Al_2O_3$	C_3A	7 - 16
CaO (free lime)		CaO	0.1 - 5.6
MgO		MgO	0.7 - 4.5

The production of cement clinker involves many chemical reactions, which mainly happen during pyroprocessing. **Figure 2-1** summarizes the cement clinker formation process during the pyroprocessing stage. This stage starts after the raw materials are fed to the rotary kiln.

The high temperature allows chemical and physical changes. Therefore, most of the energy required and operating costs are consumed here.

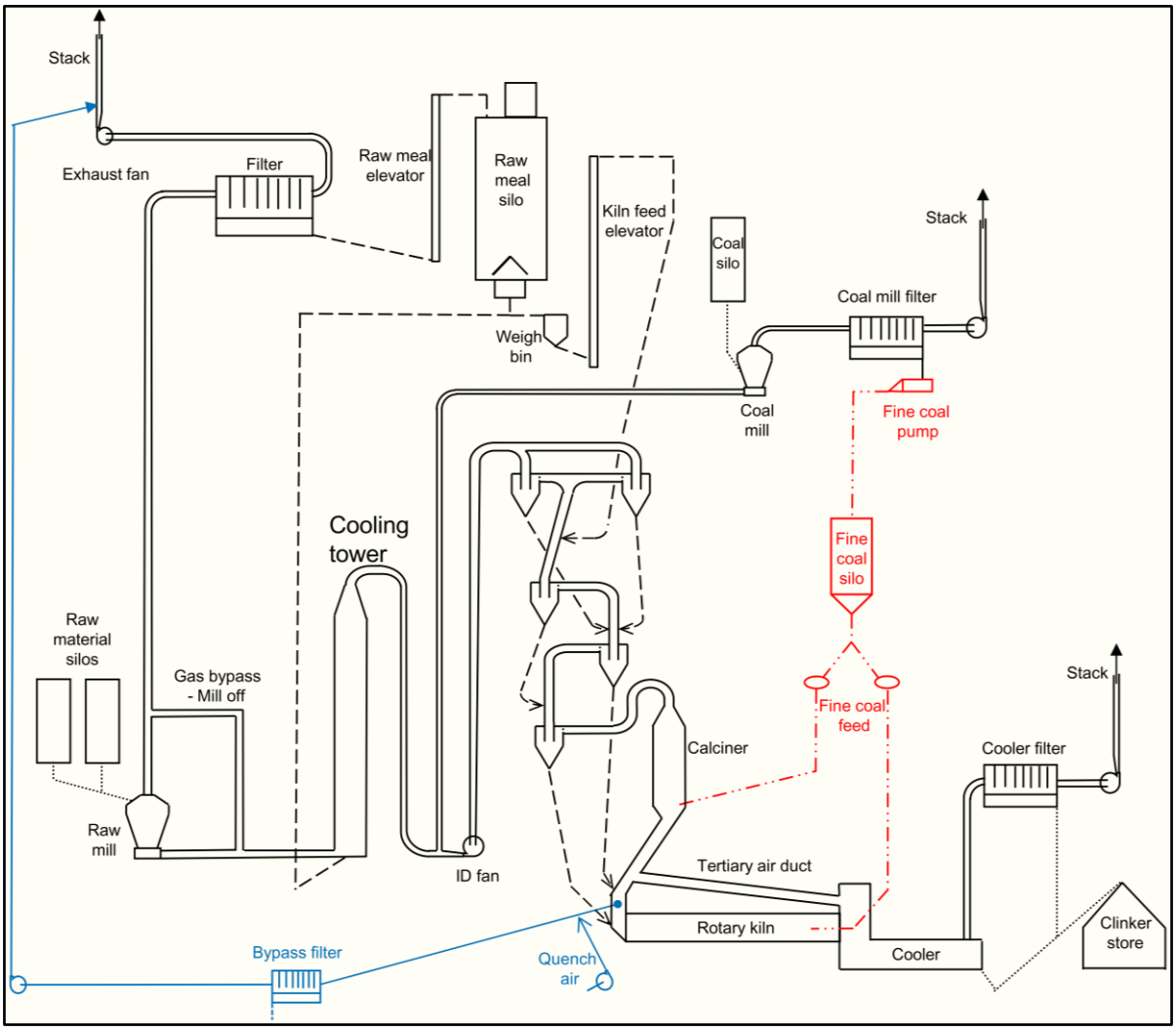

Figure 2-1: Pyroprocessing process for cement clinker formation © Elsevier, 2019 [44].

Figure 2-2 illustrates the reaction sequence and the temperatures at which they occur. The dehydration can start above 27 °C, while the dehydroxylation happens below 600 °C. The decarbonation happens between 550 °C and 1000 °C, while the aluminosilicates begin to break down above 600 °C. The solid-state reactions occur between 550 °C and 1280 °C. The latter marks the temperature when the liquid phase sintering happens. **Figure 2-3** shows that transforming the raw meal into cement clinker is associated with a temperature increase. The figure indicates that the decomposition of $CaCO_3$ into CaO and CO_2 (decarbonation) occurs above 700 °C, which marks the beginning of the formation of the cement clinker phases. Belite phase forms before alite phase, which forms at the highest temperature. The importance of C_3A and C_4AF phases for the liquid phase formation is indicated.

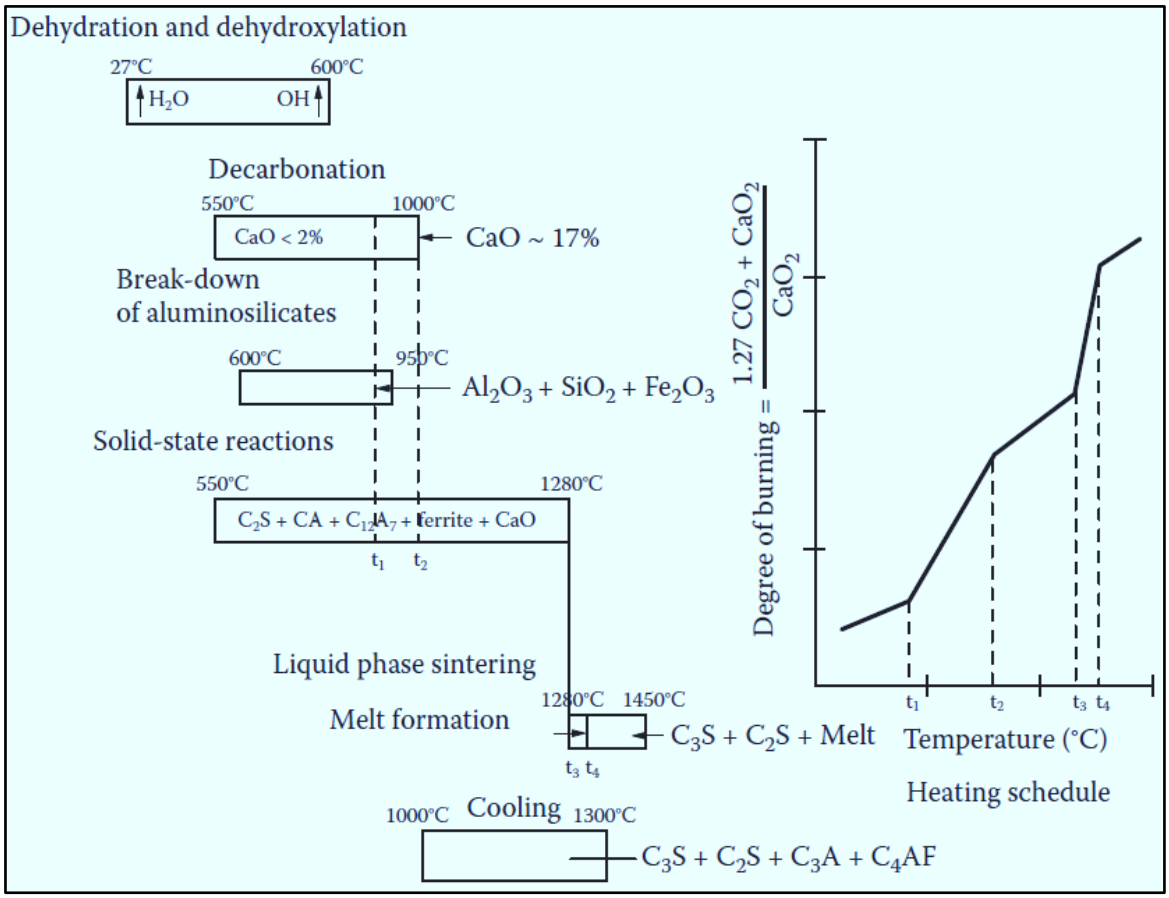

Figure 2-2: Reaction sequence during cement clinker production © Taylor & Francis Group, 2018 [45].

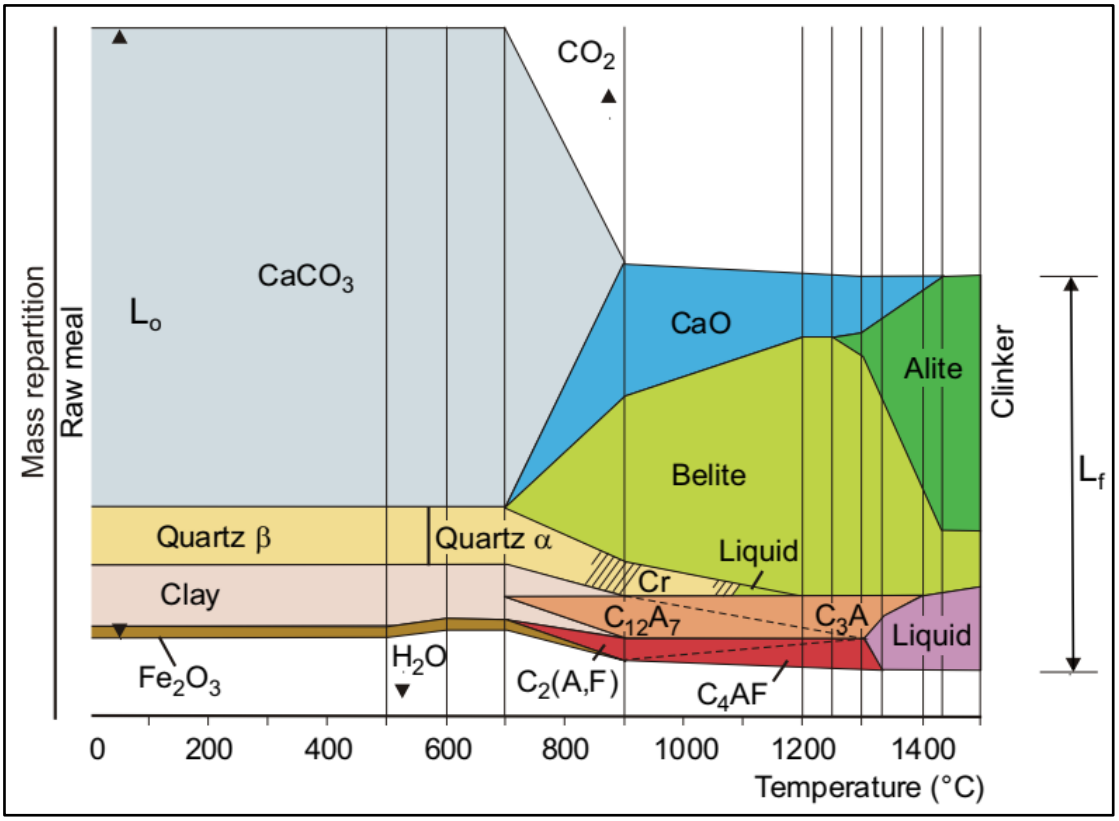

Figure 2-3: Transformation of the raw mix into cement clinker © Elsevier, 2016 [50].

2.3. Crystal structure of cement strength development phases

Several authors have indicated the four principal phases responsible for the strength development of cement **[44, 45, 47, 51–61]**. These phases are known as clinker phases. The first two phases contribute the most to the strength of cement, while the last two contribute less to strength but are very important for forming the liquid phase during firing in the clinkering process. Tricalcium silicate (alite) [$3CaO \cdot SiO_2$] hydrates and hardens rapidly, controlling the initial setting and early strength, whereas dicalcium silicate (belite) [$2CaO \cdot SiO_2$] hydrates and hardens slowly, contributing to the later age strength (generally after seven days). On the other hand, the tricalcium aluminate [$3CaO \cdot Al_2O_3$] releases a large amount of heat in the first few days, marginally contributing to early strength development. Tetracalcium aluminoferrite (ferrite) [$4CaO \cdot Al_2O_3 \cdot Fe_2O_3$] hydrates rapidly, slightly contributing to strength.

The crystal structures of cement development phases are complex. But they determine how the strength develops through reactivity with water **[43, 44, 47]**. One of the main reasons why the composition of these phases is very complicated is the isomorphism phenomenon in their elements. This phenomenon defines similarity in the crystalline structures of two or more substances of different chemical compositions. It is more pronounced for tricalcium aluminate (around 12 – 13 %) than for tetracalcium aluminoferrite (approximately 10 – 11 %), belite (about 6%), and finally alite (around 4 %). The following sections (**Sections 2.3.1** to **2.3.4**) summarize the aspects of the crystal structures of these phases towards strength development, according to Kurdowski **[43]**. In addition, the references above should be considered for more details on crystal structure formation.

2.3.1. Tricalcium silicate

Tricalcium silicate (C_3S) is the leading component of Portland cement clinker. It occupies over 55% of clinker weight and has high reactivity with water, which controls the cement paste hardening process. The crystal system of its pure compound is triclinic (T_1) and is stable at room temperature. However, the existing polymorph in clinker is monoclinic (M_1, M_3, or a mixture of them) since there are incorporated substituent ions such as Mg^{2+}, Al^{3+}, etc. **Figure 2-4** shows the seven polymorphs of C_3S and their formation temperatures. The triclinic forms (T_1, T_2, and T_3) exist at lower temperatures, from 620 °C to 980 °C, followed by the three monoclinic forms (M_1, M_2, M_3), finally reaching the rhombohedral form (R) at the highest temperature of 1070 °C. Switching forms back and forth with temperature change indicates the possibility of reversible phase transitions **[47]**.

$$T_1 \overset{620^\circ C}{\rightleftarrows} T_2 \overset{920^\circ C}{\rightleftarrows} T_3 \overset{980^\circ C}{\rightleftarrows} M_1 \overset{990^\circ C}{\rightleftarrows} M_2 \overset{1060^\circ C}{\rightleftarrows} M_3 \overset{1070^\circ C}{\rightleftarrows} R$$

Figure 2-4: Temperature formation of the C_3S polymorphs [47].

The crystal structure comprises independent SiO_4 tetrahedra joined by calcium ions also surrounded by oxygen atoms. Moreover, the crystal structure formation leads to irregular oxygen octahedra around the calcium ions. These irregularities create large voids in the structure where other atoms can find a place to occupy. The calcium ions coordination is irregular with variation in bond length from 254 to 324 pm **[43]**. Therefore, during cement paste formation, the water molecules can find enough room, indicating the substantial reactivity of C_3S and water, which explains the contribution of this phase to the strength development, especially at an early age. **Figure 2-5** illustrates the simplified representation of the structure

of tricalcium silicate. The calcium ions join the two tetrahedra columns (a) and (b). Positioning one of these columns on top of the other generates the total column. The letters A to F indicate the oxygen atoms surrounding the calcium ions, which are not part of the SiO_4 tetrahedra. Different simplifications are made, such as the whole surroundings of calcium ions that are not displayed.

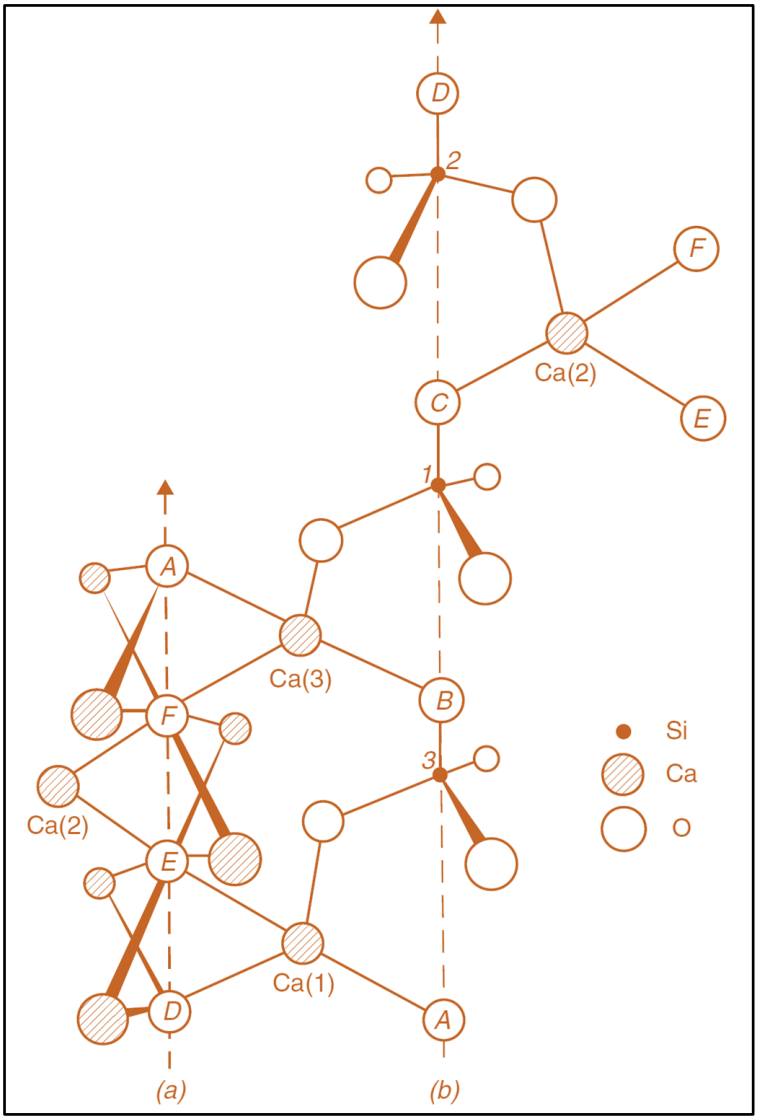

Figure 2-5: The simplified representation of the structure of tricalcium silicate © Springer, 2014 [43].

2.3.2. Dicalcium silicate

Dicalcium silicate (C_2S) makes four stable phases (α, $α'_H$, $α'_L$, and γ) at different temperatures and one unstable phase β. With a monoclinic structure, the phase β is the most present in cement and essential for its chemistry. **Figure 2-6** shows the temperature ranges for the stability of distinct polymorphic phases. This figure specifies that the polymorph γ is stable at a low temperature (< 500 °C), while the polymorphs $α'_H$ (high) and α form at high temperatures (1160 ± 10 °C and 1420 ± 5 °C, respectively). Furthermore, the phase transitions β → γ and γ → $α'_L$ are not reversible, while the others α ⇄ $α'_H$, $α'_H$ ⇄ $α'_L$, and $α'_L$ ⇄ β are.

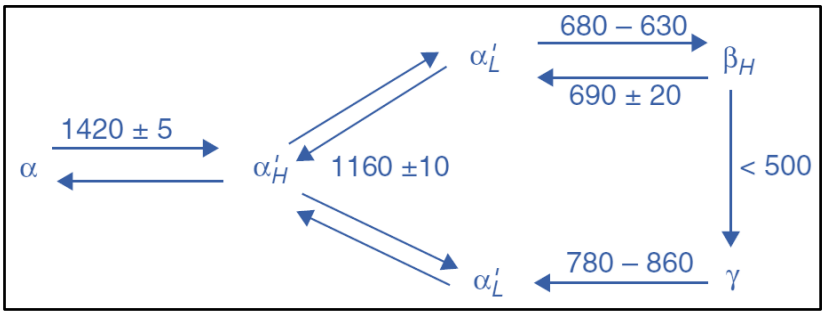

Figure 2-6: Temperature (°C) transformation of distinct C_2S phases © Springer, 2014 [43].

All polymorphs of the C_2S phase comprise independent SiO_4 tetrahedra joined by calcium atoms. However, the structural organization changes from one to another. Phase γ is stable at a low temperature with a rhombic crystal structure. With this phase, the hexagonal organization of oxygen ions creates irregularities between the silicate tetrahedra, inducing the variation in the Si–O distances from 158.9 to 172.5 pm. For phase α′ (α'_H and α'_L), the Si–O distance varies from 167 to 177 pm. This variation is from 157 to 164 pm for phase β, while the distance between the calcium and oxygen ions varies from 230 to 275 pm **[43]**. It is, therefore, noticeable that the voids created by irregularities in the structure for the C_2S phase are smaller than for the C_3S phase. Thus, the reactivity with water is reduced for C_2S than for C_3S, leading to a reduced contribution to initial strength development for C_2S. **Table 2-4** shows the structure types and calcium coordination, while **Figure 2-7** illustrates the C_2S_ β polymorph structure. The coordination of the SiO_4 tetrahedra and how the calcium atoms link them can be seen in this figure. The non-filled circles represent calcium atoms, the filled circles are silicon atoms, and the oxygen atoms constitute the triangles tetrahedra. Moreover, the numbers represent the heights of atoms.

Table 2-4: Structure of C_2S polymorphs © Springer, 2014 [43].

Phase	Structure type	Space group	Number of "molecules" in unit cell	Calcium coordination	Lattice constants, nm
γ	olivine type	orthorhombic $\frac{P2_12_12_1}{cmn}$	4	Ca(1) = 6 Ca(2) = 6	a = 0.5091 b = 0.6782 c= 1.1371
β	strongly deformed low K_2SO_4 type	monoclinic $P11\frac{2_1}{n}$	4	Ca(1) = 6 + 6 Ca(2) = 8	a = 0.928 b = 0.548 c = 0.676 b = 94°33' stabilised by Ba
α'_L	slightly deformed low K_2SO_4 type	Orthorhombic $Ccm2_1$ (others groups possible)	16	Ca(1) = 10 Ca(2) = 9	a = 1.880 b= 1.107 c = 0.685 stabilised byBa
α	Alternative type	Hexagonal $P6_3mc$	2	Ca(1) = 4 + 9 Ca(2) = 6 + 3	a = 0.545 c = 3·0.720 stabilised by V_2O_5

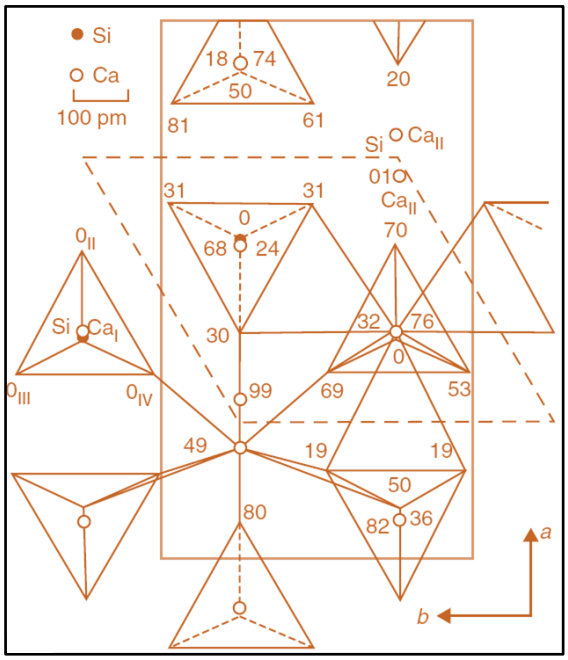

Figure 2-7: Representation of the structure of dicalcium silicate: C_2S_ β. Projection onto a – b plane © Springer, 2014 [43].

2.3.3. Tricalcium aluminate

The tricalcium aluminate (C_3A) structure comprises $[AlO_4]^{5-}$ tetrahedra. These tetrahedra form rings $[Al_6O_{18}]^{18-}$ that contain six AlO_4 groups in each corner, as illustrated in **Figure 2-8**. The rings $[Al_6O_{18}]^{18-}$ are bonded by calcium ions, occupying the holes (147 pm radius) that remain inside these rings. Different structures exist for this phase, such as the cubic structure (represented by **Figure 2-8 a**) or monoclinic and orthorhombic structures (represented by **Figure 2-8 b**) **[43]**. Since the holes remaining in the rings $[Al_6O_{18}]^{18-}$ are occupied by calcium ions, the voids not filled in the structure are limited for other atoms to find space. Therefore, during hydration, the water molecules cannot find enough space. Consequently, the reactivity with water is much reduced, making an insignificant contribution to strength development.

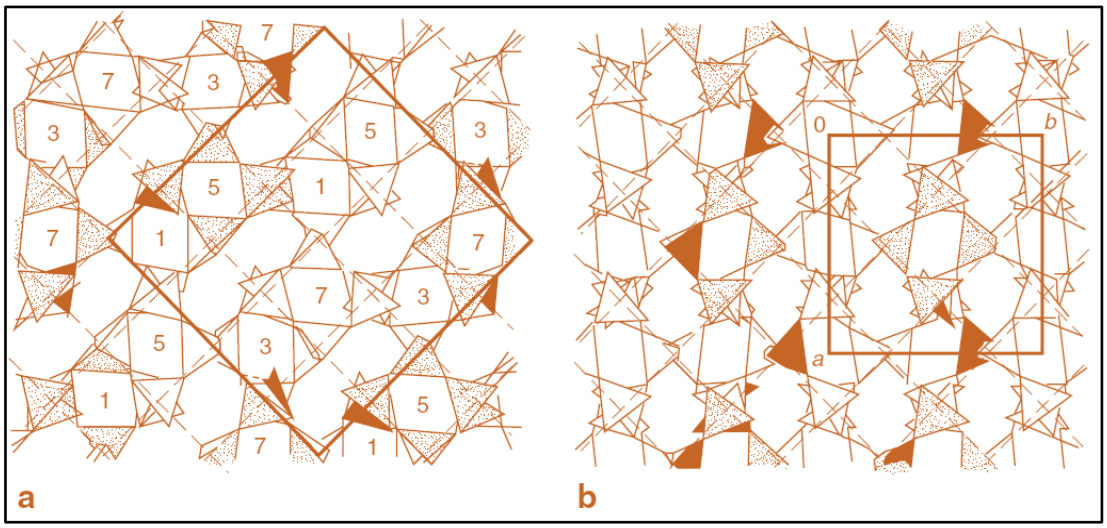

Figure 2-8: Representation of the structure of tricalcium aluminate showing the rings with six tetrahedra: a) Rings in a cubic structure, b) Rings in monoclinic and orthorhombic structures © Springer, 2014 [43].

2.3.4. Tetracalcium aluminoferrite

Figure 2-9 illustrates the structure of $Ca_2Fe_2O_5$. The total miscibility between C_2F ($Ca_2Fe_2O_5$) and C_2A ($Ca_2Al_2O_5$) makes the crystal structure of tetracalcium aluminoferrite (C_4AF) more complex. An orthorhombic lattice system with unit cell parameters a = 564, b = 1468, c = 539 pm is represented. For simplicity, the crystal structure of C_2F is illustrated within three axes, a, b, and c, with an emphasis along axis b. Through axis b, the layers of octahedra FeO_6 come next to tetrahedra FeO_4 without having common oxygen atoms. Due to the irregular coordination, there are holes between the oxygen ions occupied by Ca^{2+} ions. Besides, these calcium ions are surrounded by oxygen atoms. In addition, aluminium is generally distributed evenly between tetrahedra and octahedra **[43]**. Once again, since the calcium ions occupy the holes between the oxygen ions, the free space in the structure is limited for water molecules, contributing to minor strength development during hydration.

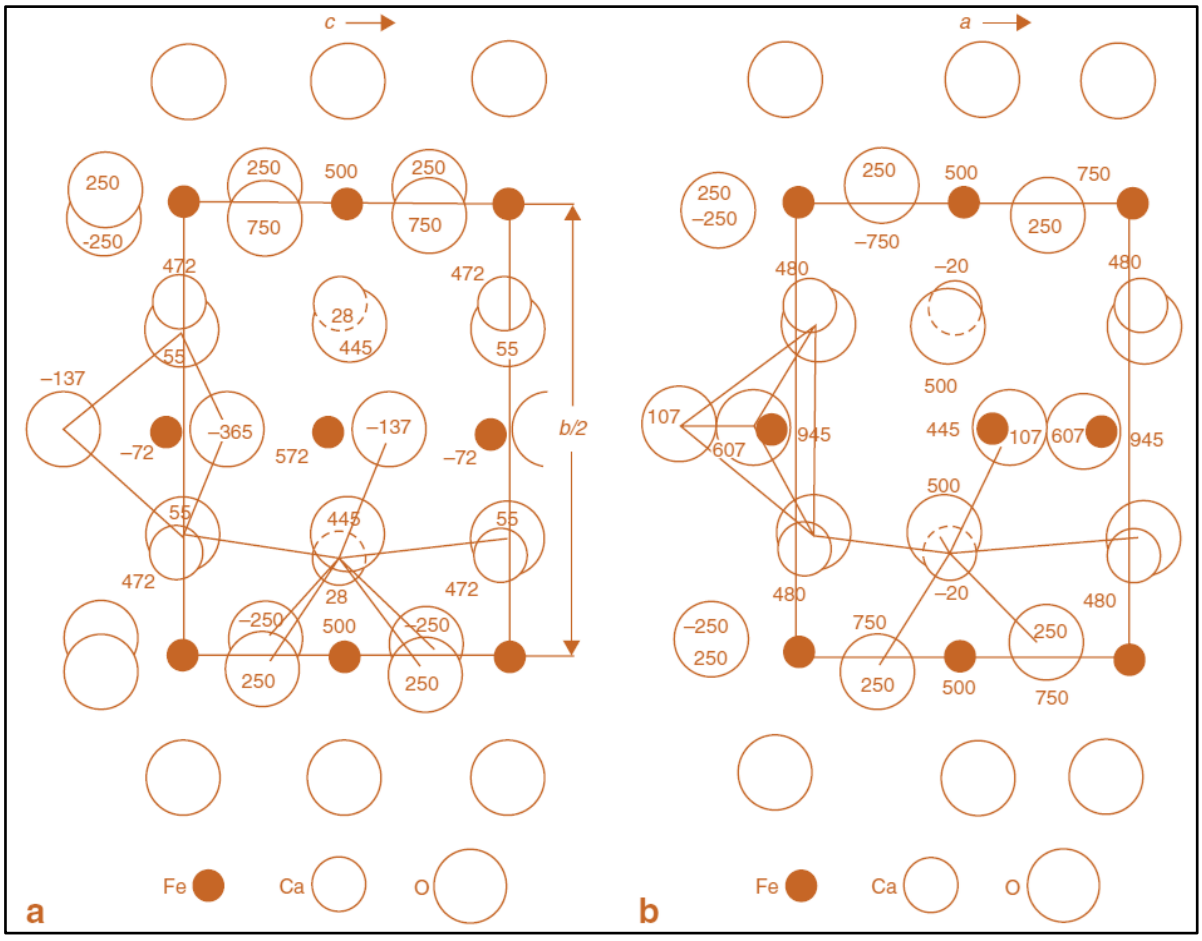

Figure 2-9: Representation of the $Ca_2Fe_2O_5$ structure: a) Through axis a b) Through axis c © Springer, 2014 [43].

2.4. Cement hydration

Cement hydration results from a mixture of cement and water during cement paste production, which is necessary for strength development. This mixture develops the binding ability of cement, allowing it to bind other materials, such as the fine aggregates (<4mm) during the production of mortar or both the fine and coarse aggregates (>4mm) during the production of concrete. Due to the chemical composition of cement, the hydration of cement is very complex and involves several chemical reactions and physical changes. Several researchers **[41, 43,**

44, 46–48, 61–63] have investigated cement hydration extensively for decades. The laboratory test results and the chemical and physical processes involved have been reported. However, as a very complex process, research is still needed to contribute to understanding cement hydration. In addition, it is necessary to investigate the hydration of cementitious materials that can replace cement to some extent to reduce the CO_2 emissions associated with cement production.

The hydration of cement results in different hydration products, and the main products are Calcium Silicate Hydrates (C-S-H) which are vital for hardening. Therefore, in a simplified way, cement hydration can be defined as a series of chemical reactions between cement particles and water, including chemical and physical processes, to form the C-S-H and other products for hardening. **Figure 2-10** indicates the phase composition of hydrated cement with time. It can be seen that the formation of hydration products increases significantly up to 28 days, and then slows down.

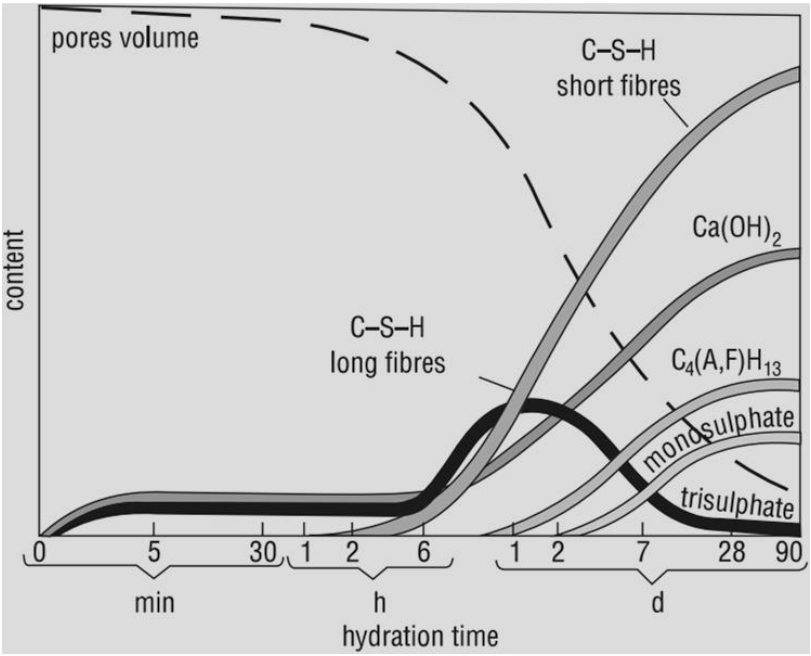

Figure 2-10: Phase composition of hydrated cement with time © Verlag Bau+ Technik GmbH, 2006 [41].

The mechanism of the hydration process is not simply breaking the bonds in crystal structure with water molecules. Alternatively, the reactions of the individual cement clinker phases with water co-occur, and therefore, there is an interference. In addition, the presence of minor components such as alkalis and sulfates modifies the composition of the liquid phase. The state parameters, such as temperature, pressure and concentration, and the cement properties, such as fineness and surface constitution, influence the hydration process **[44, 41]**.

This section discusses the hydration of cement, from the hydration of individual clinker phases to the properties of hardened cement paste. The cement hydration reactions are provided as well.

2.4.1. Hydration of clinker phases

The hydration of cement is a complex process. The chemical reaction of water with the individual clinker phases co-occurs, and minor constituents, such as alkalis and sulfates,

influence the liquid phase composition **[43]**. It is, therefore, necessary to discuss the hydration chemistry of clinker phases individually to understand their interaction during the hydration of cement later **[44, 46, 47]**. This section discusses the hydration process of all clinker phases; the tricalcium silicate (C_3S), dicalcium silicate (C_2S), tricalcium aluminate (C_3A), and tetracalcium aluminoferrite (C_4AF). However, more emphasis is given to C_3S as the principal clinker phase that dominates the early strength development **[49, 41]**. Several references are used to discuss these individual clinker phases **[41, 43, 44, 46–48, 61, 62, 50, 64, 65]**.

2.4.1.1. Hydration of tricalcium silicate (C_3S) and dicalcium silicate (C_2S) phases

It is essential to focus on the hydration process of the C_3S phase. This phase is the most dominant and vital constituent of cement clinker that significantly controls its strength development from setting to hardening **[44]**. Furthermore, it can represent the model for cement reaction with water because its heat evolution rate with time during hydration is similar to the overall rate of heat evolution in cement **[43, 50]**.

Several authors have specified the complexity of the reaction of C_3S with water and the need for more research for complete understanding **[46, 44, 47, 50, 56, 51, 60]**. Nevertheless, they have specified that the reaction products are calcium silicate hydrate (C-S-H) and calcium hydroxide (CH). **Equation (2.1)** indicates the hydration of C_3S. The x and y ratios of C/S and H/S, respectively, are the intrinsic characteristic of the C-S-H. CH is a defined hydrate phase, but the C/S and H/S ratios are variable. Moreover, C-S-H is poorly crystalline. This variability of C/S and H/S ratios and the C-S-H structure and chemical composition influence the hydration of C_3S. Details can be found in the indicated references.

$$C_3S+(3-x+y)H \rightarrow C_x\text{-}S\text{-}H_y+(3-x)CH \tag{2.1}$$

Two different hypotheses can explain what happens in the initial stage of hydration of C_3S. These are the congruent and incongruent dissolution. For the incongruent dissolution, it is believed that only the release of calcium ions into the solution occurs, and a layer rich in silicate is formed at the surface. This layer absorbs the calcium ions dissolved in the solution to form C-S-H. Increasing the C/S ratio in the solution is associated with forming C-S-H for the congruent dissolution. A saturated solution with the equilibrium is developed following a congruent dissolution **[43]**. **Equation (2.2)** indicates this solution.

$$Ca_3SiO_5+H_2O \rightleftarrows 3Ca^{2+}_{aq}+SiO^{4-}_4+2OH^-_{aq} \tag{2.2}$$

Section **2.3.2** states that the β polymorph is the C_2S polymorph mostly occurring in cement. Therefore, it is the most interesting. The hydration of β-C_2S is similar to that of C_3S since both phases form the C-S-H and CH. However, the progress of hydration of β-C_2S is slower, and the amount of CH produced is much less. Kurdowski **[43]** specified that this amount is three times lower, while Bye **[46]** indicated it is about five times lower than for C_3S. Equation **(2.3)** shows the hydration of C_2S.

$$C_2S+(2-x+y)H \rightarrow C_x\text{-}S\text{-}H_y+(2-x)CH \tag{2.3}$$

2.4.1.2. Hydration of tricalcium aluminate (C_3A) and tetracalcium aluminoferrite (C_4AF) phases

The hydration reactions of aluminates with gypsum (calcium sulfate [$CaSO_4$]) form the two groups of phases named the trisulfoaluminoferrite hydrates (AFt) and monosulfoaluminoferrite hydrates (AFm) **[50]**. Ettringite [$C_3A{\cdot}3CaSO_4{\cdot}2H_2O$], the main AFt, is formed when C_3A reacts with the sulfate ions under gypsum addition. However, when the concentration of gypsum in the solution becomes low, ettringite can react with aluminate ions ($Al[OH_4]^-$) to form the monosulphate phase [$C_3A{\cdot}CaSO_4{\cdot}12H_2O$] (AFm) **[43]**. Ettringite is a crystalline phase, successfully detectable by XRD and identified as needle-like or rod-like crystals in SEM. **Figure 2-11** shows the structural model of ettringite. The mint circles represent the water molecules, the blue structures the CaO_8 polyhedra, the yellow structures the SO_4^{2-} tetrahedra, and the red structures the $Al(OH)_6^{3-}$ octahedra.

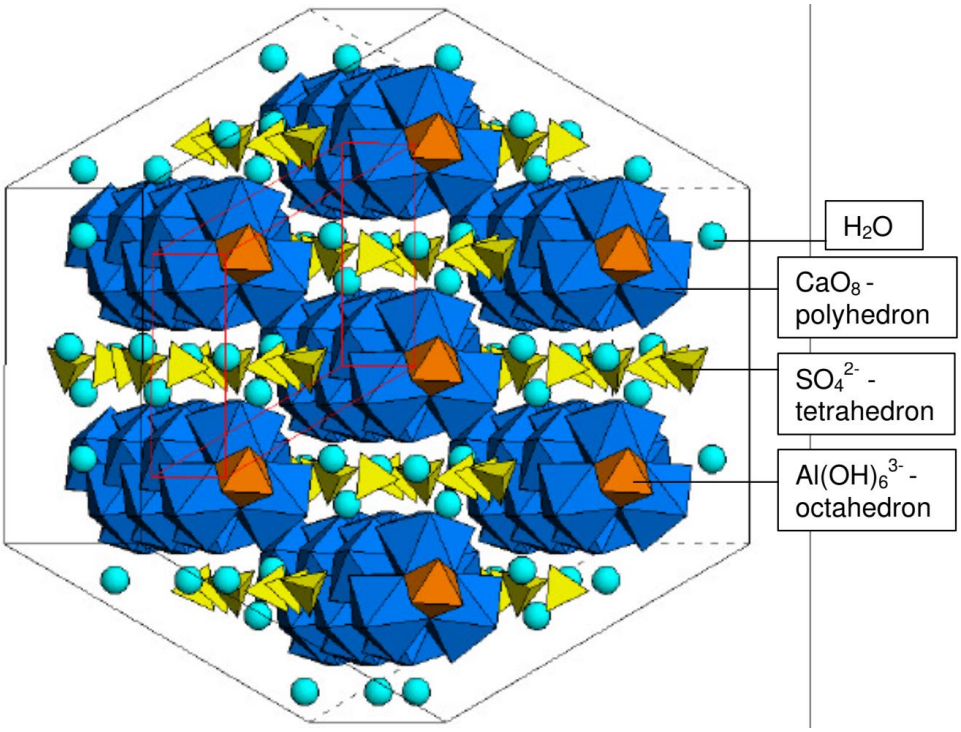

Figure 2-11: Structural model of ettringite [66].

C_3A is the most reactive cement clinker phase. Thus, its hydration mainly affects the rheological properties of cement paste **[43, 50, 44]**. Similarly, depending on the conditions, its hydration can lead to a flash set, a very rapid and unwanted setting that negatively affects the mechanical properties. Therefore, it is vital to consider the hydration of C_3A in the absence or presence of calcium hydroxide (portlandite) and calcium sulfate (gypsum).

In the absence of gypsum and portlandite, the hydration of C_3A rapidly results in gel products that grow at the surface of the C_3A grains. These products then crystallize into the hexagonal hydrates C_2AH_8 and C_4AH_{19}. The precipitation from the liquid phase by diffusion of ions through the layer of hexagonal hydrates contributes to more C_2AH_8 and C_4AH_{19}. Subsequently, these hydrates transform into the cubic C_3AH_6, which is thermodynamically stable. This transformation is necessary to disrupt the layer of hexagonal hydrates that slow down the hydration by acting as a barrier, and therefore, the hydration speed increases again. In the presence of portlandite, only the hexagonal hydrates C_4AH_{19} form due to deceleration of the reaction rate, which avoids the flash set. Once more, these hydrates convert to the stable cubic

C_3AH_6 **[47, 44, 43, 46]**. **Equation (2.4)** shows the hydration reaction of C_3A in the absence of gypsum, while **Figure 2-12** illustrates the process.

$$2C_3A+21H \rightarrow C_4AH_{19}+C_2AH_8 \rightarrow 2C_3AH_6+9H \quad (2.4)$$

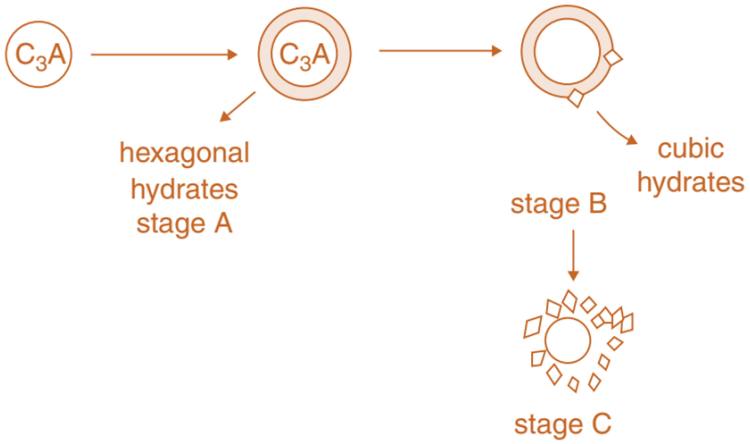

Figure 2-12: The process of hydration of C_3A in the absence of gypsum © Springer, 2014 (After Ref. [43]).

In the presence of gypsum ($C\bar{S}H_2$), there is the precipitation of ettringite according to **Equation (2.5)**:

$$C_3A+3C\bar{S}H_2+26H \rightarrow C_6A\bar{S}_3H_{32} \quad (2.5)$$

However, as discussed above, when there is a depletion of ettringite, monosulfoaluminate forms according to **Equation (2.6)**:

$$2C_3A+C_6A\bar{S}_3H_{32}+4H \rightarrow 3C_4A\bar{S}H_{12} \quad (2.6)$$

Figure 2-13 illustrates the process of hydration of C_3A in the presence of gypsum.

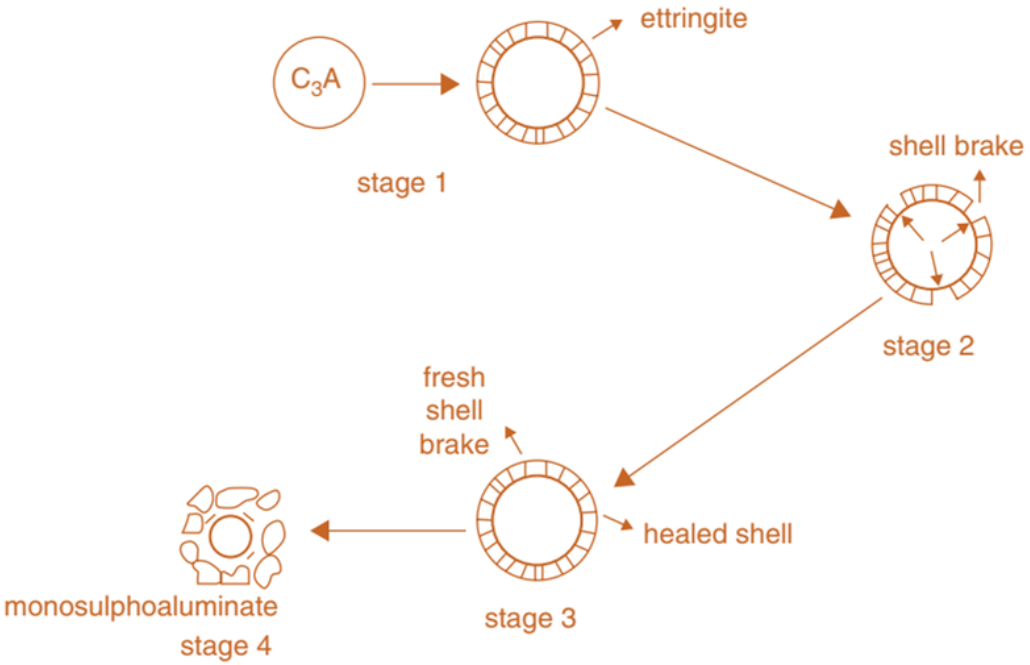

Figure 2-13: The process of hydration of C_3A in the presence of gypsum © Springer, 2014 (After Ref. [43]).

The hydration process of C_4AF is similar to that of C_3A. In the absence of gypsum, the AFm phases $C_4(A,F)H_{19}$ and $C_2(A,F)H_8$ form initially. These metastable iron substituted phases then convert into $C_3(A,F)H_6$, which decomposes to C_3AH_6 and $Fe(OH)_3$ at high temperatures. In the presence of gypsum, an iron-substituted AFt phase forms and then converts into AFm with gypsum depletion. The ferrite-ettringite ($C_6(A,F)\bar{S}_3H_{32}$) forming is similar to the ettringite from the C_3A hydration. However, some proportion of aluminium is replaced by iron during the hydration of C_4AF. **Equation (2.7)** represents the hydration of C_4AF in the presence of gypsum, while **Equation (2.8)** represents the hydration of C_4AF after gypsum depletion.

$$C_4AF+3C\bar{S}H_2+21H \rightarrow C_6(A,F)\bar{S}_3H_{32}+(F,A)H_3 \quad (2.7)$$

$$C_4AF+C_6(A,F)\bar{S}_3H_{32}+7H \rightarrow 3C_4(A,F)\bar{S}_3H_{12}+(F,A)H_3 \quad (2.8)$$

2.4.2. Cement hydration stages

Many researchers **[41, 43, 46–48, 50]** specify the five stages of cement hydration, identified with a heat flow curve obtained by the isothermal calorimetry. These stages include the pre-induction period (stage I), the induction period (stage II), the acceleration period (stage III), the deceleration period (stage IV), and the curing phase (stage V). **Figure 2-14** shows the heat flow curve and stages of cement hydration by the isothermal calorimetry. The figure indicates the heat flow rate and the duration concerning each stage.

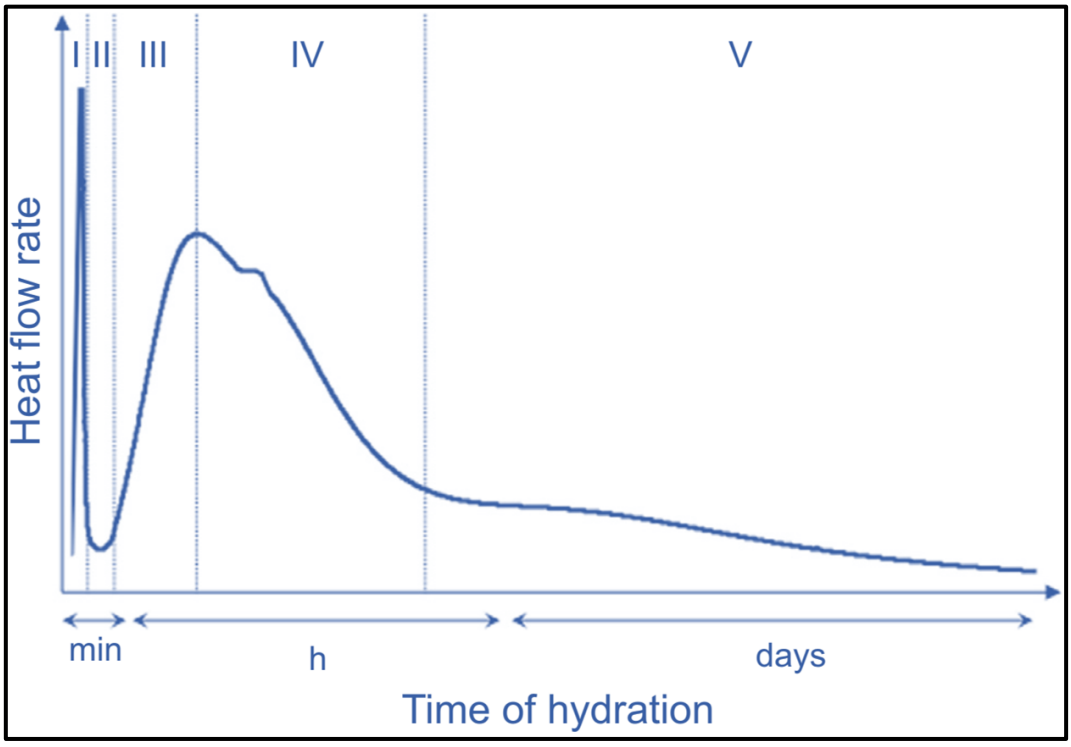

Figure 2-14: Heat flow curve and stages of cement hydration by isothermal calorimetry © Elsevier, 2016 [50].

The following section briefly describes the chemical processes involved in the stages of cement hydration.

- **Pre-induction period (I):**

  This stage starts immediately after contact between water and cement and lasts a few minutes. Rapid dissolution of alkali sulfates, calcium sulfate, tricalcium silicate (C_3S), and tricalcium aluminate (C_3A) happens. The dissolution of C_3S produces the C-S-H phase, while C_3A produces the ettringite (AFt) phase after reacting with calcium ions (Ca^{2+}) and sulfate ions (SO_4^{2-}). Both phases precipitate at the cement particle surface. Only a tiny fraction of dicalcium silicate reacts in this stage, while the ferrite phase reacts similarly to C_3A. The deposition of the hydration products layer on the cement grain surfaces slows the early fast hydration down.

- **Induction period (II):**

  This stage is characterized by a slowdown of the hydration reaction and, therefore, a low heat release. It lasts for a few hours. The C-S-H layer covers the surfaces of silicates and blocks their hydration. Additionally, a dense layer of ettringite on the aluminate surfaces prevents them from further dissolution. As a result, the concentration of Ca^{2+}in the liquid phase becomes supersaturated, but that of SO_4^{2-} remains constant due to more dissolution of calcium sulfate.

- **Acceleration period (III):**

  During this stage, the nucleation and growth of hydration products result in hydration acceleration. It is characterized by high heat release and lasts for several hours. More C-S-H is formed following the acceleration of hydration of C_3S. Moreover, the C_2S starts to hydrate considerably, contributing to the C-S-H formation. The concentration of Ca^{2+} in the liquid phase reduces due to the concurrence precipitation of the calcium hydroxide (portlandite) that happens alongside strength formation. Besides, the concentration of SO_4^{2-} also decreases as the calcium sulfate dissolves fully. This total dissolution leads to additional AFt formation and the adsorption of SO_4^{2-} on the C-S-H surface. Furthermore, portlandite crystals grow into the interstices of the grains of clinker phases, and the C-S-H grow into the pore solution. Therefore, the viscosity of the cement paste increases, leading to a rigid consistency and early strength development.

- **Deceleration period (IV):**

  This stage starts after the second peak is reached, which indicates the transition from the acceleration period to the deceleration period. A decrease in non-reacted cement clinker constituents impacts the slowing down of the hydration rate. As a result, the heat of hydration decreases progressively. However, the formation of the C-S-H phase continues due to the hydration of the remaining amount of C_3S and C_2S. On the other hand, the concentration of SO_4^{2-} in the liquid phase decreases as the calcium sulfate depletes. Hence, the monosulfoaluminate phase is formed after the ettringite reacts with the remaining C_3A.

- **Curing phase (V):**

  After deceleration, the cement hydration process continues for months or years until all the cement clinker constituents have reacted. However, it is necessary to have the required water/cement ratio; otherwise, the hydration may stop before all clinker constituents have

reacted. Since there is a small amount of remaining cement clinker constituents, the hydration is diffusion-controlled and progresses very slowly, having a minor influence on the heat flow. This stage is characterized by the polycondensation of SiO_4 tetrahedra that increases the C-S-H chain length. Thus, the mechanical strength increases continuously but at a considerably low rate.

2.4.3. Factors influencing the strength development of cement paste

The formation of hydrated products during the hydration of cement, i.e. the formation of calcium silicate hydrates and calcium aluminate hydrates, is the principal process for the strength development of cement paste. However, some other aspects need to be considered for the strength development of cement. The influence of these aspects is briefly described below:

- **Clinker composition:**

C_3S contributes to very high short-time strength development, and then the strength increases gradually. On the other hand, C_2S contributes to low short-time strength development but reaches a reasonably high final strength. Both the C_3A and C_4AF contribute little to strength development. Therefore, the hydration of individual clinker phases contributes to different strength development rates. Furthermore, the content of these specific clinker phases depends on the cement type. **Figure 2-15** shows the contribution of the individual clinker phases to strength development. The compressive strength is evaluated with respect to the duration of hydration.

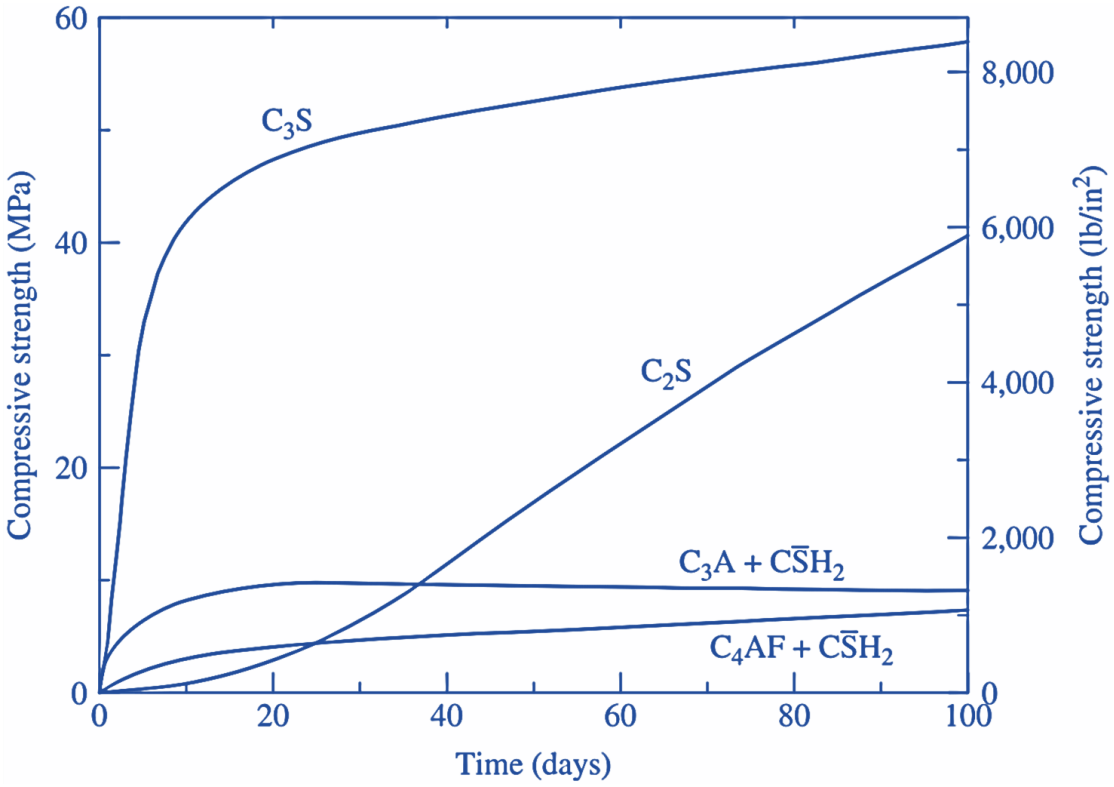

Figure 2-15: Contribution of the individual clinker phases to strength development in relation to hydration time © John Wiley & Sons, 2011 [49].

- **Cement composition:**

Several researchers have investigated the influence of cement composition on the strength development of cement paste **[67–74]**. These authors have indicated the complexity of this

influence, which depends on the interactive ratios of clinker phases, the condition of calcium sulfate (gypsum) added, and the minor oxides included.

The interference between the reactions of clinker phases during hydration modifies the contribution of each one to the strength development separately. Therefore, the relationship between the ratio of clinker phases and cement strength is not linear, and cement strength is not the sum of the strengths of individual clinker phases. Nevertheless, C_3S is the principal phase contributing to the strength of cement for all hydration times.

Although the clinker phase composition is the main factor determining the strength development of cement, the extent is influenced by the other cement constituents. For example, the presence of minor oxides affects the achievable cement strength. The oxides that have been extensively investigated include the alkali oxides K_2O and Na_2O **[67, 68, 70, 75, 76]**. In general, the initial strength of cement increases with an increase in these alkali oxides content, but strength after 28 days decreases. However, the results are not uniform. Also, the type and amount of gypsum added to control the setting influences the total strength of cement. With the same cement composition, the highest strength is achieved with the type and amount of gypsum that obtains the optimal delayed setting. The quantity of gypsum that results in the optimum strength depends on the clinker phase composition, the hydration time, the fineness of cement, and the type of gypsum added **[77, 69, 78, 68, 79]**.

- **Additives:**

The effect of additives is to accelerate or retard hardening. Several additives can accelerate the hardening of cement paste. These additives include calcium chloride (CaCl), calcium bromide (CaBr), sodium chloride (NaCl), magnesium chloride (MgCl), calcium sulfate ($CaSO_4$), calcium formate [$Ca(HCO_2)_2$], and hardened and then finely ground cement paste. They shorten the induction period of the C_3S and considerably accelerate the reaction in the following hydration phase. They also accelerate the hydration of C_2S **[53, 80–82]**. As a result, calcium silicate hydrates richer in CaO are formed, allowing hydration to proceed faster. As a result, the possible compressive strength increases. This increase is directly proportional to the increase in additive content but reaches a maximum using around 2% by mass and decreases with higher content **[44, 83, 80, 84–86, 47, 87]**. In practice, calcium sulfate is the most used; a higher quantity is needed than for setting control.

On the other hand, many other additives are used to retard the hardening of cement paste. These include heavy metal compounds (such as zinc and lead salts), phosphates, borates, silicofluorides, organic compounds (such as sugar-like compounds), and organic acids (such as tartaric acid and citric acid and their salts) **[41]**. They extend the induction period of C_3S without affecting further hardening as long as enough water is available for hydration. Therefore, storing them in water is better, and the achievable strength can be higher than without the additive. With the prolongation of the induction period of C_3S, the amount of C_3A reacting in the pre-induction period tends to increase, and a remarkable setting acceleration can result **[88–92]**. Only a few percent by mass of retardation additives is enough to delay the hardening of cement paste. It is specified that the formation of reaction-hindering hydroxide layers causes this delay. These layers form on cement grains and the surfaces of the hydration products **[93, 94, 47, 89, 95, 96]**.

- **Fineness and particle size distribution:**

The extent of cement grinding is significant for strength development. The specific surface area of cement, which results from the degree of fineness, highly influences the degree of hardening

and, therefore, the strength development. The finer the cement is ground, the more its specific surface area and degree of strength development. The reaction between the surface area of cement grains and the mixing water determines the initial hardening and the amount of hydration products formed. However, the strength increase with increasing fineness has a limit, which is reached for late strengths than early strengths **[97–101]**.

Similarly, different researchers have investigated the influence of the particle size distribution of cement on the strength development of cement paste **[102, 98, 101, 97, 72, 103]**. **Figure 2-16** shows the strength development of cement paste per particle size fractions. The finest proportion (< 3µm) of cement particles is essential for the early hardening and strength development, while the portion between 3µm and 25µm mainly governs the rest of strength development. A fraction greater than 50µm hardens slowly and does not significantly control the strength development **[41]**. Therefore, the achievable strength increases with the narrowing of the particle size distribution, i.e. with an increase in the percentage of fines.

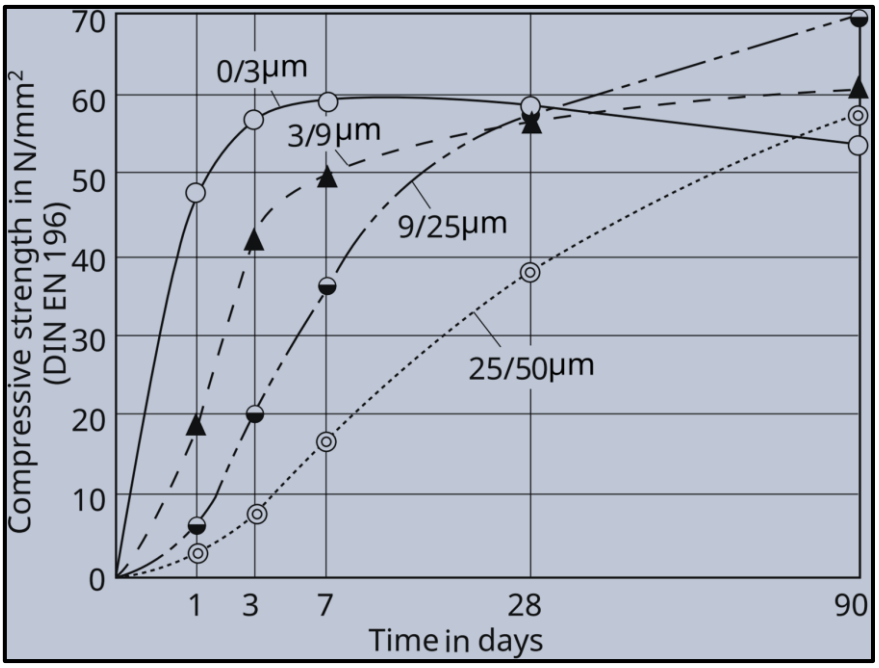

Figure 2-16: The strength development of cement paste per particle size fraction © Verlag Bau+ Technik GmbH, 2006 [41].

- **Water cement (w/c) ratio:**

The w/c ratio highly influences the strength development of cement paste. Strength develops through hydration, which cannot happen without adding water to cement. Hydration allows the formation of hydration products essential for setting, hardening, and, therefore, strength development. The w/c ratio < 0.4 is enough for complete hydration, but more water may be required for necessary workability **[41]**. However, excess water causes the formation of voids called capillary pores, reducing the strength of cement stone **[104, 41, 105–110]**. Hence, the amount of water that produces cement paste of standard consistency is considered the measure of water requirement. This amount depends on different factors, mainly the cement phase composition and fineness **[111–114]**. The finer the cement, the more water is required.

- **Temperature during hardening:**

Higher temperatures accelerate the hydration reactions, the setting and the hardening of the cement paste, while lower temperatures delay these processes in cement stone formation. The effect on the strength development of the cement stone depends on the cement composition. Although the initial strength is mainly affected, the final strength tends to be higher after storage at a lower temperature than higher temperature. With storage at a low temperature, more long-fiber calcium silicate hydrates form, increasing the strength. Storage at a high temperature accelerates hardening and generates structural stresses reducing strength. Additionally, it is specified that thicker layers of hydration products form on the surface of the cement grains, impeding further hydration **[115, 41, 116–118, 44]**.

2.4.4. Correlation between the microstructure and strength of cement paste

The microstructure of the hardened cement paste can be defined as the structural arrangement of the hydration products, the cement not yet hydrated, and the pores between them. Since these pores result mainly from the mixing water effects, the amount of water contained and how it is bound to the hydration products determine the physical and engineering properties of the hardened cement paste **[41, 44, 43, 46]**.

Understanding the relationship between the cement stone microstructure, the type of bonds that bind the cement paste components, and the material characteristics is essential for interpreting the strength formation. However, C-S-H, which is the vital cement paste component, is amorphous, making the interpretation complex **[44]**. Bensted and Barnes **[65]** have specified that the C-S-H gel constitutes around two-thirds of the solid phase of a typical cement paste, as indicated by **Table 2-5**.

Table 2-5: Composition of a type I hardened Portland cement paste (w/c = 0.5) © Informa UK Limited, 2002 [65].

Component	*Approximate volume %*	*Remarks*
C-S-H	50	Amorphous, includes microporosity
CH	12	Crystalline
AFm[a]	13	Crystalline
Unreacted cement	5	Depends on hydration
Capillary pores	20	Depends on w/c ratio

The strength cannot simply be associated with the cohesion forces between the cement paste components but also the porous structure of the hardened state. Essential bonds in cement paste include the ionic-atomic bonds and the van der Waals forces **[119–122]**. The idea of strength formation dependence on the interconnecting of the needle-like, fibrous C-S-H particles has been replaced by the theory of bond formation between the C-S-H crystallites. The liquid phase supersaturation controls the formation of these bonds. There is a balance between the degree of solution supersaturation and the forces keeping the crystals in position. The stresses and pressure of crystallization are linked, with lower values resulting in high strength **[123–127]**.

The curing method strongly influences the microstructure of the cement paste. Curing in water or under atmospheric conditions results in different pore structures since the latter is associated with water release during drying, causing irreversible changes in the hardened cement paste structure. Typically, the hydration products fill the space initially occupied by water and cement grains. However, drying under atmospheric conditions during hydration allows partial vaporization of water from larger pores that will not be filled with the hydration products. As a result, a very porous microstructure (including large pores) forms and reduces strength in the end **[43, 44, 46]**. Water present in cement paste can be divided into different categories, such as water adsorbed on the surface of solid phases, water in gel and capillary pores, water in hydrates and constitutional water (OH groups), crystallization water, water in the C-S-H gel structure, and free water located in macropores and additional voids **[128, 129, 107]**.

The total porosity is not a sufficient parameter to determine the strength of hardened cement paste. The pore structure, pore size distribution, morphology and size of crystals characterizing the solid phase must also be considered **[130, 131, 129, 132]**. **Jambor [133]** specified that the association between the strength and porosity is dissimilar for cement pastes resulting from the same w/c ratio with different degrees of hydration or the same degree of hydration with different w/c ratios. The w/c ratio influences both; the porosity and the properties of the hydration products. As a result, there is a lower amount of bound water on the hydration products produced from low w/c ration. Therefore, the morphology and size of the hydration products are more homogeneous, leading to increased binding capacity.

Although the porosity is insufficient to describe the strength development, it is still essential. **Taylor [134]** indicated that the forces incorporating the particles are more significant for cement paste with high porosity. Besides, having an increased amount of non-crystallized products is beneficial. On the other hand, the bonds joining the crystallites are less critical for the cement paste with low porosity. In this case, the components are very close and gain an increased potential for strength control. Nevertheless, several researchers have indicated that the influence of pore size is more important than just the total porosity. They have proven that the strength increases with a decreased mean radius of pores and higher minimum pores content in the total porosity **[135–140]**, as indicated by **Figure 2-17**. Moreover, the classical fracture mechanics applied to the cement pastes states that the total porosity does not control the strength. Instead, it is governed by the size of the biggest pores that are the source of “cracks” **[141–148]**.

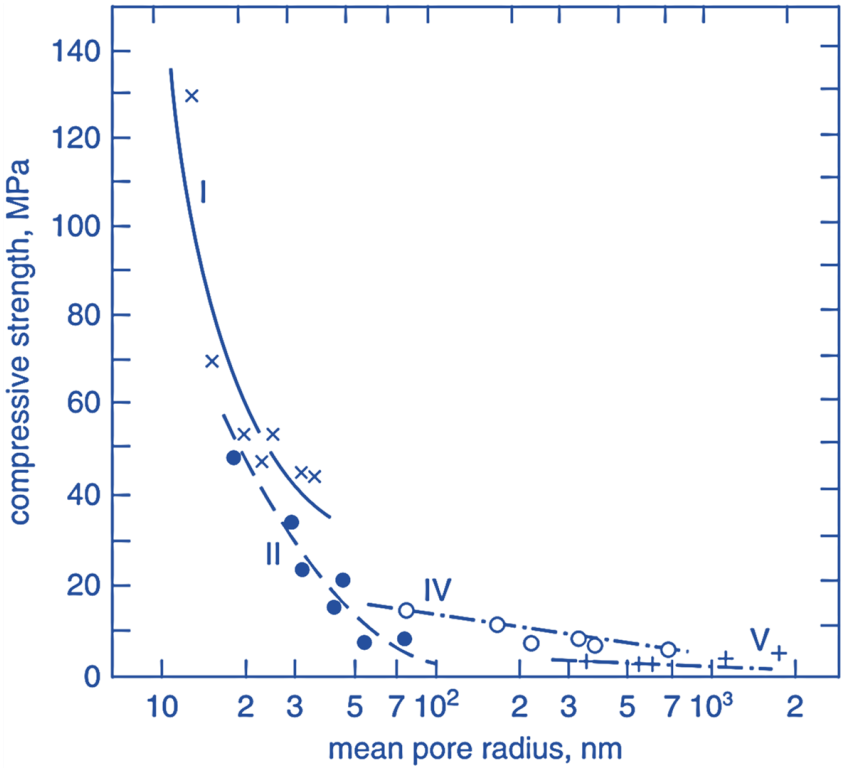

Figure 2-17: Influence of the mean pore radius on the strength of hardened cement paste. I: sample made of mainly tobermorite, II: mainly C-S-H (I), IV: 70-80% hydrogarnets and 20-30% C-S-H (I), V: mainly hydrogarnets (C_3AH_6) © Springer, 2014 [43].

2.5. Reactivation of hydrated cement and recycled concrete powders

Previous sections of this chapter have focused on the Ordinary Portland Cement (OPC), its production, structure and strength development phases, and the hydration process. The OPC was named Virgin Cement (VCe) to emphasize that it is the original material directly obtained from industry before any recycling. This section discusses the findings associated with the reactivation of Hydrated Cement Powder (HCeP) and Recycled Concrete Powder (RcCoP). The HCeP is obtained after crushing and milling the laboratory-made cement paste cured for less or equal to 28 days, while the RcCoP is obtained from recycling old concrete after many years in a building.

The reactivation of HCeP and RcCoP can be defined as the procedure combining dehydration and rehydration of dehydrated HCeP and RcCoP. Thus, dehydration can be defined as the thermal treatment process to allow the necessary chemical transformations and phase transitions to increase reactivity and recover the hydration ability. Similarly, rehydration is mixing the dehydration products and water to let the hydration process occur again.

2.5.1. Dehydration of HCeP and RcCoP

The dehydration of HCeP and RcCoP is a complex process involving different chemical transformations. Thermogravimetry (TG) and Differential Scanning Calorimetry (DSC) are the main techniques that several researchers have used to assess the chemical changes associated with thermal treatment. These transformations can recover the hydration capacity depending on the dehydration temperature **[10, 19]**. As a result, there is a release of free water and water bound to the hydration products, dehydration of hydration products and chemical decompositions leading to phase transitions.

Section 1.1 indicates the temperature ranges in which the chemical processes occur **[8, 10–15]** during the thermal treatment of HCeP and RcCoP. These chemical processes include the liberation of evaporable water from pores or cavities and the physically bound water, the transformation of C-S-H gel, the decomposition of ettringite, the dehydroxylation of portlandite, the decarbonation of calcite and the conversion of α-quartz to β-quartz. The following paragraphs provide details on the influence of these processes on the dehydrated phase formation depending on the thermal treatment temperature by comparing the results from different researchers.

Alonso et al. [11] used **Figure 2-18** to illustrate the chemical transformations resulting from the thermal treatment of cement paste for a sample submitted to a large temperature gradient from a heated to a non-heated side. They revealed that the phases present from the heated face at 650 °C (including 750 °C) were dehydrated C-S-H CaO, Larnite, and dehydrated ettringite. All these phases existed between 650 °C and 600 °C, with the calcite phase not yet decomposed. Between 600 °C and 450 °C, the phases were modified C-S-H, declining ratios of dehydrated C-S-H and CaO, and anhydrous phases such as larnite and dehydrated ettringite. Between 450 °C and 200 °C, the extant phases were portlandite, partially dehydrated C-S-H, modified C-S-H, dehydrated C-S-H, calcite, anhydrous phases and dehydrated ettringite. Between 200 °C and 100 °C, the phases present were slightly dehydrated C-S-H, portlandite, calcite, anhydrous phases, and dehydrated ettringite. The phases in the non-dehydrated region (below 100 °C) were C-S-H, portlandite, ettringite and anhydrous phases.

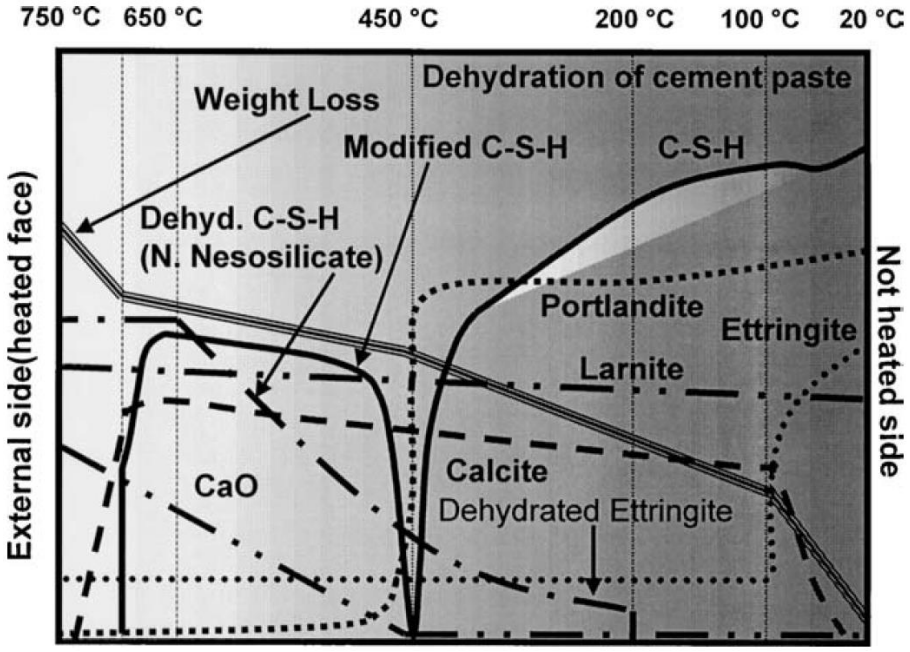

Figure 2-18: Chemical transformations resulting from thermal treatment of cement paste © Springer Nature, 2004 [11].

Many researchers used the TG and DSC techniques to assess the temperatures at which the chemical transformations happen during the thermal treatment of cementitious materials. In this regard, **Pavlik et al. [149]** performed the TG and DSC in the temperature range of 25 °C to 1000 °C in an argon atmosphere. They indicated that the thermal treatment of HCeP involves three prominent endothermic peaks. The HCeP was obtained from cement paste cured for 2, 7, and 28 days, and these curing times were compared.

The DSC results specify that the first peak occurs between 50 °C and 250 °C and is due to the release of physically bound water from pores and dehydration of C-S-H gels. Other researchers **[150, 12, 151–153, 18]** state that the dehydration of ettringite also happens below 200 °C. The second peak occurs between 420 °C to 520 °C and is due to the decomposition of portlandite. The third peak happens between 650 °C to 800 °C due to the decomposition of calcite. Additionally, the decomposition of vaterite is identified for a curing time of 7 and 28 days. However, this phase is an unstable polymorph of calcium carbonate, and its decomposition point is not always identifiable.

The TG results indicate that the chemical transformations happening at these three prominent peaks are associated with mass loss, which increases with peak intensities. The first peak is associated with a mass loss of about 12% for HCeP cured for two days. This mass loss is the highest as the first peak is the most intense. The second peak mass loss is about 3 % for a two days cured sample, while the mass loss for the third peak is around 2.5 %. The mass loss decreases with the hydration, except for the third peak, which mainly results from carbonation. Several other authors confirm the presence of these three prominent peaks, although the chemical transformation temperature ranges may vary slightly **[154–166]**. **Figure 2-19** shows the DSC-TG curves of thermally treated HCeP according to Pavlik et al. **[149]**.

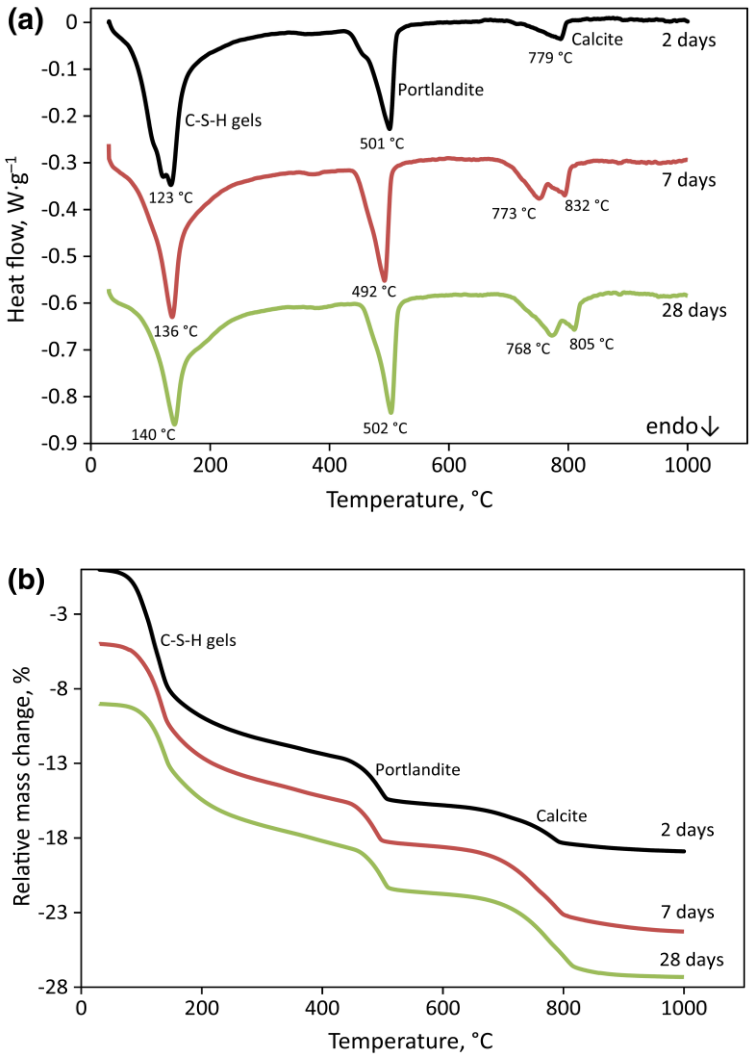

Figure 2-19: DSC-TG curves of thermally treated HCeP according to Pavlik et al.(a) DSC; (b) TG © Springer Nature, 2016 [149].

Shui et al. [18] confirmed the three principal peaks related to the thermal treatment HCeP but also identified a peak associated with the conversion of α'-quartz to β-quartz, occurring around 576 °C, during thermal treatment of the Fine Recycled Concrete Aggregates (FRcCoA) obtained from crushing and milling of concrete used for many years. **Figure 2-20** shows the DSC-TG curves of thermally treated HCeP and FRcCoA according to Shui et al.

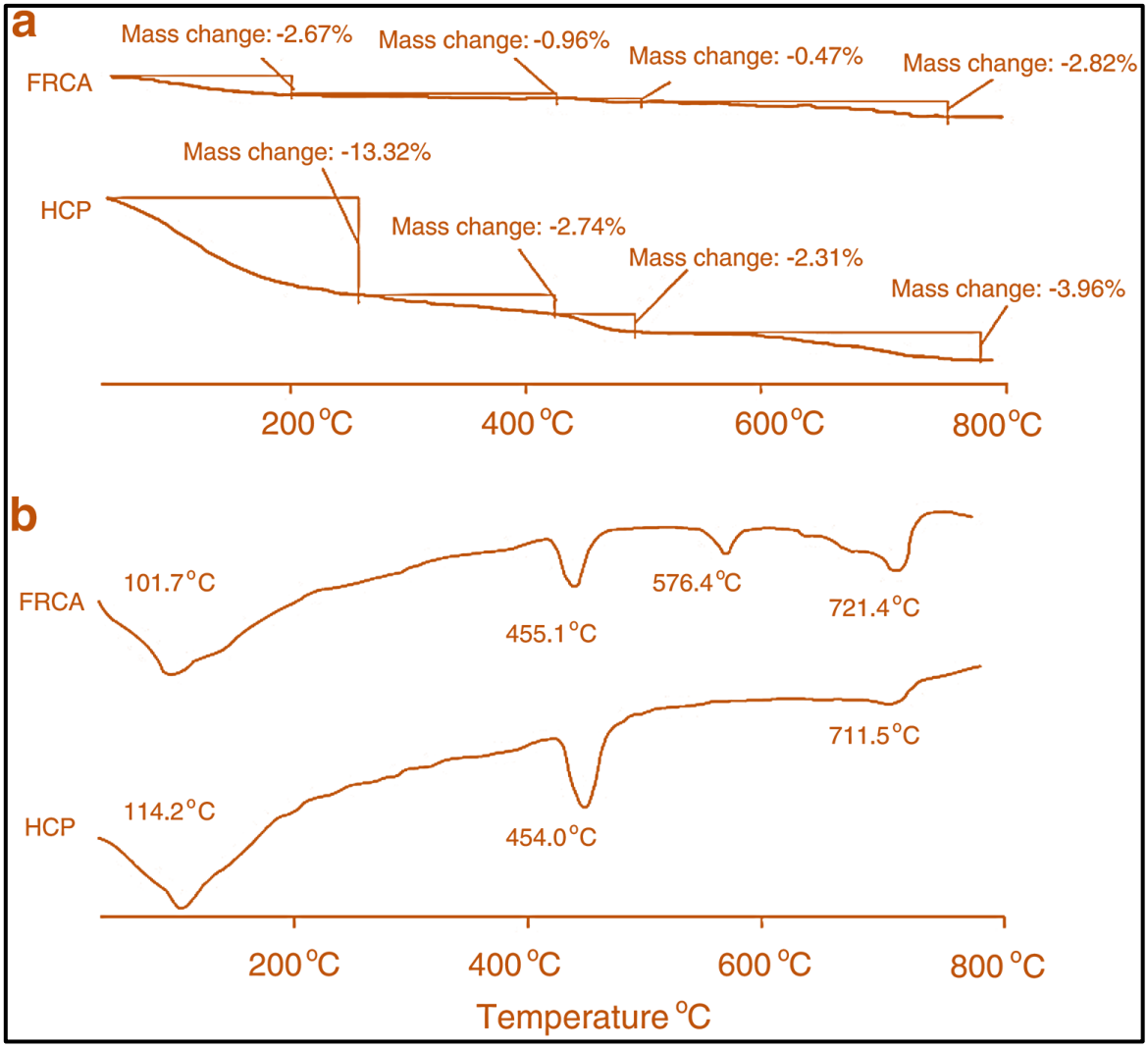

Figure 2-20: DSC-TG curves of thermally treated HCeP and FRcCoA according to Shui et al. (a) TG; (b) DSC © Elsevier, 2008 [18].

The phase transitions associated with thermal treatment are the main factor that controls the rehydration ability and, therefore, hydraulic binding properties. In **Table 2-6, Carriço et al. [24]** showed the phase transitions that happen in the thermoactivated cementitious materials by different selected authors. The current phases are presented according to the dehydration temperatures. These dehydrated phases are influenced by the treatment time, the heating rate, the cooling procedure, the particle size, and, more importantly, the material type.

Table 2-6: Phase transitions in thermoactivated cementitious materials © Elsevier, 2020 [24].

Treatment temperature (°C)	Treatment duration (hours)	Heating rate (°C/min)	Cooling procedure	Particle size (μm)	Dehydrated phases	Precursor material
200	1	10	Natural cooling	<75	C-S-H, CH, C_2S, $CaCO_3$, 4CaO. $Al_2O_3Fe2O_3$	Fine recycled concrete aggregates
500					CH, CaO, C_2S, $CaCO_3$, 4CaO. $Al_2O_3Fe_2O_3$	
800					CaO, C_2S, $CaCO_3$, 4CaO. $Al_2O_3Fe_2O_3$	
400	1	n.d	Rapid cooling	n.d	β-C_2S, CH	Cement paste
650					β-C_2S, CaO	
900					β-C_2S, CaO	
750	1	n.d	Rapid cooling	n.d	–	Concrete
700, 750, 800	1.5	10	Natural cooling	n.d	–	Cement paste
650	4	10	Rapid cooling	<75	–	Cement paste
600	2	n.d	n.d	<75	quartz, tobermorite, CaO, β-C_2S, $CaAl_2Si2O_8$	Autoclave aereated concrete
700					quartz, tobermorite, β-C_2S, $CaAl_2Si_2O_8$, CaO, CS	
800					quartz, β-C_2S, $CaAl_2Si_2O_8$, CaO, CS, α-C_2S	
900					quartz, β-C_2S, $CaAl_2Si_2O_8$, CaO, CS, α-C_2S	
200	2	5	n.d	<125	CH, $CaCO_3$, C_2S, C_4AF	Cement paste
400					CH, $CaCO_3$, C_2S, C_4AF	
600					CH, $CaCO_3$, anhydrite II, C_2S, C_4AF	
800					CH, $CaCO_3$, anhydrite II, C_2S, C_4AF	
300, 500, 650	2	10	Rapid cooling	<150	–	Cement paste
660–940	2.5	10	Natural cooling	<75	A′-C_2S, β-C_2S, $CaCO_3$, C_4AF, CaO	Cement paste
700	1.5	10	600 °C/min	<100	α'_H-C_2S, γ-C_2S, CH, $C_{12}A_7$, C_4AF, $CaSO_4$	Cement paste
800					α'_H-C_2S, β-C_2S, CaO, $C_{12}A_7$, C_4AF	
900					β-C_2S, α'_H-C_2S, CaO, $Ca_5(SiO_4)_2SO_4$, C_4AF	
120	8	7	Natural cooling	<150	CH, 1.2 nm tobermorite, jennite, $CaCO_3$	Cement paste
450					0.96 nm tobermorite, disordered jennite, $CaCO_3$	
750					C_2S, CaO, CS	
600	4	n.d	Natural cooling	<100	–	Waste concrete
500	2	n.d	n.d	<150	quartz, $CaMg(CO_3)_2$, $CaCO_3$, C_2S, $Ca(OH)_2$	Cement paste

In comparison to ordinary cement, they specified that dehydrated cement contains no tricalcium silicate (C_3S) phase, increased amount of free lime, and the dicalcium silicate (C_2S) phase is present in different polymorphs (α'-C_2S and β-C_2S). Moreover, dehydrated cement can comprise partially dehydrated phases, residual hydration products, and anhydrous cement products. Therefore, the differences in the hydraulic properties of ordinary and dehydrated types of cement are expected. Since the C_3S phase is the most highly reactive and controls the strength development to the highest extent **[49]**, the dehydrated cement is expected to develop less strength after rehydration.

XRD is a typical technique to identify the phase transitions resulting from the thermal treatment of HCeP and RcCoP. Several authors have previously used this technique successively. **Real et al. [167]** used it to identify the phase transitions in the thermoactivated recycled cement treated between 400 °C and 900 °C. They labelled the ordinary cement as PC, the untreated hydrated cement powder as NT, and thermoactivated recycled cement as RC, followed by the dehydration temperature. The NT was obtained from a CEM I 42.5R cement type mixed with water (w/c of 0.55) crushed, ground and milled after three months of curing.

Figure 2-21 shows the XRD analysis of PC, NT and RC, showing all the phases present. The PC contains the typical clinker phases, such as larnite (β-C_2S), alite (C_3S) and gypsum, while the NT contains the characteristic phases of PC paste, such as portlandite (CH), C-S-H and ettringite, with calcite and other carbonated aluminate phases, resulting from the carbonation of the paste during storage and milling. The RC treated at 400 °C to 500 °C indicates that the decomposition of hydration products leads to the dehydration of C-S-H into tobermorite and the disappearance of ettringite. The RC treatment from 600 °C and above specifies complete depolymerization of C-S-H indicated by the absence of tobermorite. As a result, the C_2S peak number and intensity increase. The RC treated at 600 °C to 750 °C contains α_L'-C_2S, the highly reactive polymorph of C_2S, which suggests the optimum strength development dehydration temperature range, while the presence of many peaks of less reactive polymorph β-C_2S in the RC treated at 800 °C and 900 °C suggests a decrease in strength after subsequent rehydration.

Figure 2-21: XRD analysis of PC, NT and RC. ∆ portlandite; † calcite; * ettringite; ∞ gypsum; © CaO; ■ C_3S; ● tobermorite; ▼ C-S-H; x β-C_2S; ▲ α'$_L$-C_2S; ○ C_3A; □ calcium aluminum iron oxide; ◊ brownmillerite; Φ alumohydrocalcite; ⊖ calcium aluminum oxide carbonate hydrate [167].

Similarly, **Florea et al. [8]** investigated the phase transitions resulting from the thermal treatment of Recycled Concrete Fines (RcCoF). The RcCoF was produced by crushing and milling the laboratory-made concrete (a mixture of ordinary cement, sand, gravel and water) after curing for around one year. The Smart Crushing (SC) method was used for concrete separation into initial components. This method doesn't crush all the constituents arbitrarily as the ordinary crusher. Instead, it uses a limited crushing force that will not harm the aggregates so that the cementitious fines can be separated from coarse aggregates.

Figure 2-22 shows the XRD analysis of the gravel, RCF-20, RCF-500, and RCF-800 samples. The thermal treatment of RcCoF results in similar phases, but different chemical transformations occur. They assessed these changes by considering two heating temperatures, 500 °C and 800 °C, and labelled the dehydrated RcCoF materials as RCF-500 and RCF-800. In addition, they denoted the untreated RCF-20. The XRD analysis reveals that the single main phase in the gravel sample used in the concrete mixture is α-quartz (SiO_2), while all the other samples (RCF-20, RCF-500, and RCF-800) contain α-quartz, C_2S, portlandite, calcite and lime.

However, the reduction of the portlandite peak intensity for RCF-500 reveals that the portlandite phase decomposition had started. In contrast, the presence of more intense peaks of lime for RCF-800 shows the decomposition of calcite into lime. The increase of the C_2S peak intensities in the RCF-800 specifies an enhanced formation of a calcium-rich silicate phase, which is a positive indication of strength development. Nevertheless, crushed silica aggregates contribute to the presence of α-quartz, which dominates the phase content in all samples, deteriorating the strength development.

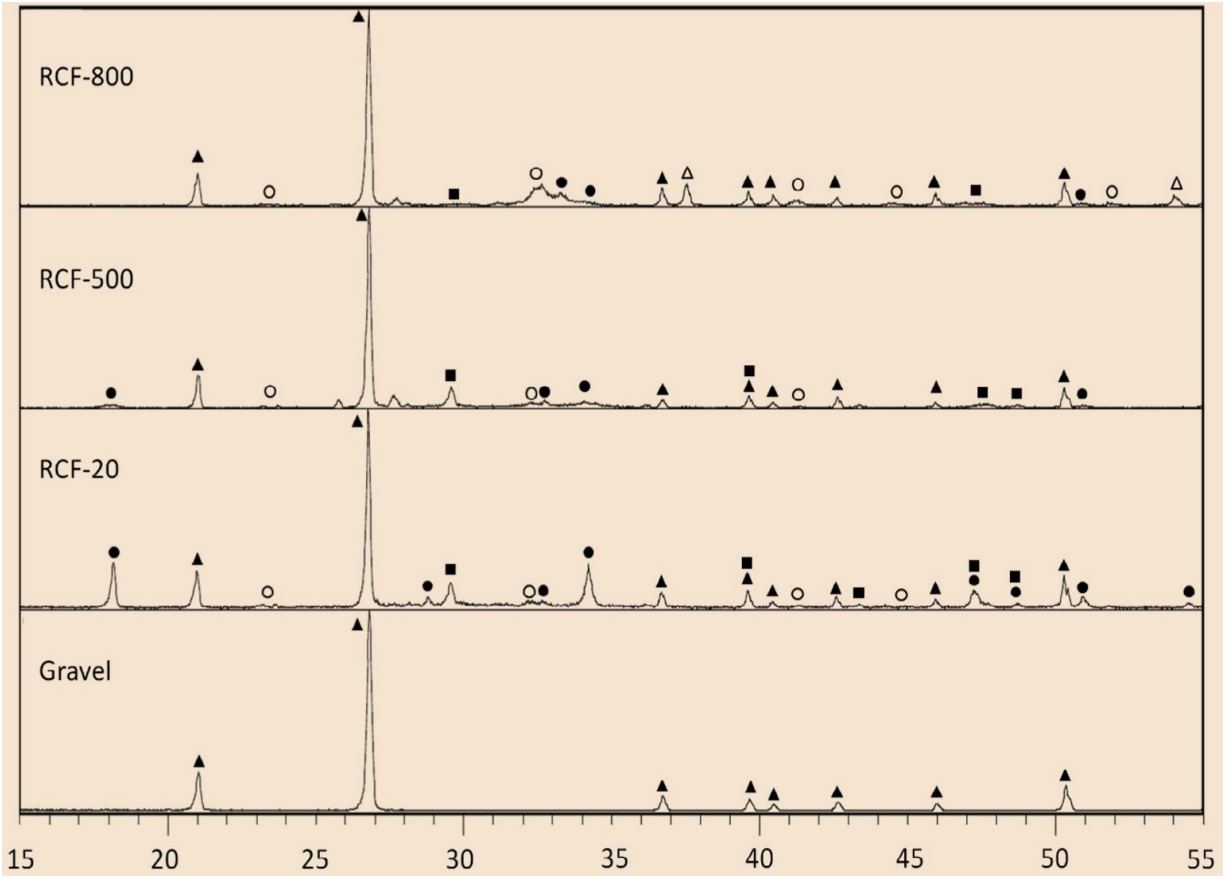

Figure 2-22: XRD analysis of the gravel, RCF-20, RCF-500, and RCF-800 samples. ▲ α-Quartz; ○ C_2S; ● portlandite; ■ calcite; and ∆ lime © Elsevier, 2014 [8].

2.5.2. Rehydration of HCeP and RcCoP

The hydration ability can be recovered through dehydration of HCeP and RcCoP. Upon contact of the dehydrated samples with water, the initial hydration products, such as the C-S-H gel, ettringite and portlandite, are recovered **[16, 18, 20, 15, 168, 11, 10, 26, 169, 40, 170, 17]**. However, the identification of the optimum temperature is necessary. Therefore, the rehydration allows for assessing the extent to which thermal treatment recovered the hydration ability. Nevertheless, the problems resulting from thermal treatment were reported, such as rapid setting time, higher water demand, and lower achieved mechanical strength. The following paragraphs compare the results from different researchers to provide details on the relationship between the thermal treatment temperature and rehydration ability.

Xuan and Shui [20] and **Shui et al. [16]** indicated that the rehydration behavior of dehydrated cement paste (DhCeP) depends on a combination of the dehydration temperature and the initial w/c used to produce the hydrated cement paste (HCeP). **Figure 2-23** and **Figure 2-24** indicate that the water demand for standard consistency generally increases with dehydration temperature while the setting time decreases, respectively. For the DhCeP, the lower initial w/c requires less water than the higher initial w/c. They specified that, at the same dehydration temperature, the higher initial w/c leads to a higher content of dehydrated hydration phases of DhCeP. Additionally, the content in the latter phases increases with an increase in dehydration temperature. Therefore, the higher the initial w/c and the dehydration temperature, the higher the water demand.

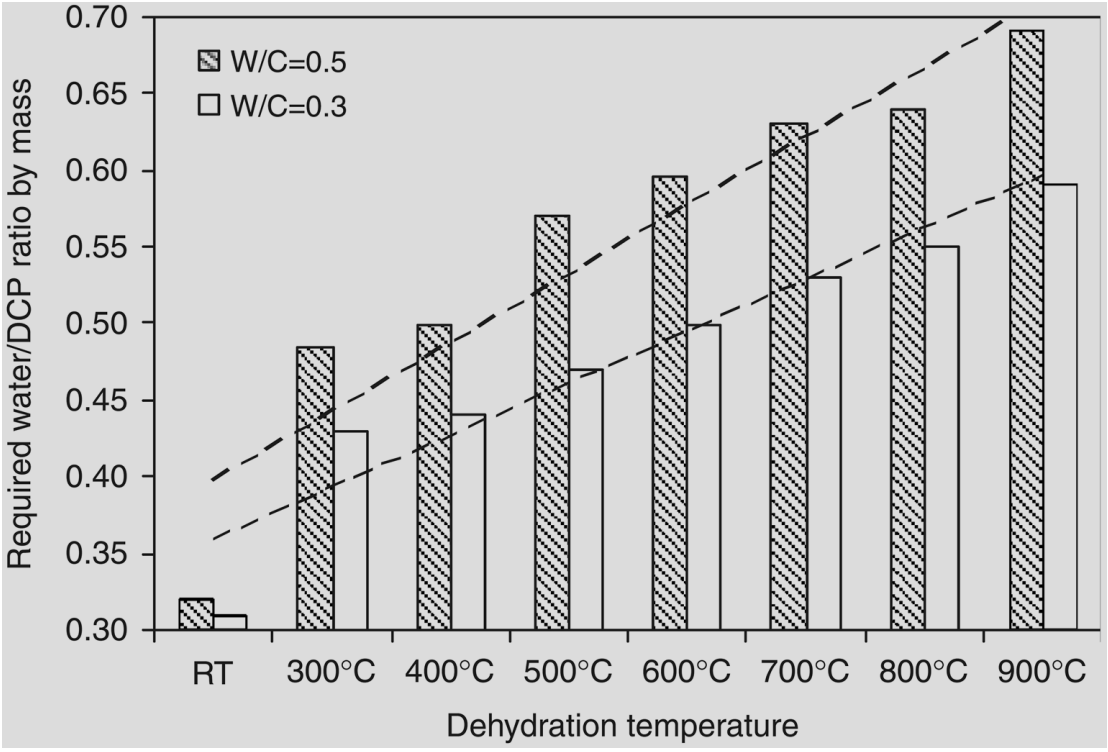

Figure 2-23: Water demand of DhCeP for standard consistency [20].

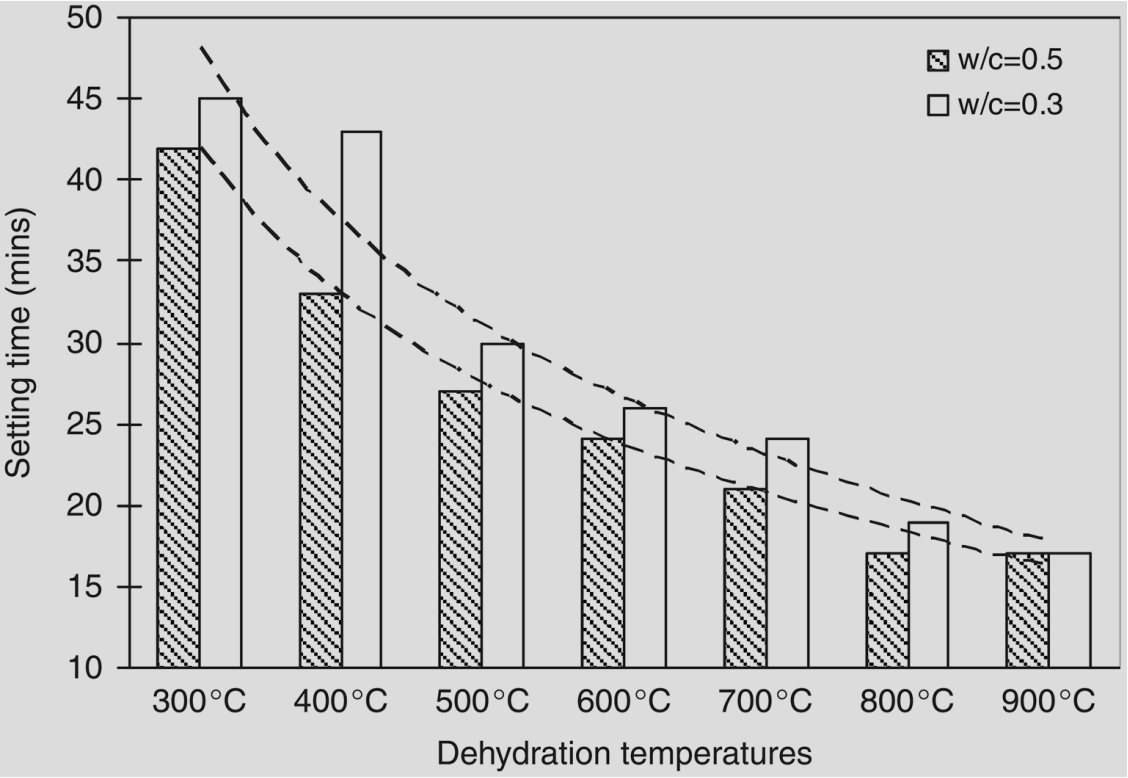

Figure 2-24: Initial setting time of DhCeP with standard consistency [20].

Two principal factors were identified as responsible for the increase in water demand of the DhCeP. The first factor is a change in the physical properties of DhCeP compared to ordinary cement. The DhCeP has a higher Blaine surface area. The second factor is the immediate reaction of water with some dehydration products, such as free CaO and ettringite, increasing the water demand. The higher Blaine surface area of DhCeP also results in a fast setting time, indicating that the dehydration products quickly react with water. This behavior was explained by the metastable state of the dehydrated phases, which can polymerize each other to form new products again, such as CaO. Similarly, the depolymerized C-S-H gel of DhCeP can transform into C–S–H gel again after a quick reaction with water. They indicated that the polymerization process does not require conquering the protective layer effect and nucleation process **[18, 171]**.

The reduced setting time of DhCeP can harm the fresh and hardened properties. For example, it can result in shrinkage cracks that are the weakness zones on the paste. Therefore, several authors have investigated possibilities of extending the setting time in DhCeP without considerably affecting the mechanical strength. These solutions include the addition of set retarders **[21]** and gypsum in different proportions **[21, 172, 173]**.

The dehydration temperature influences the achievable strength of the DhCeP after rehydration. **Real et al. [167]** specified that the thermal treatment forms C_2S polymorphs of different reactivity. They revealed that a treatment temperature of 650 °C results in the formation of the highest amount of α_L'-C_2S, which is the most reactive polymorph of C_2S. With treatment above 650 °C, the amount of α_L'-C_2S decreases and β-C_2S increases. Therefore, the optimum strength is developed with treatment at 650 °C. **Shui et al. [16]** indicated a potential transformation of dehydrated hydration phases over 800 °C, emphasizing the optimum dehydration temperature not to be above 800 °C. Nevertheless, it is necessary to allow complete dehydration and depolymerization occurring above 400 °C **[167, 16, 20, 174]**.

Figure 2-25 and **Figure 2-26** show the mechanical strengths of DhCeP at different curing days, according to Shui et al. and Real al., respectively.

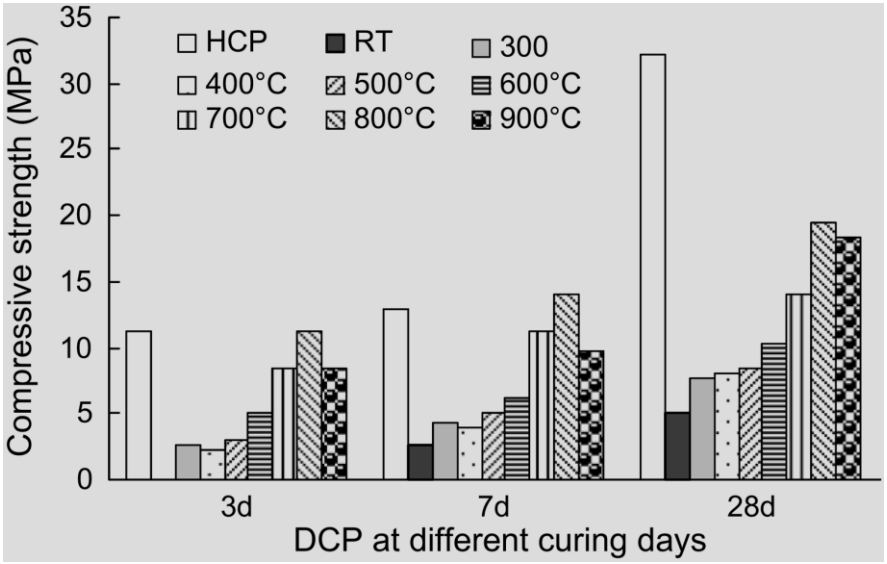

Figure 2-25: Compressive strengths of DhCeP at different curing days according to Shui et al. © Elsevier, 2009 [16].

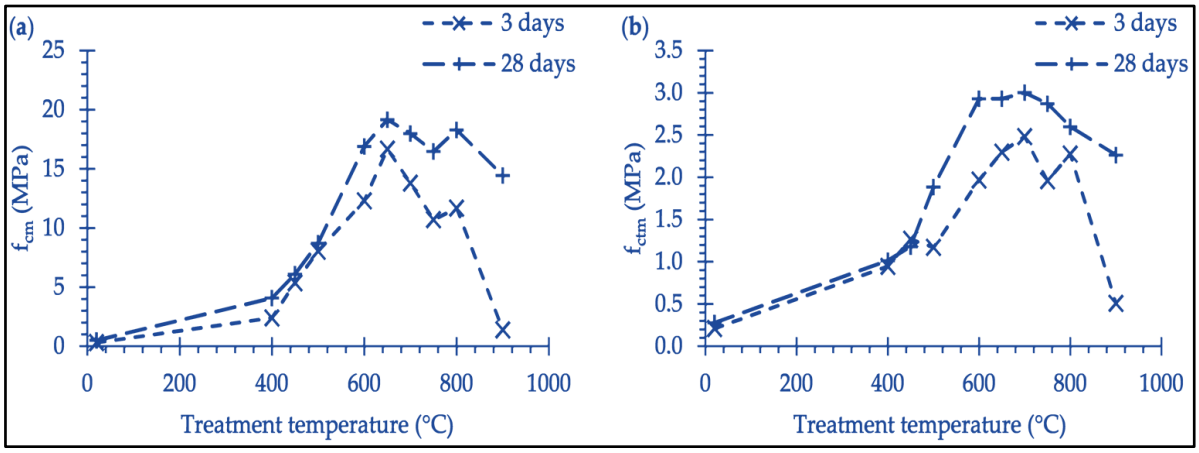

Figure 2-26: Mechanical strengths of DhCeP at different curing days according to Real al. [167].

Several parameters can influence the best dehydration temperature. However, as previously discussed, the optimum range was confirmed as 400 °C to 800 °C in all circumstances. These factors include, among others, the w/c ratio, the particle fineness, the production procedure (crushing, grinding and milling), and the forerunner material (especially the type of cement used initially). Low mechanical strength was reported when the forerunner material is concrete or mortar because the quantity of rehydratable products is minor. Thus, separation methods require optimization. **Table 2-7** indicates the optimum compressive strengths after 28 days using 100% thermoactivated cement, obtained by different researchers according to the review by **Carriço et al. [24]. Figure 2-27** illustrates the variation between the optimum compressive strengths obtained by various researchers, where it can be observed that the compressive strength constantly decreases above 800 °C.

Table 2-7: Optimum compressive strengths after 28 days using 100% thermoactivated cement © Elsevier, 2020 [24].

Precursor material	Treatment temperature (°C)	Time at annealing temperature (min)	Matrix	w/c	$f_{cm,28d}$ (MPa)	
					28 days	f_{cmTAC}/f_{cmOPC} (%)
Recycled concrete fines	500	60	Paste	0.40	8.0	*n.d.
Cement paste	800	150	Paste	0.64	19.5	*n.d.
Cement paste	800	150	Paste	0.50	20.0	*n.d.
Autoclaved aerated Concrete	700	120	Paste	0.45	4.2	*n.d.
Cement paste	800	120	Paste	0.75	16.5	*n.d.
Cement paste	755	140	Paste	0.70	31.2	*n.d.
Cement paste	500	120	Paste	0.60	18.0	68%
Cement paste	450	480	Paste	0.55	32.3	85%
Recycled concrete fines	500	60	Mortar	0.26	4.7	*n.d.
Concrete	750	60	Mortar	0.50	12.3	21%
Cement paste	800	150	Mortar	0.93	11.6	*n.d.
Cement paste	500	120	Mortar	0.48	7.6	18%
Cement paste	600	180	Mortar	0.50	30.3	62%
Cement paste	650	180	Mortar	0.68	8.3	19%
Concrete	650	180	Mortar	0.81	0.9	2%

n.d.: not disclosed.

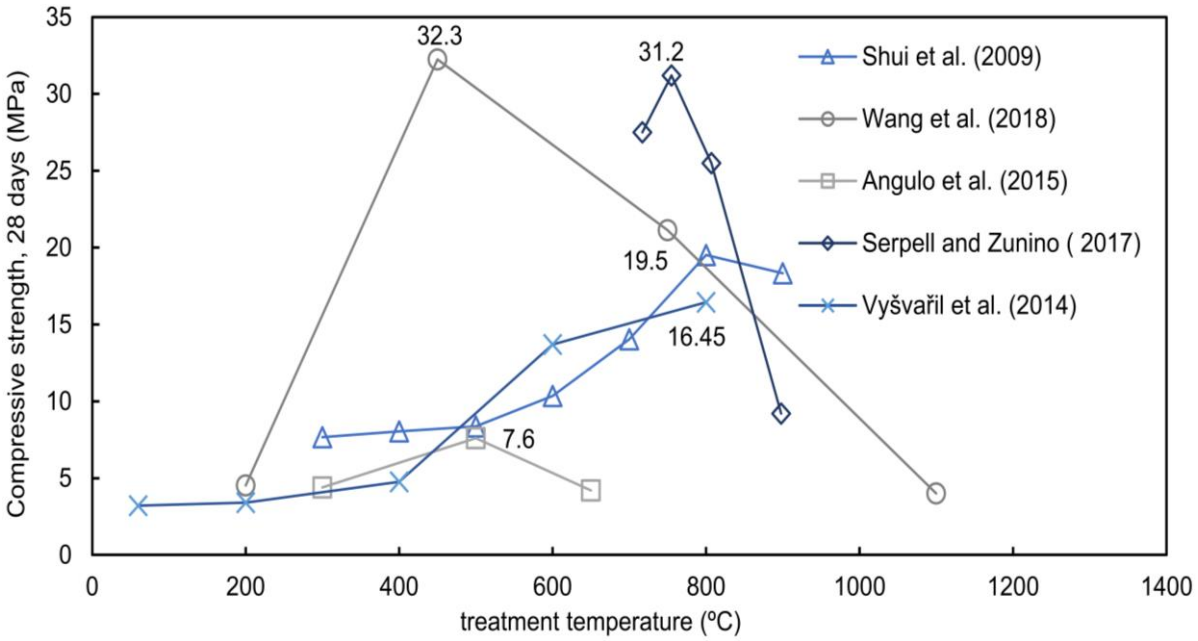

Figure 2-27: Variation between the optimum compressive strengths obtained by various researchers © Elsevier, 2020 [24].

The dehydration temperature also impacts the porosity and the microstructure of the DhCeP after rehydration. The thermal treatment results in a modified morphology with a rough surface and loose structure when the initial material is Ordinary Portland Cement (OPC). As a result, the porosity of DhCeP is higher than that of HCeP **[175, 22]**. Similarly, in **Figure 2-28**, **Real et al. [167]** show that the OPC (named PC) exhibits organized angular shape particle agglomerates. In contrast, the untreated HCeP (NT) exhibits fewer angular particles with various shapes. The DhCeP (thermally treated HCeP; named RC) particles were also less angular with a rounder shape.

Additionally, compared to NT and RC, they specified that the PC morphology is smooth and non-porous resulting in a lower surface area. Thus, the thermal treatment results in finer and

rounder particles increasing the surface area. Nevertheless, they indicated a possible agglomeration of particles due to heating above 750 °C, which can reduce the surface area.

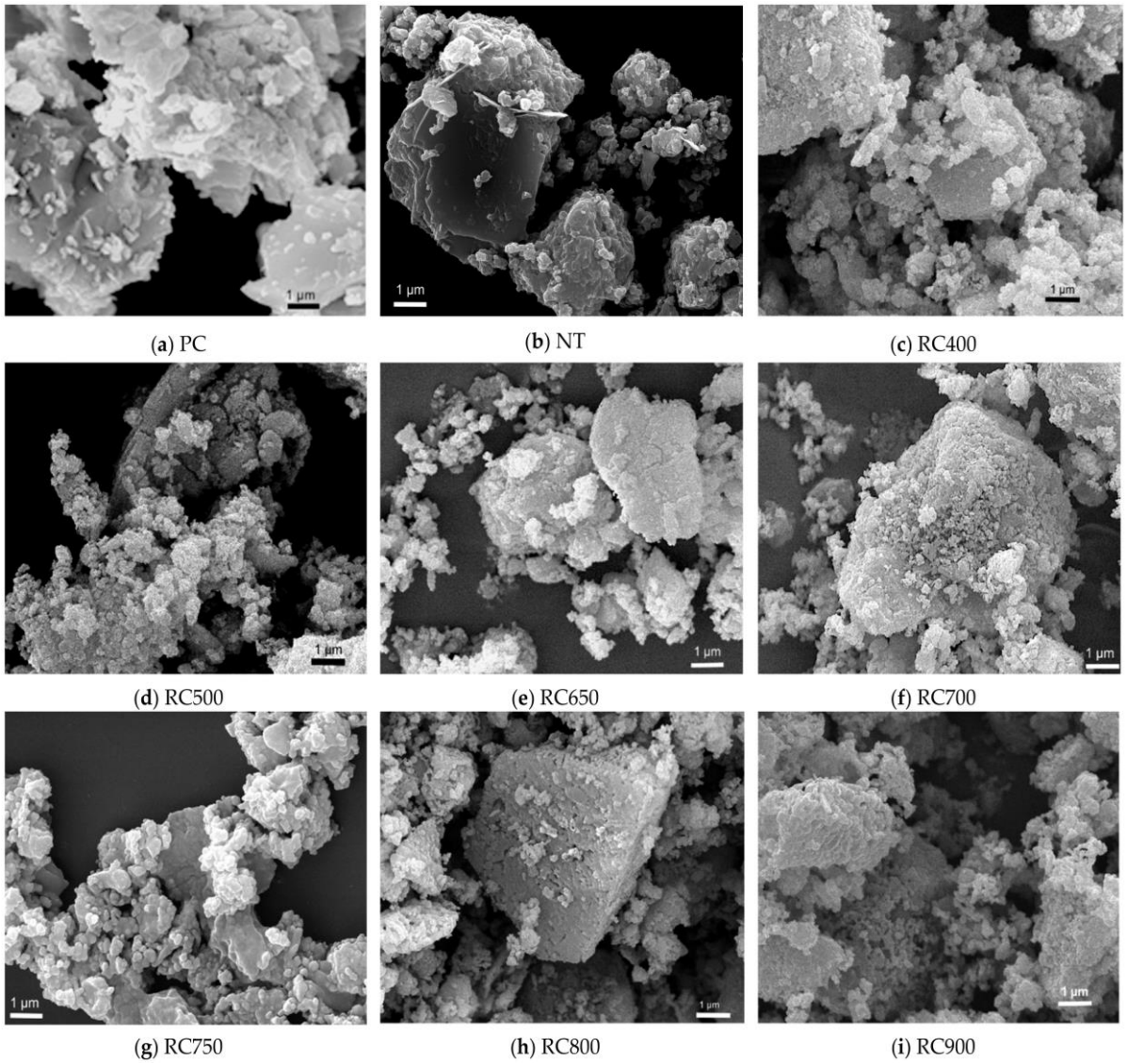

Figure 2-28: SEM images of (a) OPC (PC), (b) HCeP (NT), and DhCeP (RC) after treatment at (c) 400, (d) 500, (e) 650, (f) 700, (g) 750, (h) 800, (i) 900 [167].

Several other researchers have investigated the influence of the treatment temperature on the porosity and microstructure of DhCeP. For example, **Li et al. [176]** investigated the microstructure evolution of thermally treated cement pastes by comparing carbonated and uncarbonated conditions. **Figure 2-29** and **Figure 2-30** show the SEM images of thermally treated uncarbonated cement paste, and thermally treated carbonated cement paste, according to Li et al., respectively. They concluded that carbonation can protect the cement paste up to treatment at 500 °C. This protection was because, with carbonation, the $CaCO_3$ and calcium-modified silica gel forming the carbonated cement matrix do not decompose below 500 °C. On the other hand, portlandite (CH) decomposition causes thermal instabilities between 400 °C and 500 °C in the case of uncarbonated conditions.

Additionally, the depolymerization of C-S-H generates larger pores and microcracks between 600 °C and 720 °C. In the case of carbonated conditions, also the microstructure deteriorates in this temperature range due to the decompositions of $CaCO_3$ and calcium-modified silica gel.

Moreover, a loosely honeycombed microstructure was identified after thermal treatment at 950 °C in both conditions. At this temperature, the cement paste contains mainly β-C_2S and lime. Various other researchers obtained similar results **[160, 177–181, 174, 182]**.

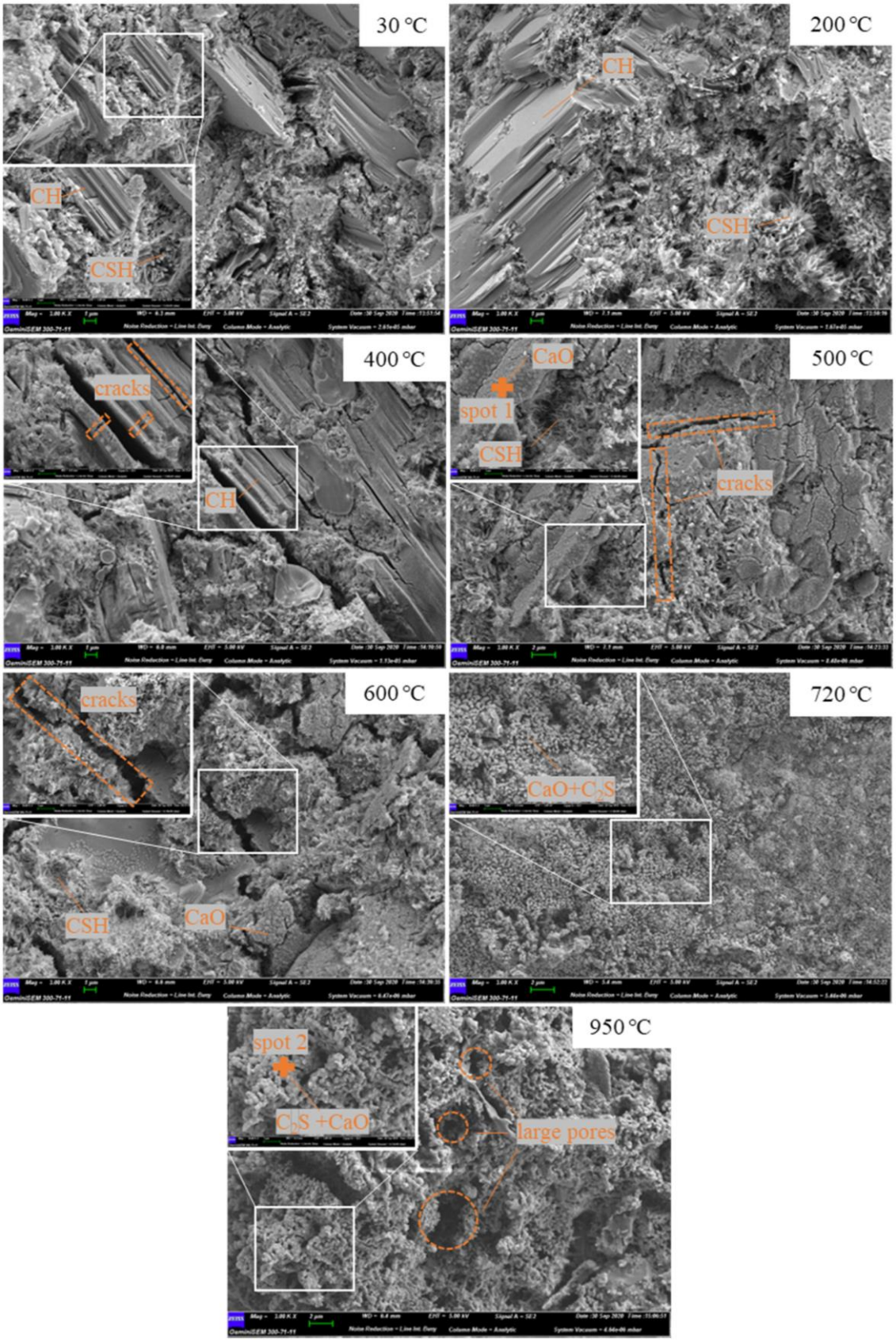

Figure 2-29: SEM images of thermally treated uncarbonated cement paste [176].

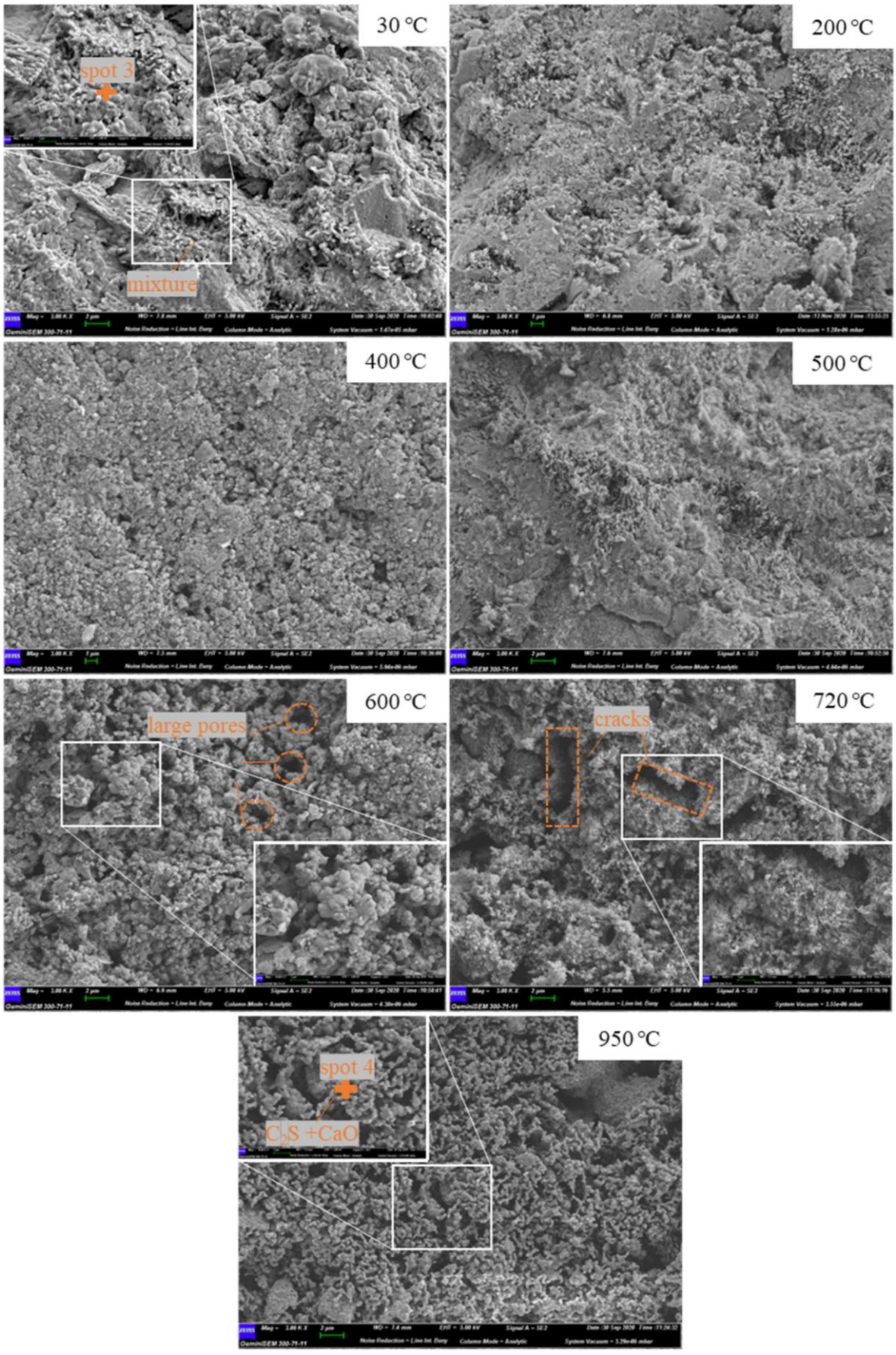

Figure 2-30: SEM images of thermally treated carbonated cement paste [176].

The MIP results of these authors (**Li et al. [176]**) show that different chemical transformations due to the thermal treatment increase porosity depending on when they occur. The extent of porosity increase was associated with the types of changes, which include decomposition of ettringite below 200 °C, partial decomposition of CH at 400 °C, complete dehydroxylation of CH to lime between 400 °C and 500 °C, depolymerization of the C-S-H phases to C_2S and decomposition of $CaCO_3$ above 600 °C **[183–187, 24, 188]**. Due to the carbonated cement matrix protection effect, the porosity is lower for the carbonated samples than the corresponding uncarbonated samples (**Figure 2-31**). Nevertheless, the pore size distribution results (**Figure 2-32**) indicate that the samples pretreated above 600 °C, especially 950 °C, contain a high fraction of big pores (harmful pores), emphasizing the low mechanical strength development with very high treatment temperatures.

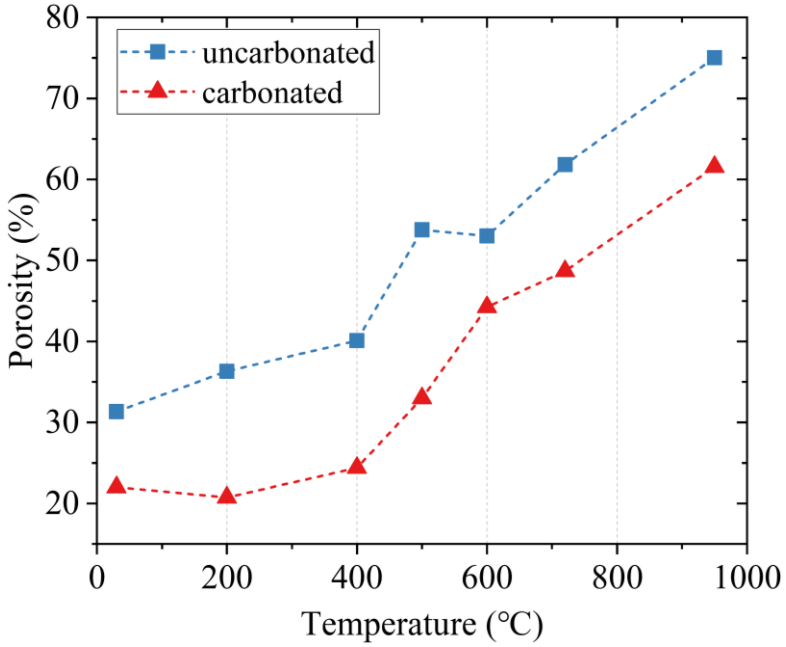

Figure 2-31: Porosity changes in thermally treated carbonated and uncarbonated cement pastes [176].

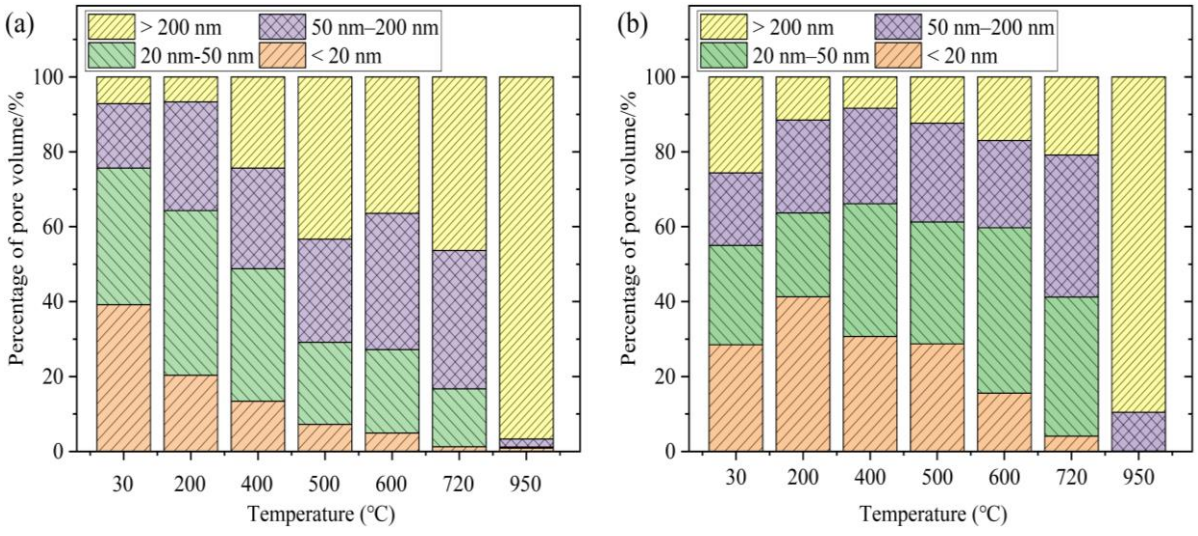

Figure 2-32: Compositions of the pore size distribution of thermally treated cement pastes (a) uncarbonated (b) carbonated [176].

2.6. Concrete recycling and production of RcCoP

The generation of Construction and Demolition Waste (CDW) has increased globally due to the enhanced need for construction, renovation, and demolition of construction structures. These wastes constitute a source of environmental problems, among others, when they are just disposed of and not recycled to a considerable extent **[6]**. Besides, the depletion of the natural resources used to produce the massive quantity of concrete needed for construction emphasizes the need to recycle CDW **[1]**.

2.6.1. Concrete recycling

Several researchers **[189–199]** have indicated that recycled CDW, mainly Recycled Concrete Aggregates (RcCoA), are used primarily in road construction (base/subbase layers) or excavation backfilling, where low-quality aggregates could be accepted. This lower quality is caused by the adhered mortar on the RcCoA (RA), resulting in increased water absorption and reduced mechanical strength. For example, **Ohemeng and Ekolu [25]** specified that when RcCoA is used in concrete, there is a thicker triple-layered Interfacial Transition Zone (ITZ) formation weaker than a single ITZ formed using natural aggregates. **Figure 2-33** compares the ITZ in concrete made with natural and recycled aggregates.

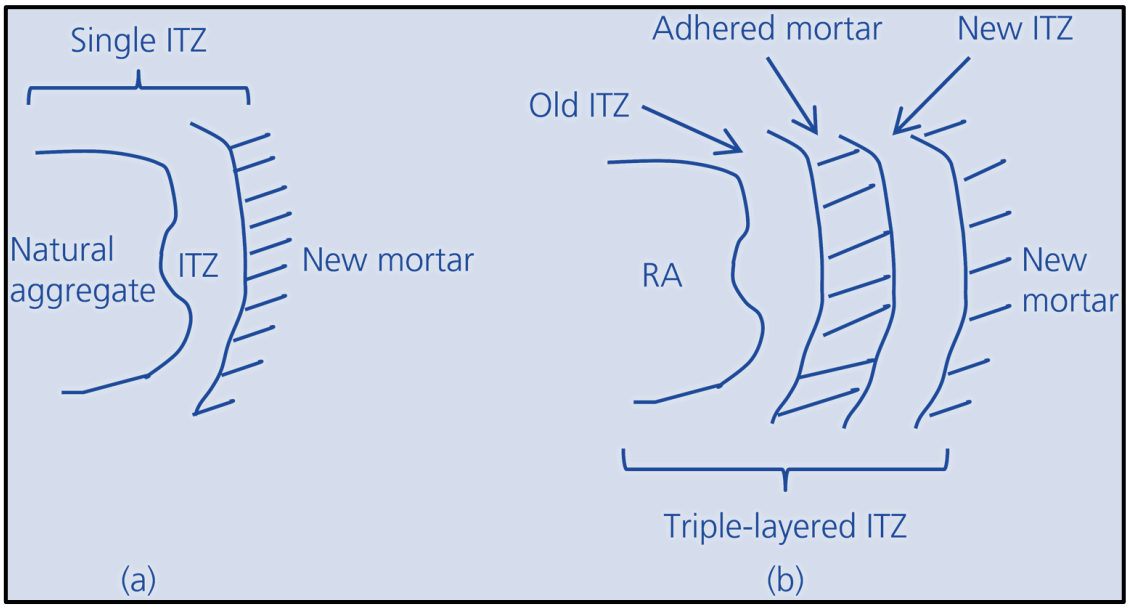

Figure 2-33: Comparison of ITZ formed in concrete made with (a) natural aggregates, (b) RcCoA [25].

Previously, the recycling of CDW has been conducted mechanically using crushers (the jaw crusher, the cone crusher and the impact crusher). The main objective of these crushers was to reduce the size of RcCoA, including crushing through aggregates, resulting in low-quality aggregates. Moreover, it was stated that the fine fraction (< 4mm or < 2mm, depending on the country) was considered waste. Hence, the whole process would be regarded as downcycling rather than recycling. **Figure 2-34** illustrates the types of crushers used to reduce the size of RcCoA. Additionally, all contaminants, such as wood, paper, plastics and metals, must be removed by different techniques, as illustrated in **Figure 2-35**.

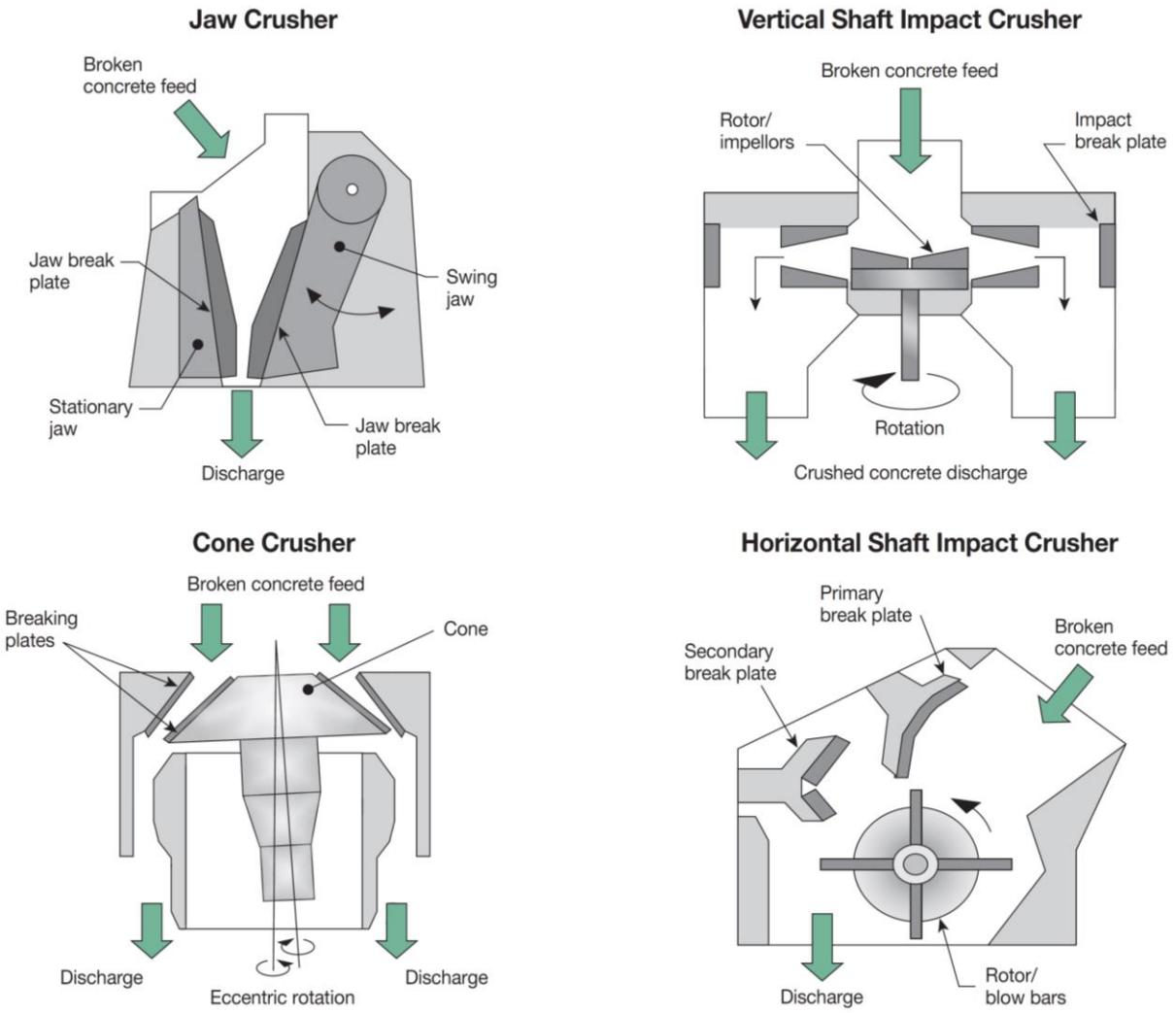

Figure 2-34: Illustration of types of crushers used to reduce the size of RcCoA [192].

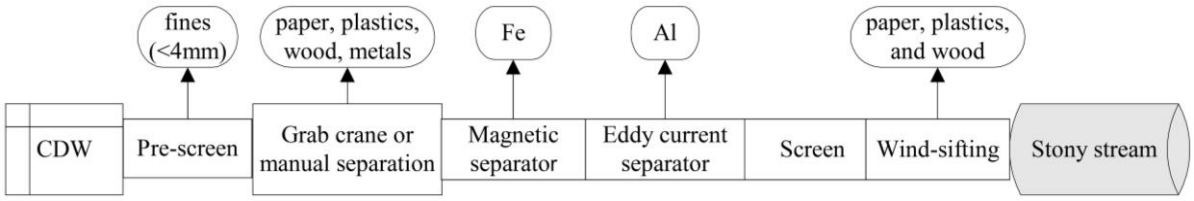

Figure 2-35: Illustration of CDW treatment for removal of contaminants [200].

Innovative processing technologies are required during the recycling of CDW to achieve the best quality RcCoA that can completely replace virgin aggregates in producing new concrete. Furthermore, ongoing demolition and large amounts of concrete fines that have been landfilled as waste gain considerable potential for reducing CO_2 emissions associated with cement production by recycling the cementitious parts **[201–203]**. **Figure 2-36** shows an example of a complete recycling of CDW into coarse and fine aggregates. The figure indicates that the concrete rubble can be used for road subbase construction as their final disposal after demolishing an old concrete structure. However, a powder comprising cementitious properties can be obtained using a high-quality aggregate manufacturing plant. This powder can be used together with fresh cement clinker from industry to produce a new type of cement to be used for constructing new concrete structures.

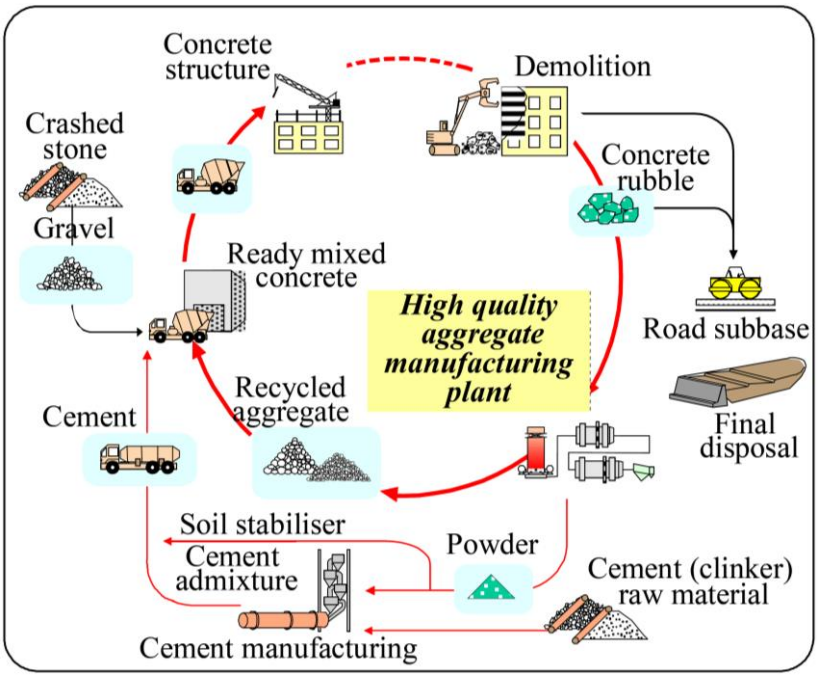

Figure 2-36: Example of complete recycling of CDW into coarse and fine aggregates [199].

2.6.2. Technologies used for the production of RcCoP

Producing Recycled Concrete Powder (RcCoP) results from different innovative processing technologies mainly based on separating the old concrete into primary constituents during recycling. These beneficiation processes can be divided into different categories, such as mechanical, chemical, thermal, electrical, or a combination of two or more **[190]**. The following Section briefly describes how these technologies operate, and the references are provided for more information:

- **Smart Crushing (SC):**

SC is a mechanical beneficiation that separates the concrete ingredients rather than crushing them like ordinary crushers. Instead, it exerts pressure between the cement paste and the aggregates. It uses a restricted force between the crushing plates (<100 MPa) that cannot crush through aggregates, which need an average crushing strength value of about 200 MPa. On the other hand, this pressure can crush through cement paste, with an average crushing strength value of less than 50 Mpa **(Schenk [204])**.

- **Electrodynamic Fragmentation (EF):**

Ultrashort (< 500 nsec) underwater pulses selectively break solid materials into fragments during the EF process. Underwater electrical discharges tend to travel along the phase boundaries in the solid material. Electrical breakdown generates a pressure wave (p = 10 GPa), breaking the composite material into its components **(Seifert et al. [205])**.

- **Thermal beneficiation:**

The thermal beneficiation technique breaks and separates the mortar and Natural Aggregates (NA) by their differences in the thermal expansion rate. Since mortar has around double the thermal expansion coefficient of NA, it expands more when heated at the same temperature. Therefore, higher differential thermal stresses develop in the mortar and break it up without

damaging the NA. Additionally, high differential thermal stresses develop at the interfacial transition zone between mortar and NA, inducing the separation of the adhering mortar and NA. A temperature of about 300 °C to 600 °C can be used for heating depending on the strength of the mortar and the type of NA **(Shima et al. [199], Noguchi [206]).**

- **Acid treatment:**

The ability of strong acids to corrode the cementitious materials easily is used to remove the mortar from the Recycled Concrete Aggregates (RcCoA) during the acid corrosion beneficiation technique **(Mindess et al. [207])**. This technique has negligible or no effects on the properties of the NA previously used when the proper treatment acid is chosen. The best strong acids for the removal of mortar on the RcCoA include sulphuric (H_2SO_4) and hydrochloric (HCL) acids **(Tam et al. [208])**. However, the acid concentration for treatment must be controlled, and additional washing stages of the corroded mortar are required **(Akbarnezhad et al. [209])**.

- **Microwave-assisted beneficiation:**

Microwave dielectric losses can heat the mortar and NA since they are dielectric materials. The heating rate is typically estimated by the attenuation factor, which is an essential characteristic of the electromagnetic properties of the material. Generally, when the attenuation factor increases, the heating rate increases exponentially. The mortar heats up faster than the NA as it has a higher attenuation factor. Additionally, soaking the RcCoA in water for a short time is beneficial to increase the differences in heating rates of mortar and NA due to the higher water absorption of mortar. As a result, differential thermal stresses are shortly generated in the mortar and its interface with the NA present in the RcCoA without inducing a noticeable temperature rise in the NA. Therefore, the adhering mortar can be removed from the RcCoA. Nevertheless, it is necessary to avoid excessive heating that can damage the integrity of the NA **(Akbarnezhad et al. [210], Ong and Akbarnezhad [191])**.

As indicated previously, two or more techniques can be combined to enhance the quality of the separated primary constituents, as shown in **Figure 2-37**, from research conducted by **(Everaert et al. [195])**.

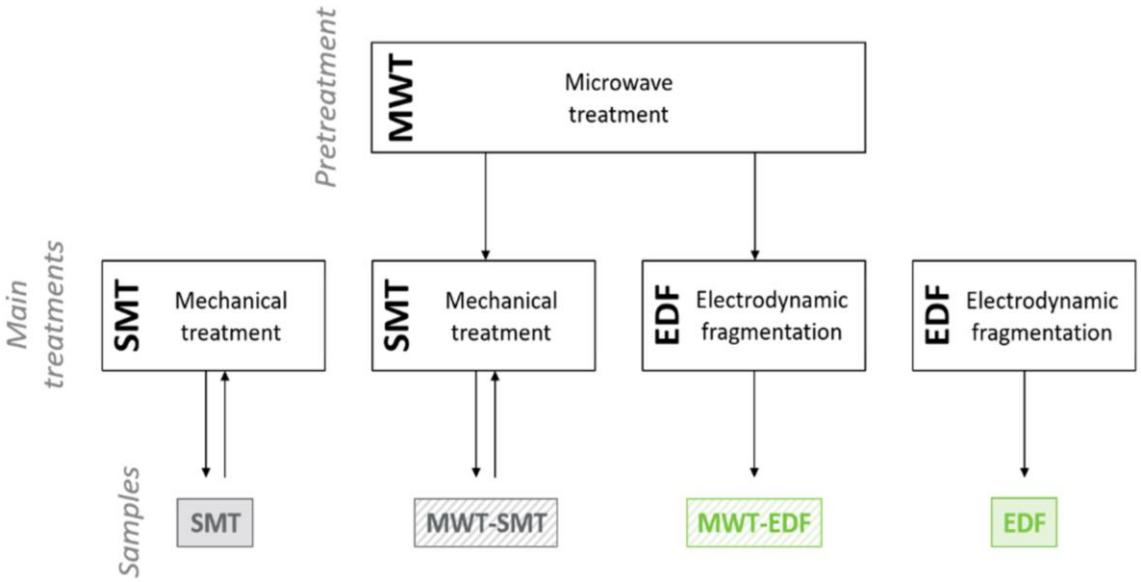

Figure 2-37: Combination of innovative processing technologies to produce recycled concrete powder [195].

The current research has considered and compared the properties of the RcCoA obtained by Smart Crushing (SC) and Electrodynamic Fragmentation (EF). More details on these techniques will be provided in the experimental methodology section.

2.7. Summary

Cement is a complex material that has been profoundly used in construction as a binder for decades. However, its production is accountable for high CO_2 emissions, and its requirement needs to be replaced to some extent. This chapter reviewed how it is produced, its characteristics, and its phase composition structures that allow it to develop strength when mixed with water through the reaction named cement hydration.

Although extensive research has been conducted on cement for decades, research on the possibility of its partial or total replacement is recent. Besides, questions such as the best method to use and how much can be replaced without affecting the mechanical strength are still open. Nevertheless, thermal treatment is one of the most promising methods and is already successfully proven for reactivating hydrated cement. Optimizing the thermal treatment process to determine the precisely best heating temperature is still in progress.

There is a lack of research on reactivating recycled concrete fines, which is the most realistic scenario. This chapter reviewed limited existing research and briefly discussed the methods for recycling old concrete to produce recycled concrete fines. Furthermore, open questions have been exposed, such as what can be the best method for producing recycled concrete fines with as much as possible cementitious properties, what can be their optimum thermal treatment temperature, and whether they can be used as a binder after thermal treatment.

3. Experimental Methodology

This chapter explains the methodology used to achieve the research objectives. It is divided into two main parts. The first part **(Section 3.1)** discusses the process used to produce the research materials, while the second part **(Section 3.2)** describes the laboratory tests used to investigate the extent of reactivation of the research materials.

3.1. The preparation process of the research materials

This research used two primary materials, Hydrated Cement Powder (HCeP) and Recycled Concrete Powder (RcCoP) leading to other materials after thermal treatment. **Sections 3.1.1 and 3.1.2** explain their production process, while **Section 3.1.3** explains their thermal treatment procedure.

3.1.1. Preparation of the Hydrated Cement Powder (HCeP)

The HCeP was obtained after the hydration of Ordinary Portland Cement (OPC) called Virgin Cement (VCe) in this research to emphasize that it is the material obtained from industry without any other transformation. The OPC type CEM I 52.5 R Wittekind (from Erwitte city in Germany) was used. First, Hydrated Cement Specimens (HCeS) were made from the mixture of OPC and water (w/c = 0.5). Then, the HCeS were prepared in prismatic steel molds 40 × 40 × 160 mm^3 and left in the molds for 24 hours in containers keeping the humidity inside. They were then cured in water for six days in a temperature control room (at ±20°C and ±65% RH) for another 21 days, according to DIN EN 12390-2. Part 2: Making and curing specimens for strength tests; German version EN 12390-2:2019. After curing, the HCeS were crushed with a jaw crusher and ground milled (by a disc milling machine) to obtain HCeP of grain size < 250 µm after sieving. **Figure 3-1** shows the sequence of steps involved in producing HCeP.

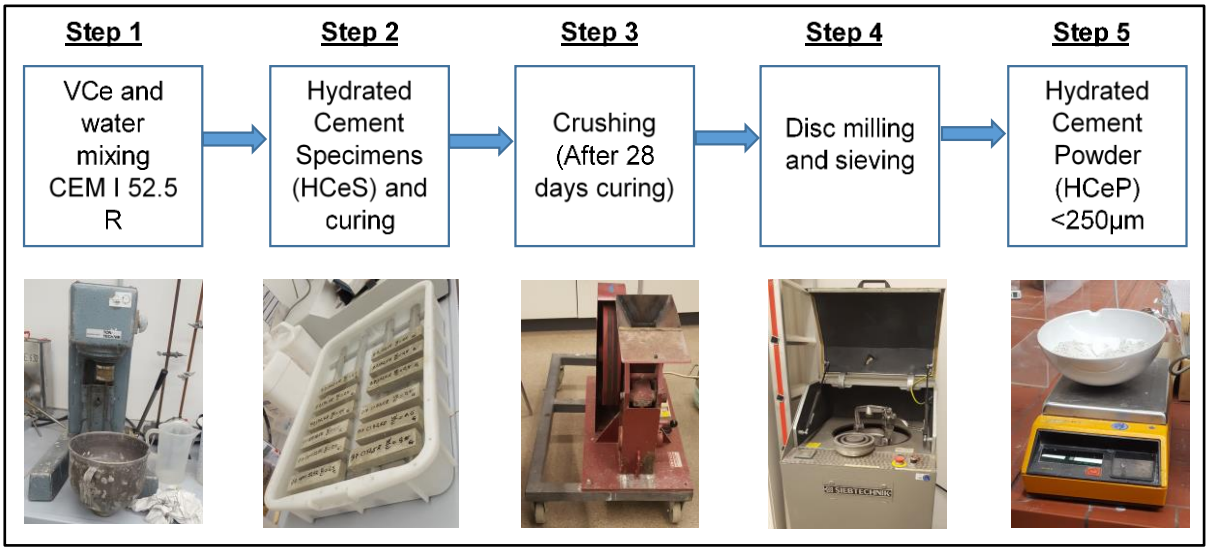

Figure 3-1: The sequence of steps involved in the preparation of HCeP.

3.1.2. Preparation of Recycled Concrete Powder (RcCoP)

The old concrete (~40 years old) was obtained from a police school in the city of Linnich in Düren district of North Rhine-Westphalia in Germany. There is no information about the composition or the exact purpose for which the concrete was manufactured. Subsequently, this old concrete was pre-treated to remove the remaining contaminants, such as wood, paper,

plastics and metals. Furthermore, before the separation process started, it was pre-washed to remove the dust and then pre-crushed with the ordinary crusher to the required size (D< 50 mm). **Figure 3-2 (a)** shows the old concrete immediately obtained from the construction site, while **Figure 3-2 (b)** shows the old concrete pre-treated, pre-washed and pre-crushed to the required size.

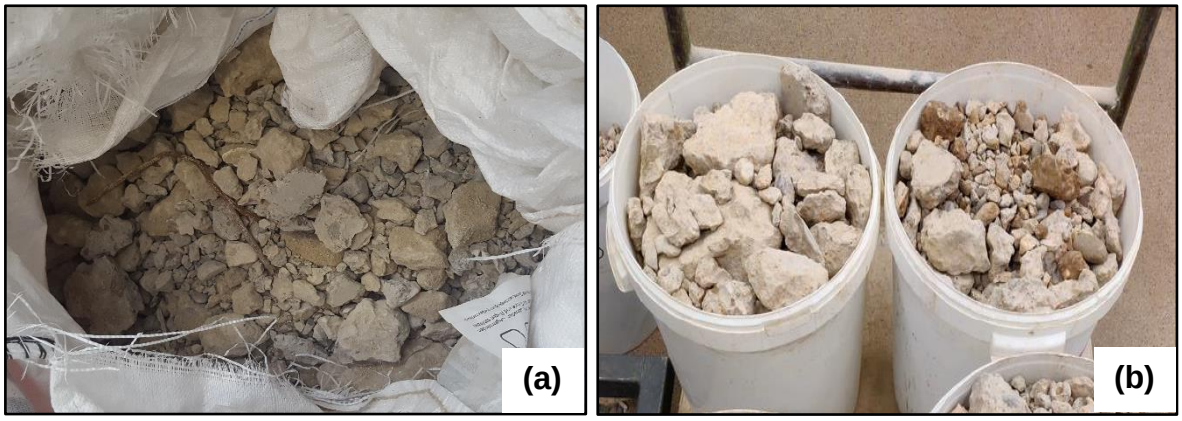

Figure 3-2: The old concrete: (a) immediately obtained from the construction site, (b) pre-treated, pre-washed and pre-crushed to the required size.

Section 2.6.2 specifies the innovative processing technologies that can produce RcCoP. These technologies are based on separating the old concrete into primary constituents rather than crushing everything like ordinary crushers. Therefore, the cementitious part of old concrete can be separated from the other components. Among these innovative technologies, Smart Crushing (SC) and Electrodynamic Fragmentation (EF) were selected for the current research. Michael Janisio and Dr.-Ing. Tommy Mielke from the Institute for Materials Science, University of Duisburg-Essen, Germany, performed the SC in Amsterdam, Netherlands. Koos Schenk, the director at SmartCrusher BV, assisted them. Margarita Mezzetti from TU Bergakademie Freiberg, Germany, performed the EF. Both techniques were performed at the laboratory level. **Sections 3.1.2.1 and 3.1.2.2** describe how these two techniques were executed.

3.1.2.1. Smart Crushing (SC)

The SC is a mechanical technique that separates the old concrete pre-treated, pre-washed and pre-crushed to the required size (D < 50mm), as described in **Section 3.1.2**. The SC method used follows the development by **Schenk** in the Netherlands, who obtained a patent in 2011 **[204]**.

Section 2.6.2 indicates that a restricted force (< 100 MPa) is exerted between the crushing plates of a Smart Crusher so that aggregates are not crushed through. Thus, the cement paste can separate from the aggregates without breaking them. The difference between the jaw crusher and Smart Crusher relies on their crushing plates. While the ordinary crusher lets two angled plates move towards each other for crushing purposes, the Smart Crusher plates are parallel. **Figure 3-3 (a)** and **Figure 3-3 (b)** show a schematic comparison of the crushing plates of a jaw crusher and a Smart Crusher, respectively. The crushing plates are marked in red.

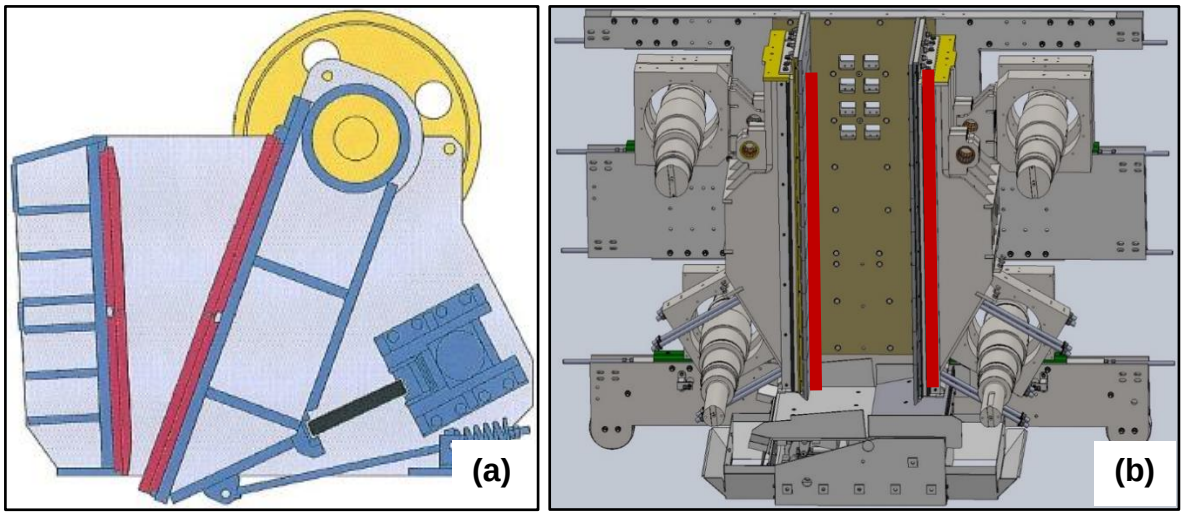

Figure 3-3: Schematic comparison of the crushing plates of (a) jaw crusher, (b) Smart Crusher [204].

3.1.2.2. Electrodynamic Fragmentation (EF)

Section 2.6.2 indicates the process involved in EF following the development made at Fraunhofer Institute for Building Physics IBP in Germany by **Seifert et al. [205]**. The underwater electrical discharges break the old concrete composite into its components. For this research, the energy per impulse was 54 Joules, and the number of impulses was 10, 15 and 20. **Figure 3-4 (a)** and **Figure 3-4 (b)** show the separation of old concrete composite into its components by the EF during the separation process and after separation, respectively. It can be seen that the matrix in **Figure 3-4 (a)** includes fines to be separated from aggregates represented by component A and component B. After separation, the filter residue from process water in **Figure 3-4 (b)** indicates the fines with cementitious properties.

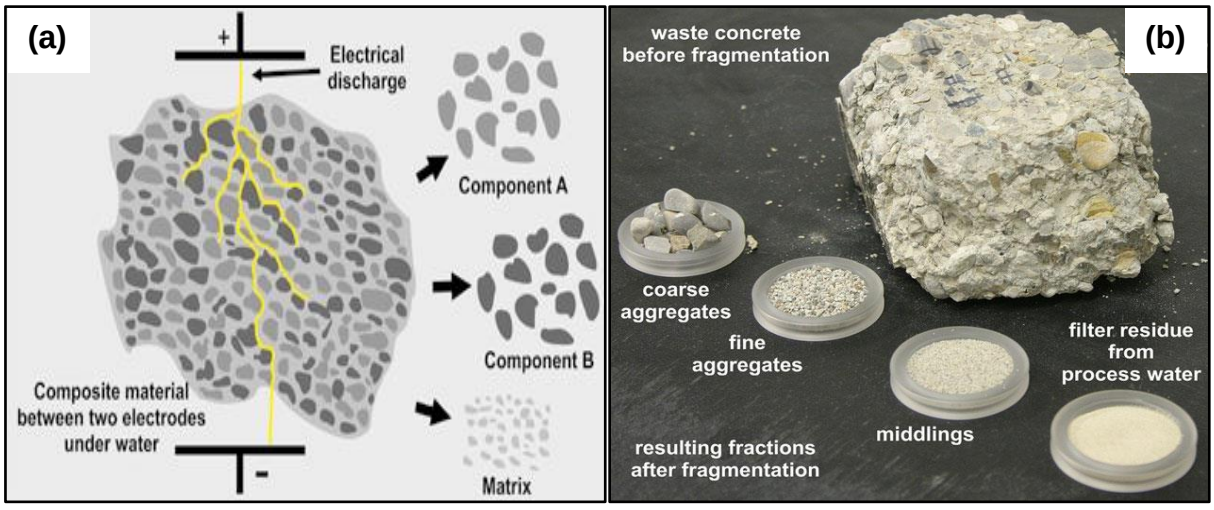

Figure 3-4: The separation of old concrete composite into its components by EF: (a) during the separation process, (b) after separation [205].

The separation of old concrete into its components by the SC and EF was followed by sieving for dividing the separated material into different grain sizes. Only the fractions <2mm (diameter) were considered for evaluating the fines phase content and thermal treatment. Six fractions were obtained, including 2-1 mm; 1-0.5 mm; 0.5-0.25 mm; 0.25-0.125mm; 0.125-

0.063 mm; and <0.063mm. Nevertheless, these materials were milled to increase the required fines for the strength test specimens. Another sieving process followed milling, and a fraction <250 µm (0.25 mm) was considered the Recycled Concrete Powder (RcCoP). The dry milling process was used with a vibrating disc mill from Siebtechnik. The material was then ground for approximately 60 seconds at 960 revolutions. **Figure 3-5** shows the filled grinding jar. The disc milling machine can be seen in **Figure 3-1.**

Figure 3-5: The filled grinding jar during the milling process.

3.1.3. The thermal treatment procedure for reactivation of the HCeP and RcCoP

The HCeP and RcCoP were heated in batches in a muffle furnace (Nabertherm) from 200 °C to 1000 °C. The heating rate was 5°C/min. Different hold times at maximum temperatures (T_{max}) were considered to compare the effect of varying hold times (1h, 3h, 5h, and 10h) on the materials. In addition, natural cooling to room temperature was used after the hold times. The HCeP and RcCoP were stored in sealed buckets or small sealed glass or plastic containers to avoid carbonation. **Figure 3-6 (a)** shows the muffle furnace (Nabertherm) used, while **Figure 3-6 (b)** illustrates the process of thermal treatment of HCeP and RcCoP.

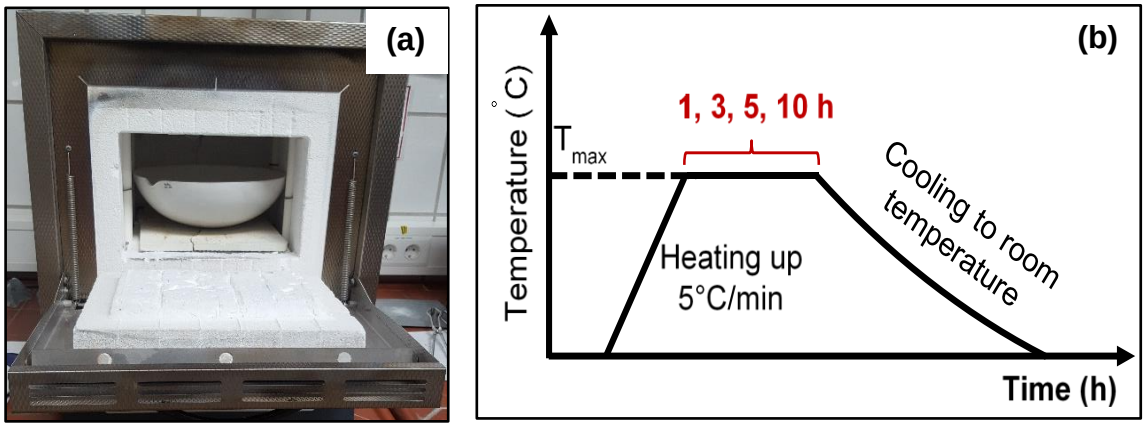

Figure 3-6: Thermal treatment of HCeP and RcCoP: (a) the muffle furnace (Nabertherm) used, (b) the process followed.

The thermal treatment of the HCeP and RcCoP produces Dehydrated Cement Powder (DhCeP) and Dehydrated Concrete Powder (DhCoP). Furthermore, the water mixed with these materials obtained after dehydration makes Rehydrated Cement Specimens (RhCeS) and Rehydrated Concrete Specimens (RhCoS). The Rehydrated Cement Powder (RhCeP) and the Rehydrated Concrete Powder (RhCoP) are obtained after crushing and milling the RhCeS and RhCoS stored in selected conditions and duration as described in **Section 3.1.1**. **Figure 3-7** shows the process applied for material and specimen preparation.

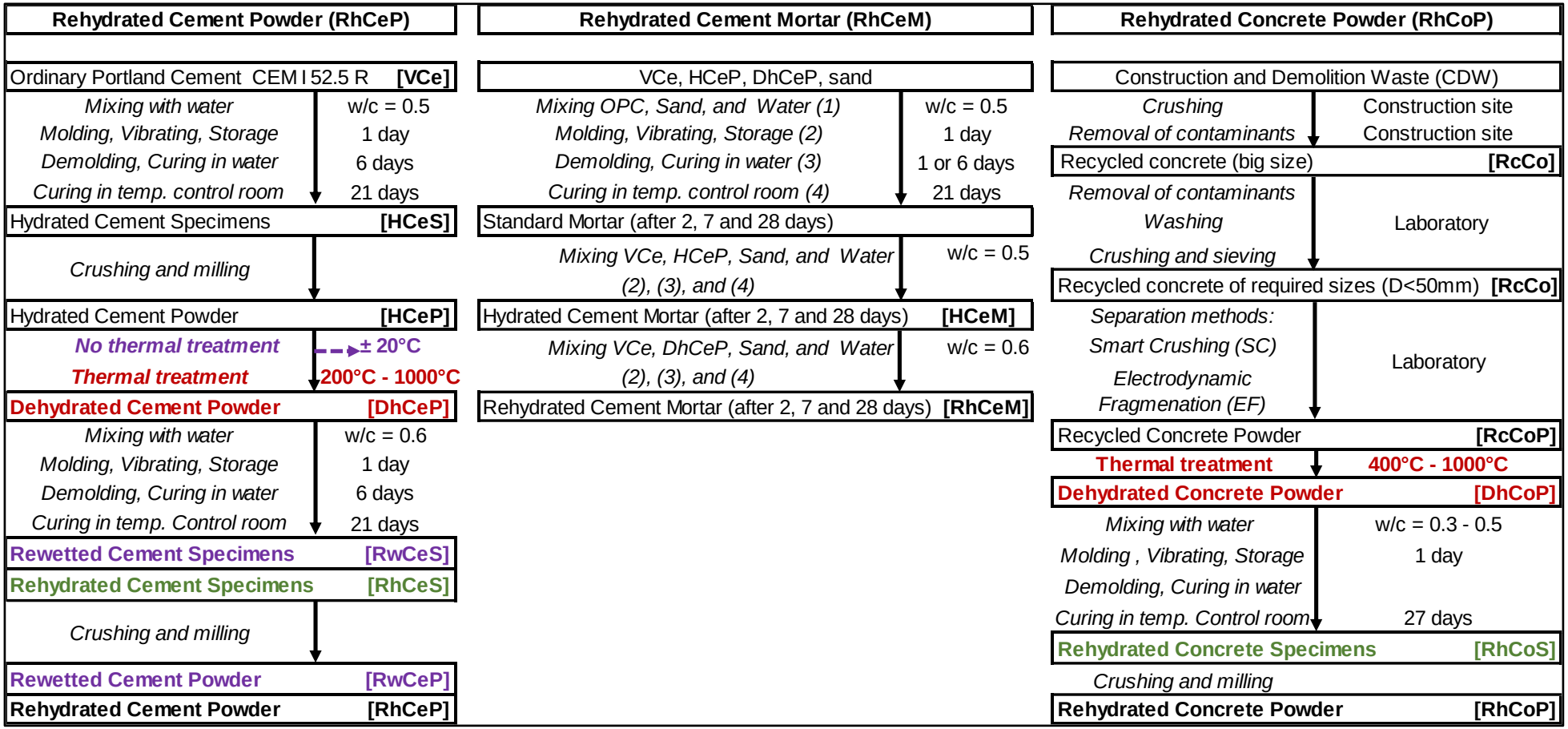

Figure 3-7: The process applied to prepare the materials and specimens.

3.2. Investigation of the extent of reactivation of the HCeP and RcCoP

The reactivation of the HCeP and RcCoP is a process that involves different chemical, physical and mechanical transformations depending on the thermal treatment temperature. Therefore, the untreated and thermally pre-treated samples were initially stored in small sealed plastic or glass containers immediately after the milling and heating processes, respectively, to avoid carbonation before conducting the measurements. **Figure 3-8** shows the storage of the samples ready for measurement.

Figure 3-8: Storage of the samples ready for measurements.

The following sections describe the methods used to assess the transformations resulting from the thermal treatment of the HCeP and RcCoP.

3.2.1. X-ray fluorescence (XRF)

The XRF measurement was used to determine the elemental composition of different powders, including VCe, HCeP, DhCeP, RcCoP, and DhCoP. Bruker S8 TIGER series 2 device was used. Measurements were taken at 4 kW with an aperture of 34 mm in a cuvette with a 4 µm Prolene® membrane from Chemplex. The 3 g powder sample was accurately weighed and distributed as a uniform layer in the cuvette on the Prolene® membrane and measured in an atmosphere of 300 mbar He.

The sample is irradiated with high-energy X-rays from the primary source during measurement. Electrons are thereby displaced from their atomic orbital positions. As a result, fluorescent X-ray radiation of different energies is emitted as the electron drops to the lower energy state. Measuring these energies helps determine the elements present in the sample. Furthermore, the measurement of the intensities of the emitted energies helps to determine the amount of each element **[211]**. **Figure 3-9** illustrates the process of XRF during measurement.

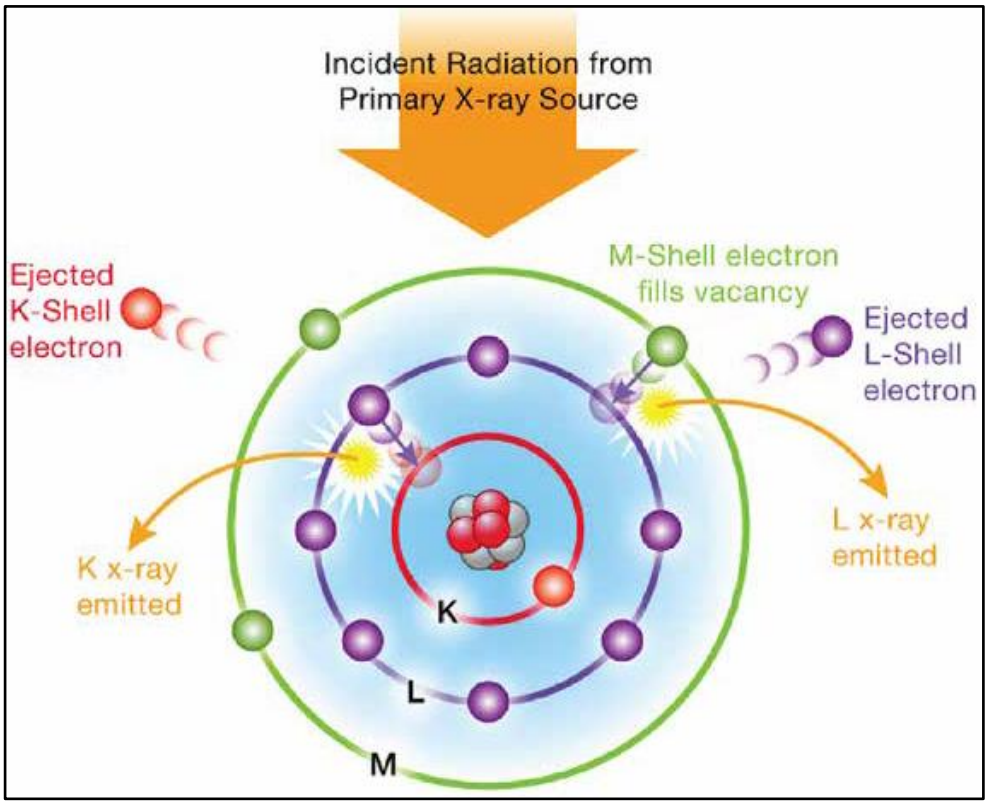

Figure 3-9: The process of XRF during measurement [212].

3.2.2. Differential Scanning Calorimetry (DSC) and Thermogravimetry (TG)

DSC was performed to identify the prominent peaks associated with the heat flow in and out of the HCeP, DhCeP, RcCoP, and DhCoP. TG measurements were conducted to determine the weight losses related to the transformations indicated by the DSC peaks. The DSC-TG measurements were performed concurrently in a NETZSCH STA 449F1 Jupiter with a silicon carbide oven in the temperature range from 25 °C to 1000 °C at 10 K/min heating and cooling rates under atmospheric pressure conditions.

The main transformations identified by the DSC for the HCeP and RcCoP include the dehydration of the C-S-H gels, the decomposition of ettringite, the dehydroxylation of portlandite, the decarbonation of calcite, and the conversion of α'-quartz to β-quartz only for the RcCoP. Furthermore, the DSC-TG measurements were conducted on the DhCeP and DhCoP for all hold times (1h, 3h, 5h, and 10h) at maximum temperatures to assess the effect of thermal treatment on the stability of these phases, which resulted in the shifting of the temperature ranges when they occurred (See **Section 4.1.2** and **Section 5.1.2**).

3.2.3. X-Ray Diffraction (XRD)

XRD was performed to identify the main crystalline phases of the VCe, HCeP, DhCeP, RhCeP, RcCoP, DhCoP, and RhCoP. An Empyrean powder diffractometer (PANalytical) with Cu Kα radiation over a 2-theta range of 10° - 70° (step size of 0.013°, scan speed 0.018°/s) was used to obtain the XRD patterns. The High Score Plus program was used to assess the crystalline phases for the qualitative analysis. Reference was made to "*A Practical Guide to Microstructural Analysis of Cementitious Materials* **[213]***"* to conduct the Rietveld refinement for the quantitative analysis.

Bragg's law describes XRD diffraction. The XRD method is based on bombing the sample with a beam of X-rays. As a result, the incident rays are diffused in different directions characterized by angles. The diffraction patterns are produced since the wavelength λ of the characteristic X-rays is in the same order of magnitude (1–100 Å) as the d-spacing between layers in the crystals. **Figure 3-10** shows a schematic illustration of the concept of XRD analysis.

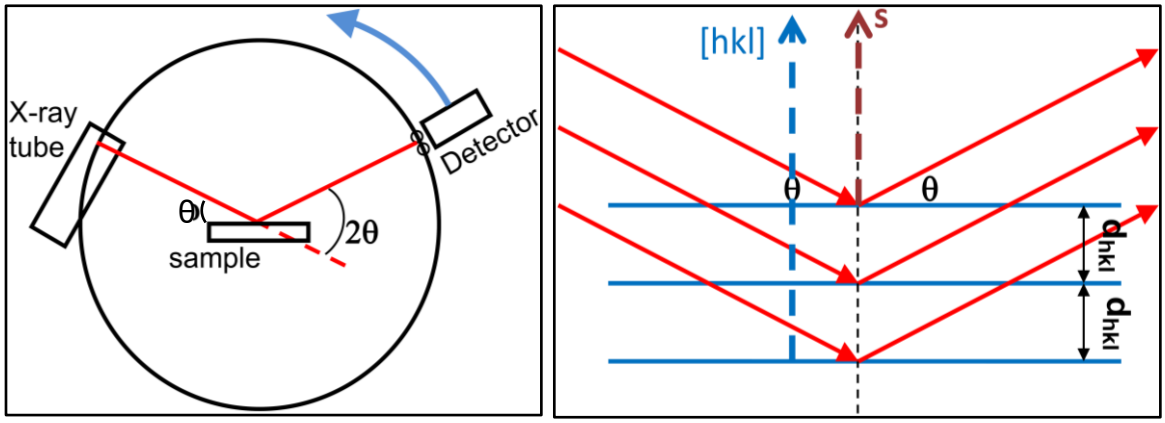

Bragg's law: $\lambda = 2d_{hkl}\sin\theta$

Where:
λ: wavelength of the characteristic X-rays
d_{hkl}: space between the lattice planes
θ: angle between the lattice planes and the incident beam

Figure 3-10: Schematic illustration of the concept of XRD analysis [214].

3.2.4. Specific surface area

The specific surface areas of VCe, HCeP and DhCeP were determined with the air permeability method (Blaine method) according to the German standard DIN EN 196-6:2018, which describes the procedure in detail. In summary, the porosity of the compacted cement bed is predetermined (e = 0.500). The cement sample is placed on top of a perforated disc (inside a cell) covered by a filter paper disc. Another filter paper disc covers the cement sample, and a plunger is used for compaction to produce the compacted cement bed. The sample density is separately measured to determine the mass required for the test. Subsequently, the time needed for the air to flow through the compacted sample is measured and used in the formula provided in the standard. Finally, the viscosity of air at the test temperature is also given in the table provided in the standard.

3.2.5. Scanning Electron Microscopy (SEM) and Energy Dispersive X-ray Spectroscopy (EDX)

SEM is a commanding technique for investigating the microstructure evolution of cementitious materials exposed to different temperature treatments. It is based on the principle that the sample surface is subjected to the electron beam in a vacuum chamber. Subsequently, different signals result from this interaction and are detected and used for image formation. The sort of interactions determines the types of signals that are generated. Three categories of signals are typically generated; the secondary electrons (SE) signal, the backscattered electrons (BSE) signal, and the characteristic X-ray emission. These signals come from different depths and volumes in the sample and provide diverse information.

In this research, the secondary electron signal was used to assess the effect of thermal treatment on the morphology and topography of the specimens (HCeS, RwCeS, RhCeS, and RhCoS). The samples were coated using a Sputter Coater Cressington MTM 10 (Au80Pd20 target). For the elemental analysis in the SEM, EDX (energy resolution < 129 eV for Mn K radiation, detector surface 100 mm^2) point analysis was used. The SEM/EDX measurements were performed with the microscope Jeol JSM 7500F (Essen). Small specimens (<1cm^3) were required. The samples were stored in a desiccator under vacuum to avoid carbonation, as shown in **Figure 3-11**.

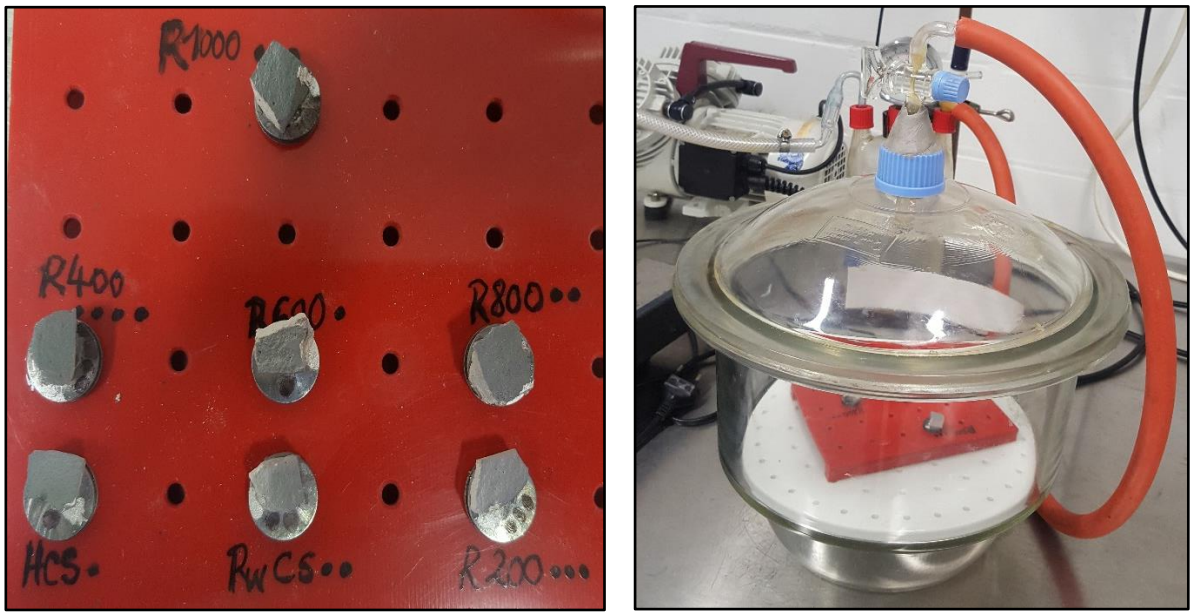

Figure 3-11: The storage of the SEM/EDX samples in a desiccator under vacuum to avoid carbonation.

3.2.6. Porosity and pore size distribution

The Mercury Intrusion Porosimetry (MIP) technique was used to evaluate the porosity and the pore size distribution resulting from the thermal treatment of the HCeP and RcCoP. MIP is based on the hypothesis that a non-wetting fluid (having a contact angle > 90°), mercury in this case, will only enter the pores under pressure. This applied pressure depends on the pore size. The relationship between the pore size and the applied pressure can be expressed by the Washburn equation, assuming a cylindrical pore geometry:

$$P = \frac{-4\gamma\cos\theta}{d} \qquad (3.1)$$

Where P is the applied pressure (Pa), γ is the surface tension of mercury (0.48 N/m), θ is the contact angle between mercury and the pore surface (140° is adopted for cementitious materials), and d is the pore diameter in (m).

The MIP is a powerful technique but has its limitations. For example, it measures the largest entrance to the pore instead of the actual pore size, and different assumptions are made. Additionally, the degree of drying influences the results enormously. The sample size to be analyzed is limited, affecting its representation of the whole volume **[215–218]**.

In this study, MIP was conducted on the specimens (HCeS, RwCeS, RhCeS, and RhCoS) produced from the mixture of water with the DhCeP and DhCoP or the untreated HCeP and

RcCoP. Different assumptions were made, such as the maximum test pressure of 400 MPa, the mercury surface tension of 0.48 N/m, and the mercury contact angle of 140°. Only small pieces of specimens were required, and the samples were cut from the center whenever possible. A small hammer, forceps and tweezers were used to prepare the required sample size (~1x1x1cm^3) and mass (~1.6-2.0 grams) for measurement. The samples were stored under vacuum inside the MIP device for approximately 20 minutes before the pressure was used to ensure they were moisture-free, as shown in the red circle in **Figure 3-12**. The mercury storage is shown in the blue circle. Stefan Nawrath, a technician at the Institute for Materials Science at the University of Duisburg-Essen in Germany, performed the MIP.

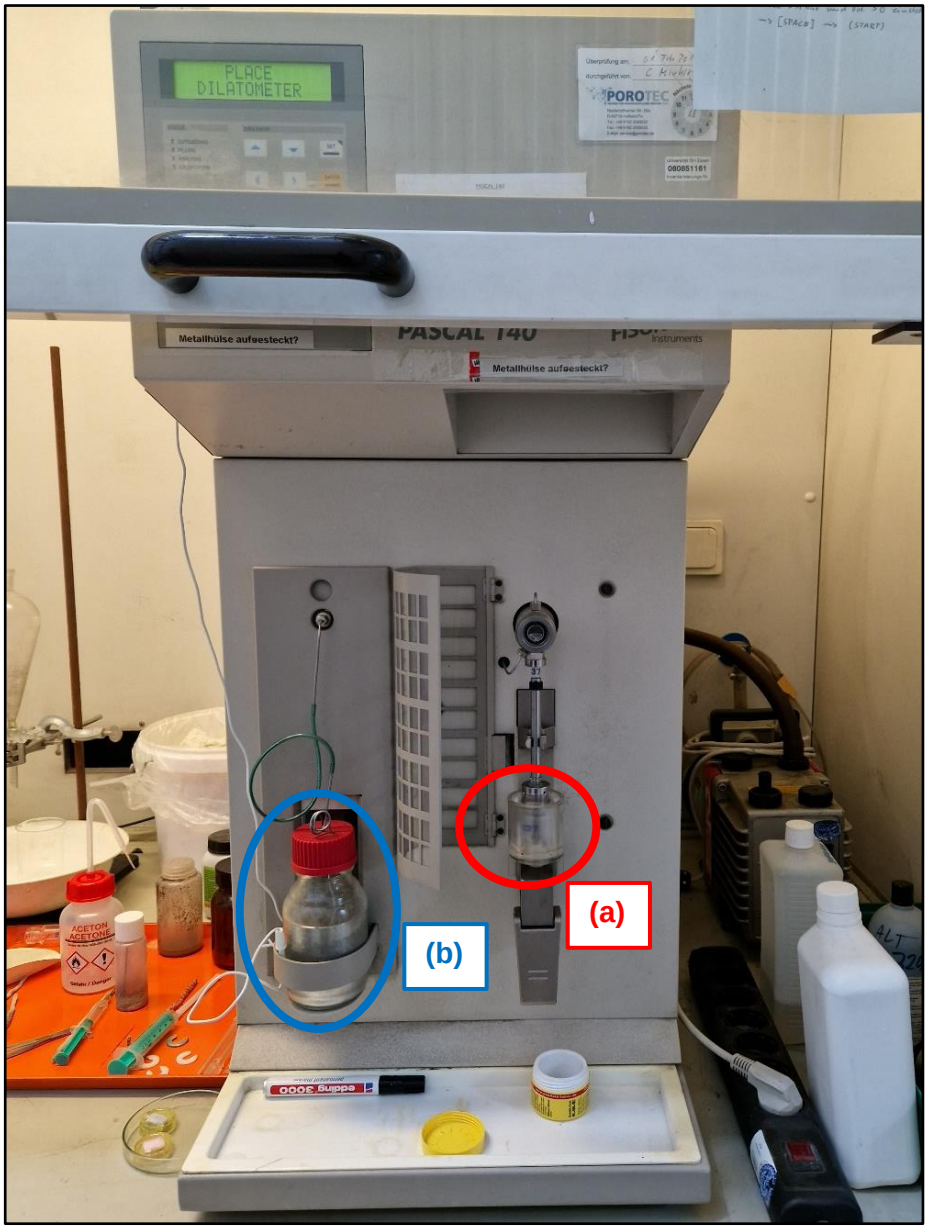

Figure 3-12: Illustration of porosity measurement by the MIP technique. (a) sample storage under vacuum, (b) mercury storage.

3.2.7. Determination of strength

The strengths of the specimens (RhCeS and RhCoS) made from a mixture of water and the thermal pre-treated powders (DhCeP and DhCoP) were determined to evaluate the extent of reactivation of the untreated powders (HCeP and RcCoP). Whenever possible, both the compressive and flexural strengths were assessed. The w/c used for the HCeP was 0.5, while that used for DhCeP was above 0.6 as they require more water for the same consistency. Additionally, the superplasticizer (2% by mass), MC-PowerFlow 1102 (MC Bauchemie, Bottrop, Germany), was necessary to control the setting time and regulate the hydration process of the DhCeP, especially for powders treated at temperatures above 600 °C. On the other hand, the w/c used for the RcCoP and DhCoP was less (0.37 – 0.46) due to the high quartz (SiO_2) content and the reduced content of the VCe phases. The trial and error method was used, but a complete standard consistency test should be conducted to evaluate the accurate w/c associated with every treatment temperature. **Table 3-1** shows the w/c used to determine the strengths of HCeS, RhCeS, RcCoS, and RhCoS.

Table 3-1: The w/c used for compressive and flexural strength determination.

Hydrated Cement Powder (HCeP)							
Sample type	VCe	HCeP	DhCeP200	DhCeP400	DhCeP600	DhCeP800	DhCeP1000
w/c	0.50	0.60	0.60	0.62	0.68	0.70	0.72
Recycled Concrete Powder (RcCoP)							
Sample type	VCe	RcCoP	DhCoP200	DhCoP400	DhCoP600	DhCoP800	DhCoP1000
w/c	0.50	0.37	0.40	0.42	0.43	0.44	0.46

A CEN standard sand conforming to ISO 679 (Beckum/Germany) was used for mortar production to evaluate the effect of DhCeP in mortar, named Rehydrated Cement Mortar (RhCeM). The mortar mix ratio was selected according to DIN EN 196-1 Section 6, with (450 ± 2) g of VCe, HCeP, DhCeP or a mixture; (1350 ± 5) g of sand; and (225 ± 1) g of water. The compressive and flexural strengths were evaluated on mortar using 100% VCe or replaced with DhCeP (10%, 20%, and 30%). In addition, the complete influence of the optimum heating temperature (100% DhCeP600) on mortar was assessed.

Prismatic steel molds (40×40×160 mm^3) were used to make the standard-size specimens. The compressive and flexural strengths were measured after 2, 7, and 28 days, including curing for 1 day in the mold, 6 days in water, and 21 days in the temperature control room (at ±20°C and ±65% RH). Nevertheless, the compressive strength was also evaluated on small-size specimens (20×20×20 mm^3) produced with cubic silicone molds due to the limited quantity of materials, especially the DhCoP. Error! Reference source not found. shows the sizes of molds u sed to make the specimens, while the process applied for the preparation of materials and specimens is shown in **Figure 3-7**.

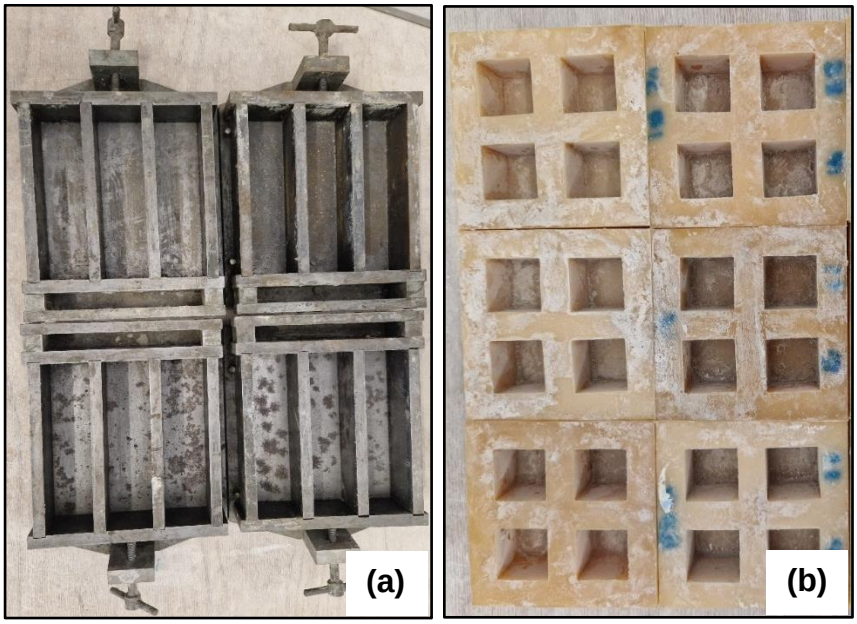

Figure 3-13: The sizes of molds used to produce the specimens: (a) the standard size, (b) the small size.

The flexural strength was measured only on standard-size specimens using a three-point bending method. The sample had two fixed supports at 20 mm from the edges, while the load was applied in the center and gradually increased until failure. At least three specimens were tested for each sample type and the average was considered. The compressive strength was measured on the two halves obtained per each sample after flexural strength. Thus, the average of six measurements was considered for each sample. The bottom and top edges of the sample were fixed (uniaxial compression), and the applied load gradually increased until the sample broke. The obtained maximum loads applied are used to calculate the strength based on the cross-sectional area. **Figure 3-14 (a)** and **Figure 3-14 (b)** indicate the differences between the sample supports during the flexural and compressive strength measurements.

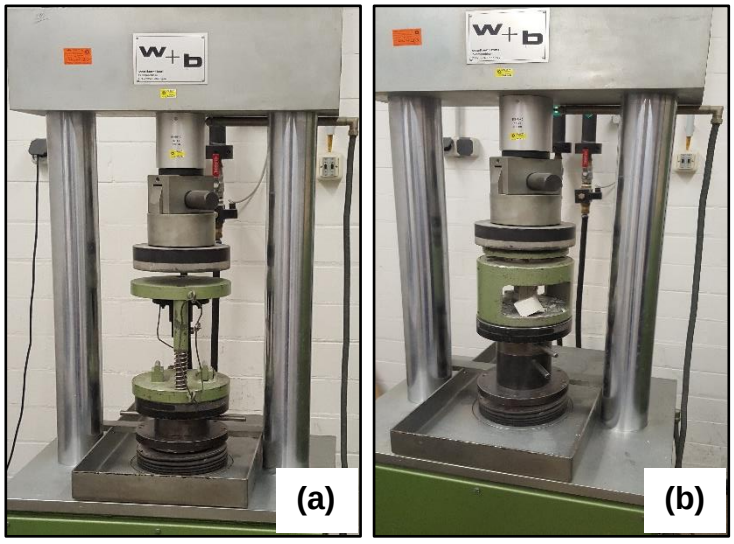

Figure 3-14: Differences between the sample supports during the flexural (a) and compressive (b) strength measurements

4. Reactivation of hydrated cement powder through thermal treatment

This chapter discusses the results associated with the thermal reactivation of 28 days Hydrated Cement Powder (HCeP) at different temperatures from 200 °C to 1000 °C. Section **4.1.1** illustrates the X-ray Diffraction (XRD) and the X-ray Fluorescence (XRF) results, Section **4.1.2** the Differential Scanning Calorimetry and Thermogravimetry **(**DSC-TG) results, Section **4.1.3** the specific surface area, and Section **4.1.4** the Scanning Electron Microscopy and Energy Dispersive X-ray Spectroscopy (SEM and EDX) results. Finally, Section **4.2** discusses the results and concludes on the potential optimum thermal treatment temperature depending on the chemical and physical changes occurring.

4.1. Experimental results

4.1.1. XRD and XRF

Figure 4-1 (a) shows the XRD patterns of Dehydrated Cement Powder (DhCeP) obtained after thermal treatment of HCeP at different temperatures, while **Figure 4-1** (b) shows the XRD patterns of RhCeP obtained after the reaction of DhCeP with water for 28 days at room temperature. It can be observed that the XRD patterns and peak intensities associated with different phases vary according to the thermal treatment temperatures in **Figure 4-1 (a)**. The XRD patterns of the VCe display notable differences in comparison to the other patterns. For example, the portlandite phase peaks are not identified in the VCe, because portlandite results from the reaction of VCe phases with water. The portlandite phase peaks exist for the DhCeP samples, and their intensities change according to the treatment temperature. The peak intensities are similar for DhCeP200_1h and DhCeP400_1h. They become less intense after treatment at 400 °C and almost disappear after treatment at 1000 °C.

Moreover, there are similarities between the diffraction patterns of the HCeP to the DhCeP400_1h with comparable phase peaks and intensities. Differences occur between the diffraction patterns from DhCeP400_1h to DhCeP600_1h, such as the increase of peak intensities for the calcium silicate phases, especially the dicalcium silicate phases (C_2S_β and C_2S_α). Concurrently, the tobermorite peaks disappear. Some similarities exist between the diffraction patterns of DhCeP600_1h to DhCeP800_1h, with differences such as lime peaks in the DhCeP800_1h. The diffraction pattern of DhCeP1000_1h is dissimilar, presenting some new phase peaks, such as silicocarnotite.

The reaction of these DhCeP generates similarities in the reaction patterns of the RwCeP to the RhCeP800_1h as indicated in **Figure 4-1 (b)**. The diffraction pattern of RhCeP1000_1h is dissimilar again. Moreover, the XRD patterns comparing different hold times (1h, 3h, 5h, and 10h) at maximum temperatures for the same dehydration temperatures show similarities. These diffraction patterns are provided in **Appendix 1.2**.

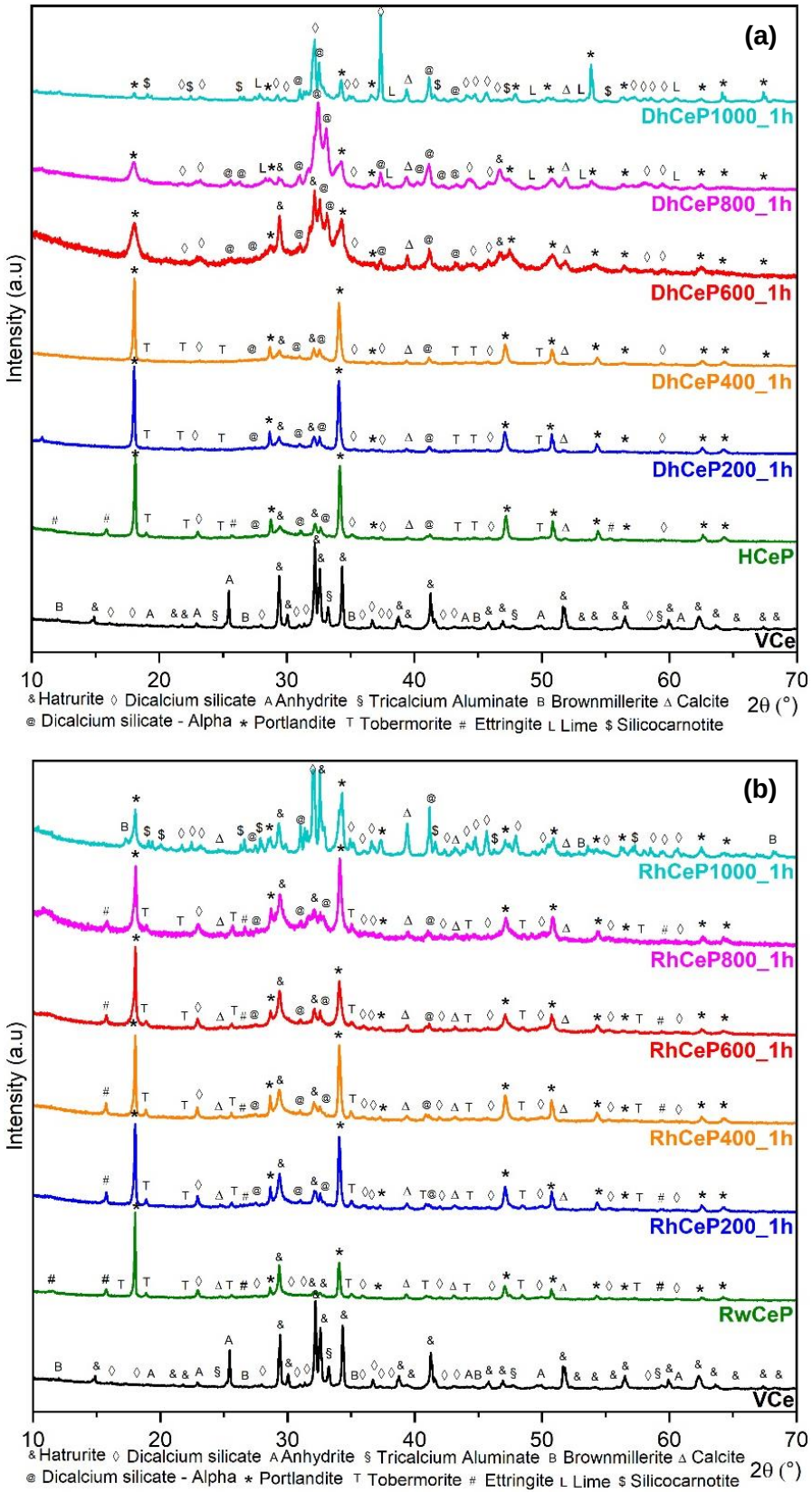

Figure 4-1: XRD patterns of (a) DhCeP obtained after thermal treatment at different temperatures for a hold time of 1h at maximum temperature. (b) RhCeP obtained after the reaction of DhCeP with water at room temperature.

The XRD phase contents in weight percentage were investigated to identify the above similarities and dissimilarities resulting from the thermal treatment temperatures. **Table 4-1** and **Table 4-2** indicate the phase contents (wt. %) of DhCeP and RhCeP from the XRD spectra after Rietveld refinement, respectively. **Figure 4-2** and **Figure 4-3** illustrate the effects of thermal treatment temperature on the phase formation of the DhCeP and RhCeP for a hold time of 1h at maximum temperature, based on the phase contents, respectively. The phase contents associated with 3h, 5h, and 10h of hold times are provided in **Appendix 1.1**.

Table 4-1: Phase content (weight %) of the Dehydrated Cement Powder (DhCeP) from XRD spectra after Rietveld refinement (± 0.5%).

Phase	VCe	HCeP	DhCeP 200_1	DhCeP 400_1	DhCeP 600_1	DhCeP 800_1	DhCeP 1000_1
Ettringite $[Ca_6Al_2(SO_4)_3(OH)_{12}\cdot 26H_2O]$		7.0%					
Portlandite $[Ca(OH)_2]$		26.0%	23.5%	23.5%	15.0%	1.5%	1.0%
Dicalcium Silicate $[Ca_2SiO_4]$	21.0%	14.0%	13.0%	7.0%	12.0%	14.0%	61.0%
Dicalcium Silicate - Alpha			0.5%	10.0%	49.0%	62.5%	8.0%
Hatrurite $[Ca_3SiO_5]$	71.0%	4.0%	3.5%	4.0%	16.5%	7.0%	
Brownmillerite $[Ca_2(Al,Fe)_2O_5]$	1.0%	4.0%	0.5%	0.1%	0.5%	2.0%	3.0%
Tricalcium Aluminate $[Ca_3Al_2O_6]$	3.0%				2.5%		0.3%
Anhydrite $[CaSO_4]$	4.0%						
Tobermorite (C-S-H) $[Ca_5Si_6O_{16}(OH)_2]$		41.5%	58.0%	54.5%			
Calcite $[CaCO_3]$		3.5%	1.0%	1.0%	4.5%	0.5%	
Silicocarnotite $[Ca_5Si_2SO_{12}]$							11.5%
Calcium Silicide $[CaSi_2]$						0.1%	
Lime $[CaO]$						12.5%	15.0%

Table 4-2: Phase content (weight %) of the Rehydrated Cement Powder (RhCeP) from XRD spectra after Rietveld refinement (± 0.5%).

Phase	RwCeP	RhCeP 200_1	RhCeP 400_1	RhCeP 600_1	RhCeP 800_1	RhCeP 1000_1
Ettringite $[Ca_6Al_2(SO_4)_3(OH)_{12}\cdot 26H_2O]$	10.0%	9.5%	12.0%	8.0%	2.0%	
Portlandite $[Ca(OH)_2]$	20.5%	18.5%	20.0%	18.5%	25.5%	17.5%
Dicalcium Silicate $[Ca_2SiO_4]$	14.0%	14.0%	15.0%	16.0%	21.5%	60.0%
Dicalcium Silicate - Alpha		0.5%	2.5%	2.0%	2.5%	0.2%
Hatrurite $[Ca_3SiO_5]$	2.5%	1.0%	2.5%	4.0%	1.0%	2.0%
Brownmillerite $[Ca_2(Al,Fe)_2O_5]$		0.1%				0.5%
Tobermorite (C-S-H) $[Ca_5Si_6O_{16}(OH)_2]$	37.0%	40.0%	38.0%	41.0%	35.5%	
Calcite $[CaCO_3]$	16.0%	16.5%	10.0%	10.5%	12.0%	1.0%
Silicocarnotite $[Ca_5Si_2SO_{12}]$						16.0%
Calcium Silicide $[CaSi_2]$						1.0%
Tricalcium Dialuminium Oxide Hexahydrate $[H_{12}Al_2Ca_3O_{12}]$						2.0%

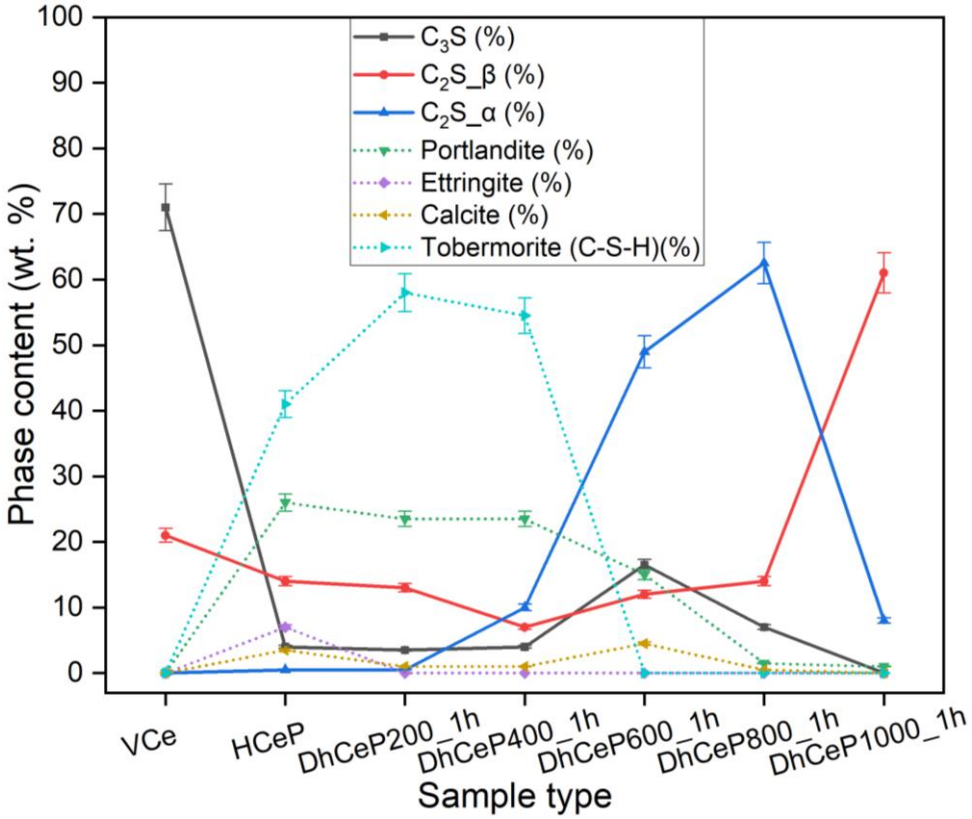

Figure 4-2: Illustration of the effect of thermal treatment temperature on the phase formation of the DhCeP for a hold time of 1h at maximum temperature by the XRD results.

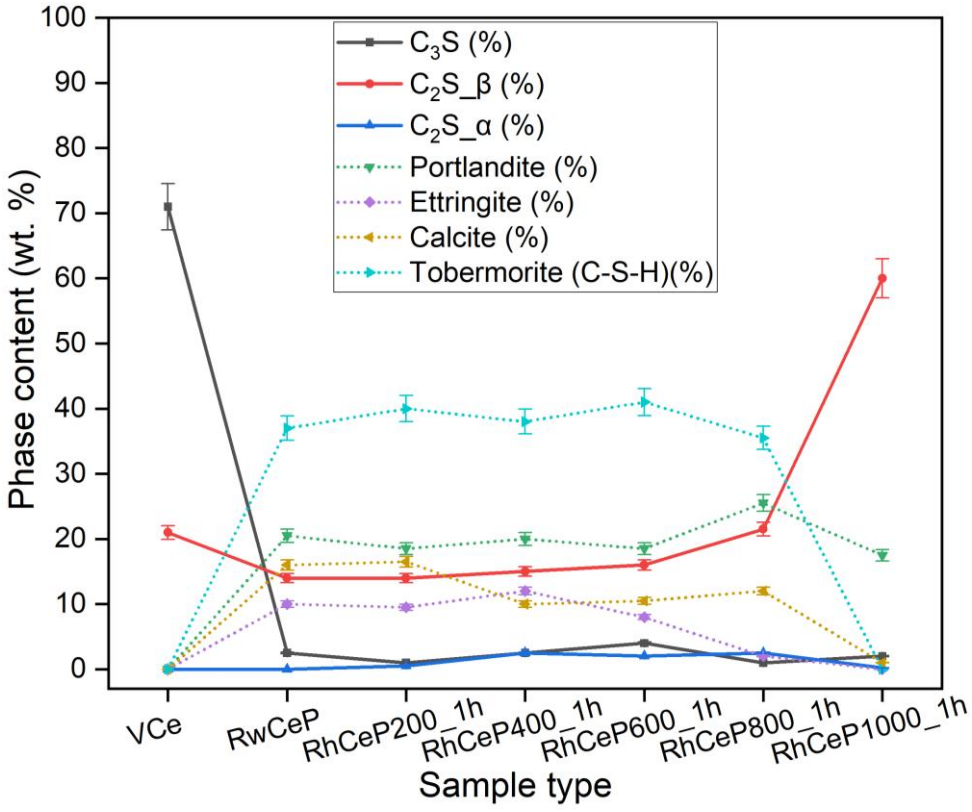

Figure 4-3: Illustration of the effect of thermal treatment temperature on the phase formation of the RhCeP for a hold time of 1h at maximum temperature by the XRD results.

Figure 4-2 indicates that C_3S dominates the VCe phase content compared to the other samples, while the DhCeP600_1h contains the second higher percentage but is still very low compared to the VCe. The DhCeP1000_1h includes no C_3S but the highest percentage of C_2S_β. A much higher percentage of C_2S_α is formed in the other thermally treated samples, especially the DhCeP600_1h and DhCeP800_1h. Only the HCeP presents ettringite ($Ca_6Al_2(SO_4)_3(OH)_{12}\cdot 26H_2O$), while the amount of portlandite ($Ca(OH)_2$) shows an evident decrease in the samples treated at a temperature higher than 400 °C. The formation of tobermorite [C-S-H] ($Ca_5Si_6O_{16}(OH)_2$) is identified from the HCeP to DhCeP400_1h and then tends to disappear. A significant content of free lime in the DhCeP800_1h and DhCeP1000_1h should be noted in **Table 4-1**.

Figure 4-3 indicates the presence of a comparatively similar content of tobermorite percentage in the RwCeP and all the RhCeP except for the RhCeP1000_1h, where it is not identified. Similarly, the rewetted and all rehydrated samples present the ettringite phase except the RhCeP1000_1h. The percentages of C_3S and C_2S_α are minimal in the rewetted and all the rehydrated samples, while the RhCeP1000_1h still shows the highest amount of C_2S_β. The portlandite content is similar in the rewetted and all the rehydrated samples, while the calcite content is generally higher than in the dehydrated samples.

The hold time was changed from 1 to 10 hours. The corresponding results are compared for each treatment temperature. **Figure 4-4** compares the effect of different hold times (1h, 3h, 5h, and 10h) at maximum temperatures on the phase formations during the thermal treatment process. The principal phase formations are analyzed individually. The C_3S phase is minimal in all samples regardless of the hold time compared to the VCe. Generally, the hold time for 1 hour offers the highest weight percentages, and the hold time for 10 hours offers the lowest amount for all thermal treatment temperatures concerning the formation of the C_3S phase.

Conversely, the C_2S_β phase content is highest for all thermal treatment temperatures for a hold time of 10 hours. In addition, the DhCeP1000 contains the highest weight percentages of the C_2S_β phase for all hold times compared to the other samples. Thus, the highest treatment temperature (1000 °C) and the more extended hold time (10 h) cause the formation of more C_2S_β than the other calcium silicate phases (C_3S and C_2S_α). Therefore, this is not beneficial as the C_2S_β phase is less reactive than C_3S and C_2S_α (Refer to **Section 2.3**).

On the other hand, similarities between the evolution of the formation of C_3S and C_2S_α phases with the hold time can be observed. The hold time of 10 hours does not offer the highest content of the C_2S_α phase, formed for a hold time of 1 or 3 hours. Also, the highest amount of the C_3S phase is produced by a hold time of 1 hour. Moreover, the formation of the amounts of tobermorite (C-S-H) and portlandite phases are generally higher for a hold time of 1 hour and decrease for hold times of 5 or 10 hours. The decomposition of tobermorite and portlandite phases during the thermal treatment process is beneficial for establishing calcium silicate phases.

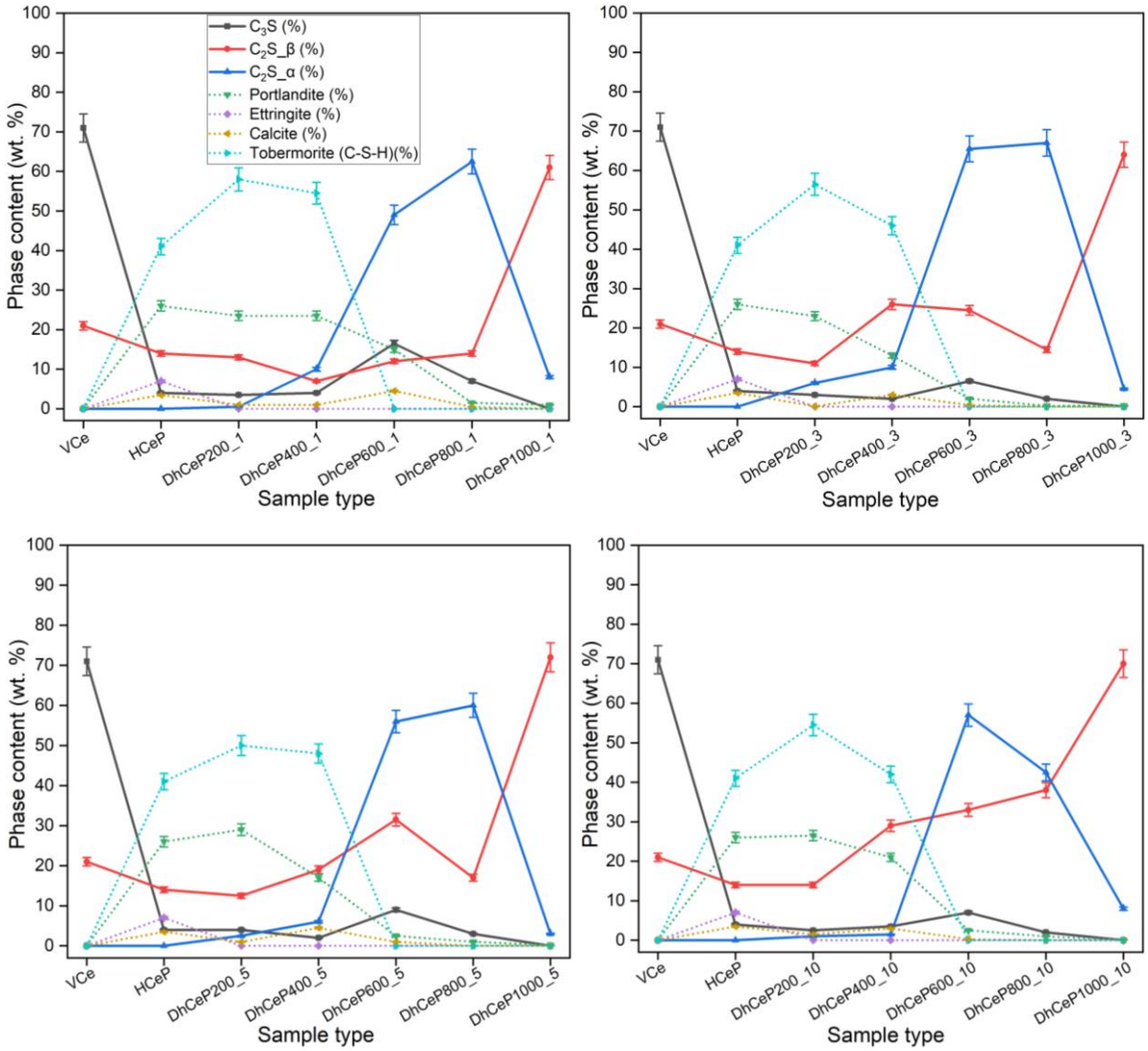

Figure 4-4: Comparison of the effect of thermal treatment temperature on the phase formation of the DhCeP for different hold times (1h, 3h, 5h, and 10h) at maximum temperatures by the XRD results.

XRF was conducted to identify the chemical compositions as given in weight percentages of the VCe, HCeP, and DhCeP to evaluate the potential phase formations during thermal treatment or after mixing them with water to assess their rehydration behavior and strength development. **Table 4-3** shows that the two primary oxides (CaO and SiO_2) bound in the phases constitute approximately 90% of the weight for all samples. The three other notable oxides are SO_3, Al_2O_3, and Fe_2O_3, counting between 7% and 10% depending on the sample type. Six other oxides (MgO, K_2O, Na_2O, TiO_2, SrO, and P_2O_5) are present in minor percentages counting for 3 to 4%. The remaining oxides, such as ZnO, MnO, CuO, ZrO_2, Cr_2O_3, NiO, Rb_2O, V_2O_5, MoO_3, CoO, and BaO, are insignificant. Furthermore, **Figure 4-5** compares different hold times to identify their effect on the content of the primary bound oxides, CaO and SiO_2, indicating that their contents are, respectively, similar for all thermal treatment temperatures and hold times, considering the error bars.

Table 4-3: Chemical composition (given in wt. %) of the VCe, HCeP, and DhCeP for a hold time of 1h at maximum temperature.

Oxide	VCe	HCeP	RwCeP	D200_1h	D400_1h	D600_1h	D800_1h	D1000_1h
CaO	67.6%	69.4%	69.7%	68.7%	67.8%	67.2%	68%	69.8%
SiO_2	20.5%	20.3%	19.8%	20.7%	21.4%	21.9%	21.1%	20.2%
SO_3	4.3%	3.4%	3.3%	3.4%	3.5%	3.5%	3.6%	2.8%
Al_2O_3	3.5%	3.2%	3.2%	3.3%	3.5%	3.6%	3.5%	3.4%
Fe_2O_3	1.6%	1.7%	1.7%	1.6%	1.6%	1.5%	1.5%	1.6%
MgO	0.9%	0.8%	0.8%	0.8%	0.8%	0.9%	0.9%	0.9%
K_2O	0.7%	0.4%	0.5%	0.5%	0.5%	0.5%	0.5%	0.4%
Na_2O	0.3%	-	0.1%	0.1%	0.2%	0.2%	0.2%	0.1%
TiO_2	0.2%	0.2%	0.2%	0.2%	0.2%	0.2%	0.2%	0.2%
SrO	0.2%	0.2%	0.2%	0.2%	0.2%	0.2%	0.2%	0.2%
P_2O_5	0.1%	0.1%	0.1%	0.1%	0.1%	0.1%	0.1%	0.1%

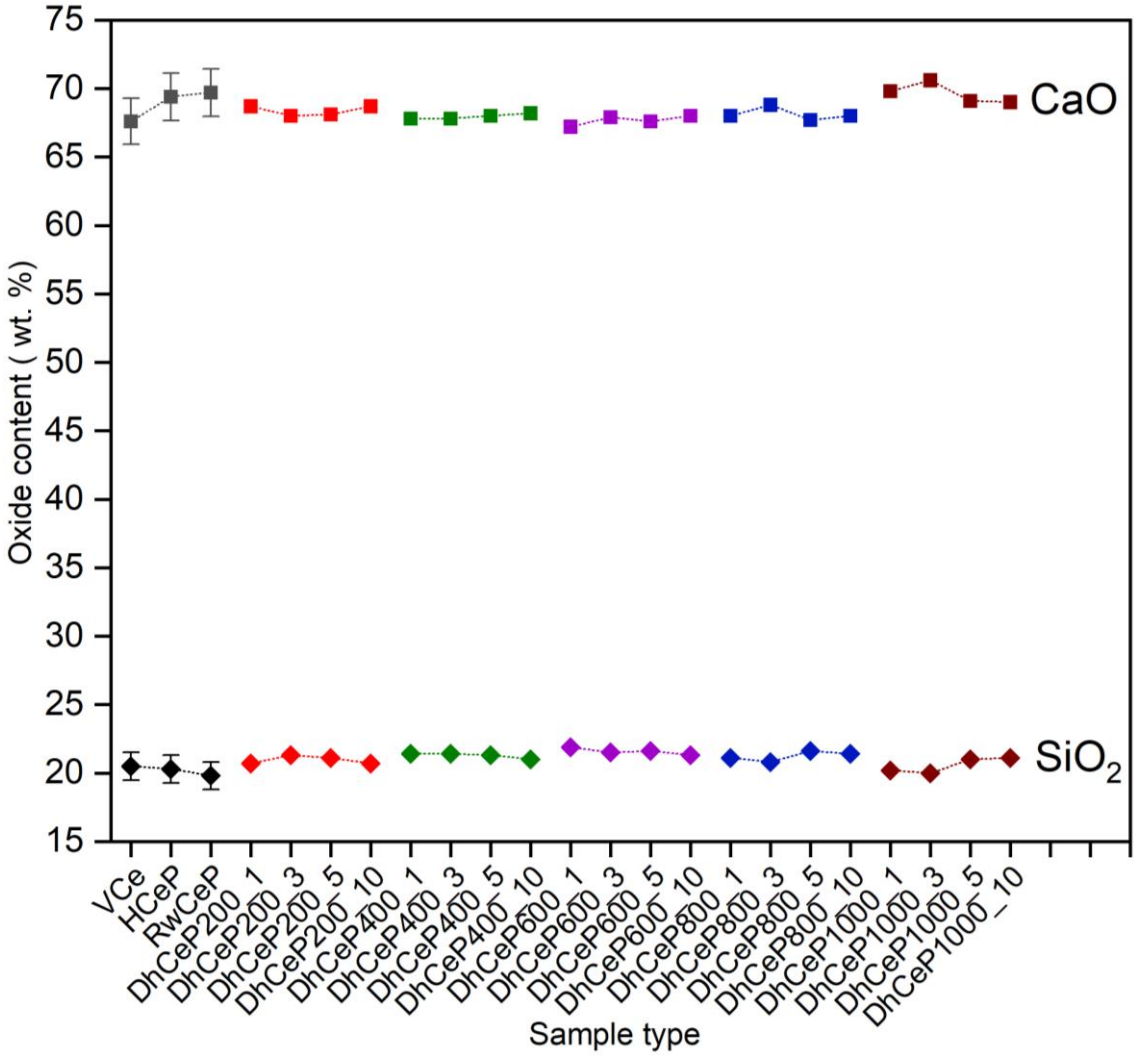

Figure 4-5: Comparison of the CaO and SiO_2 contents in the VCe, HCeP, and DhCeP for different hold times (1h, 3h, 5h, and 10h) at maximum temperatures. The error bars are representative of all samples.

4.1.2. DSC – TG

DSC was performed to identify the heat flow as a function of mass loss resulting in different decomposition peaks representing the chemical transformations in the system. The TG determines the mass losses specified by the changes in slopes corresponding to the appearance of the peaks. **Figure 4-6** shows the three principal peaks of the HCeP in the heating treatment range from 25 °C to 1000 °C. The first peak occurs at 120 °C, the second at 455 °C, and the third at 695 °C. These peaks are named according to the phases undergoing the chemical transformations.

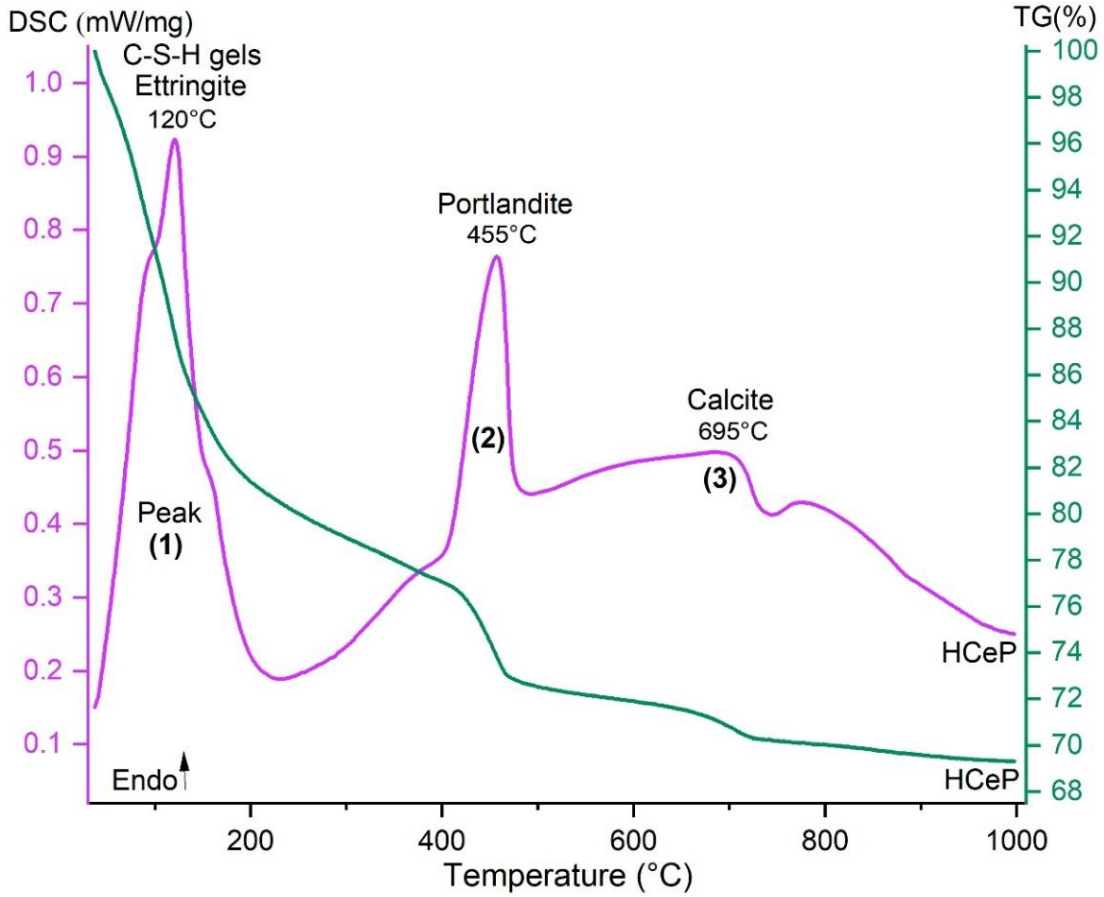

Figure 4-6: DSC (mW/mg) and TG (% mass loss) curves of Hydrated Cement Powder (HCeP) for a heating treatment up to 1000 °C at a 10 K/min heating rate.

The DSC and TG curves of HCeP and DhCeP (D200_1h to D1000_1h) for a hold time of 1h at maximum temperature are compared in **Figure 4-7**. The figure shows that only the HCeP and the DhCeP200_1h (D200_1h) contain the first peak. All the samples display the second peak, but there is a position shift for thermal treatment above 400 °C. These shifts are linked to the decreases in peak intensities and, therefore, the resulting mass losses. The liberation of chemically bound water during pre-treatment above the decomposition point of portlandite (above 400 °C) influences the new decomposition point of the recrystallized portlandite during DSC measurement. Peak three generally disappears above D600_1h or changes position considerably. Correspondingly, **Table 4-4** indicates the presence of peaks, the peak temperatures, mass loss sections and percentages associated with the pre-treatment for a hold time of 1h at maximum temperature. The comparison of the DSC (mW/mg) and TG (% mass loss) curves of HCeP and DhCeP for hold times of 3h, 5h, and 10h are provided in **Appendix 1.3**, while the peaks and mass loss analysis is provided in **Appendix 1.4**.

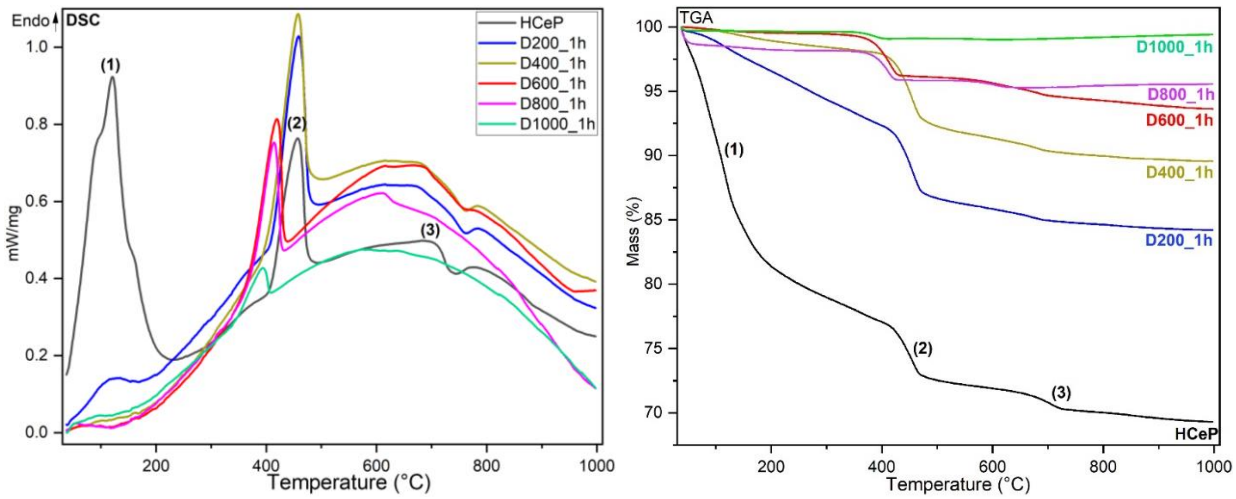

Figure 4-7: Comparison of DSC (mW/mg) and TG (% mass loss) curves of HCeP and DhCeP (D200 to D1000) for a hold time of 1h at maximum temperature.

Table 4-4: DSC - TG peaks and mass loss analysis for the HCeP and DhCeP for a hold time of 1h at maximum temperature.

Sample type	Identified peaks	Peak temperature (± 3°C)	Mass loss section (± 5°C)	Mass loss percentage (± 0.3%)
HCeP	Peak 1 (C-S-H; Ettringite)	120 °C	95 °C - 135 °C	10.5%
	Peak 2 ($Ca(OH)_2$)	455 °C	435 °C - 470 °C	3.0%
	Peak 3 ($CaCO_3$)	695 °C	675 °C - 725 °C	1.0%
D200_1h	Peak 1	125 °C	85 °C - 165 °C	2.0%
	Peak 2	456 °C	435 °C - 470 °C	3.0%
	Peak 3	670 °C	650 °C - 700 °C	0.5%
D400_1h	Peak 1 (non-identified)			
	Peak 2	456 °C	430 °C - 470 °C	3.5%
	Peak 3	680 °C	660 °C - 700 °C	0.5%
D600_1h	Peak 1 (non-identified)			
	Peak 2*	418 °C	405 °C - 430 °C	1.7%
	Peak 3	680 °C	660 °C - 700 °C	0.4%
D800_1h	Peak 1 (non-identified)			
	Peak 2*	412 °C	395 °C - 425 °C	1.3%
	Peak 3	610 °C	590 °C - 620 °C	0.3%
D1000_1h	Peak 1 (non-identified)			
	Peak 2*	395°C	375°C - 405°C	0.4%
	Peak 3 (non-identified)			

Figure 4-8 indicates the effect of treatment with different hold times (1h, 3h, 5h, and 10h) at maximum temperatures on the DSC-TG curves of the DhCeP (D400 – D1000). The analysis of the effect of different hold times is not evident, but there are more similarities between the hold times for 1 hour and 3 hours compared to 5 and 10 hours. The last two hold times (5 and 10

hours) generate a slight shift in peak position with a decrease in the peak intensities, which can indicate thermal instabilities.

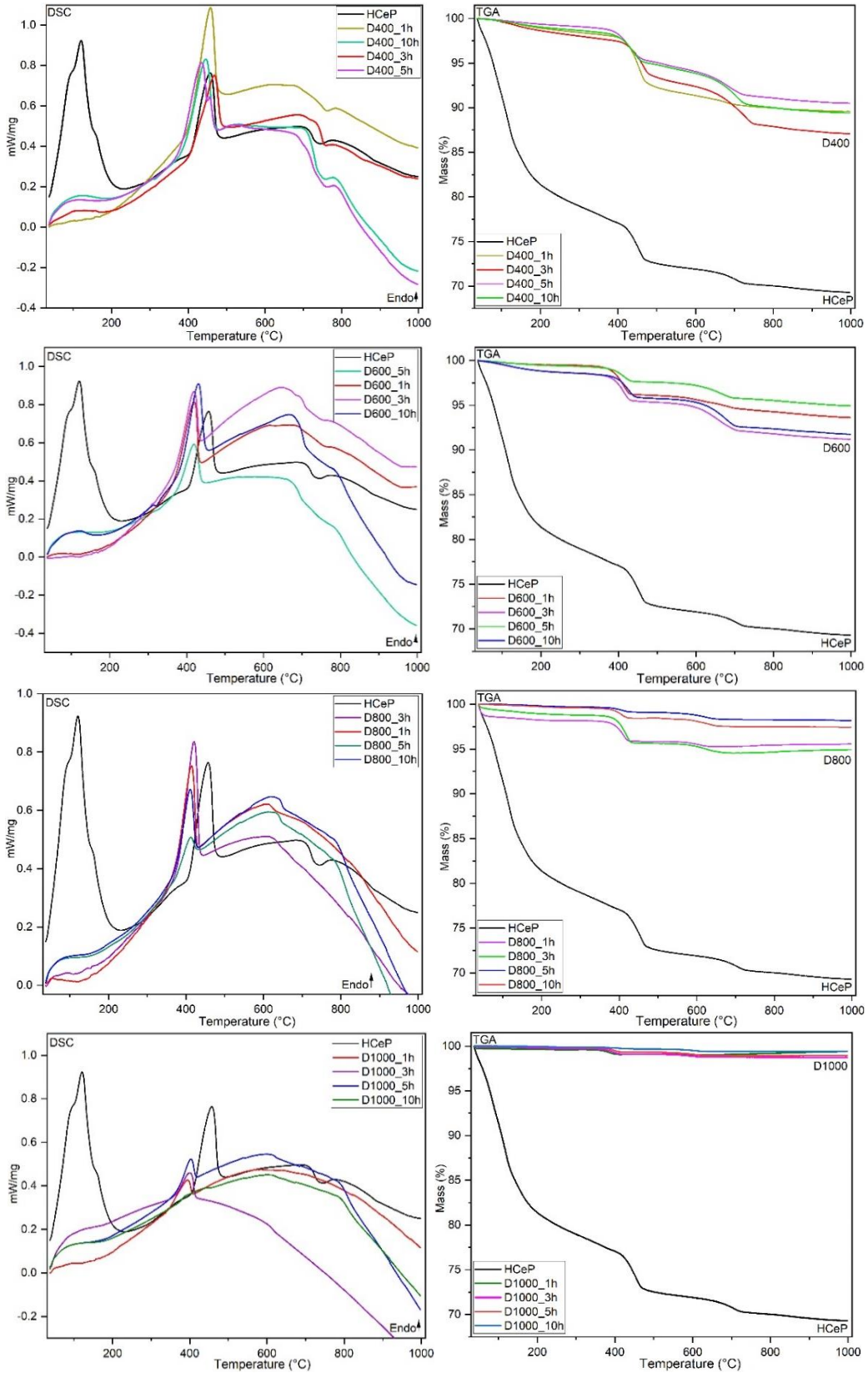

Figure 4-8: Comparison of DSC (mW/mg) and TG (% mass loss) curves of DhCeP (D200 to D1000) dehydrated at the same temperature for different hold times (1h, 3h, 5h, and 10h).

4.1.3. Specific surface area

The specific surface areas of the VCe and DhCeP are determined using the air permeability method (Blaine method) described in **Section 3.2.4**. **Figure 4-9** shows that thermal treatment at low and intermediate temperatures increases the specific surface area. The surface area of the D200_1h is considerably higher than that of VCe. However, there is an unexpected decrease in the specific surface area as the pre-treatment temperature increases. The agglomeration of particles may be the cause of this decrease, especially for pre-treatment at high temperatures. D1000_1h has the lowest specific surface area, so a certain degree of sintering sets in at 1000 °C. The details on the calculation of the specific surface areas of the VCe and the DhCeP for a hold time of 1h at maximum temperature are provided in **Appendix 1.5**.

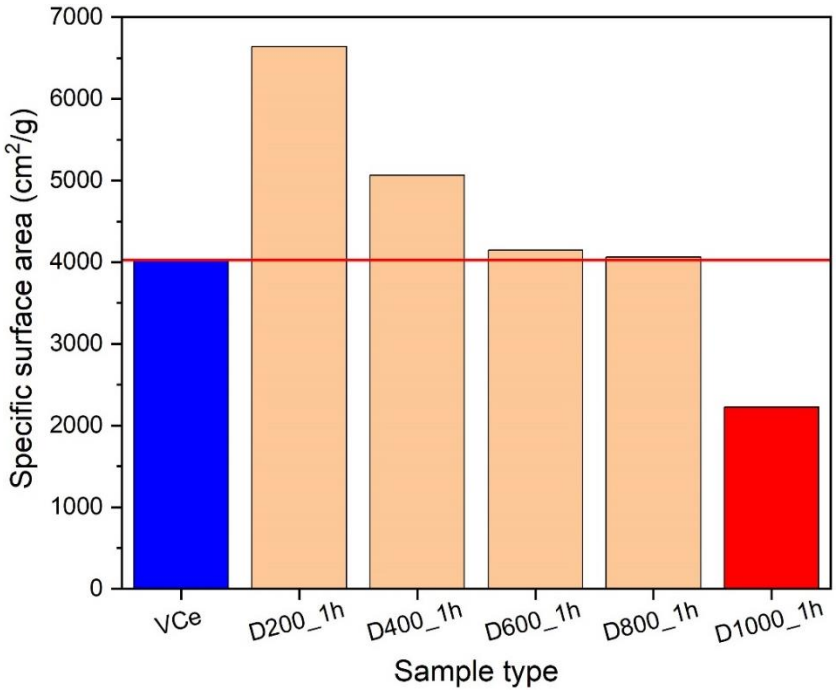

Figure 4-9: Comparison of the specific surface areas of the VCe and DhCeP for a hold time of 1h at maximum temperature.

4.1.4. SEM and EDX

The SEM analysis is essential to investigate the microstructure evolution resulting from the thermal treatment of HCeP at different temperatures. Besides, the topography and morphology associated with phase formations can be identified. Moreover, the EDX complement the SEM for the elemental analysis. **Figure 4-10** indicates the SEM and EDX images of the HCeS that result from the mixing of VCe and water, the RwCeS (Rs20) that results from mixing the HCeP and water (without thermal pre-treatment), and the RhCeS (Rs200 to Rs1000) with water (after thermal pre-treatment).

The EDX analysis reveals the intensity of chemical elements contained per point analyzed, which contributes to identifying phases and their topographies and morphologies. The HCeS serves as a reference for the other samples. There are similarities between the microstructures of Rs20, Rs200, and Rs400. All three samples contain a high amount of ettringite phase identified as needle-like features. Alternatively, the Rs600 has a more condensed microstructure showing a decrease in the ettringite phase and an increase in the di/tri-calcium silicate (C_2S/C_3S)

phases. Due to their similar chemical composition, the later phases were not identified separately using EDX analysis. The Rs800 contains a highly fine microstructure, while the Rs1000 contains a remarkably different microstructure, topography and morphology compared to the other samples.

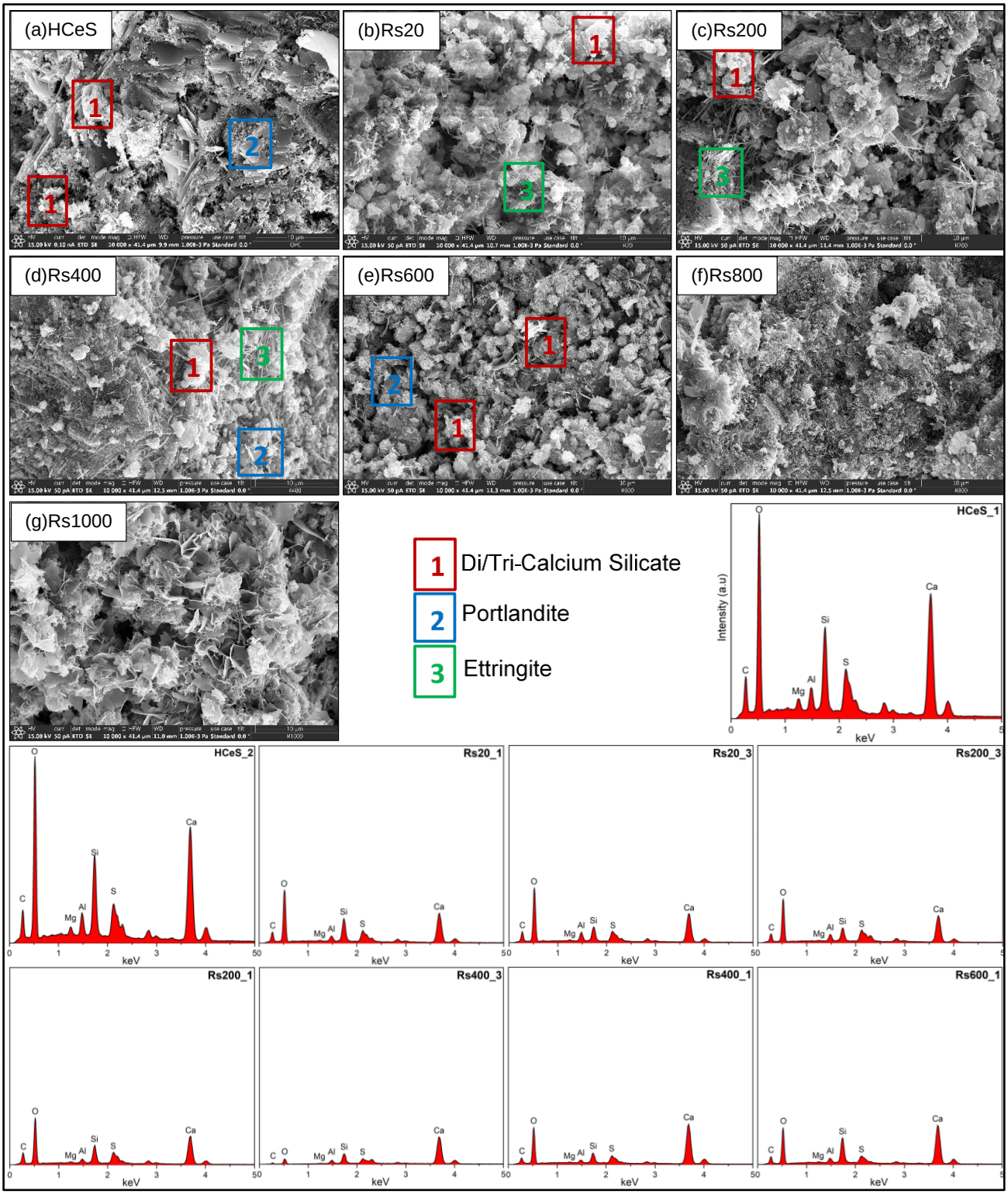

Figure 4-10: SEM and EDX images of (a) Hydrated cement Specimen (HCeS), (b) Rewetted Cement Specimen (RwCeS ‘’Rs20’’) (no thermal pre-treatment) and (c-g) Rehydrated Cement Specimens (RhCeS ‘’Rs200 to Rs1000’’) (after thermal pre-treatment). The EDX images indicate the intensity of chemical elements contained per point analyzed.

4.2. Discussion of the results

This section systematically discusses the results of the thermal treatment of HCeP towards the potential for strength development and particularly the expected optimum treatment temperature after comparison with the VCe results serving as reference. The XRD compares the phase development at each thermal treatment temperature, while the XRF compares the chemical compositions. The DSC compares the peaks illustrating the chemical transformations resulting from thermal treatment, while the TG compares the weight losses associated with these peaks. The specific surface area reveals the potential reactivity after thermal treatment. A higher specific surface area is usually associated with higher reactivity. The SEM demonstrates the microstructure resulting from thermal treatment, illustrating the topography and morphology associated with phase formations, and the EDX determines the local elemental composition. The details of the results directing to the conclusion on the potential optimum treatment temperature will be confirmed by the strength test results that will be discussed later. This section discusses the results of DhCeP and RhCeP obtained by thermal treatment of the RhCeP at different temperatures for a hold time of 1h at maximum temperature. The comparison of the effect of varying hold times (1h, 3h, 5h, and 10h) discussed in **Section 4.1.1** specifies similarities between hold time for 1 and 3 hours and the disadvantages of higher hold times.

Figure 4-1 (a) and **(b)** illustrate the XRD patterns of DhCeP and RhCeP, respectively. Combining these figures gives an insight into the phase formations resulting from the thermal treatment of HCeP (DhCeP) and after mixing the pre-heated HCeP with water (RhCeP). From **Figure 4-1 (a)**, strong similarities in phase content are found from HCeP to DhCeP400_1h, indicating that no significant chemical transformations happen with thermal treatment below 400 °C. However, a clear pattern and phase content change is seen from DhCeP400_1h to DhCeP600_1h, indicating a significant chemical transformation. Another similarity is seen from DhCeP600_1h to DhCeP800_1h, while the DhCeP1000_1h is dissimilar. The following paragraph explains these similarities and differences.

Although the decomposition of the ettringite phase occurs in the range from 20° C to 400 °C, the C-S-H phase is present. C-S-H is the main phase resulting from the hydration of VCe. Above 400 °C, the C-S-H decomposes, forming dicalcium silicate phases (alpha and beta) and changing the diffraction pattern. At 1000 °C, the calcium silicate phases are destroyed, and new phases form in the system. **Table 4-1** shows that the HCeP as a reference material before thermal treatment contains major crystalline phases such as ettringite, portlandite, dicalcium silicate and tobermorite (C-S-H). The chemical compositions and weight percentages of these phases can be found in **Table 4-1**. The ettringite phase disappears in all dehydrated samples (from DhCeP200_1h to DhCeP1000_1h). In contrast, the tobermorite phase disappears above thermal treatment at 400°C. This difference indicates that ettringite decomposes below 200 °C during heating, while tobermorite can still exist, as its decomposition happens above 450 °C **[219, 220]**. Nevertheless, the ettringite phase reappears in RhCeP (from RhCeP200_1h to RhCeP800_1h), specifying that the process is reversible due to the chemical reactions between the DhCeP and water (see **Figure 4-1 (b)**). Since the decomposition of C-S-H generates clinker phases in the system and such phases are associated with strength development **[43, 44]**, a high strength is expected to form above thermal treatment at 400 °C.

The thermal treatment process can produce free lime (CaO), which is disadvantageous for the strength formation of the DhCeP materials. **Figure 4-1 (a)** exhibits a decrease in peak intensities of the portlandite phase above DhCeP400_1h. In contrast, the calcite phase generally

disappears above DhCeP600_1h (see **Table 4-1**), specifying the decomposition of portlandite and calcite above 400 and 600 °C, according to the dehydroxylation: $Ca(OH)_2 \rightarrow CaO + H_2O$ and decarbonation: $CaCO_3 \rightarrow CaO + CO_2$) reactions. **Table 4-1** shows a high content of free lime in DhCeP800_1h and DhCeP1000_1. Thus, the carbonation of the starting material (HCeP) must be avoided during thermal treatment. Free lime leads to faster setting time and expansion problems negatively affecting strength development **[221, 222]**. Additionally, it highlights the expected excessive thermal treatment at 800 °C and 1000 °C that destroys the reformed binding phases.

Mainly, the strength development can be evaluated by the content of calcium silicate phases (C_3S, C_2S_β, and C_2S_α). The higher the percentage of these phases, an achievable higher strength is expected. However, the individual contribution of these phases to the strength is different. The C_3S is a very rapidly reacting phase and contributes the most to strength, especially at an early age (first week), while the C_2S_β slowly contributes to strength at an early age and faster at a later stage (**Figure 2-15**) **[44, 43, 49]**. The C_2S_α is a polymorph of C_2S that is stable at high temperatures. It is more reactive than C_2S_β. Different researchers, such as **Real et al. [167]** and **Ji et al. [223]**, have stated the formation of this highly active polymorph (C_2S_α) during thermal treatment. However, they have specified that it transforms into C_2S_β as the temperature increases above 800 °C. The same situation is identified in this research.

Table 4-1 and **Figure 4-2** indicate a high percentage of C_2S_α in DhCeP600_1h and DhCeP800_1h, while the content of C_2S_β is much lower. On the other hand, the amount of C_2S_β in DhCeP1000_1h is considerably higher than C_2S_α. Additionally, there is a high content of different phases, such as silicocarnotite, while no tobermorite (C-S-H) forms with rehydration (**Table 4-2** and **Figure 4-3**). **Shui et al. [16]** have specified the possible transformation of partially dehydrated hydration phases over 800 °C. Therefore, the best thermal treatment range is above 400 °C but below 800 °C. Considering that DhCeP600_1h is in the best range and tends to have the highest C_3S content, 600 °C is the optimum heating temperature. However, complete strength recovery cannot be expected to be achieved as the VCe contains an enormously high content of C_3S that is not recoverable due to its rapid reactivity and formation at very high temperatures. The expected very low strength development of the RwCeP (no thermal treatment) results from the previously non-reacted fraction of HCeP that enables a minor rebinding ability.

The XRF results in **Table 4-3** indicate similarities between the chemical compositions of the VCe, HCeP, and DhCeP, especially the five compounds most present (CaO, SiO_2, SO_3, Al_2O_3, and Fe_2O_3). The primary compounds of the strength development phases (CaO, SiO_2) are in the same proportion. The CaO is always the highest, between 67% and 70%, as for the VCe. This behavior specifies the potential for forming strength development phases during thermal treatment. However, chemical transformations are required.

Figure 4-6 displays the three prominent peaks of HCeP during heat treatment. The first peak is due to water loss, essentially from the dehydration of the C–S–H gels and decomposition of ettringite. It occurs at 120 °C, and its corresponding mass loss (10.5%) happens between 95 and 135 °C. The second peak is due to the dehydroxylation of portlandite and occurs at 455 °C. Its related mass loss (3%) happens between 435 and 470 °C. Lastly, the third peak is caused by the decarbonation of calcite. It occurs at 695 °C, and the resulting mass loss (1%) happens between 675 and 725 °C. Several other researchers have indicated these phase transitions and have obtained the same ranges **[12, 224, 149, 225]**.

According to **Figure 4-7**, only DhCeP200_1h presents the first peak in DSC among the dehydrated samples. Its resulting mass loss (2%) ranges between 85 -165 °C. Thus, the decomposition of ettringite is complete in this range **[11]**, which agrees with the XRD results. All the dehydrated samples present the second peak. Therefore, the decomposition of portlandite is not complete by thermal treatment since the dehydroxylation reaction of portlandite is expected to be achieved with treatment below 600 °C. These results agree with the XRD results **(Table 4-1)**. Nevertheless, this peak shifts to the lower temperatures for the samples pre-treated above 400 °C and the mass losses decrease from 3% for DhCeP200_1 to 0.4% for DhCeP1000_1. Therefore, we can conclude that the thermal stability of the recrystallized portlandite is not the same as that of the original portlandite from the VCe. The third peak is tiny and tends to disappear above pre-treatment at 600 °C, specifying that more liberation of CO_2 through decomposition of calcite happens with treatment at 800 °C and 1000 °C. Accordingly, the XRD results indicate that calcite content reduces or disappears with these temperatures **(Table 4-1)**. **Sabeur et al. [226]** have identified the same scenario.

The thermal treatment procedure increases the specific surface area (**Figure 4-9**) leading to faster reactivity of the obtained materials. Initially, the change in specific surface area results from altering the VCe particles during the crushing and milling process to get the HCeP. The transformations and decompositions from thermal treatment influence the specific surface area. Thus, reactivity is associated with the porous morphology of grains, the formation of free lime and the content of calcium silicate phases. Nevertheless, the resulting faster reactivity does not necessarily imply better hydration ability, which depends on the phase contents. Alternatively, quick reactivity can affect the microstructure and strength development when it is not regulated. Thus, the following paragraph on SEM and EDX results discusses the microstructure resulting from the thermal treatment of HCeP.

Different steps can be identified during the rehydration process of DhCeP according to the SEM images (**Figure 4-10**). Initially, there is an evolution of the ettringite phase content from specimens obtained without pre-heating the HCeP (Rs20 in **Figure 4-10 b**) up to those obtained after pre-heating of HCeP at 400 °C (Rs400 in **Figure 4-10 d**). No other substantial changes happen within these treatment temperatures. The XRD results (**Table 4-2**) agree with this observation. Subsequently, no more growth of the ettringite phase content occurs with heating the HCeP at 600 °C (Rs600 in **Figure 4-10 e**). Instead, the ettringite phase content decreases while more calcium silicate phases form. As a result, the overall structure is more dense, which is expected to increase the obtainable mechanical strength. The pre-heating of HCeP at 800 °C (Rs800 in **Figure 4-10 f**) results in highly reactive material not permitting reliable workability of the rehydrated products, leading to heterogeneous microstructures, expected to lower the strength values. Lastly, the pre-heating of HCeP at 1000 °C (Rs1000 in **Figure 4-10 g**) exhibits a different microstructure with new crystalline phases. Besides, the XRD results specify that the ettringite and C–S–H phases disappear entirely with this pre-heating temperature. Therefore, there is a possible alteration of already dehydrated hydration products **[16, 17]**, expected to lower the strength results considerably.

Although the combination of XRD, XRF, DSC-TG, specific surface area, and SEM/EDX results can already provide insights on the optimum thermal treatment, the strength development results and how porosity can affect them are required for further assessment for confirmation and conclusion.

5. Reactivation of recycled concrete powder through thermal treatment

This chapter is organized as the previous chapter (**Chapter 4**). It discusses the experimental results related to the reactivation of Recycled Concrete Powder (RcCoP) by thermal treatment at temperatures ranging from 400 °C to 1000 °C. This powder was obtained by Smart Crushing (SC) and Electrodynamic Fragmentation (EF). The powders obtained by these two methods are analyzed and compared for each treatment temperature. A comparison with the HCeP serving as a reference material is made. Subsequently, the potential optimum thermal treatment temperature for the RcCoP is concluded.

5.1. Experimental results

5.1.1. XRD and XRF

Figure 5-1 (a) shows the XRD patterns of DhCoP obtained from thermally treated RcCoP produced by Smart Crushing (SC), while **Figure 5-1 (b)** shows the XRD patterns of DhCoP obtained from thermally treated RcCoP produced by Electrodynamic Fragmentation (EF). All RcCoP samples had a hold time of 1 hour at their respective maximum temperatures. The figures show similarities between the RcCoP treated at the same temperatures irrespective of their separation process.

Although the thermal treatment didn't significantly modify the XRD patterns of the SC20 and EF20 (the RcCoP before thermal treatment), there is an increase of calcium silicate phase peaks (C_3S, C_2S_β, and C_2S_α) in the samples treated above 400 °C. More C_2S_α peaks are obtained with thermal treatment at 800 °C, but the overall small presence of C_3S is higher at 600 °C. The highest content of C_2S_β is at 800 °C and 1000 °C. The thermal treatment at 1000 °C leads to a significant amount of the akermanite phase ($Ca_2MgSi_2O_7$), a newly produced phase. Nevertheless, quartz and coesite (SiO_2) peaks dominate every untreated and thermally treated sample. According to the phase content derived from the XRD spectra after Rietveld refinement, shown in **Table 5-1** and **Table 5-2,** the samples contain between 55 % and 76 % of SiO_2. Additionally, the illustration of the effect of thermal treatment temperature on the phase formation in **Figure 5-2** and **Figure 5-3** emphasizes the dominance of quartz and coesite (SiO_2) content. It is also necessary to highlight a significant amount of calcite and vaterite ($CaCO_3$) below the thermal treatment at 800 °C in all samples. SC800_1 and EF800_1 have higher contents of C_2S_α, 26 % and 25 % respectively, but are both much less than SiO_2 content.

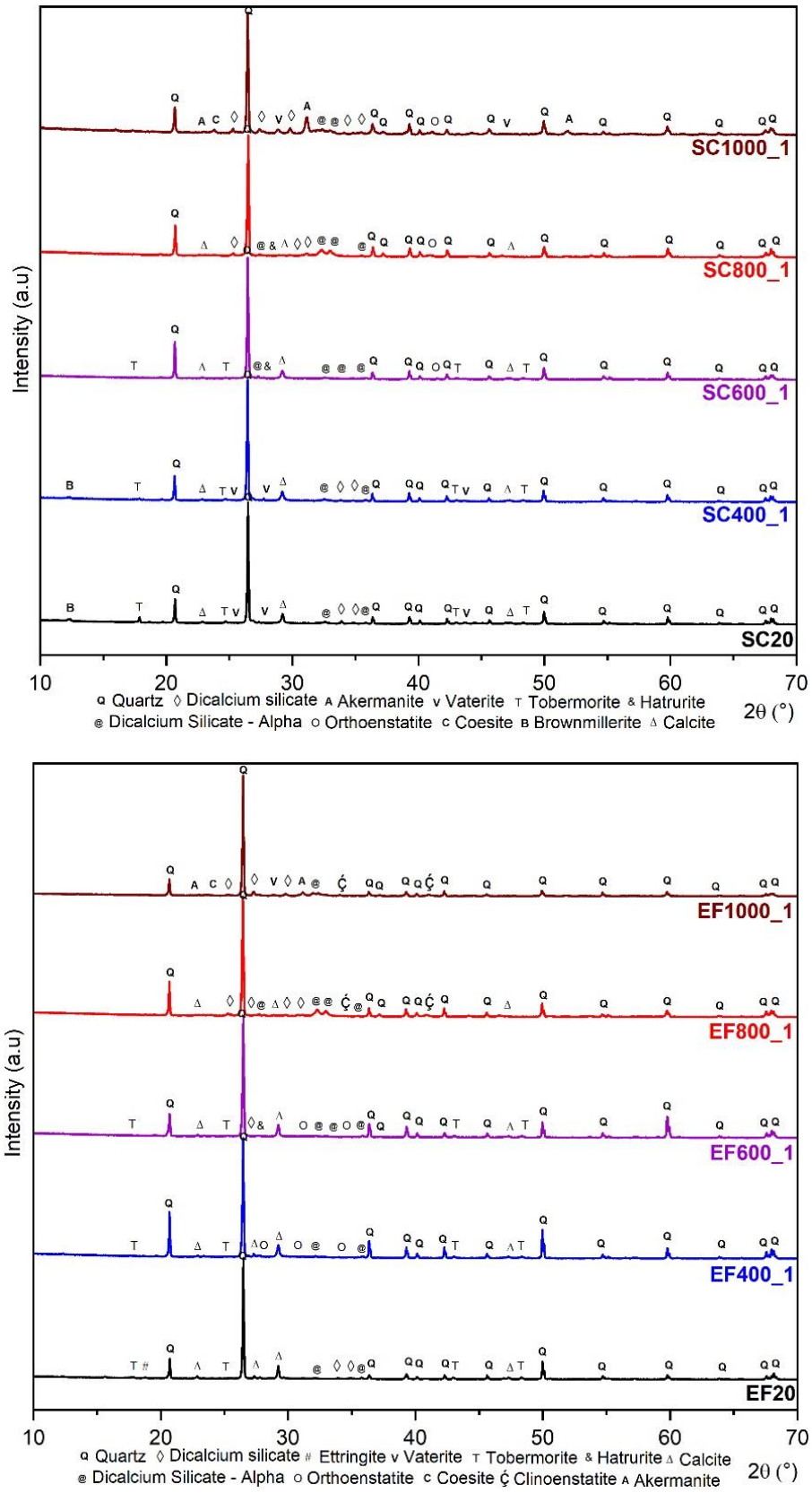

Figure 5-1: XRD patterns of DhCoP obtained after thermal treatment at different temperatures for a hold time of 1h at maximum temperature. (a) Produced by Smart Crushing (SC) (b) Produced by Electrodynamic Fragmentation (EF).

Table 5-1: Phase content (wt. %) of the Dehydrated Concrete Powder (DhCoP) obtained by Smart Crushing (SC) from XRD spectra after Rietveld refinement (± 0.5%).

Phase	SC20_1	SC400_1	SC600_1	SC800_1	SC1000_1
Quartz [SiO_2]	69.5%	66.5%	73.5%	60.5%	48.5%
Coesite [SiO_2]	1.0%	3.0%	0.5%	1.5%	7.0%
Calcite [$CaCO_3$]	17.0%	13.5%	17.0%	1.0%	
Vaterite [$CaCO_3$]	7.5%	10.5%			1.0%
Portlandite [$Ca(OH)_2$]	0.5%			0.5%	
Dicalcium Silicate [Ca_2SiO_4]	1.0%	1.0%		5.0%	3.0%
Dicalcium Silicate - Alpha	0.5%		1.5%	26.0%	3.0%
Hatrurite [Ca_3SiO_5]		0.5%	2.5%	1.0%	
Tobermorite (C-S-H) [$Ca_5Si_6O_{16}(OH)_2 \cdot 4H_2O$]	1.0%	0.5%	2.5%		
Brownmillerite [$Ca_2(Al,Fe)_2O_5$]	2.0%	1.0%		1.0%	
Orthoenstatite [$Mg_2Si_2O_6$]		3.5%	2.5%		7.5%
Akermanite [$Ca_2MgSi_2O_7$]				1.5%	30.0%
Lime [CaO]				1.5%	
Clinoenstatite [$Mg_2Si_2O_6$]				0.5%	

Table 5-2: Phase content (wt. %) of the Dehydrated Concrete Powder (DhCoP) obtained by Electrodynamic Fragmentation (EF) from XRD spectra after Rietveld refinement (± 0.5%).

Phase	EF20_1	EF400_1	EF600_1	EF800_1	EF1000_1
Quartz [SiO_2]	65.0%	52.0%	76.0%	67.0%	59.0%
Coesite [SiO_2]		9.5%		1.0%	
Calcite [$CaCO_3$]	19.5%	12.5%	18.0%	0.5%	
Vaterite [$CaCO_3$]					2.0%
Ettringite [$Ca_6Al_2(SO_4)_3(OH)_{12} \cdot 26H_2O$]	4.0%				
Dicalcium Silicate [Ca_2SiO_4]	1.5%		2.0%	4.0%	27.0%
Dicalcium Silicate - Alpha	0.3%	0.5%	0.5%	25.0%	0.5%
Hatrurite [Ca_3SiO_5]		0.3%	1.0%		0.3%
Tobermorite (C-S-H) [$Ca_5Si_6O_{16}(OH)_2 \cdot 4H_2O$]	9.5%	7.0%	1.5%		
Brownmillerite [$Ca_2(Al,Fe)_2O_5$]				0.1%	
Orthoenstatite [$Mg_2Si_2O_6$]		15.0%	1.0%		
Akermanite [$Ca_2MgSi_2O_7$]				0.5%	11.0%
Lime [CaO]				0.3%	
Clinoenstatite [$Mg_2Si_2O_6$]				1.5%	
Zeolite [SiO_2]		3.0%			

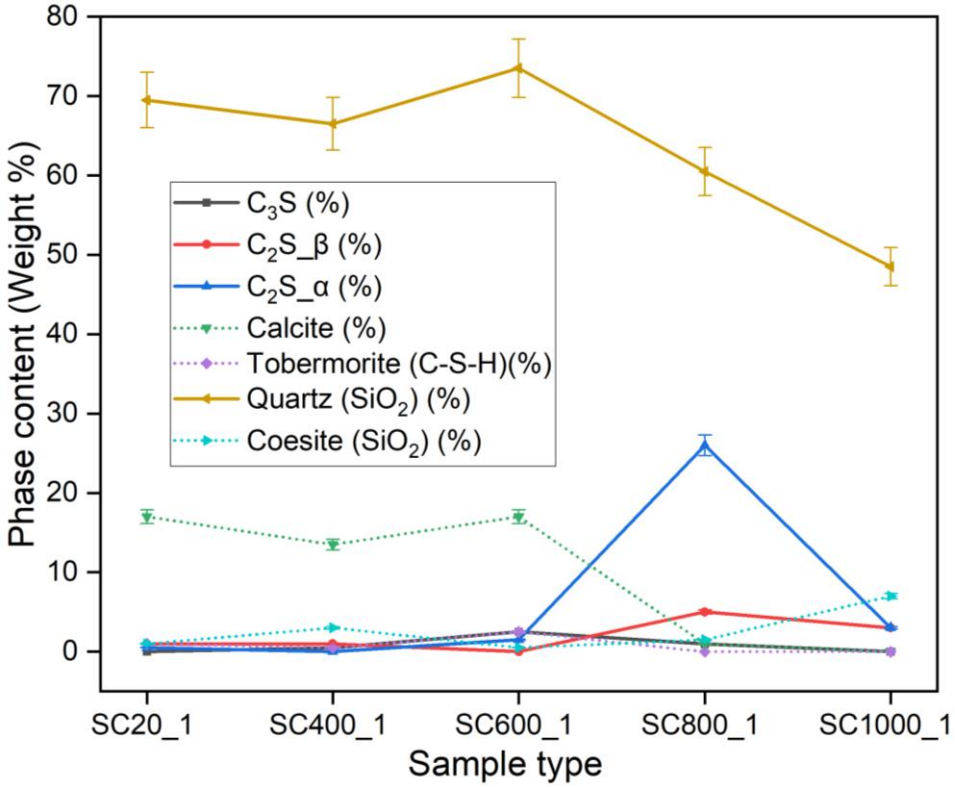

Figure 5-2: Illustration of the effect of thermal treatment temperature on the phase formation of the DhCoP obtained by Smart Crushing (SC) for a hold time of 1h at maximum temperature.

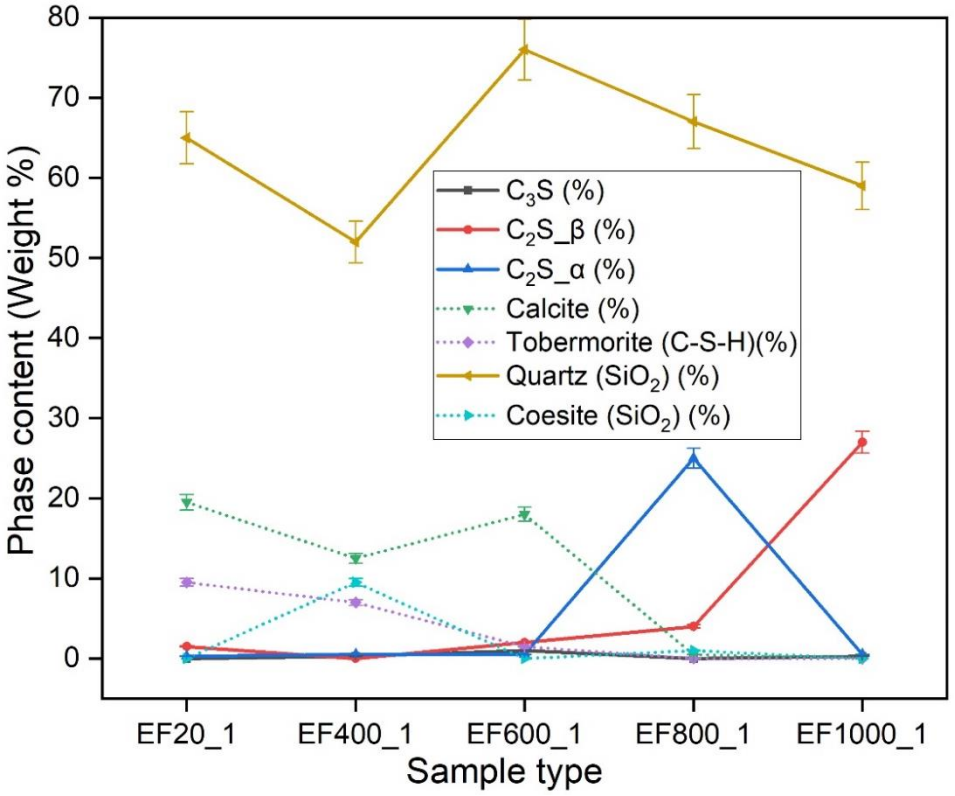

Figure 5-3: Illustration of the effect of thermal treatment temperature on the phase formation of the DhCoP obtained by Electrodynamic Fragmentation (EF) for a hold time of 1h at maximum temperature.

The XRD phase contents resulting from 3h, 5h, and 10h of hold time are provided in **Appendices 2.1** and **2.2** for the Smart Crushed (SC) and Electrodynamic Fragmented (EF) recycled powders, respectively, while the XRD patterns comparing different hold times (1h, 3h, 5h, and 10h) at maximum temperatures for the same dehydration temperatures are provided in **Appendices 2.3** and **2.4** for the SC and EF recycled powders, respectively.

The effect of thermal treatment temperature on the phase formation of the DhCoP (SC and EF, respectively) for different hold times (1, 3, 5, and 10h) at maximum temperatures are compared in **Figure 5-4** and **Figure 5-5**. Generally, the hold time for 1 and 3 hours offers higher contents of the strength development phases for all thermal treatment temperatures than the hold time for 5 and 10 hours. However, the latter hold times tend to increase the content of C_2S_β for SC600 and EF800 considerably. Conversely, the change in hold times doesn't significantly modify the phase content of SiO_2. There is no consistency in the hold time that offers the highest percentage of each phase for all treatment temperatures.

The hold time for 1 hour offers the highest percentage of C_3S phase in the samples SC600 and SC800, the highest amount of C_2S_α phase in SC600, SC1000, and EF800, and the highest quantity of C_2S_β phase in SC400, SC800, SC1000, and EF1000. Therefore, the hold time for 1 hour offers more contents of calcium silicate phases for the RcCoP produced by SC than by EF.

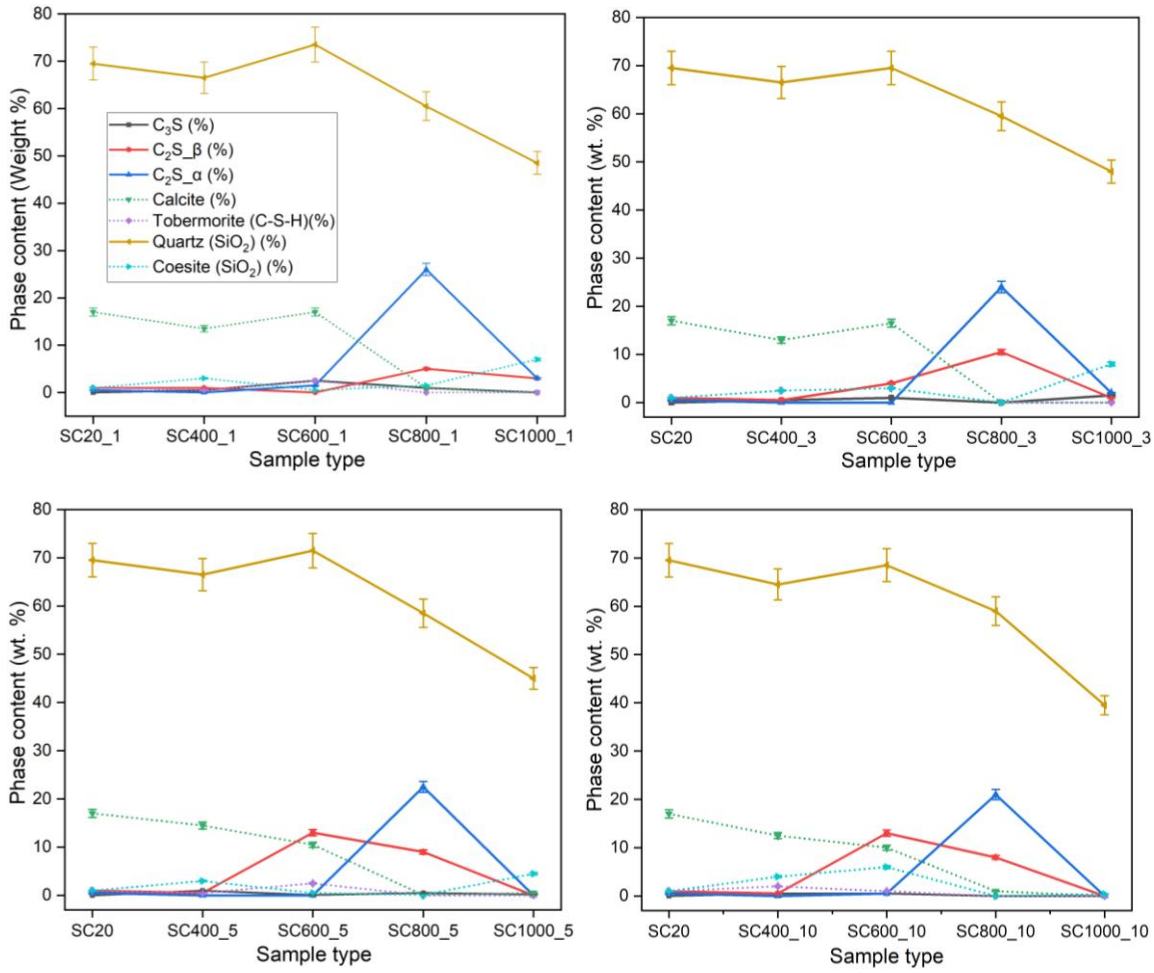

Figure 5-4: Comparison of the effect of thermal treatment temperature on the phase formation of the DhCoP obtained by Smart Crushing (SC) for different hold times (1h, 3h, 5h, and 10h) at maximum temperatures.

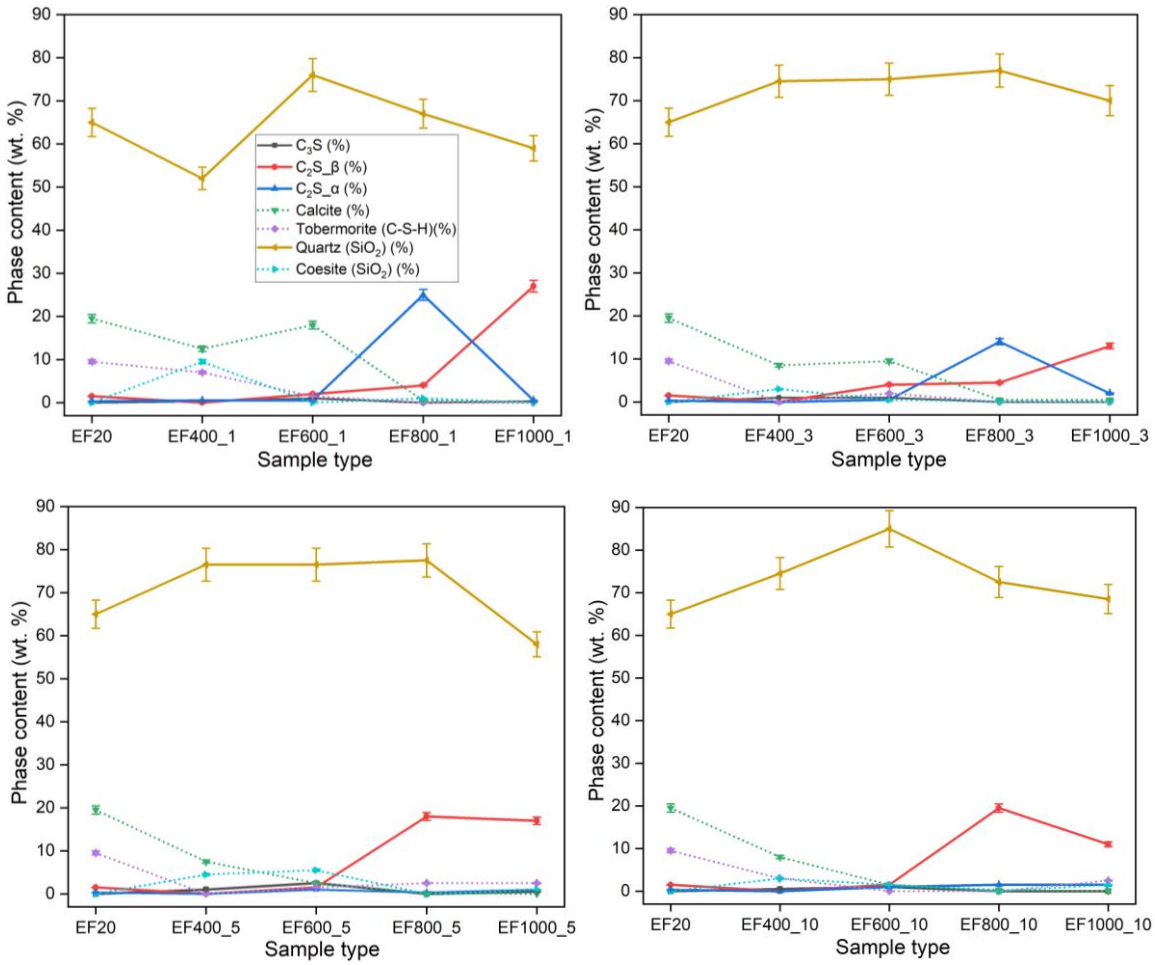

Figure 5-5: Comparison of the effect of thermal treatment temperature on the phase formation of the DhCoP obtained by Electrodynamic Fragmentation (EF) for different hold times (1h, 3h, 5h, and 10h) at maximum temperatures.

As for the DhCeP, XRF was conducted to identify the chemical composition of the DhCoP. Only the principal oxides (CaO and SiO_2), bound in the phases, constitute the weight percentage between 80% and 85% for all samples and for both RcCoP production methods (SC and EF), as shown in **Table 5-3** and **Table 5-4.** The SiO_2 has higher percentages (between 49% and 66%) than the CaO for this material for all treatment temperatures. Furthermore, Al_2O_3 and Fe_2O_3 are less dominant, weighing 6%-8% and 3%-5%, respectively. Then, SO_3, MgO, and K_2O weigh < 2% each, while TiO_2, Na_2O, MnO, and P_2O_5 weigh < 1% each. The weight percentages of the remaining oxides, such as SrO, ZrO_2, ZnO, CuO, Cr_2O_3, PbO, NiO, Rb_2O, BaO, and As_2O_3 are negligible (weighing < 0.1% each), and they are not likely to be found as bound in the principal phases.

Table 5-3: Chemical composition (given in wt. %) of the DhCoP obtained by Smart Crushing (SC) for a hold time of 1h at maximum temperature.

Oxide	SC20	SC400_1h	SC600_1h	SC800_1h	SC1000_1h
SiO_2	66.4%	53.6%	54.7%	49.7%	50.2%
CaO	18.4%	28.4%	27.3%	30.9%	31.1%
Al_2O_3	6.9%	7.6%	7.9%	7.8%	7.9%
Fe_2O_3	3.3%	4.5%	4.4%	4.8%	4.9%
SO_3	1.5%	1.8%	1.8%	2.5%	1.7%
MgO	1.3%	1.6%	1.6%	1.7%	1.8%
K_2O	1.2%	1.3%	1.2%	1.2%	1.1%
TiO_2	0.3%	0.5%	0.4%	0.5%	0.5%
Na_2O	0.3%	0.3%	0.3%	0.4%	0.3%
MnO	0.1%	0.1%	0.1%	0.1%	0.1%
P_2O_5	0.1%	0.1%	0.1%	0.1%	0.1%

Table 5-4: Chemical composition (given in wt. %) of the DhCoP obtained by Electrodynamic Fragmentation (EF) for a hold time of 1h at maximum temperature.

Oxide	EF20	EF400_1h	EF600_1h	EF800_1h	EF1000_1h
SiO_2	66.3%	53.2%	53.4%	49.3%	51%
CaO	19%	31.5%	32.2%	31%	33.5%
Al_2O_3	6.4%	6.5%	6%	7.9%	6.7%
Fe_2O_3	3.5%	3.3%	3%	4.9%	3.6%
SO_3	1.5%	2.5%	2.4%	2.5%	2.1%
K_2O	1.2%	1%	1%	1.3%	0.8%
MgO	0.9%	0.9%	0.8%	1.8%	1%
Na_2O	0.5%	0.3%	0.4%	0.3%	0.4%
TiO_2	0.3%	0.3%	0.3%	0.5%	0.3%
P_2O_5	0.1%	0.1%	0.1%	0.1%	0.1%

The comparison of different hold times (see **Figure 5-6**) indicates that the hold time didn't influence the content of the principal bound oxides (CaO and SiO_2) in the SC samples. Moreover, it shows that the content of CaO increases for thermal treatment above 600 °C while the amount of SiO_2 decreases. On the other hand, the hold time influences the content of the principal bound oxides in the EF samples, as indicated in **Figure 5-7**. In the samples EF400, EF800, and EF1000, the amounts of CaO decrease, while those of SiO_2 increase with the hold times for 3h, 5h, and 10h. Conversely, in the sample EF600, the contents of CaO and SiO_2 are similar between hold times for 1h, 3h, and 5h. The hold time of 10h results in a decrease and increase of CaO and SiO_2, respectively.

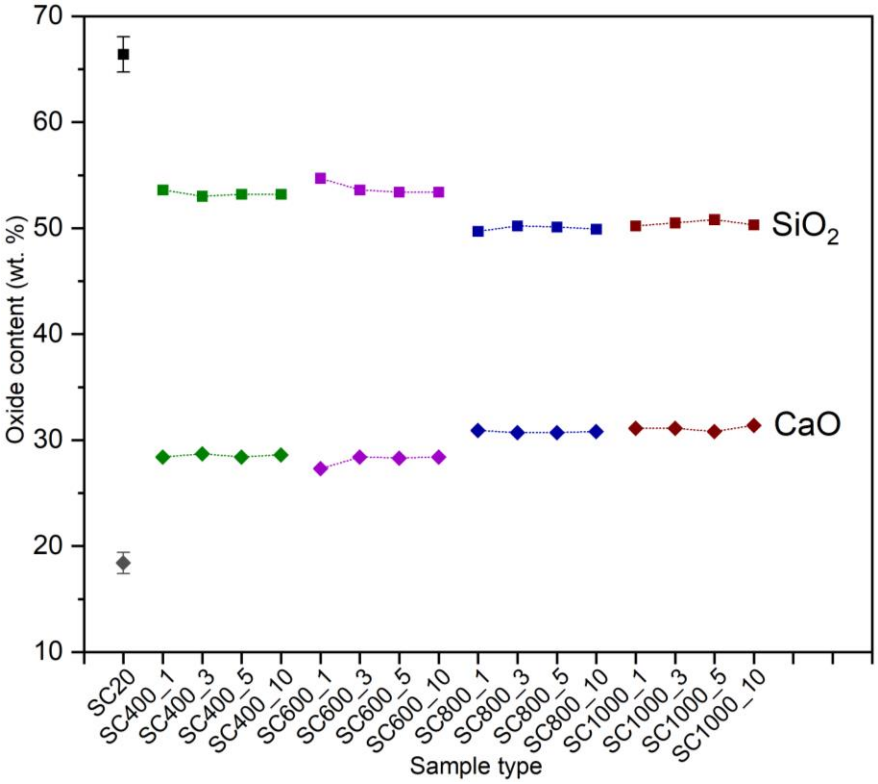

Figure 5-6: Comparison of the CaO and SiO_2 contents in the DhCoP obtained by Smart Crushing (SC) after hold time at different times (1h, 3h, 5h, and 10h). The error bar is representative of all samples.

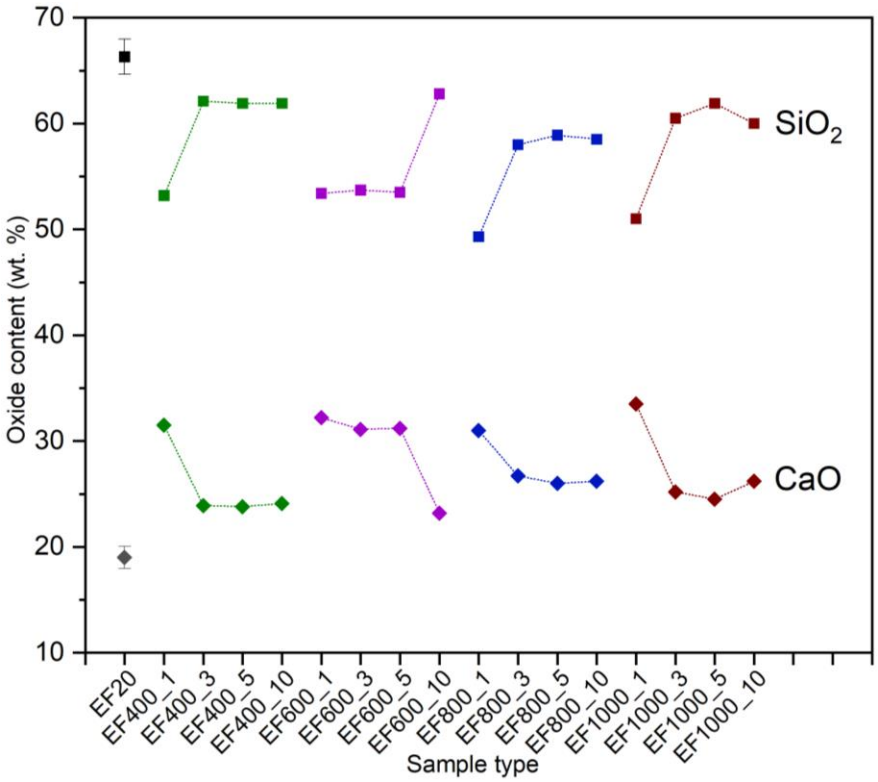

Figure 5-7: Comparison of the CaO and SiO_2 contents in the DhCoP obtained by Electrodynamic Fragmentation (EF) after hold time at different times (1h, 3h, 5h, and 10h). The error bar is representative of all samples.

5.1.2. DSC – TG

Figure 5-8 and **Figure 5-9** show the four prominent peaks of the RcCoP in the heating treatment range from 25 °C to 1000 °C for the SC and EF samples, respectively. The four peaks occur at similar temperatures for the SC and EF samples and correspond to the same chemical transformations for each peak. Respectively for the SC and EF samples, peak 1 occurs at 100 °C and 85 °C, peak 2 occurs at 435 °C and 425 °C, peak 3 occurs at 580 °C, and peak 4 occurs at 725 °C and 720 °C. Within the temperature error in the sample, these values are identical.

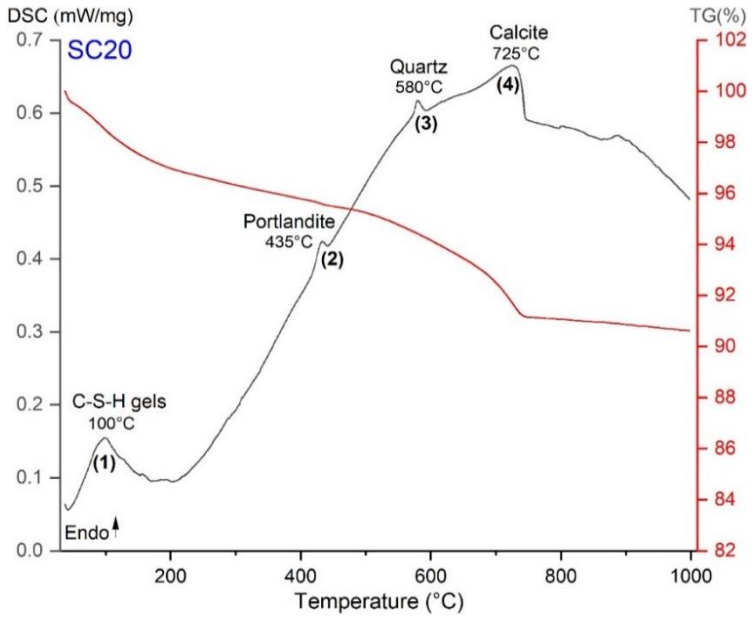

Figure 5-8: DSC (mW/mg) and TG (% mass loss) curves of Recycled Concrete Powder (RcCoP) obtained by Smart Crushing (SC) for a heating treatment up to 1000 °C at a 10 K/min heating rate.

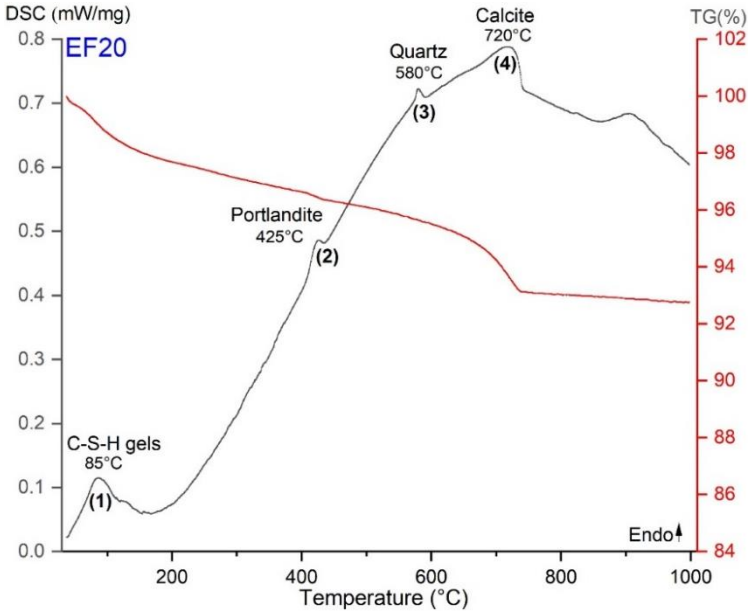

Figure 5-9: DSC (mW/mg) and TG (% mass loss) curves of Recycled Concrete Powder (RcCoP) obtained by Electrodynamic Fragmentation (EF) for a heating treatment up to 1000 °C at a 10 K/min heating rate.

The comparisons of the DSC and TG curves of RcCoP (SC20 and EF20) and DhCoP (SC400 to SC1000 and EF400 to EF1000) for a hold time of 1h at maximum temperature are shown in **Figure 5-10** and **Figure 5-11**. The first peaks are only identified in SC20 and EF20. The second peak is less intense and tends to disappear for thermal treatment above 400 °C. However, in SC800 and EF800, the second peak reappears with a shifted position compared to SC20, EF20, SC400, and EF400. The third peak has a low intensity, as well, but is present in every sample at the same temperatures. In contrast, the fourth peak is comparatively more intense than the second and third and disappears with thermal treatment above 600 °C.

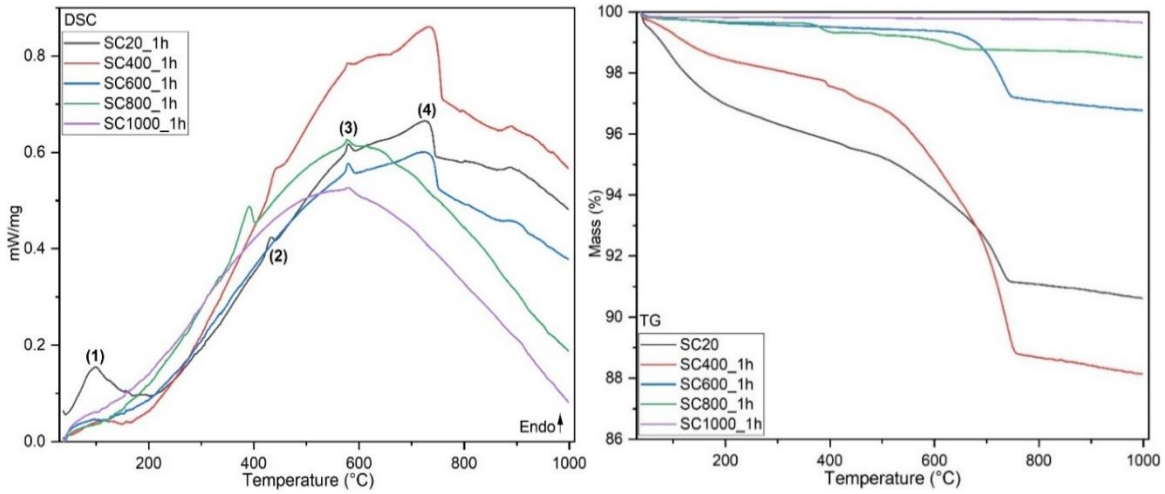

Figure 5-10: Comparison of DSC (mW/mg) and TG (% mass loss) curves of DhCoP (SC400 to SC1000) obtained by Smart Crushing (SC) for a hold time of 1h at maximum temperature.

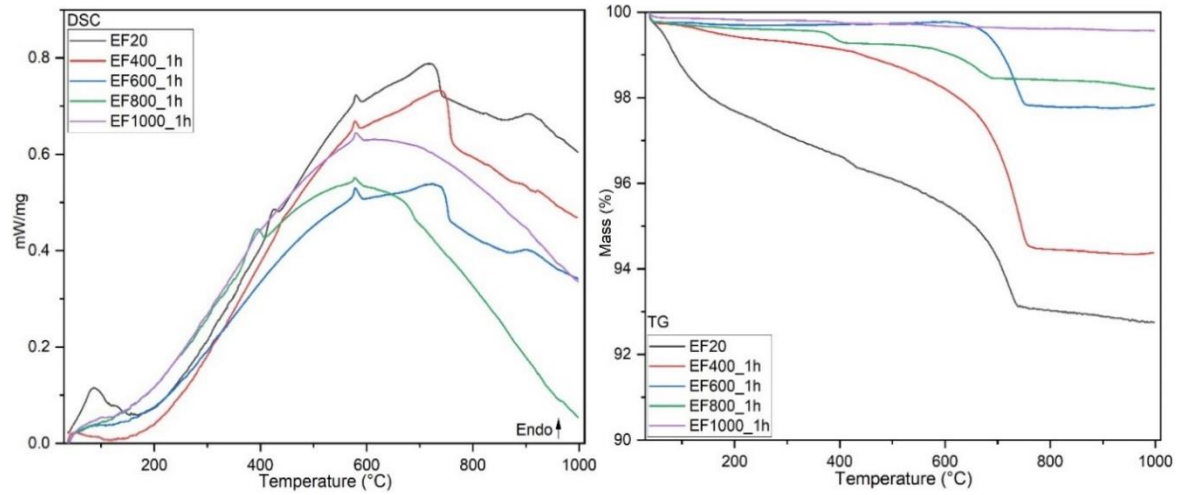

Figure 5-11: Comparison of DSC (mW/mg) and TG (% mass loss) curves of DhCoP (EF400 to EF1000) obtained by Electrodynamic Fragmentation (EF) for a hold time of 1h at maximum temperature.

The identification of all DSC-TG peaks and the analysis of their respective mass losses for the SC and EF samples for a hold time of 1h at maximum temperature are indicated in **Table 5-5** and **Table 5-6**, respectively. Peak 4 has the most significant mass loss percentage for all samples, especially the SC400 and EF400. The comparisons of DSC (mW/mg) and TG (% mass loss) curves of the RcCoP (SC20 and EF20) and DhCoP (SC400 to SC1000, and EF400 to EF100) for hold times of 3h, 5h, and 10h for the SC and EF are provided in **Appendix 2.5** and **Appendix 2.6**, respectively. The peaks and mass loss analysis are provided in **Appendix 2.7** and **Appendix 2.8**, respectively.

Table 5-5: DSC - TG peaks and mass loss analysis for the RcCoP (SC20) and DhCoP obtained by Smart Crushing (SC) for a hold time of 1h at maximum temperature.

Sample type	Identified peaks	Peak temperature (± 3°C)	Mass loss percentage (± 0.3%)
SC20	Peak 1 (C-S-H)	100 °C	2.5%
	Peak 2 ($Ca(OH)_2$)	435 °C	negligible
	Peak 3 (SiO_2)	580 °C	-
	Peak 4 ($CaCO_3$)	725 °C	4.1%
SC400_1h	Peak 1 (non-identified)		
	Peak 2	443 °C	negligible
	Peak 3	578 °C	-
	Peak 4	735 °C	7.9%
SC600_1h	Peak 1 (non-identified)		
	Peak 2 (non-identified)		
	Peak 3	578 °C	-
	Peak 4	730 °C	2.2%
SC800_1h	Peak 1 (non-identified)		
	Peak 2	390 °C	negligible
	Peak 3	578 °C	-
	Peak 4 (negligible)		
SC1000_1h	Peak 1 (non-identified)		
	Peak 2 (non-identified)		
	Peak 3	578 °C	-
	Peak 4 (non-identified)		

Table 5-6: DSC - TG peaks and mass loss analysis for the RcCoP (EF20) and DhCoP obtained by Electrodynamic Fragmentation (EF) for a hold time of 1h at maximum temperature.

Sample type	Identified peaks	Peak temperature (± 3°C)	Mass loss percentage (± 0.3%)
EF20	Peak 1 (C-S-H)	85 °C	1.7%
	Peak 2 ($Ca(OH)_2$)	425 °C	negligible
	Peak 3 (SiO_2)	580 °C	-
	Peak 4 ($CaCO_3$)	720 °C	2.6%
EF400_1h	Peak 1 (non-identified)		
	Peak 2	443 °C	negligible
	Peak 3	578 °C	-
	Peak 4	741 °C	4.2%
EF600_1h	Peak 1 (non-identified)		
	Peak 2 (non-identified)		
	Peak 3	578 °C	-
	Peak 4	735 °C	1.9%
EF800_1h	Peak 1 (non-identified)		
	Peak 2	395 °C	negligible
	Peak 3	578 °C	-
	Peak 4 (negligible)		
EF1000_1h	Peak 1 (non-identified)		
	Peak 2	393 °C	negligible
	Peak 3	578 °C	-
	Peak 4 (non-identified)		

Figure 5-12 and **Figure 5-13** indicate that hold times don't considerably influence the positions of peaks or their intensities for the same thermal treatment temperatures for both SC and EF samples.

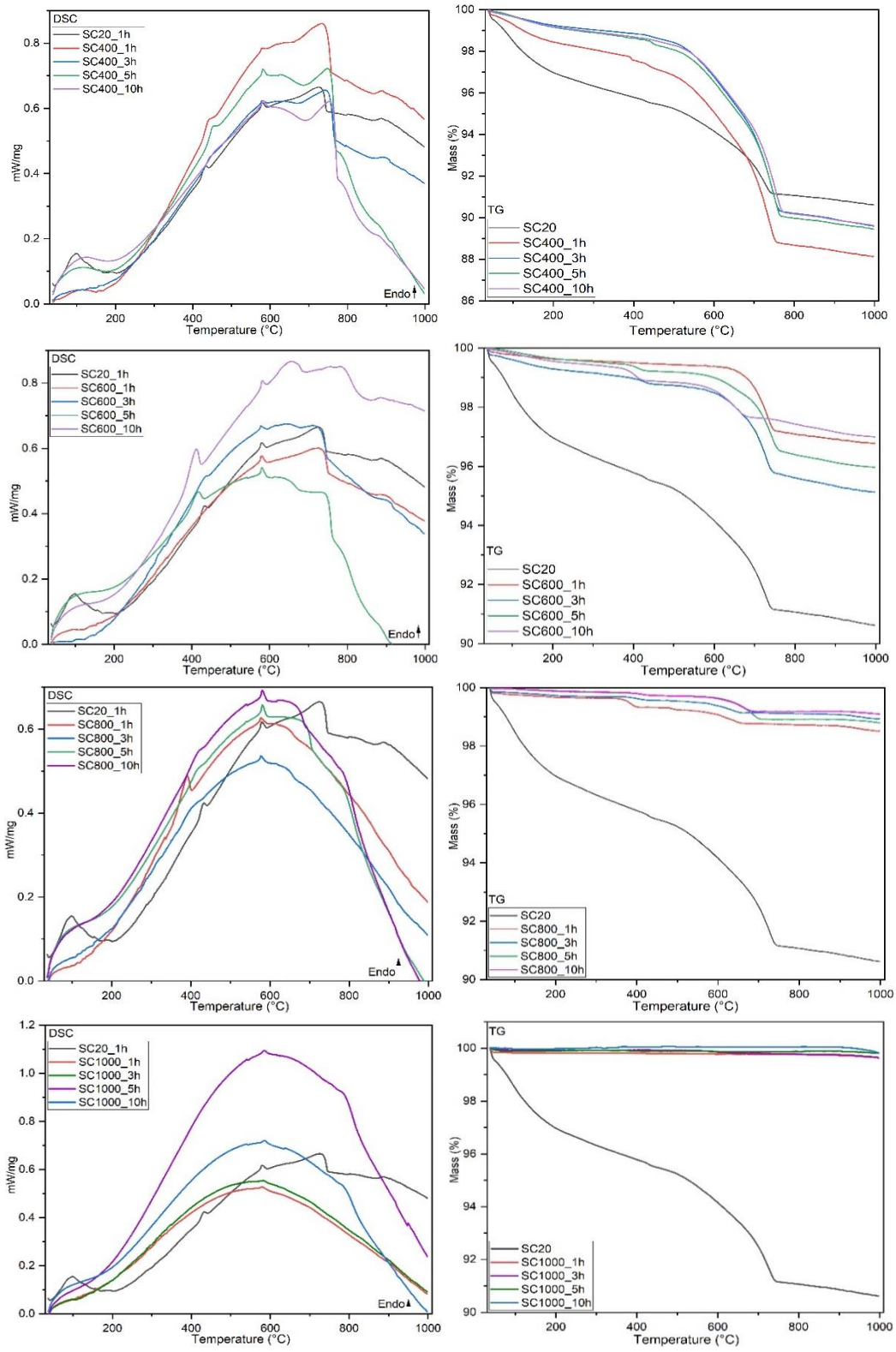

Figure 5-12: Comparison of DSC (mW/mg) and TG (% mass loss) curves of DhCoP (SC400 to SC1000) obtained by Smart Crushing (SC), dehydrated by the same temperature for different hold times (1h, 3h, 5h, and 10h).

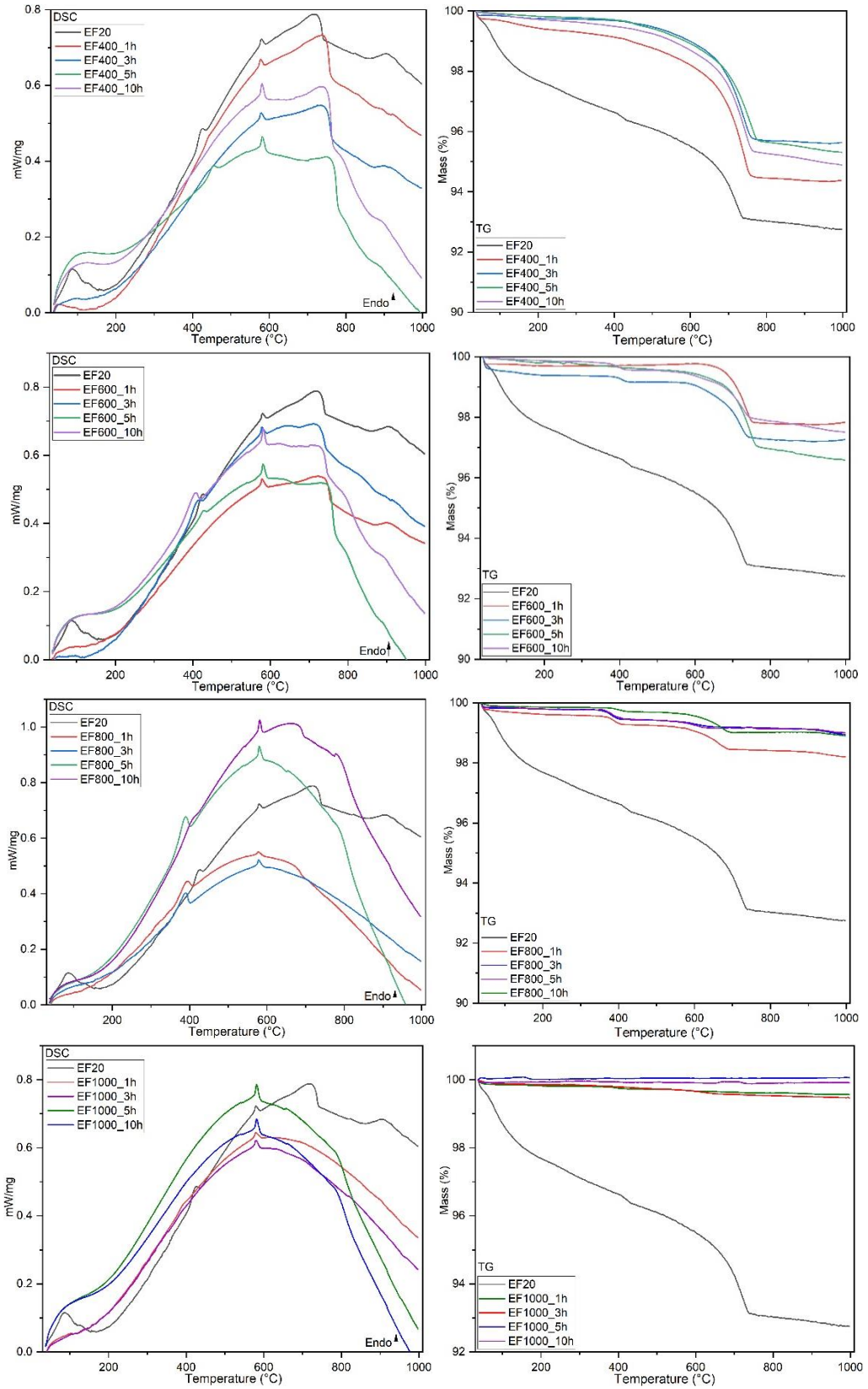

Figure 5-13: Comparison of DSC (mW/mg) and TG (% mass loss) curves of DhCoP (EF400 to EF1000) obtained by Electrodynamic Fragmentation (EF), dehydrated by the same temperature for different hold times (1h, 3h, 5h, and 10h).

5.1.3. SEM and EDX

Figure 5-14 and **Figure 5-15** show the SEM and EDX images of SC and EF specimens before and after thermal treatment. The dominance of the quartz phase (SiO_2) is apparent in every sample, highlighting that the thermal treatment does not significantly influence the presence of this particular phase. For example, the trigonal (SiO_2_α) and hexagonal (SiO_2_β) giant crystals of the SiO_2 phase can be identified in the EF600_1h and SC1000_1h, respectively. The prevalent presence of the SiO_2 phase is confirmed by the high intensities of Si and O_2 on the EDX images in contrast to the other chemical elements.

All examined specimens (SC and EF) present needle-like shapes that vary in thickness. Some samples, such as SC800 and EF800, display more thin needles than others. Typically, these needles are identified as the ettringite phase, as confirmed for the HCeS, RwCeS and RhCeS (see **Section 4.1.4**). However, the thin needles are presumably the calcium silicate phases (C_2S or C_3S) for the SC and EF specimens, while thicker needles are ettringite phases according to the EDX analysis. The presence of calcium silicate phases identified as thin needles, especially the C_2S, in the SC800 and EF800 specimens can be supported by a high weight percentage of this phase (~30 %), as indicated by the XRD spectra after Rietveld refinement (see **Table 5-1** and **Table 5-2**).

The topography and morphology of the SC1000_1h and EF1000_1h are different from the ones of the other specimens resulting from thermal treatment at lower temperatures. Massive crystals of the SiO_2 phase dominate the SC1000_1h and EF1000_1h, and the existence of distinct shapes specify the occurrence of new phases. Accordingly, the XRD results (see **Table 5-1** and **Table 5-2**) show that a high content of the akermanite phase ($Ca_2MgSi_2O_7$) occurs in these samples.

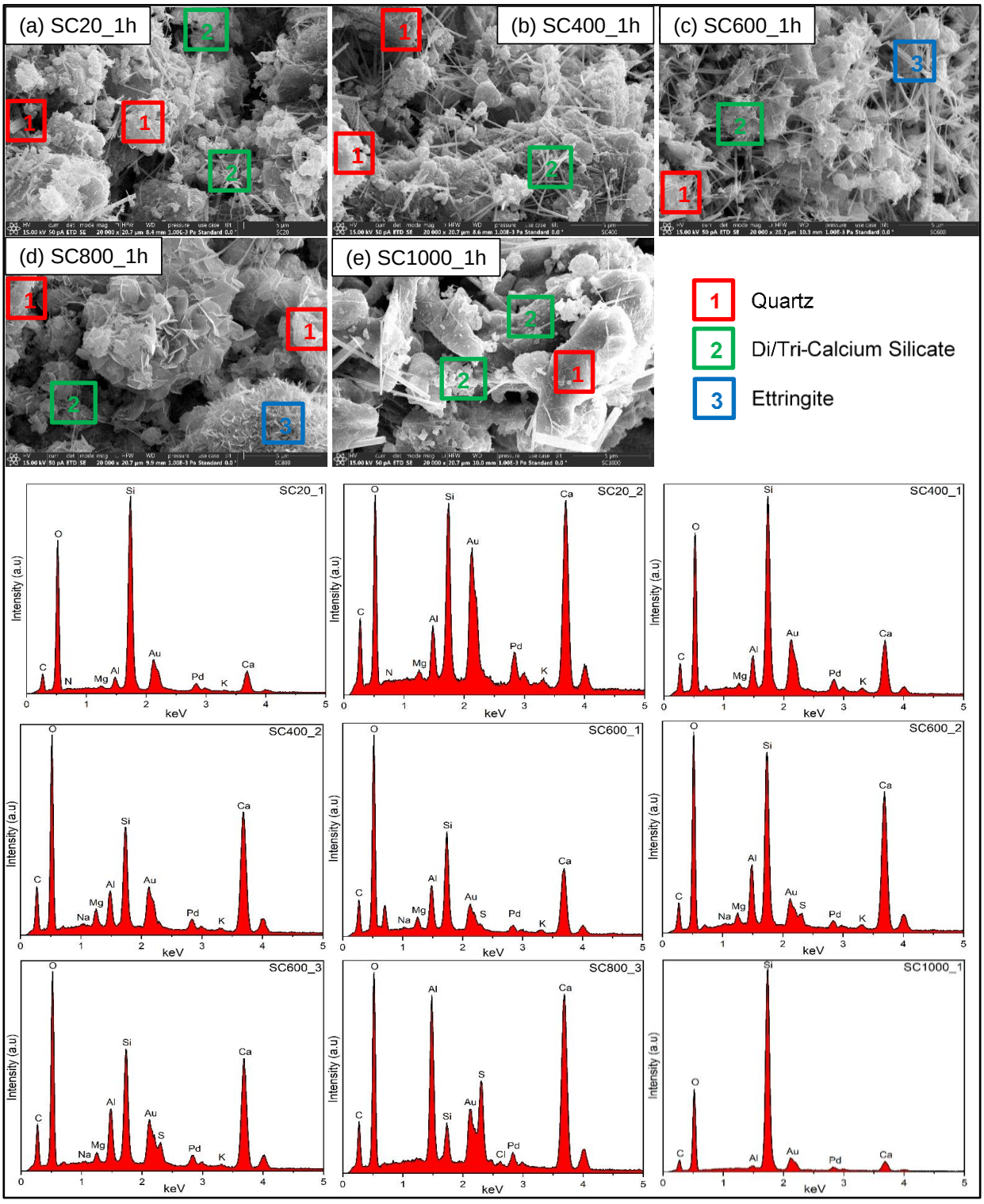

Figure 5-14: SEM and EDX images of Rehydrated Concrete Specimen (RhCoS) produced from the Recycled Concrete Powder (RcCoP) obtained by Smart Crushing (SC): (a) without thermal treatment, (b-e) after thermal treatment at different temperatures for a hold time of 1h at maximum temperature. The EDX images indicate the intensity of chemical elements contained per point analyzed.

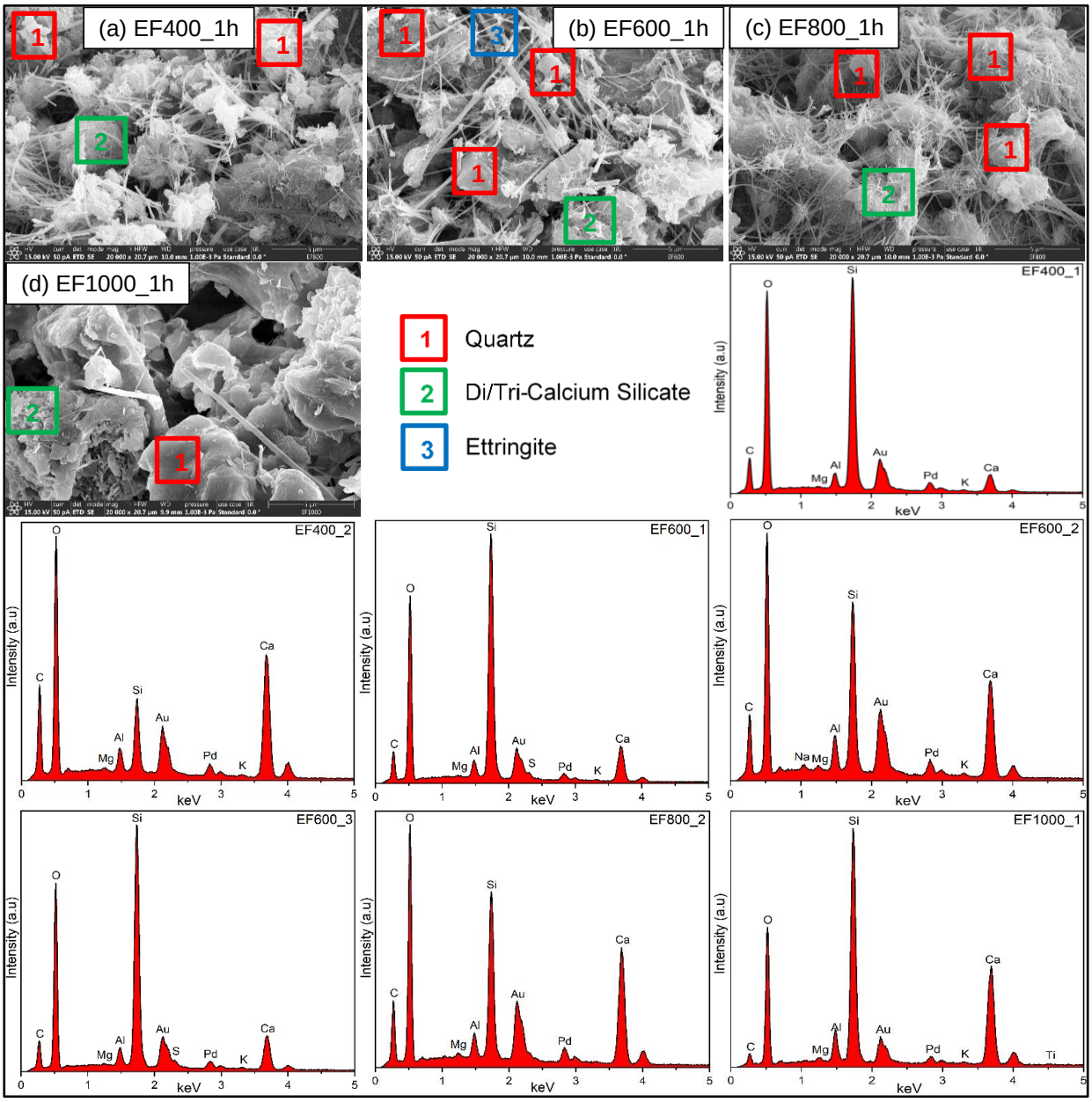

Figure 5-15: SEM and EDX images of Rehydrated Concrete Specimen (RhCoS) produced from the Recycled Concrete Powder (RcCoP) obtained by Electrodynamic Fragmentation (EF) after thermal treatment at different temperatures for a hold time of 1h at maximum temperature. The EDX images indicate the intensity of chemical elements contained per point analyzed.

5.2. Discussion of the results

This section discusses the results of DhCoP and RhCoP at various temperatures for a hold time of 1h at maximum temperature towards the potential for strength development. The comparison is made between the samples obtained by SC and EF methods. The effect of several hold times (1h, 3h, 5h, and 10h) on phase formation can be found in **Section 5.1.1** and is illustrated by **Figure 5-4** and **Figure 5-5** for SC and EF, respectively.

The most noticeable observation is that the XRD results after thermal treatment of RcCoP (**Figure 5-1**) do not show significant differences in the patterns resulting from different treatment temperatures after the SC and EF separation techniques. These XRD patterns are similar to the XRD patterns of the non-thermally treated RcCoP (SC20 and EF20). The phase contents also show these similarities (**Table 5-1** and **Table 5-2**). The quartz and coesite (SiO_2) peaks dominate the phase contents for all the sample types, accounting for more than 55% of the weight. Compared to the thermally treated HCeP, the high percentage of SiO_2 content indicates that the hydration ability is much less recoverable. The sand fines are not successfully separated with calcium silicate phases during the separation process. Similarly, little mechanical strength is achievable, because SiO_2 is not a typical strength development phase. The thermal treatment of RcCoP does not decompose the SiO_2, but only the conversion of SiO_2_α to SiO_2_β occurs **[8, 18]**.

Evaluating the expected strength development after thermal treatment of RcCoP by the content of calcium silicate phases (C_3S, C_2S_β, and C_2S_α) reveals that the treatment at 600 °C and 800 °C is of the highest interest, as these phases are less present in the samples treated below 600 °C. On the other hand, the material treated at 1000 °C develops a considerable content of akermanite ($Ca_2MgSi_2O_7$), suggesting a possible alteration of already dehydrated hydration phases, thus affecting the attainable strength. Generally, 800 °C leads to noticeably higher content of C_2S_β and C_2S_α phases than 600 °C, but the amount of the C_3S phase tends to be slightly higher for 600 °C than for 800 °C. However, the content of C_3S is low (< 3%), so it is not expected to act as the main phase controlling the overall strength development, as it is for the VCe. Considering other factors influencing the achievable strength, such as the curing conditions, the setting time and the porosity, the potential optimum heating temperature is not evident at this stage, and the strength results are necessary for further evaluation.

The XRF results of thermally treated RcCoP for a hold time of 1h at maximum temperature (**Table 5-3** and **Table 5-4**) indicate the presence of the principal oxides forming the calcium silicate phases that control the strength development. However, the content of SiO_2 is higher than that of CaO for all sample types (SC and EF). These oxides (SiO_2 and CaO) are bound in the calcium silicate phases. Typically, the content of CaO is higher than SiO_2 in the VCe **[49, 41]**, which is the case for all thermally treated HCeP. The samples gained from the concrete have some residual sand content despite the previous separation efforts. Thus, having a higher content of bound SiO_2 indicates a reduced potential for strength recovery after thermal treatment of RcCoP. Nevertheless, the heating of RcCoP increases the amount of bound CaO and reduces that of SiO_2, emphasizing the benefit of the thermal treatment process on RcCoP towards strength development. Alternatively, the comparison of different hold times (**Figure 5-6** and **Figure 5-7**) reveals that the hold time for 3h, 5h, and 10h again tends to reduce the CaO content and increase the SiO_2 content, suggesting possible instabilities with higher hold times compared to 1 hour, and likely a lower strength development capability.

An investigation of the characteristic chemical transformations during the thermal treatment of RcCoP is again needed to gather information on the material behavior towards the reactivation potential for strength development. The DSC-TG results are used to assess these transformations. **Figure 5-8** and **Figure 5-9** show that the three prominent peaks found during the thermal treatment of HCeP are also present for the RcCoP (SC and EF). However, these peaks do not occur at the same temperatures, and the corresponding mass losses differ.

In the SC20 and EF20 samples, the first peak occurs due to dehydration of the C–S–H gels and decomposition of ettringite at 100 °C and 85 °C, respectively, which is earlier than in HCeP, where it occurs at 120 °C. The corresponding mass losses for SC20 (2.5%) and EF20 (1.7%) are significantly lower than for HCeP (10.5%). This remarkable difference is due to the absence or minor content of ettringite and C-S-H in SC20 and EF20, as shown by the RXD results in **Table 5-1** and **Table 5-2**, making the first peak less intense. Therefore, the potential for strength development is also affected because both phases are essential, especially the C-S-H. Additionally, the intensities and corresponding mass losses of peak 2 (due to the dehydroxylation of portlandite) for the SC20 and EF20 are negligible compared to the HCeP for the same reasons. However, peak 3 (due to the decarbonation of calcite) is more intense, and the corresponding mass losses are higher for the SC20 and EF20 than the HCeP, signifying that carbonation happened during the service life of the original concrete from which the RcCoP is obtained. Peak 3 for HCeP corresponds to peak 4 for the SC20 and EF20 samples as there is a new peak 3 due to the conversion of SiO_2_α to SiO_2_β, occurring at around 580 °C **[8, 18, 227–231]**. This peak is not associated with mass loss as no decomposition happens.

Figure 5-10 and **Figure 5-11** indicate the loss of bound water and decomposition of ettringite below 200 °C because no thermally treated RcCoP contains peak 1. The XRD results (**Table 5-1** and **Table 5-2**) confirm this behavior. Peak 2 is generally negligible for all treated samples, while the peak 4 intensity increases from SC20 and EF20 to SC400_1h and EF400_1h, respectively, and disappears above 600 °C. Therefore, more CO_2 is liberated during the thermal treatment of RcCoP compared to HCeP. On the other hand, peak 3 is present regardless of the treatment temperature, without any perceptible shift in position and with consistent intensity. Thus, as expected, SiO_2 is a thermally stable phase not decomposed by thermal treatment **[232–239]**. Moreover, it is expected to affect strength development negatively, because it is not a typical strength-forming phase and is dominant according to the XRD results. Noticeably, all the peaks are located on an enormous primary curve that is not part of the general understanding of the present peaks. This curve is caused by the heat properties of the sample materials, essentially the heat capacity, which is also influenced by the thermal treatment temperatures. It is, therefore, not considered for chemical transformation analysis. However, it may also be associated with the presence of amorphous phases, such as the C-S-H.

The dominance of the SiO_2 phase is also manifested in the microstructure assessment resulting from the thermal treatment of RcCoP for both the SC and EF samples. The EDX results confirm that giant crystals of SiO_2 are present in the SC1000_1h and EF600_1h. All the other SC and EF samples also contain these crystals of different sizes. Therefore, very little strength development can be expected for all RcCoP samples, as the crystals of a non-strength forming phase mainly control it. Besides, for thermally treated RcCoP samples, the strength-forming phases (C_2S and C_3S) are identified as dispersed slim needle-like features, compared to the thicker ones representing ettringite. Nevertheless, a clear distinction between the two cannot be easily made. The strength-forming phases are identified as broken-like substances

in thermally treated HCeP, offering them a higher surface area and increased potential for reaction with water, thus, bearing a higher ability for strength development.

6. Porosity and strength development

This chapter analyzes the porosity and strength of the Rehydrated Cement Specimens (RhCeS) and the Rehydrated Concrete Specimens (RhCoS). It is divided into four main parts, the first displaying the strength results (**Section 6.1**), the second the porosity results (**Section 6.2**), the third combining strength and porosity results (**Section 6.3**), and the fourth discussing the results (**Section 6.4**). These sections are also divided into sub-sections.

Section 6.1.1 illustrates the compressive and flexural strengths of the Hydrated Cement Specimens (HCeS), the Rewetted Cement Specimens (RwCeS) and the Rehydrated Cement specimens (RhCeS) obtained from the mixture of Virgin Cement (VCe), Hydrated Cement Powder (HCeP), and Dehydrated Cement Powder (DhCeP) with water, respectively. **Section 6.1.2** illustrates the compressive strengths of the Recycled Concrete Specimens (RcCoS) and the Rehydrated Concrete Specimens (RhCoS) obtained from a mixture of the Recycled Concrete Powder (RcCoP) and Dehydrated Concrete Powder (DhCoP) with water, respectively. The powders obtained by SC and EF are compared.

Sections 6.2.1 and **6.2.2** illustrate the porosity resulting from thermal treatment on the RhCeS and RhCoS by Mercury Intrusion Porosimetry (MIP), respectively, while **Section 6.3** has no sub-sections. **Sections 6.4.1** and **6.4.2** discuss the strength and porosity results, respectively.

6.1. Strength results

6.1.1. Strength of RhCeS

Figure 6-1 (a) to **(c)** show the process used to produce and test the strength of RhCeS_1h, and **Figure 6-1 (d)** shows the two pieces obtained after flexural strength testing of the RhCeS_1h from **Figure 6-1 (c)**. Both these pieces were used to test the compressive strength of the samples obtained after each thermal treatment temperature (RhCeS200_1h to RhCeS1000_1h). **Figure 6-1 (b)** indicates that the coloration of the powders changes depending on the thermal treatment temperature. While the VC is greyish-brown, the hydration causes a color change to chalky-white in the HCeP. The color becomes dark with an increase in the thermal treatment temperature. It stays chalky-white up to HCeP400, and the color of VCe lies between DhCeP600 and DhCeP800, which can already suggest the best heating temperatures.

Figure 6-2 indicates that the compressive and flexural strengths of the HCeS, which is produced from the VCe, are the highest compared to the other specimens, while the RwCeS, obtained without thermal treatment of the HCeP, offers the lowest strengths. The RhCeS600_1h produces the second-highest strength and is considerably higher than all the RhCeS. The RhCeS1000_1h has minor compressive strength after 7 days but increases better than the RhCeS200_1h after 28 days. Correspondingly, the compressive strength for all samples increases from 7 to 28 days. On the other hand, the flexural strength of RhCeS600_1h decreases significantly from 7 to 28 days. The flexural strength only rises from 7 to 28 days for the RhCeS1000_1h samples.

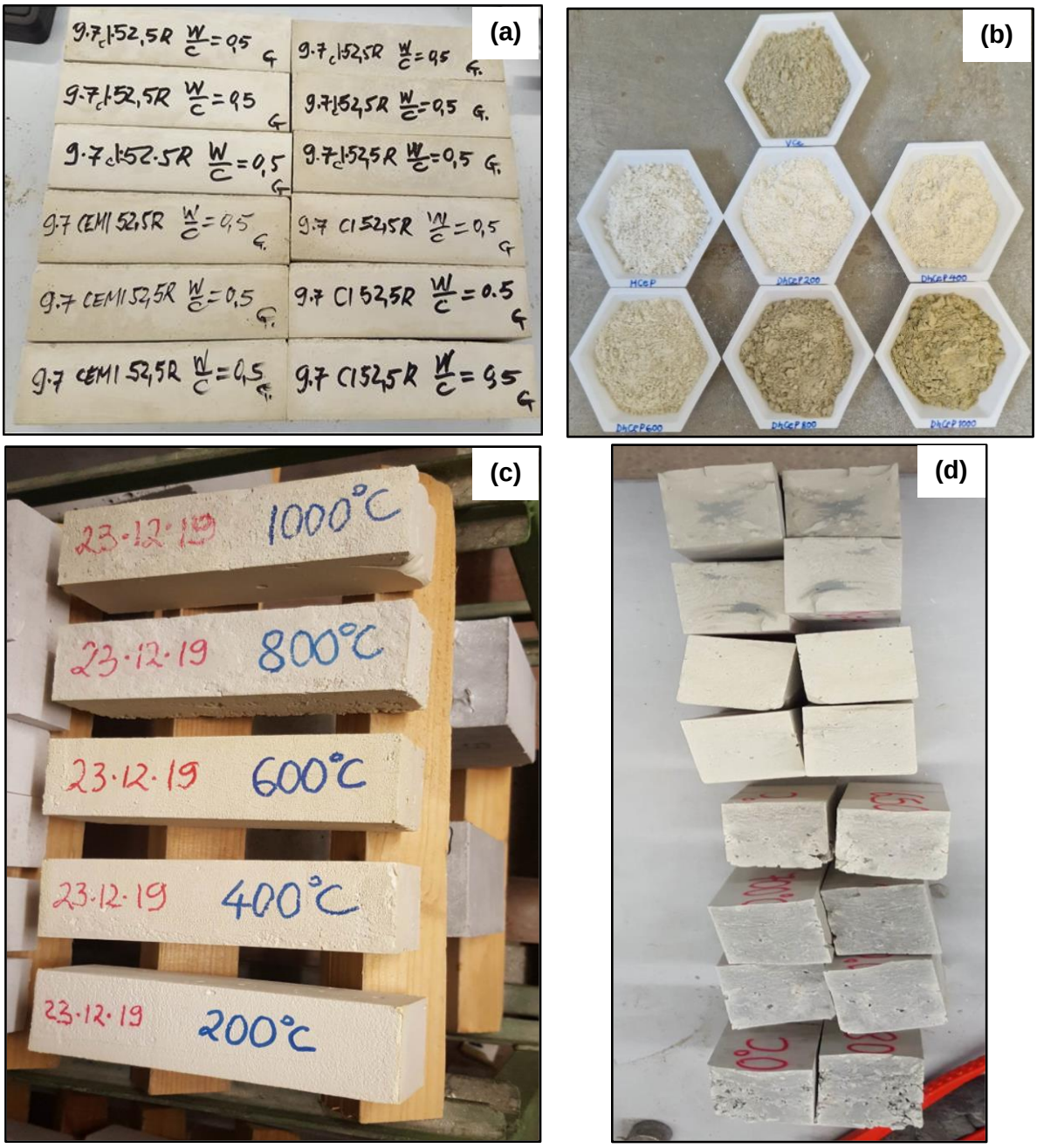

Figure 6-1: Representation of the strength testing of the Rehydrated Cement specimens (RhCeS): (a) Hydrated Cement Specimens (HCeS), (b) Hydrated Cement Powder (HCeP and Dehydrated Cement Powders (DhCeP) obtained after heating the HCeP at different temperatures, (c) RhCeS and (d) Pieces of RhCeS after flexural strength testing.

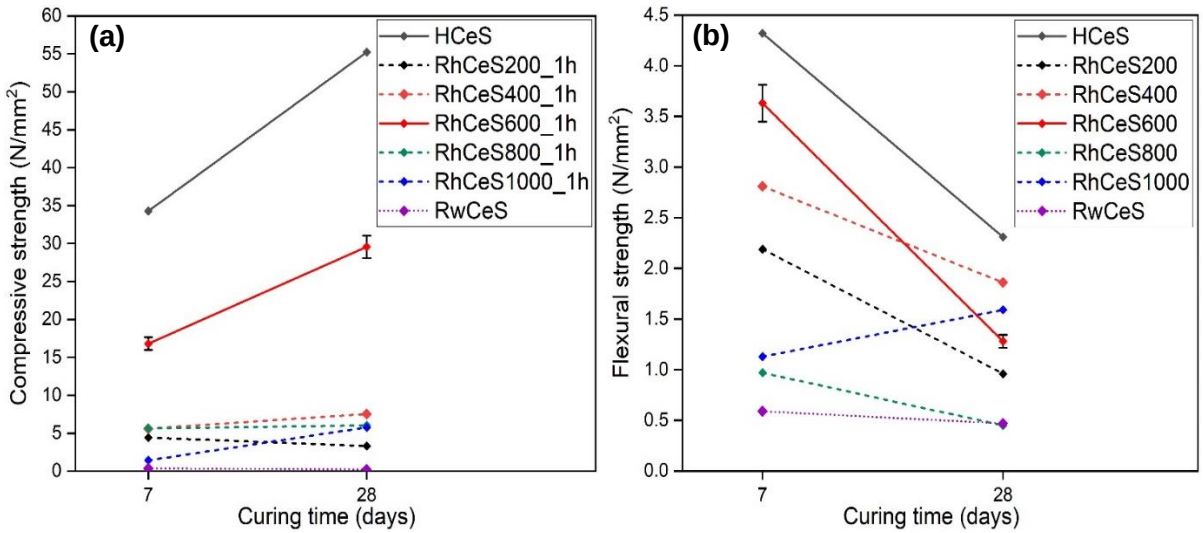

Figure 6-2: (a) Compressive and (b) flexural strengths of the standard size Hydrated (H), Rewetted (Rw) and Rehydrated Cement Specimens (RhCeS) thermally treated at different temperatures for a hold time of 1h at maximum temperature. The error bars are representative of all samples.

Figure 6-3 shows the compressive and flexural strengths of the Standard Mortar (SM), the HCeM and the RhCeM. The SM was obtained using 100% VCe, while the HCeM and RhCeM were obtained after different replacement percentages of VCe by HCeP or DhCeP (from 10% to 100%), respectively. Additionally, in the case of 100% replacement of VCe by the DhCeP600_1h in the RhCeM600_1h, a superplasticizer was used to retard the setting time by regulating the hydration process to evaluate the improvement in the strength achieved compared to the absence of a superplasticizer.

The compressive and flexural strengths of these mortars were tested after 2, 7, and 28 days. Generally, the compressive strength increases with the curing time (from 2 to 28 days) for the same thermal treatment temperature. It decreases with an increase in the proportion of VCe replacement for all curing times. The RhCeM600_1h shows the best compressive strength of all RhCeM and HCeM for the same curing time and percentage of VCe replacement. It achieves comparable compressive strength as the SM when 20% VCe replacement by DhCeP600_1h is made in the RhCeM. The replacement of VCe by 100% DhCeP600_1h indicates that lower compressive strength is achieved. Nevertheless, using a superplasticizer allows us to achieve relatively good results.

The flexural strength results don't follow the same trend as the compressive results. Although they tend to decrease with an increase in the proportion of VCe replacement, they don't necessarily increase with the curing time (from 2 to 28 days). Also, the RhCeM600_1h does not mostly show the best flexural strength of all RhCeM for the same curing time and percentage of VCe replacement as expected. Thus, the thermal treatment temperature slightly influences the strength development, and no specific trend exists.

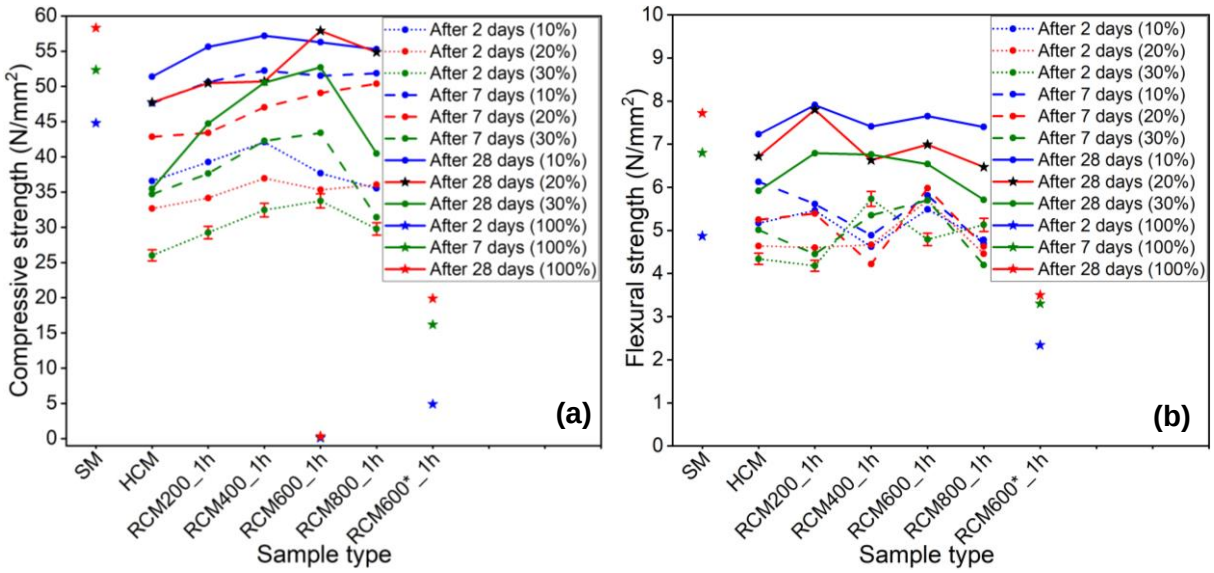

Figure 6-3: Comparison of (a) compressive and (b) flexural strengths of Standard Mortar (SM), Hydrated Cement Mortar (HCeM) and Rehydrated cement mortar (RhCeM), with different replacement percentages of VCe by HCeP or DhCeP. The hold time was conducted for 1 hour. The error bars are the same for all points. RhCeM600*_1h means that the specimens were prepared using a superplasticizer (2%).

Figure 6-4 compares the compressive strengths of small-size (20×20×20 mm^3) RhCeS thermally treated at different temperatures and hold times of 1h, 3h, 5h, and 10h. The hold time slightly influences the achievable compressive strength, but there is no consistency for all thermal treatment temperatures. For the RhCeS400 and RhCeS600, the compressive strength increases marginally with an increase in hold time, but the RhCeS600_3h has a lower compressive strength than RhCeS600_1h. For the RhCeS800 and RhCeS1000, the compressive strength doesn't increase with the hold time at all. It remains the same or slightly decreases. Nevertheless, the compressive strengths for the same thermal treatment temperatures are similar regardless of the hold time.

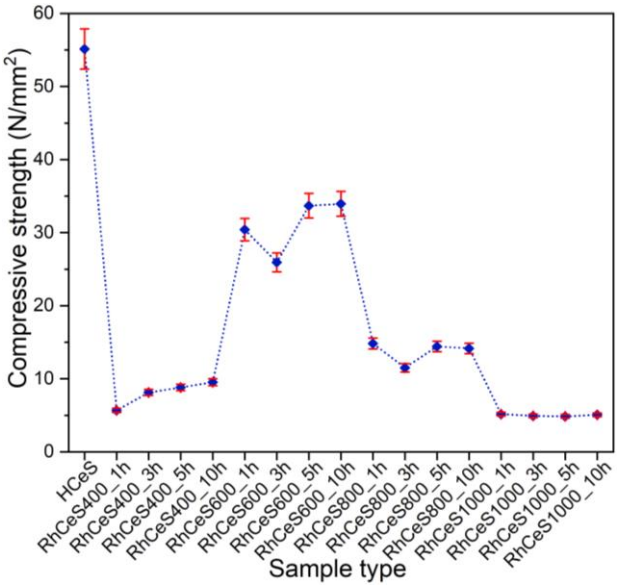

Figure 6-4: Comparison of the compressive strengths of small-size (20×20×20 mm^3) Rehydrated Cement Specimens (RhCeS) thermally treated at different temperatures for hold times of 1, 3, 5, and 10 hours.

6.1.2. Strength of RcCoS

Figure 6-5 (a) shows the DhCoP obtained after thermal treatment of the RcCoP, while **Figure 6-5 (b)** shows the small specimens obtained after mixing the DhCoP with water. **Figure 6-5 (a)** and **(b)** indicate that the thermal treatment of RcCoP results in reddish brown color, emphasizing the domination of quartz (SiO_2) (Refer to Chapter 5).

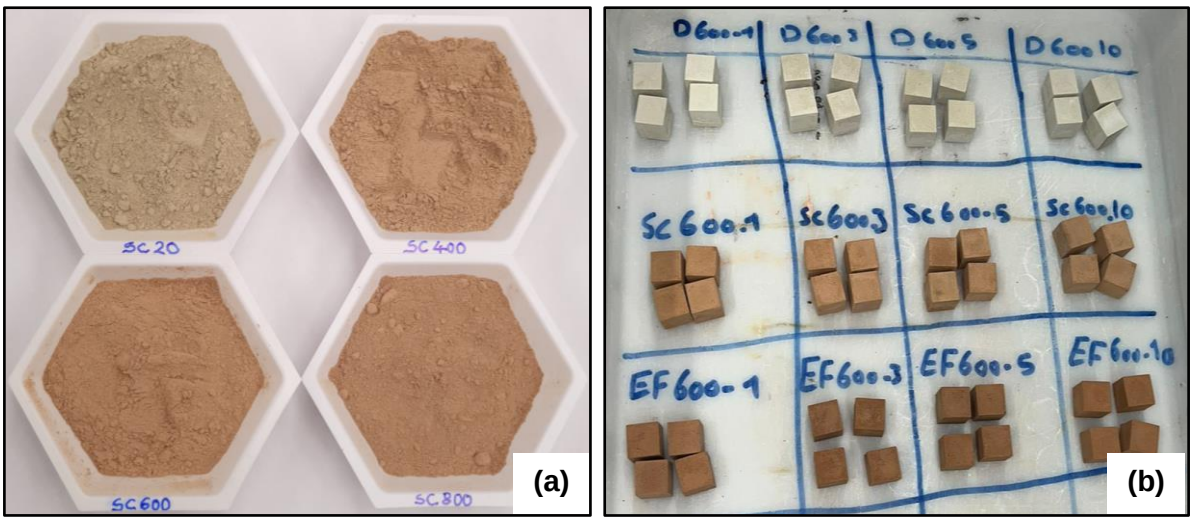

Figure 6-5: (a) Dehydrated Concrete Powder (DhCoP) after thermal treatment of the Recycled concrete Powder (RcCoP) at different temperatures and (b) the resulting small-size Rehydrated Concrete Specimens (RhCoS).

Figure 6-6 (a) and **(b)** compare the compressive strengths of SC20 and EF20 samples with the SC and EF specimens after thermal treatment at different temperatures and hold times, respectively. The compressive strengths of SC600 and EF600 are the highest. SC800 and EF800 are the second highest, while SC1000 and EF1000 are the smallest.

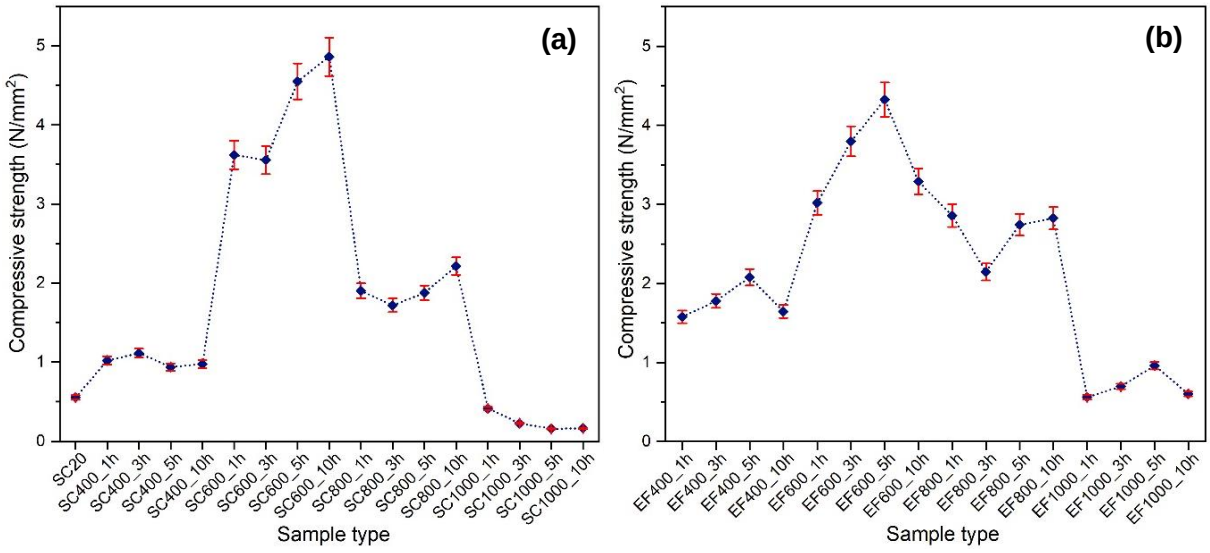

Figure 6-6: Comparison of the compressive strengths of the small-size Rehydrated Concrete Specimens (RhCoS) produced from the Recycled Concrete Powder (RcCoP) preheated at different temperatures for several hold times (1, 3, 5, and 10h). (a) Obtained by Smart Crushing (SC) and (b) obtained by Electrodynamic Fragmentation (EF).

Although the hold time tends to influence the achievable compressive strength, no consistent results were achieved. The compressive strength increases with the hold times for specimens such as SC600 and SC800, decreases for SC1000, and remains almost unchanged for SC400. It increases with the hold time of up to 5 hours but decreases with 10 hours in EF400, EF600, and EF1000. It remains unchanged for the EF800, except for the hold time of 3 hours, where it reduces. The comparison of SC and EF specimens with the VCe in **Figure 6-7** indicates that the compressive strength of SC and EF specimens is much lower than that of VCe for all hold times. Here, only the SC results are compared to the VCe for illustration because **Figure 6-6** specifies that the SC and EF results are similar.

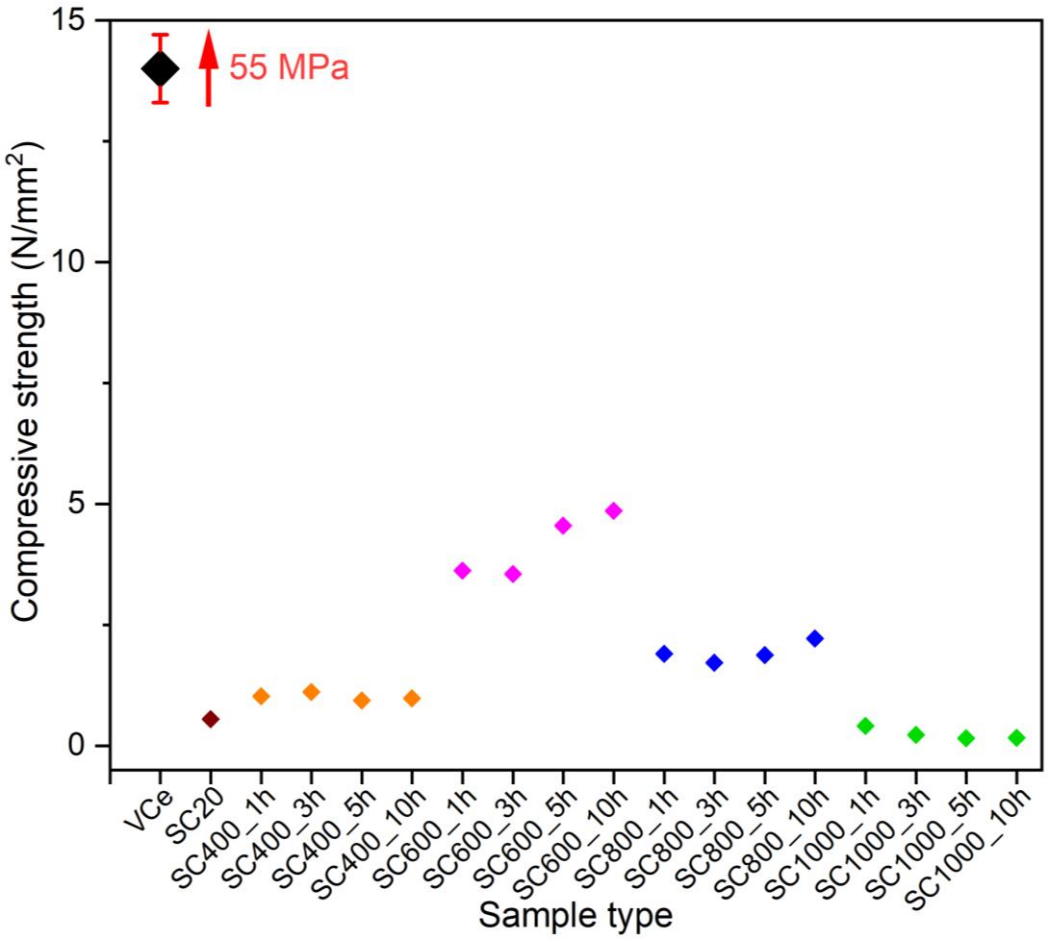

Figure 6-7: Comparison of the compressive strengths of the Virgin Cement (VCe) and the Rehydrated Concrete Specimens (RhCoS) produced from the Recycled Concrete Powder (RcCoP) obtained by Smart Crushing (SC) after thermal treatment at different temperatures for several hold times.

6.2. Porosity results

6.2.1. Porosity of RhCeS

Figure 6-8 compares porosity results of standard size HCeS and RhCeS after thermal treatment at different temperatures for a hold time of 1h at maximum temperature. The HCeS serves as a reference, and its porosity is the lowest after 7 and 28 days compared to the RhCeS. Generally, there is an increase of porosity after 7 to 28 days, but the porosity of HCeS does not increase considerably as for the RhCeS. Furthermore, the porosity of RhCeS600_1h is the lowest of all RhCeS both after 7 and 28 days. **Figure 6-8 (b)** also indicates that the cumulative pore size distribution of the HCeS after 28 days is the least for all samples, while the RhCeS600_1h is the lowest of all RhCeS. Additionally, the RhCeS600_1h has the lowest value of pore diameter.

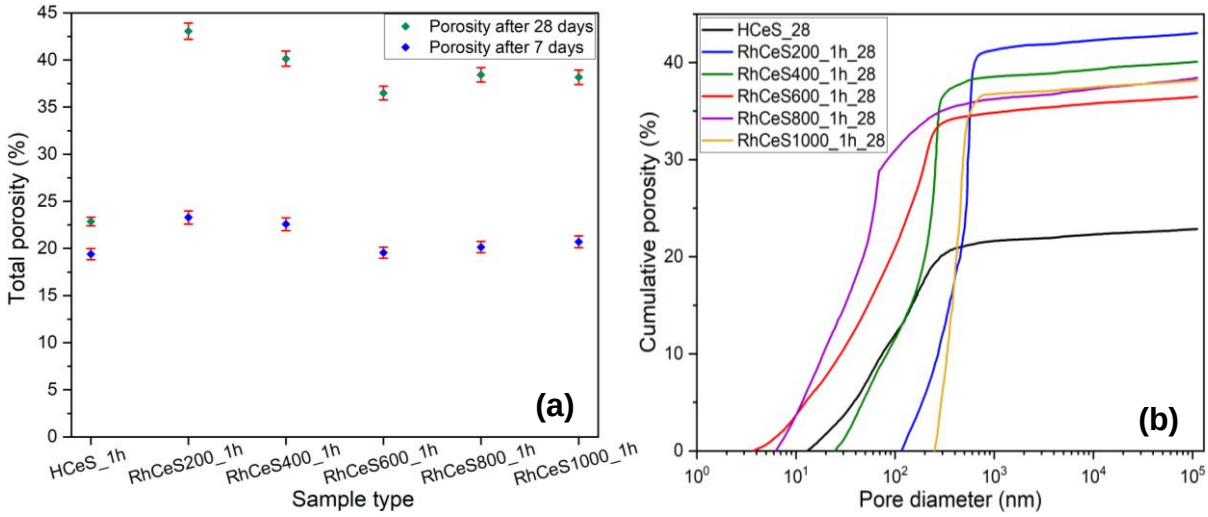

Figure 6-8: Comparison of porosity of the standard size specimens (40×40×160 mm^3) of the HCeS and RhCeS manufactured from the HCeP thermally treated at different temperatures for a hold time of 1h at maximum temperature (a) and the cumulative pore size distribution after 28 days (b).

Figure 6-9 shows the porosity results for the small specimens (20×20×20 mm^3) of HCeS and RhCeS after 28 days of curing. Generally, the porosity increases compared to the standard-size specimens made from the same material. As for the standard-size specimens, the porosity and the cumulative pore size distribution of the HCeS are smaller than the RhCeS. The porosity of RhCeS600_1h is similar to that of RhCeS1000_1h, and both are the lowest among the RhCeS samples. However, RhCeS1000_1h comprises bigger pores, as **Figure 6-9 (b)** indicates. In addition, **Figure 6-10** shows that the HCeS has the lowest median pore diameter, while the RhCeS1000_1h has the largest for both the small and standard-size specimens. The RhCeS600_1h has the smallest median pore diameter among the RhCeS samples.

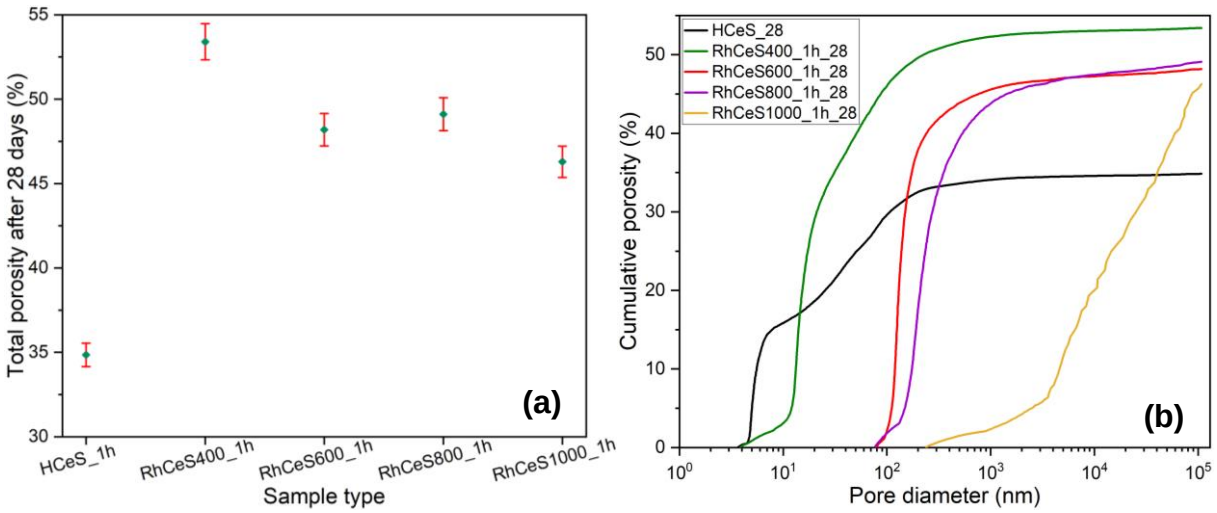

Figure 6-9: Porosity of the small size specimens (20×20×20 mm^3) of the HCeS and RhCeS manufactured from the HCeP thermally treated at different temperatures for a hold time of 1h at maximum temperature (a), and the cumulative pore size distribution after 28 days (b).

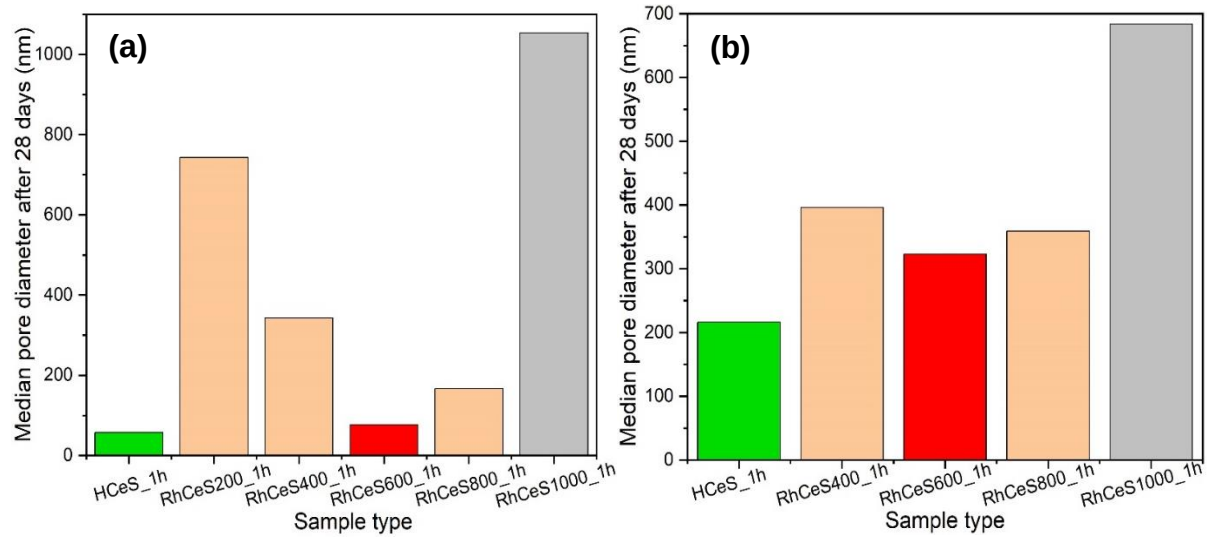

Figure 6-10: Comparison of the median pore diameters of the HCeS and RhCeS manufactured from the HCeP thermally treated at different temperatures for a hold time of 1h at maximum temperature. (a) Standard-size specimens and (b) small-size specimens.

The results of total porosities, cumulative pore size distributions, and median pore diameters do not display the pore volumes associated with each pore diameter. Thus, the differential pore volume distribution curves are required. The peaks of these curves indicate the most frequent diameters, which are, therefore, dominant. They are the critical pore diameters.

Figure 6-11 (a) and **(b)** compare differential pore size distribution curves of the HCeS and RhCeS for standard-size and small-size specimens, respectively. There are more similarities than dissimilarities in the curves of both specimen sizes. The most crucial similarity is that the critical pore diameters range from 10^2 nm to 10^3 nm for all specimens and both specimen sizes. However, the standard-size RhCeS800_1h_28 shows its critical pore diameter at around 10 nm with a round peak. Another similarity is that the HCeS_28 displays the lowest peak for both specimen sizes. Moreover, the HCeS_28 shows two peaks specifying a bimodal distribution, while all other samples tend to or are entirely unimodal. Furthermore, the RhCeS600_1h_28 and RhCeS800_1h_28 display the lowest peaks for both specimen sizes among all thermally

treated samples. Dissimilarities between specimen sizes also exist. The RhCeS1000_1h_28 shows the most intense peak for small-size specimens but not for standard-size specimens. The standard-size RhCeS200_1h_28 peak is significantly intense compared to the other samples.

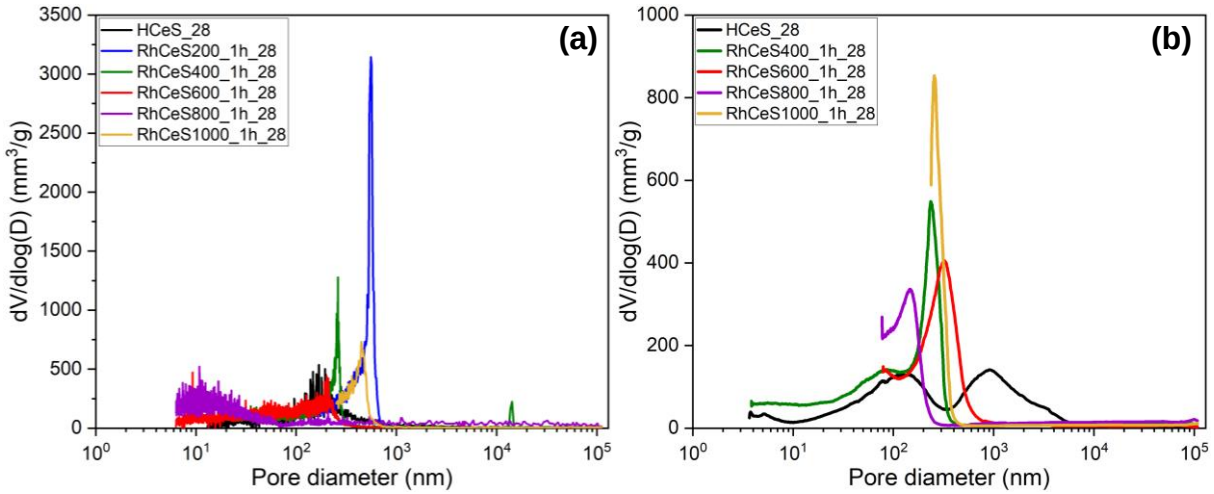

Figure 6-11: Comparison of differential pore size distribution curves of the HCeS and RhCeS manufactured from the HCeP thermally treated at different temperatures for a hold time of 1h at maximum temperature. (a) Standard-size specimens (40×40×160 mm^3) and (b) small-size specimens (20×20×20 mm^3). The raw data are preserved for (a) because averaging for smoothing would completely change the meaning of the plots.

6.2.2. Porosity of RcCoS

Figure 6-12 shows the porosity results of RcCoS and RhCoS for both the SC and EF samples after 28 days of curing. Generally, the porosity of EF samples is smaller than that of the SC samples for the same thermal treatment temperatures. The porosities of specimens resulting from thermal treatment at 600 °C and 800 °C are similar for both SC and EF samples, respectively. While SC400_1h has the lowest porosity of all SC samples, EF600_1h has the lowest for all EF samples. On the other hand, the porosities of SC1000_1h and EF1000_1h are much higher than those measured for the other SC and EF samples. This result is emphasized by **Figure 6-12 (b)**, indicating that SC1000_1h and EF1000_1h contain bigger pores than the other samples. Also, **Figure 6-13** shows that the SC1000_1h and EF1000_1h have the highest median pore diameters, while the SC600_1h and EF600_1h have the smallest compared to the other SC and EF samples.

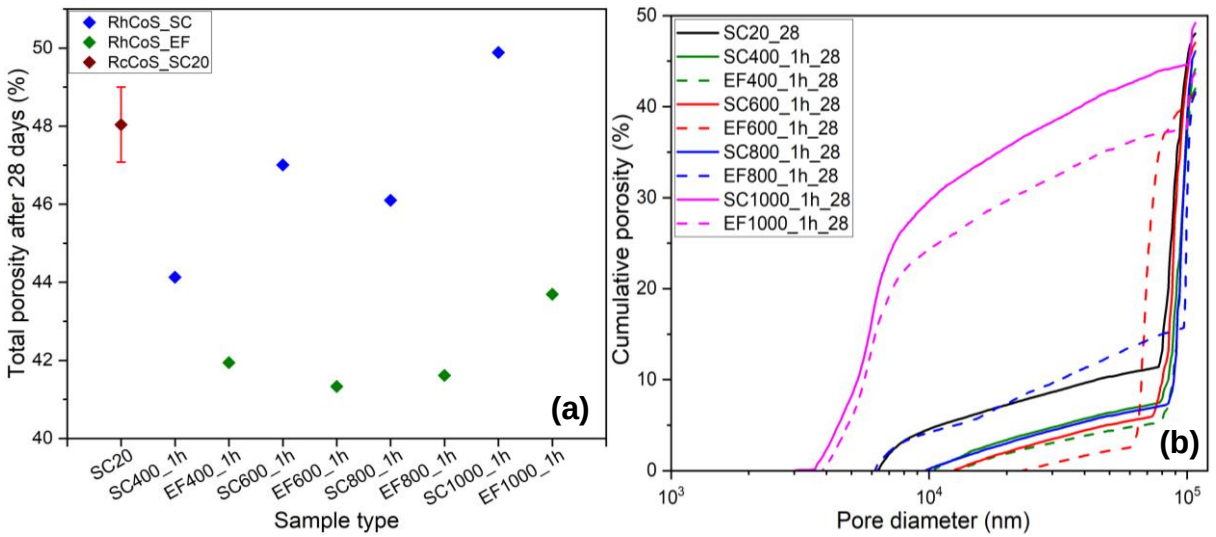

Figure 6-12: Comparison of porosity of small specimens of the RcCoS and RhCoS manufactured from the RcCoP obtained by both the Smart Crushing and Electrodynamic Fragmentation (EF) thermally treated at different temperatures for a hold time of 1h at maximum temperature (a) and the cumulative pore size distribution after 28 days (b). The error bar is representative of all samples.

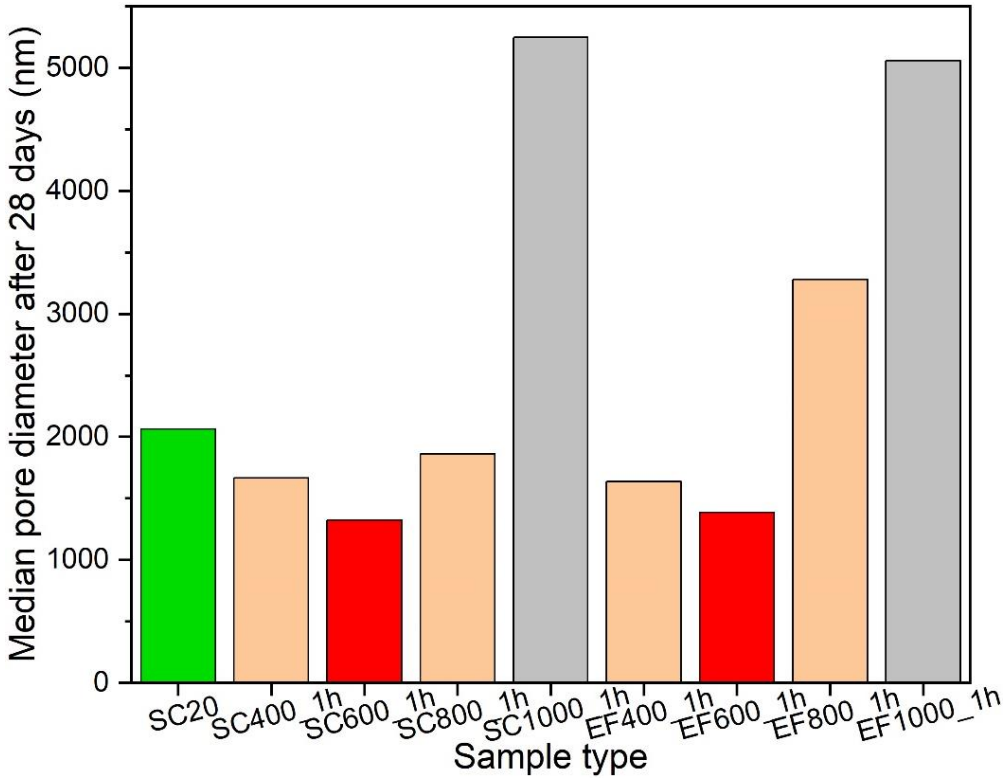

Figure 6-13: Comparison of the median pore diameters of small specimens of the RcCoS and RhCoS manufactured from the RcCoP obtained by both Smart Crushing (SC) and Electrodynamic Fragmentation (EF) thermally treated at different temperatures for a hold time of 1h at maximum temperature.

As for the RhCeS, the differential pore volume distribution curves are plotted to investigate the pore volumes connected to all pore diameters. **Figure 6-14 (a)** and **(b)** compare differential pore size distribution curves of small-size (20×20×20 mm^3) specimens of the RcCoS and RhCoS produced from the RcCoP obtained by SC and EF, respectively. The results from both separation methods are similar. The critical pore diameters are located between $4×10^3$ nm and $2×10^4$ nm. The SC1000_1h_28 and EF1000_1h_28 peaks are significantly intense compared to the other samples, while the SC600_1h_28 and EF600_1h_28 peaks are the lowest. Additionally, SC1000_1h_28 and EF1000_1h_28 curves show more biggest pores (> $2×10^4$ nm).

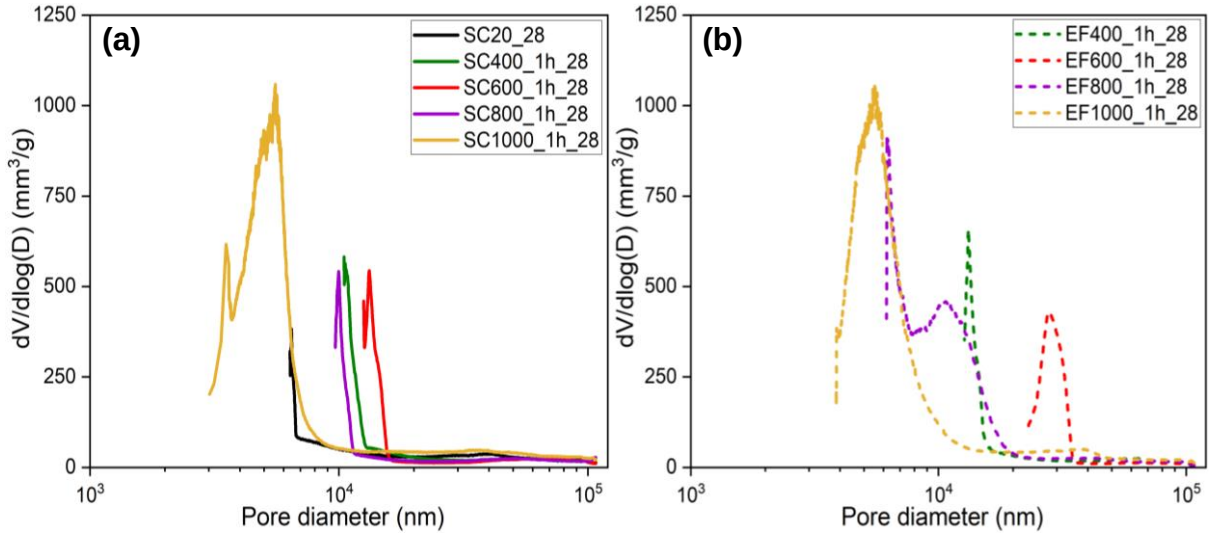

Figure 6-14: Comparison of differential pore size distribution curves of small-size specimens of the RcCoS and RhCoS manufactured from the RcCoP thermally treated at different temperatures for a hold time of 1h at maximum temperature. (a) RcCoP obtained by Smart Crushing (SC) and (b) RcCoP obtained by Electrodynamic Fragmentation (EF).

6.3. Correlation between compressive strength, porosity, and median pore diameter

This section combines the compressive strength results, porosity results and median pore diameters to highlight the relationship between them. **Figure 6-15** indicates that the relationship is similar for the RhCeS regardless of the specimen size. The higher the compressive strength, the smaller the porosity and median pore diameter and the smaller the compressive strength, the higher the porosity and median pore diameter. Among the rehydrated specimens, RhCeS600_1h has the highest compressive strength corresponding to the lowest porosity and median pore diameter. The median pore diameter of the RhCeS1000_1h is significantly the highest and corresponds to the lowest compressive strength.

There is a similarity between the results of RhCoS and RhCeS. High compressive strength corresponds to low porosity and median pore diameter and vice versa, as shown in **Figure 6-16**. Moreover, between the rehydrated specimens, the SC600_1h and EF600_1h have the highest compressive strengths corresponding to the lowest median pore diameters. However, the porosity is lowest for EF600_1h but not for SC600_1h. Thus, secondary factors, such as the degree of vibration of the fresh mortar, affect the porosity results. Nevertheless, the SC1000_1h and EF1000_1h have the lowest compressive strengths corresponding to the highest porosities and median pore diameters.

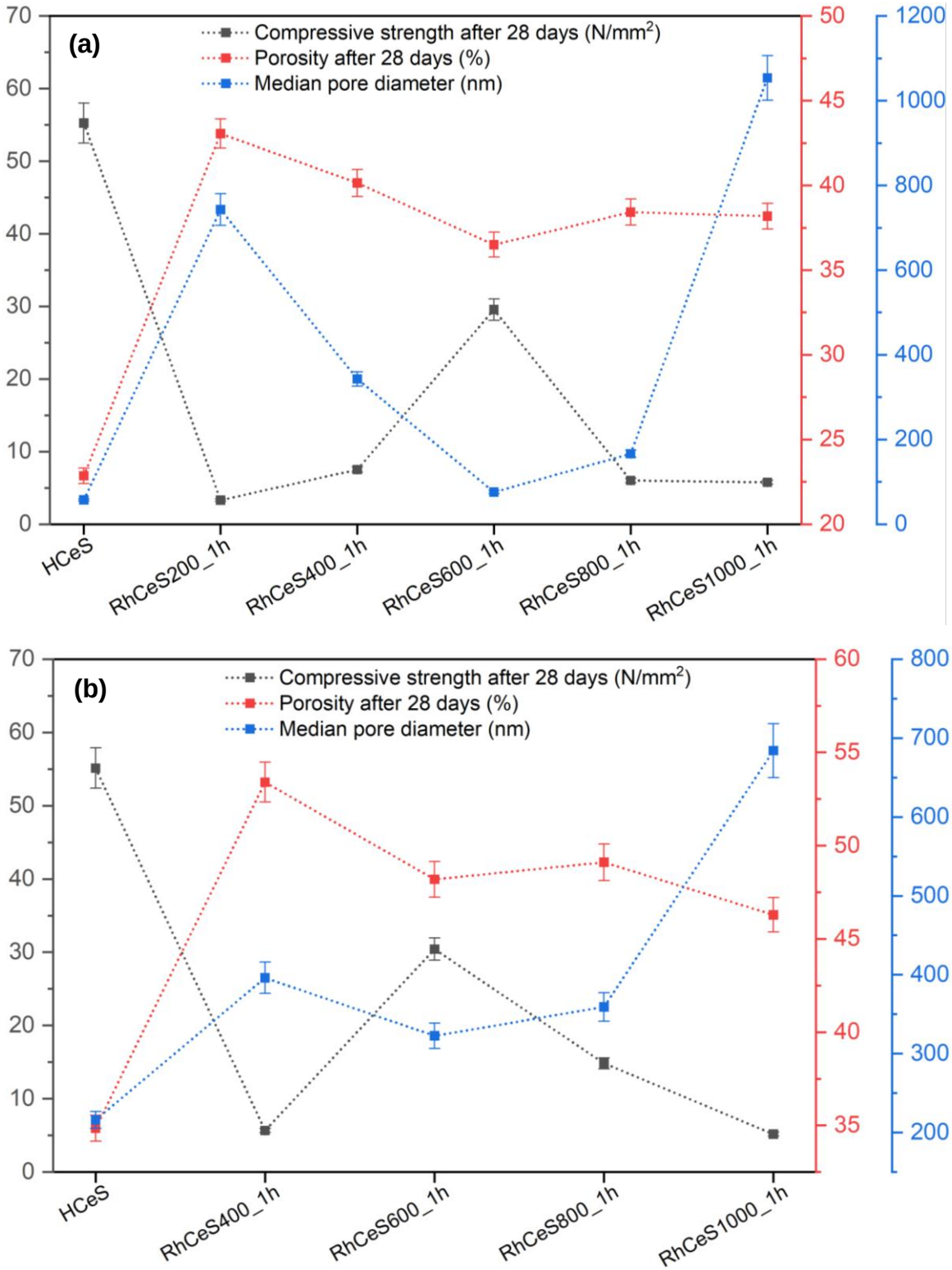

Figure 6-15: Combined compressive strength results, porosity results and median pore diameters for the Rehydrated Cement Specimens (RhCeS): (a) Standard-size specimens (40×40×160 mm^3), (b) Small-size specimens (20×20×20 mm^3).

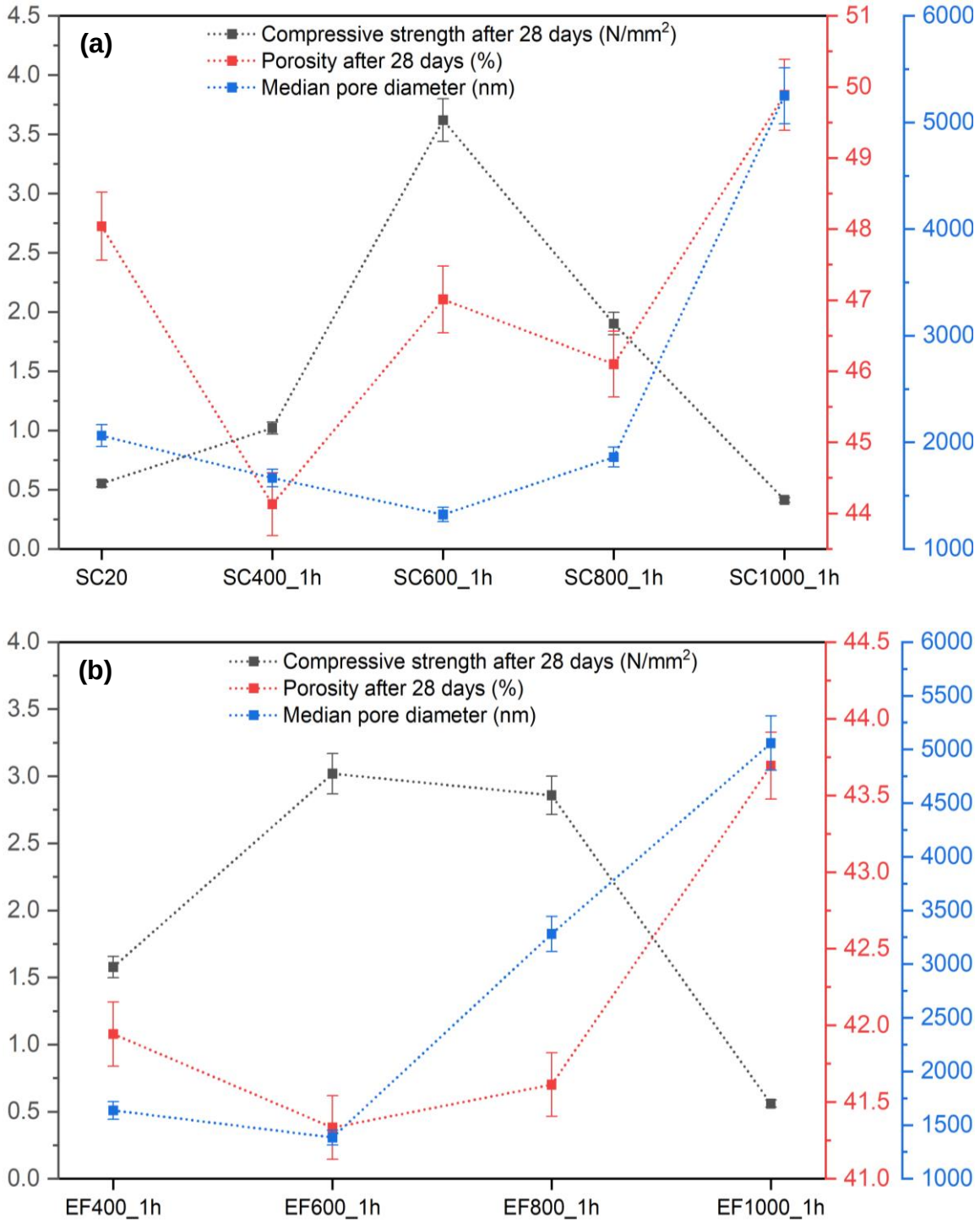

Figure 6-16: Combined compressive strength results, porosity results and median pore diameters for the small-size (20×20×20 mm^3) Rehydrated Concrete Specimens (RhCoS): (a) From the Recycled Concrete Powder (RcCoP) obtained by Smart Crushing (SC), (b) From the RcCoP obtained by Electrodynamic Fragmentation (EF).

6.4. Discussion of the results

6.4.1. Discussion of strength results

The combination of previous results (XRD, XRF, DSC-TG, and SEM/EDX) explains the expectations on the achievable strengths depending on the temperatures used to heat the HCeP and RcCoP. The DSC-TG results specify the chemical transformations happening due to the thermal treatment temperatures, and the XRF results give an insight into the phase formation by indicating the influence of the weight percentages of the bound oxides. The XRD results describe the phase formations associated with different temperature treatments, while the SEM/EDX results describe their influence on the microstructure. The connection between these changes and strength development is also provided within these results. The following sections link these results with the strength measurements to explain the relationship between the thermal treatment temperature and the obtainable optimum strength.

Figure 6-2 (a) and **(b)** show that the compressive and flexural strengths of the HCeS (obtained by a mixture of 100% VCe with water) are the highest compared to the untreated and all thermally treated HCeP resulting specimens. Thus, the total recovery of strength development ability by thermal treatment of HCeP is not reached. The strength recovery difference can be explained by the presence of high content of the C_3S phase in VCe (71% according to the XRD results (**Table 4-1**), which cannot be recovered in DhCeP (thermally treated HCeP) samples. The C_3S is highly reactive and is the main phase controlling strength development, especially at early age (first week) **[43, 44, 49]**. Several researchers believe this phase completely reacts with water; only a few state that a small percentage can remain unhydrated **[17]**.

The untreated HCeP specimens (RwCeS) show insignificant compressive and flexural strengths compared to those obtained from thermally treated HCeP (RhCeS), indicating that thermal treatment can recover the strength development ability. This recovery is due to converting hydration products to dehydration products with a regained hydration capacity. However, these dehydration products depend on the temperature in the thermal treatment process. **Figure 6-2 (a)** and **(b)** show that thermal treatment at 600 °C produces the specimens with the highest compressive and flexural strengths. Therefore, the thermal treatment at 600 °C is considered optimum. The XRD results (**Table 4-1**) indicate the presence of C_2S_β, C_2S_α and the highest amount of the C_3S phase, which are the principal phases contributing to strength development. Additionally, there is a complete decomposition of the C-S-H phase that leads to the formation of these phases.

On the other hand, the DhCeP1000_1 contains no C_3S phase at all, much less C_2S_α, and no presence of the C-S-H phase after rehydration. Moreover, significant new phases, such as silicocarnotite (11.5%), indicate a possible transformation of already formed dehydration products resulting in decreased strength **[16]**. Similarly, Alonso and Fernandes **[11]** stated that C–S–H gel is transformed into a newly formed nesosilicate phase above 750 °C, generating a strength decrease. Furthermore, a high free lime (CaO) content in DhCeP800_1h and DhCeP1000_1h confirms this strength decrease due to its influence, as explained in **Section 4.2**.

Figure 6-6 (a) and **(b)** show that the compressive strengths of the specimens obtained from thermally treated RcCoP (RhCoS (both SC and EF samples)) are generally low compared to RhCeS. While approximately 55% of strength formation ability could be recovered for the RhCeS (RhCeS600), only less than 10% could be recovered for the RhCoS (SC600 and EF600) (**Figure 6-7**). The highest strength recovery is again produced with thermal treatment

at 600 °C, as for the RhCoS. Although there is a higher content of C_2S_β and C_2S_α phases in SC800 and EF800 than in SC600 and EF600, the amount of the C_3S phase is marginally higher at 600 °C than at 800 °C (**Table 5-1** and **Table 5-2**). Besides, higher temperature treatment will likely reduce workability and increase porosity by initiating a brief setting time. Furthermore, SC1000 and EF1000 contain a significant amount of new phases, such as Akermanite (30% and 11%, respectively), indicating the possibility of transformation of previously dehydrated phases as for the RhCeS. Nevertheless, an enormously high amount of SiO_2 phase (quartz and coesite) in all RhCoS samples, which is not a strength-forming phase, explains the recovery of less than 10% of strength development ability.

The replacement of VCe in the mortar with different percentages of DhCeP ((10, 20, 30, and 100%) helps to evaluate the changes in binding to the sand fraction depending on the temperature used for the thermal treatment of HCeP. The reference for the assessment is the Standard Mortar (SM), made of 100% VCe. The other two types of mortar are the Hydrated Cement Mortar (HCeM) and the Rehydrated Cement Mortar (RhCeM), produced by replacing VCe with different percentages of HCeP and DhCeP, respectively. **Figure 6-3 (a)** shows a clear trend in the compressive strength results that increase with curing time and decrease with an increase of VCe replacement for the same treatment temperatures. However, **Figure 6-3 (b)** shows no specific trend in the flexural strength results. The explanation can be that the total sample is loaded during the compression test, allowing the whole set of internal flaws to be tested. In contrast, a small portion of the sample is loaded during flexural testing.

The thermal treatment at 600 °C still produces mortars with the highest compressive strength, and the replacement of VCe with DhCeP600_1h up to 20% offers comparatively the same compressive strength as the SM. An increase in replacement percentage decreases the compressive strength considerably. The replacement of 100% VCe by RhCeM600_1h, using the superplasticizer to regulate the setting time, achieves 34% and 45% of the compressive and flexural strengths of the SM, respectively. Therefore, the total binding ability cannot be recovered for the same reasons related to the material phase composition, as previously specified. However, porosity resulting from thermal treatment is also an essential factor to consider for the achievable mechanical strength.

6.4.2. Discussion of porosity results

Typically, porosity decreases with curing time until complete hydration happens, as the hydration products fill the voids **[240–243]**. However, as displayed in **Figure 6-8 (a)**, the porosity of the HCeS and all RhCeS samples increases from 7 to 28 days of curing. Several possible reasons can explain this behavior. In all probability, the storage of the samples cured for 7 days under a vacuum inside the device before porosity measurement left some residual water in the tiny pores, affecting the porosity results. This statement can be supported by a much higher inaccessible porosity by Mercury Intrusion Porosimetry (MIP) of 22-41% for the samples cured for 7 days compared to those cured for 28 days, that is 7-15%, as shown by the results in **Appendix 3**. Additionally, due to the significant water content, the porosity after 7 days is similar for the HCeS and all RhCeS samples. Therefore, the hydration reaction needs more time to form the necessary hydration products. For these reasons, we can consider the comparison of porosity after 28 days more realistic than after 7 days.

Figure 6-8 (a) shows that the porosity after 28 days of the RhCeS samples is higher than that of the HCeS. This difference can be explained by the formation of capillary pores through continuous water loss during drying and the generation of smaller gel pores by the hydration reactions. In the case of the hydration of RhCeS, the hydration reactions are much faster than

for the HCeS; thus, the porosity formation rate is higher. Moreover, the fresh paste cannot densify adequately in a medium viscosity regime, and more and bigger pores form inside the material. Therefore, using chemical additives can be a solution for controlling the setting time of the RhCeS, especially with high pre-treatment temperatures.

The combination of the DSC-TG and XRD results can explain the porosity development resulting from thermal treatment at different temperatures (**Figure 6-8 (a)**). The porosity is much higher for RhCeS200_1h (and all other RhCeS) than HCeS due to the removal of the physically bound water from the C–S–H gel and the decomposition of ettringite **[35, 244, 245]**. At the same time, a small amount of calcium silicate phases (C_3S, C_2S_α, and C_2S_β) is formed for the RhCeS200_1h (refer to **Table 4-1**) and doesn't produce the required rehydration products that fill the voids. There is a similarity between the porosities of RhCeS200_1h and RhCeS400_1h because the alteration of hydration products is not pronounced in this temperature range. Portlandite coexists with calcite **[12, 14]**. Moreover, the formation of calcium silicate phases is similar.

The decrease of porosity from RhCeS400_1h to RhCeS600_1h is associated with the decomposition of portlandite. The XRD pattern (**Figure 4-1**) indicates that portlandite is an intense peak. Its decomposition produces the CaO, the principal bound oxide for forming calcium silicate phases. The high amount of these phases in RhCeS600 contributes to the formation of rehydration products that reduce porosity by filling the voids. In contrast, the porosities above thermal treatment at 600 °C (RhCeS800_1h and RhCeS1000_1h) are similar. The decarbonation of calcite happens. Since the calcite phase is present in small amounts, and its decomposition is shown by a tiny peak (**Figure 4-6**), the decarbonation does not change much regarding forming calcium silicate phases. Thus, the phase contents, especially the calcium silicate phases, contribute to the non-identical filling of the voids with the rehydration products. Therefore, the RhCeS600_1h has the lowest porosity of all RhCeS samples as it has the highest content of calcium silicate phases, especially more C_3S. Additionally, it has a minor cumulative pore diameter and the lowest value for median pore diameter (**Figure 6-8 (b)**). Both reasons confirm that 600 °C is the optimum thermal treatment temperature.

The porosity after 28 days of small specimens of HCeS and RhCeS indicates similarities in the porosity development to the standard-size specimens depending on the thermal treatment temperature (**Figure 6-9 (a)**). Furthermore, the comparison of material pore diameters is similar to the one for the standard-size specimens with little differences (**Figure 6-9 (b)**). Hence, the porosity results of small size RcCoS (SC20 and EF20) and RhCoS (SC400_1h - SC1000_1h and EF400_1h - EF1000_1h) (**Figure 6-12 (a)** and **(b)**, and **Figure 6-13**) are theoretically expected to be reliable for the analysis of dependence on thermal treatment temperature used. However, the compressibility during vibration and curing conditions can easily affect the results due to the small size, which makes their vibration less consistent, with their generally weak compressive strength. The much higher porosity, pore diameter and median pore diameter associated with the pre-treatment at 1000 °C for SC1000_1h and EF1000_1h are detectable. Therefore, they account for the lowest strength development capacity. Alternatively, the least median pore diameter for the SC600_1h and EF600_1h stipulates the potential for optimum strength development.

The porosity and the pore diameter are associated with the ability to produce hydration products (for the untreated materials HCeS and SC20) and rehydration products (for thermally treated materials RhCeS400_1h to RhCeS1000_1h, SC400_1h to SC1000_1h, and EF400_1h to EF1000_1h) that fill the voids. **Figure 6-15** and **Figure 6-16** show that the highest

compressive strength is always achieved with thermal treatment at 600 °C, and the lowest porosity and pore diameters are obtained compared to other treatment temperatures. It is, therefore, proven that the formation of rehydration products, mainly the calcium silicate phases, is optimum at this temperature. The necessary chemical transformation and phase transitions happen. Lower treatment temperatures (200 °C and 400 °C) allow insufficient chemical transformations, while very high temperatures (800 °C and 1000 °C) result in overheating, causing the alteration of already formed dehydration products.

The differential pore volume distribution curves are essential for assessing the pore volumes linked to each pore diameter. The critical pore diameters are specified by the curves having the most intense peaks. The critical pore diameter range (10^2 nm to 10^3 nm) of the HCeS and RhCeS (**Figure 6-11**) indicates that the pores are big enough to influence the achievable strength for both the standard-size and small-size specimens. The unexpected critical pore diameter of 10 nm for the standard-size RhCeS800_1h_28 may have resulted from the workability problems associated with a rapid setting that allowed the formation of cracks during the vibration process, as shown by its highest amount of biggest pores (> 10^3 nm) compared to other samples. The lowest peak of HCeS_28 specifies the most dense specimen compared to the others. Due to the clinker phase composition of HCeP, especially the C_3S, the hydration products fill the voids during the drying process. Thus, the bimodal distribution is associated with the pores resulting from drying out and hydration reaction.

The lowest peaks of RhCeS600_1h_28 and RhCeS800_1h_28 among thermally treated samples are associated with a higher content (wt. %) of calcium silicate phases (refer to **Table 4-1**), which allows an enhanced filling during the hydration process. Since the RhCeS200_1h_28 and RhCeS400_1h_28 have the lowest content (wt. %) of calcium silicate phases, a more intense peak at critical pore diameter occurs. Alternatively, the RhCeS1000 mainly comprises C_2S_β as a calcium silicate phase. As this phase reacts later during hydration alongside the rapid setting caused by treatment at a high temperature (1000 °C), an intense peak at critical pore diameter also occurs.

The critical pore diameter range (4×10^3 nm and 2×10^4 nm) of the small-size RcCoS and RhCoS (SC and EF) (**Figure 6-14**) specify that the pores significantly influence the attainable strength. These critical pore diameters are higher than those of HCeS and RhCeS because the thermally treated SC and EF samples contain a small amount (wt. %) of calcium silicate phases to form the hydration products that fill the voids. Instead, they are dominated by SiO_2, which does not develop hydration products. SC1000_1h_28 and EF1000_1h_28 present the most intense critical pore diameters due to the rapid setting that generates pores. In contrast, SC600_1h_28 and EF600_1h_28 display the lowest critical pore diameters due to a higher amount (wt. %) of calcium silicate phases (refer to **Table 5-1** and **Table 5-2**) alongside a higher setting time, allowing the filling of voids progressively.

7. Conclusions and recommendations

7.1. Conclusions

The main objective of this research was to assess the effect of thermal treatment on Hydrated Cement Powder (HCeP) and Recycled Concrete Powder (RcCoP) for the recovery of hydration ability, referred to as the rehydration of HCeP and RcCoP. This rehydration occurs after the mixture of water with dehydrated HCeP and RcCoP as a result of the thermal treatment process. The heating temperatures used range between 200 °C and 1000 °C. While the chemical phase composition of Virgin Cement (VC) is well known, it was found that the phase compositions of Dehydrated Cement Powder (DhCeP) and Dehydrated Concrete Powder (DhCoP) are as complex, yet very different, because dehydration products are formed. These products cause the formation of additional new phases and dissimilarity in the weight percentages for the same phase types. Furthermore, the highest temperature was not essentially the best for strength development. Thus, the optimum thermal treatment temperature was investigated by using various laboratory techniques.

The heating process leads to different properties of DhCeP and DhCoP compared to VCe. These properties include higher water demand, faster reactivity with water and shorter setting time. Besides, they are connected with the changes in the microstructure of the obtained Rehydrated Cement Specimens (RhCeS) and Rehydrated Concrete Specimens (RhCoS) after the mixture of DhCeP and DhCoP with water. These changes in microstructure and their associated porosity and mechanical strength were also investigated. The highly reactive cement type CEM I 52.5 R was used to produce the HCeP to assess the highest possible strength recovery by thermal treatment. It was confirmed that VCe could be replaced in mortar by DhCeP to some extent without affecting the mechanical strength. Therefore, using reactivated cement as an additive could help save CO_2 emissions without negatively affecting the quality.

In the reactivation process of RcCoP, an additional step, the separation from aggregates, influences the quality, making it more complex. Two techniques, Smart Crushing (SC) and Electrodynamic Fragmentation (EF), were used, and their results are compared. The consideration for reactivation of RcCoP reflects the actual industrial situation. It is beneficial for overcoming environmental problems caused by the depletion of natural raw materials required to make concrete and disposal of Construction and Demolition Waste (CDW).

For both reactivations of HCeP and RcCoP, the optimum heating temperature to produce the best mechanical strength is much less compared to ~1450 °C required for producing VCe. Thus, energy can be saved in addition to reducing CO_2 emissions. The following are the conclusions made from this research:

- Thermal treatment is beneficial for the reactivation of HCeP and RcCoP by converting them into DhCeP and DhCoP, respectively. The XRD results show that the recovery of strength development phases, essentially the calcium silicates, is possible within these obtained powders (DhCeP and DhCoP). The hydration ability is regained, and their rehydration can develop strength to a considerable extent. Pre-treatment between 400°C to 800°C produces the DhCeP and DhCoP of the best calcium silicate phase content, which can be considered the optimum range. However, compared to the VCe, the unhydrated tricalcium silicate (C_3S) remains in small amounts. At the same time, a considerable quantity of dicalcium silicate alpha (C_2S_α) is formed that VCe does not

contain. This behavior indicates that the total recovery of hydration ability cannot be achieved. The C_2S_α is not as reactive as C_3S but more reactive than C_2S_β, which benefits strength formation. The amount of these phases is minimal in the DhCoP compared to the DhCeP, implying that substantially less rehydration ability and strength development can be achieved in DhCoP regardless of the thermal treatment temperature. Furthermore, all the DhCoP samples contain an enormously high amount of SiO_2 phase (quartz and coesite), which is not a strength formation phase.

- For both materials, pre-treatment at 600 °C indicates the potential for the highest mechanical strength development. In addition to resulting in a significant amount of C_2S_β and C_2S_α, it shows the highest content of the unhydrated C_3S. Besides, the decomposition of the C-S-H phase is complete above 400 °C. 800 °C produces too much free lime (CaO), affecting strength development, leading to faster setting time and inducing expansion. On the other hand, the dissimilarities and formation of new crystalline phases in the HCeP and RcCoP pre-treated at 1000 °C suggest the transformation of already dehydrated hydration phases, negatively affecting the strength development. The effect of different hold times (1h, 3h, 5h, and 10h) at maximum temperatures indicates similarities between the hold time for 1h and 3h, and then between 5h and 10h. Still, there is no consistency for all thermal treatment temperatures. The contents of C_3S and C_2S_α are generally higher for 1h and 3h hold times, and they reduce for 5h and 10h hold times, while the amount of C_2S_ β tends to increase. Thus, hold time for 5h and 10h is not beneficial, as the most reactive and strength-forming phases tend to decrease.

- The DSC-TG results complement the XRD results and confirm that the required chemical transformations happen during the thermal treatment of HCeP and RcCoP. The decomposition of ettringite is complete below 250 °C, while the dehydration of C–S–H gels starts. The dehydroxylation of portlandite happens above 400 °C in the HCeP and RcCoP but is not complete for all pre-treatment temperatures. Nevertheless, there is a peak shift for the materials pre-treated above 400 °C, indicating that the thermal stability of the recrystallized portlandite is not the same as the original portlandite from the VCe. Besides, this peak is tiny for the RcCoP, specifying a reduced contribution to the formation of dehydrated phases compared to the HCeP. The decomposition of calcite happens above 600 °C in the HCeP and RcCoP. However, the peak associated with this decomposition tends to disappear with pre-treatment above 600 °C, indicating that more expulsion of CO_2 happens. Moreover, it is more intense for the RcCoP than HCeP, denoting much more ejection of CO_2 and possible carbonation during the service life of the original concrete from which the RcCoP is produced.

- Another peak exists at around 580 °C only for the RcCoP and all the DhCoP samples. This peak is not associated with mass loss, indicating any decomposition. Instead, it is related to the conversion of α-quartz to β-quartz. SiO_2 is a thermally stable phase not decomposed by thermal treatment during this research, emphasizing its negative influence on strength development. The effect of different hold times reveals no consistency, but the hold times for 1h and 3h again display some similarities over 5h and 10h. The peak intensities tend to decrease and shift positions with the latter, demonstrating thermal instabilities.

- The comparison of the compressive and flexural strengths after the use of 100% untreated (RwCeS) and thermally treated HCeP (RhCeS) confirms that thermal treatment can recover the strength development ability by converting the hydration products to the dehydration products with a better content of strength development phases, namely the calcium silicate phases. The presence of these phases in RhCeS and RhCoS specifies that the hydration capacity is regained to a considerable extent. However, the total hydration capacity and recovery of strength development ability cannot be recovered as the compressive and flexural strengths of HCeS (from VCe) are higher than those of RhCeS and RhCoS. Approximately 55% of strength formation ability was recovered for the RhCeS. On the other hand, only <10% of strength formation ability was achieved for the RhCoS because the content of calcium silicate phases is insignificant and highly dominated by the presence of the SiO_2 (quartz and coesite) phase. This non-recovery of total strength can be explained by the content of a very high amount of C_3S phase in the VCe that cannot be regained in the DhCeP and DhCoP. This phase is the most reactive and controls strength development to the greatest extent, especially at an early age (first week).

- The effect of different hold times (1h, 3h, 5h, and 10h) at maximum temperatures exhibits more similarities in the compressive strengths of the RhCeS than those of the RhCoS for the same pre-treatment temperatures. However, the dependence of strength development on the pre-treatment temperatures is respected for all hold times, and the results are in the same range. Besides, different factors, such as vibration difficulties for the fresh cement paste, can influence the results. Thus, the hold time of 1h is reliable. The thermal treatment of HCeP and RcCoP at 600 °C produces the best strength for both materials after using 100% of them to make the specimens. Furthermore, the replacement of VCe by DhCeP reveals that RhCeM600_1h produces the highest strength of all RhCeM for equivalent VCe replacement percentages. VCe can be replaced up to 20% by DhCeP600_1h in mortar without affecting the mechanical strength. Using 100% DhCeP600_1h achieves 34% of the compressive strength of the standard mortar (made of 100%VCe) and 45% of the flexural strength. This temperature is, therefore, considered the optimum thermal treatment temperature. Within this research, smaller steps have been tested.

- There are similarities in all results for thermally treated RcCoP obtained by Smart Crushing (SC) and Electrodynamic Fragmentation (EF). The phase contents and percentages are similar according to the XRD results, and the DSC-TG results show the same peaks related to different chemical transformations during heat treatment. These peaks are associated with similar mass losses and happen at similar temperatures. XRD and SEM confirm the domination of phase content by the SiO_2 phase, which is disadvantageous for strength development. Thus, neither method successfully separated sand (SiO_2) and cementitious materials.

- Thermal treatment influences the porosity and microstructure of the obtained rehydrated specimens. Generally, it results in higher porosity than the one of HCeS (from VCe) by producing the materials (DhCeP and DhCoP) that hydrate much faster, especially for very high pre-treatment temperatures, increasing the porosity formation rate. Thus, the densification of the fresh paste from these materials in a medium viscosity regime is inadequate, influencing the formation of a higher number and voluminous pores. Therefore, using chemical additives is necessary to regulate the

setting time. Moreover, the pre-treatment temperature, which determines the phase contents in the DhCeP and DhCoP, impacts the porosity by contributing to different filling of the voids during hydration. For both materials, the pre-treatment at 600 °C produces the lowest porosity and median pore diameter due to its formation of the best content of calcium silicate phases. Similarly, the SEM results indicate the most densified rehydration products and compact structure at this pre-treatment temperature for the RhCeS600, while the domination of SiO_2 crystals characterizes all the RhCoS. On the other hand, the pre-treatment at 1000 °C forms the highest porosity, pore diameter and median pore diameter, denoting the lowest strength development potential.

7.2. Recommendations

Although this research has achieved the primary goal, different areas can be improved to collect more details contributing to the knowledge of thermally treated cementitious materials. Some suggestions are made for future research about the areas that were not in the present scope. The following are the recommendations from this research:

- The XRD is the essential technique for studying the phase composition of thermally treated HCeP and RcCoP. However, the thermal treatment was conducted in the furnace, and the materials were transferred to the XRD device after cooling down. This process can lead to the chemical transformation of thermally treated materials, such as carbonation. Besides, different batches of materials are used for different pre-treatment temperatures, which can influence slight differences in the phase composition of materials, even before the thermal treatment process. It is, therefore, recommended to use in situ high-temperature XRD.

- The pre-treatment at 600 °C produced the best content of calcium silicate phases, conducting to the optimum strength development. However, the temperature interval was high (200 °C) due to time constraints. It is recommended to consider less temperature interval, such as 50 °C, for the optimum temperature range (400 °C - 800 °C), especially around 600 °C.

- A high calcite content was found in the RcCoP, suggesting possible carbonation of the original concrete used to produce the RcCoP. Nevertheless, the properties of the original concrete were not available to evaluate how much carbonation may have happened. Furthermore, the amount and type of cement used in producing the original concrete were also unknown. Due to these reasons, it is recommended to use recycled concrete with known properties or manufacture the concrete in the laboratory to simulate ideal conditions.

- The percentage of the SiO_2 phase in the RcCoP was still very high, even after the separation process for both SC and EF, which affected the strength development negatively. Therefore, investing more time into separation and improving the settings when necessary is recommended. Additionally, it is desirable to consider using other separation methods, such as thermal separation, acid treatment, and microwave-assisted.

- The difficulties associated with the vibration of fresh cement specimens, especially for small specimens (20×20×20 mm^3), can influence the achievable strength and the

porosity formation. Accordingly, it is recommended to consider the perfect vibration setup allowing fixing the molds to optimize the relationship between phase composition and strength development.

- Different techniques were considered to investigate the phase composition and microstructure resulting from the thermal treatment of HCeP and RcCoP, as described in the experimental methodology (**Section 3.2**). However, these are not all the techniques that can be used, and other techniques can contribute to collecting more details. These techniques include, among others, X-ray Micro-Computed Tomography (micro-CT), Fourier Transform Infrared (FT-IR) Spectroscopy, Transmission Electron Microscopy (TEM), Isothermal Calorimetry (IC), Atomic Force Microscopy (AFM), and ^{29}Si Nuclear Magnetic resonance Spectroscopy (^{29}Si-NMR).

- Although the complexity associated with the thermal reactivation of HCeP and RcCoP is indicated, the current results are promising because the reactivation potential is somewhat achieved, especially for the RcCoP. Therefore, it is necessary to continue research in this field to improve the degree of reactivation in the hope of contributing to the solution to the climate crisis.

List of Figures

Figure 2-1: Pyroprocessing process for cement clinker formation © Elsevier, 2019 [44]. 7
Figure 2-2: Reaction sequence during cement clinker production © Taylor & Francis Group, 2018 [45]. 8
Figure 2-3: Transformation of the raw mix into cement clinker © Elsevier, 2016 [50]. 8
Figure 2-4: Temperature formation of the C_3S polymorphs [47]. 9
Figure 2-5: The simplified representation of the structure of tricalcium silicate © Springer, 2014 [43]. 10
Figure 2-6: Temperature (°C) transformation of distinct C_2S phases © Springer, 2014 [43]. 11
Figure 2-7: Representation of the structure of dicalcium silicate: C_2S_ β. Projection onto a – b plane © Springer, 2014 [43]. 12
Figure 2-8: Representation of the structure of tricalcium aluminate showing the rings with six tetrahedra: a) Rings in a cubic structure, b) Rings in monoclinic and orthorhombic structures © Springer, 2014 [43]. 12
Figure 2-9: Representation of the $Ca_2Fe_2O_5$ structure: a) Through axis a b) Through axis c © Springer, 2014 [43]. 13
Figure 2-10: Phase composition of hydrated cement with time © Verlag Bau+ Technik GmbH, 2006 [41]. 14
Figure 2-11: Structural model of ettringite [66]. 16
Figure 2-12: The process of hydration of C_3A in the absence of gypsum © Springer, 2014 (After Ref. [43]). 17
Figure 2-13: The process of hydration of C_3A in the presence of gypsum © Springer, 2014 (After Ref. [43]). 17
Figure 2-14: Heat flow curve and stages of cement hydration by isothermal calorimetry © Elsevier, 2016 [50]. 18
Figure 2-15: Contribution of the individual clinker phases to strength development in relation to hydration time © John Wiley & Sons, 2011 [49]. 20
Figure 2-16: The strength development of cement paste per particle size fraction © Verlag Bau+ Technik GmbH, 2006 [41]. 22
Figure 2-17: Influence of the mean pore radius on the strength of hardened cement paste. I: sample made of mainly tobermorite, II: mainly C-S-H (I), IV: 70-80% hydrogarnets and 20-30% C-S-H (I), V: mainly hydrogarnets (C_3AH_6) © Springer, 2014 [43]. 25
Figure 2-18: Chemical transformations resulting from thermal treatment of cement paste © Springer Nature, 2004 [11]. 26
Figure 2-19: DSC-TG curves of thermally treated HCeP according to Pavlik et al.(a) DSC; (b) TG © Springer Nature, 2016 [149]. 27
Figure 2-20: DSC-TG curves of thermally treated HCeP and FRcCoA according to Shui et al. (a) TG; (b) DSC © Elsevier, 2008 [18]. 28
Figure 2-21: XRD analysis of PC, NT and RC. ∆ portlandite; † calcite; * ettringite; ∞ gypsum; © CaO; ■ C_3S; ● tobermorite; ▼ C-S-H; X β-C_2S; ▲ α'$_L$-C_2S; O C_3A; □ calcium aluminum iron oxide; ◊ brownmillerite; Φ alumohydrocalcite; Θ calcium aluminum oxide carbonate hydrate [167]. 31
Figure 2-22: XRD analysis of the gravel, RCF-20, RCF-500, and RCF-800 samples. ▲ α-Quartz; O C_2S; ● portlandite; ■ calcite; and ∆ lime © Elsevier, 2014 [8]. 32
Figure 2-23: Water demand of DhCeP for standard consistency [20]. 33
Figure 2-24: Initial setting time of DhCeP with standard consistency [20]. 34
Figure 2-25: Compressive strengths of DhCeP at different curing days according to Shui et al. © Elsevier, 2009 [16]. 35
Figure 2-26: Mechanical strengths of DhCeP at different curing days according to Real al. [167]. 35

Figure 2-27: Variation between the optimum compressive strengths obtained by various researchers © Elsevier, 2020 [24]. 36
Figure 2-28: SEM images of (a) OPC (PC), (b) HCeP (NT), and DhCeP (RC) after treatment at (c) 400, (d) 500, (e) 650, (f) 700, (g) 750, (h) 800, (i) 900 [167]. 37
Figure 2-29: SEM images of thermally treated uncarbonated cement paste [176]. 38
Figure 2-30: SEM images of thermally treated carbonated cement paste [176]. 39
Figure 2-31: Porosity changes in thermally treated carbonated and uncarbonated cement pastes [176]....40
Figure 2-32: Compositions of the pore size distribution of thermally treated cement pastes (a) uncarbonated (b) carbonated [176]....40
Figure 2-33: Comparison of ITZ formed in concrete made with (a) natural aggregates, (b) RcCoA [25]....41
Figure 2-34: Illustration of types of crushers used to reduce the size of RcCoA [192]....42
Figure 2-35: Illustration of CDW treatment for removal of contaminants [200]. 42
Figure 2-36: Example of complete recycling of CDW into coarse and fine aggregates [199].43
Figure 2-37: Combination of innovative processing technologies to produce recycled concrete powder [195]....44
Figure 3-1: The sequence of steps involved in the preparation of HCeP. 46
Figure 3-2: The old concrete: (a) immediately obtained from the construction site, (b) pre-treated, pre-washed and pre-crushed to the required size....47
Figure 3-3: Schematic comparison of the crushing plates of (a) jaw crusher, (b) Smart Crusher [204]. 48
Figure 3-4: The separation of old concrete composite into its components by EF: (a) during the separation process, (b) after separation [205]....48
Figure 3-5: The filled grinding jar during the milling process. 49
Figure 3-6: Thermal treatment of HCeP and RcCoP: (a) the muffle furnace (Nabertherm) ...49
Figure 3-7: The process applied to prepare the materials and specimens. 51
Figure 3-8: Storage of the samples ready for measurements. 52
Figure 3-9: The process of XRF during measurement [212]. 53
Figure 3-10: Schematic illustration of the concept of XRD analysis [214]. 54
Figure 3-11: The storage of the SEM/EDX samples in a desiccator under vacuum to avoid carbonation. 55
Figure 3-12: Illustration of porosity measurement by the MIP technique. (a) sample storage under vacuum, (b) mercury storage....56
Figure 3-13: The sizes of molds used to produce the specimens: (a) the standard size, (b) the small size. 58
Figure 3-14: Differences between the sample supports during the flexural (a) and compressive (b) strength measurements....58
Figure 4-1: XRD patterns of (a) DhCeP obtained after thermal treatment at different temperatures for a hold time of 1h at maximum temperature. (b) RhCeP obtained after the reaction of DhCeP with water at room temperature. 60
Figure 4-2: Illustration of the effect of thermal treatment temperature on the phase formation of the DhCeP for a hold time of 1h at maximum temperature by the XRD results. 62
Figure 4-3: Illustration of the effect of thermal treatment temperature on the phase formation of the RhCeP for a hold time of 1h at maximum temperature by the XRD results. 62
Figure 4-4: Comparison of the effect of thermal treatment temperature on the phase formation of the DhCeP for different hold times (1h, 3h, 5h, and 10h) at maximum temperatures by the XRD results....64
Figure 4-5: Comparison of the CaO and SiO_2 contents in the VCe, HCeP, and DhCeP for different hold times (1h, 3h, 5h, and 10h) at maximum temperatures. The error bars are representative of all samples. 65

Figure 4-6: DSC (mW/mg) and TG (% mass loss) curves of Hydrated Cement Powder (HCeP) for a heating treatment up to 1000 °C at a 10 K/min heating rate. 66
Figure 4-7: Comparison of DSC (mW/mg) and TG (% mass loss) curves of HCeP and DhCeP (D200 to D1000) for a hold time of 1h at maximum temperature. 67
Figure 4-8: Comparison of DSC (mW/mg) and TG (% mass loss) curves of DhCeP (D200 to D1000) dehydrated at the same temperature for different hold times (1h, 3h, 5h, and 10h). 68
Figure 4-9: Comparison of the specific surface areas of the VCe and DhCeP for a hold time of 1h at maximum temperature. 69
Figure 4-10: SEM and EDX images of (a) Hydrated cement Specimen (HCeS), (b) Rewetted Cement Specimen (RwCeS ''Rs20'') (no thermal pre-treatment) and (c-g) Rehydrated Cement Specimens (RhCeS ''Rs200 to Rs1000'') (after thermal pre-treatment). The EDX images indicate the intensity of chemical elements contained per point analyzed. 70
Figure 5-1: XRD patterns of DhCoP obtained after thermal treatment at different temperatures for a hold time of 1h at maximum temperature. (a) Produced by Smart Crushing (SC) (b) Produced by Electrodynamic Fragmentation (EF). 75
Figure 5-2: Illustration of the effect of thermal treatment temperature on the phase formation of the DhCoP obtained by Smart Crushing (SC) for a hold time of 1h at maximum temperature. 77
Figure 5-3: Illustration of the effect of thermal treatment temperature on the phase formation of the DhCoP obtained by Electrodynamic Fragmentation (EF) for a hold time of 1h at maximum temperature. 77
Figure 5-4: Comparison of the effect of thermal treatment temperature on the phase formation of the DhCoP obtained by Smart Crushing (SC) for different hold times (1h, 3h, 5h, and 10h) at maximum temperatures. 78
Figure 5-5: Comparison of the effect of thermal treatment temperature on the phase formation of the DhCoP obtained by Electrodynamic Fragmentation (EF) for different hold times (1h, 3h, 5h, and 10h) at maximum temperatures. 79
Figure 5-6: Comparison of the CaO and SiO_2 contents in the DhCoP obtained by Smart Crushing (SC) after hold time at different times (1h, 3h, 5h, and 10h). The error bar is representative of all samples. 81
Figure 5-7: Comparison of the CaO and SiO_2 contents in the DhCoP obtained by Electrodynamic Fragmentation (EF) after hold time at different times (1h, 3h, 5h, and 10h). The error bar is representative of all samples. 81
Figure 5-8: DSC (mW/mg) and TG (% mass loss) curves of Recycled Concrete Powder (RcCoP) obtained by Smart Crushing (SC) for a heating treatment up to 1000 °C at a 10 K/min heating rate. 82
Figure 5-9: DSC (mW/mg) and TG (% mass loss) curves of Recycled Concrete Powder (RcCoP) obtained by Electrodynamic Fragmentation (EF) for a heating treatment up to 1000 °C at a 10 K/min heating rate. 82
Figure 5-10: Comparison of DSC (mW/mg) and TG (% mass loss) curves of DhCoP (SC400 to SC1000) obtained by Smart Crushing (SC) for a hold time of 1h at maximum temperature. 83
Figure 5-11: Comparison of DSC (mW/mg) and TG (% mass loss) curves of DhCoP (EF400 to EF1000) obtained by Electrodynamic Fragmentation (EF) for a hold time of 1h at maximum temperature. 83
Figure 5-12: Comparison of DSC (mW/mg) and TG (% mass loss) curves of DhCoP (SC400 to SC1000) obtained by Smart Crushing (SC), dehydrated by the same temperature for different hold times (1h, 3h, 5h, and 10h). 85
Figure 5-13: Comparison of DSC (mW/mg) and TG (% mass loss) curves of DhCoP (EF400 to EF1000) obtained by Electrodynamic Fragmentation (EF), dehydrated by the same temperature for different hold times (1h, 3h, 5h, and 10h). 86

Figure 5-14: SEM and EDX images of Rehydrated Concrete Specimen (RhCoS) produced from the Recycled Concrete Powder (RcCoP) obtained by Smart Crushing (SC): (a) without thermal treatment, (b-e) after thermal treatment at different temperatures for a hold time of 1h at maximum temperature. The EDX images indicate the intensity of chemical elements contained per point analyzed. 88
Figure 5-15: SEM and EDX images of Rehydrated Concrete Specimen (RhCoS) produced from the Recycled Concrete Powder (RcCoP) obtained by Electrodynamic Fragmentation (EF) after thermal treatment at different temperatures for a hold time of 1h at maximum temperature. The EDX images indicate the intensity of chemical elements contained per point analyzed. 89
Figure 6-1: Representation of the strength testing of the Rehydrated Cement specimens (RhCeS): (a) Hydrated Cement Specimens (HCeS), (b) Hydrated Cement Powder (HCeP and Dehydrated Cement Powders (DhCeP) obtained after heating the HCeP at different temperatures, (c) RhCeS and (d) Pieces of RhCeS after flexural strength testing. 94
Figure 6-2: (a) Compressive and (b) flexural strengths of the standard size Hydrated (H), Rewetted (Rw) and Rehydrated Cement Specimens (RhCeS) thermally treated at different temperatures for a hold time of 1h at maximum temperature. The error bars are representative of all samples. 95
Figure 6-3: Comparison of (a) compressive and (b) flexural strengths of Standard Mortar (SM), Hydrated Cement Mortar (HCeM) and Rehydrated cement mortar (RhCeM), with different replacement percentages of VCe by HCeP or DhCeP. The hold time was conducted for 1 hour. The error bars are the same for all points. RhCeM600*_1h means that the specimens were prepared using a superplasticizer (2%). 96
Figure 6-4: Comparison of the compressive strengths of small-size (20×20×20 mm^3) Rehydrated Cement Specimens (RhCeS) thermally treated at different temperatures for hold times of 1, 3, 5, and 10 hours. 96
Figure 6-5: (a) Dehydrated Concrete Powder (DhCoP) after thermal treatment of the Recycled concrete Powder (RcCoP) at different temperatures and (b) the resulting small-size Rehydrated Concrete Specimens (RhCoS). 97
Figure 6-6: Comparison of the compressive strengths of the small-size Rehydrated Concrete Specimens (RhCoS) produced from the Recycled Concrete Powder (RcCoP) preheated at different temperatures for several hold times (1, 3, 5, and 10h). (a) Obtained by Smart Crushing (SC) and (b) obtained by Electrodynamic Fragmentation (EF). 97
Figure 6-7: Comparison of the compressive strengths of the Virgin Cement (VCe) and the Rehydrated Concrete Specimens (RhCoS) produced from the Recycled Concrete Powder (RcCoP) obtained by Smart Crushing (SC) after thermal treatment at different temperatures for several hold times. 98
Figure 6-8: Comparison of porosity of the standard size specimens (40×40×160 mm^3) of the HCeS and RhCeS manufactured from the HCeP thermally treated at different temperatures for a hold time of 1h at maximum temperature (a) and the cumulative pore size distribution after 28 days (b). 99
Figure 6-9: Porosity of the small size specimens (20×20×20 mm^3) of the HCeS and RhCeS manufactured from the HCeP thermally treated at different temperatures for a hold time of 1h at maximum temperature (a), and the cumulative pore size distribution after 28 days (b)...100
Figure 6-10: Comparison of the median pore diameters of the HCeS and RhCeS manufactured from the HCeP thermally treated at different temperatures for a hold time of 1h at maximum temperature. (a) Standard-size specimens and (b) small-size specimens. 100
Figure 6-11: Comparison of differential pore size distribution curves of the HCeS and RhCeS manufactured from the HCeP thermally treated at different temperatures for a hold time of 1h at maximum temperature. (a) Standard-size specimens (40×40×160 mm^3) and (b) small-size specimens (20×20×20 mm^3). The raw data are preserved for (a) because averaging for smoothing would completely change the meaning of the plots. 101

Figure 6-12: Comparison of porosity of small specimens of the RcCoS and RhCoS manufactured from the RcCoP obtained by both the Smart Crushing and Electrodynamic Fragmentation (EF) thermally treated at different temperatures for a hold time of 1h at maximum temperature (a) and the cumulative pore size distribution after 28 days (b). The error bar is representative of all samples. 102
Figure 6-13: Comparison of the median pore diameters of small specimens of the RcCoS and RhCoS manufactured from the RcCoP obtained by both Smart Crushing (SC) and Electrodynamic Fragmentation (EF) thermally treated at different temperatures for a hold time of 1h at maximum temperature. 102
Figure 6-14: Comparison of differential pore size distribution curves of small-size specimens of the RcCoS and RhCoS manufactured from the RcCoP thermally treated at different temperatures for a hold time of 1h at maximum temperature. (a) RcCoP obtained by Smart Crushing (SC) and (b) RcCoP obtained by Electrodynamic Fragmentation (EF). 103
Figure 6-15: Combined compressive strength results, porosity results and median pore diameters for the Rehydrated Cement Specimens (RhCeS): (a) Standard-size specimens (40×40×160 mm^3), (b) Small-size specimens (20×20×20 mm^3). 104
Figure 6-16: Combined compressive strength results, porosity results and median pore diameters for the small-size (20×20×20 mm^3) Rehydrated Concrete Specimens (RhCoS): (a) From the Recycled Concrete Powder (RcCoP) obtained by Smart Crushing (SC), (b) From the RcCoP obtained by Electrodynamic Fragmentation (EF). 105

List of Tables

Table 2-1: Classification of cement types according to DIN EN 197-1 standard. 5
Table 2-2: Representative oxide composition of a general-purpose Portland cement © John Wiley & Sons, 2011 [49]. 6
Table 2-3: Typical German cement clinker phase composition © Verlag Bau+ Technik GmbH, 2006 [41]. 6
Table 2-4: Structure of C_2S polymorphs © Springer, 2014 [43]. 11
Table 2-5: Composition of a type I hardened Portland cement paste (w/c = 0.5) © Informa UK Limited, 2002 [65]. 23
Table 2-6: Phase transitions in thermoactivated cementitious materials © Elsevier, 2020 [24]. 29
Table 2-7: Optimum compressive strengths after 28 days using 100% thermoactivated cement © Elsevier, 2020 [24]. 36
Table 3-1: The w/c used for compressive and flexural strength determination. 57
Table 4-1: Phase content (weight %) of the Dehydrated Cement Powder (DhCeP) from XRD spectra after Rietveld refinement (± 0.5%). 61
Table 4-2: Phase content (weight %) of the Rehydrated Cement Powder (RhCeP) from XRD spectra after Rietveld refinement (± 0.5%). 61
Table 4-3: Chemical composition (given in wt. %) of the VCe, HCeP, and DhCeP for a hold time of 1h at maximum temperature. 65
Table 4-4: DSC - TG peaks and mass loss analysis for the HCeP and DhCeP for a hold time of 1h at maximum temperature. 67
Table 5-1: Phase content (wt. %) of the Dehydrated Concrete Powder (DhCoP) obtained by Smart Crushing (SC) from XRD spectra after Rietveld refinement (± 0.5%). 76
Table 5-2: Phase content (wt. %) of the Dehydrated Concrete Powder (DhCoP) obtained by Electrodynamic Fragmentation (EF) from XRD spectra after Rietveld refinement (± 0.5%). .76
Table 5-3: Chemical composition (given in wt. %) of the DhCoP obtained by Smart Crushing (SC) for a hold time of 1h at maximum temperature. 80
Table 5-4: Chemical composition (given in wt. %) of the DhCoP obtained by Electrodynamic Fragmentation (EF) for a hold time of 1h at maximum temperature. 80
Table 5-5: DSC - TG peaks and mass loss analysis for the RcCoP (SC20) and DhCoP obtained by Smart Crushing (SC) for a hold time of 1h at maximum temperature. 84
Table 5-6: DSC - TG peaks and mass loss analysis for the RcCoP (EF20) and DhCoP obtained by Electrodynamic Fragmentation (EF) for a hold time of 1h at maximum temperature. 84

References

1. Meyer C (2009) The greening of the concrete industry. Cement and Concrete Composites 31(8): 601–605. doi: 10.1016/j.cemconcomp.2008.12.010
2. Imbabi MS, Carrigan C, McKenna S (2012) Trends and developments in green cement and concrete technology. International Journal of Sustainable Built Environment 1(2): 194–216. doi: 10.1016/j.ijsbe.2013.05.001
3. Adesina A (2020) Recent advances in the concrete industry to reduce its carbon dioxide emissions. Environmental Challenges 1: 100004. doi: 10.1016/j.envc.2020.100004
4. Collivignarelli MC, Cillari G, Ricciardi P et al. (2020) The Production of Sustainable Concrete with the Use of Alternative Aggregates: A Review. Sustainability 12(19): 7903. doi: 10.3390/su12197903
5. Javadabadi MT, Kristiansen DDL, Redie MB et al. (2019) Sustainable Concrete: A Review. IJSCER: 126–132. doi: 10.18178/ijscer.8.2.126-132
6. Matias D, Brito J de, Rosa A et al. (2013) Mechanical properties of concrete produced with recycled coarse aggregates - influence of the use of superplasticizers. Construction and Building Materials 44: 101–109
7. Malhotra VM Role of supplementary cementing materials in reducing greenhouse gas emissions. Concrete technology for a sustainable development in the 21st century. In: Gjorv OE, Sakai K, editors, vol 226, 35 (2000)
8. Florea MVA, Ning Z, Brouwers HJH (2014) Activation of liberated concrete fines and their application in mortars. Construction and Building Materials 50: 1–12. doi: 10.1016/j.conbuildmat.2013.09.012
9. Xinwei M, Zhaoxiang H, Xueying L (2010) Reactivity of Dehydrated Cement Paste from Waste Concrete Subjected to Heat Treatment. Second International Conference on Sustainable Construction Materials and Technologies
10. Castellote M, Alonso C, Andrade C et al. (2004) Composition and microstructural changes of cement pastes upon heating, as studied by neutron diffraction. Cement and Concrete Research 34(9): 1633–1644. doi: 10.1016/S0008-8846(03)00229-1
11. Alonso C, Fernandez L (2004) Dehydration and rehydration processes of cement paste exposed to high temperature environments. Journal of Materials Science 39(9): 3015–3024. doi: 10.1023/B:JMSC.0000025827.65956.18
12. Alarcon-Ruiz L, Platret G, Massieu E et al. (2005) The use of thermal analysis in assessing the effect of temperature on a cement paste. Cement and Concrete Research 35(3): 609–613. doi: 10.1016/j.cemconres.2004.06.015
13. Farage M, Sercombe J, Gallé C (2003) Rehydration and microstructure of cement paste after heating at temperatures up to 300 °C. Cement and Concrete Research 33(7): 1047–1056. doi: 10.1016/S0008-8846(03)00005-X
14. Stepkowska ET, Blanes JM, Franco F et al. (2004) Phase transformation on heating of an aged cement paste. Thermochimica Acta 420(1-2): 79–87. doi: 10.1016/j.tca.2003.11.057
15. Yu R, Shui Z, Dong J (2013) Using Dehydrated Cement Paste as New Type of Cement Additive. MJ 110(4). doi: 10.14359/51685786
16. Shui Z, Xuan D, Chen W et al. (2009) Cementitious characteristics of hydrated cement paste subjected to various dehydration temperatures. Construction and Building Materials 23(1): 531–537. doi: 10.1016/j.conbuildmat.2007.10.016
17. Wang G, Zhang C, Zhang B et al. (2015) Study on the high-temperature behavior and rehydration characteristics of hardened cement paste. Fire Mater. 39(8): 741–750. doi: 10.1002/fam.2269

18. Shui Z, Xuan D, Wan H et al. (2008) Rehydration reactivity of recycled mortar from concrete waste experienced to thermal treatment. Construction and Building Materials 22(8): 1723–1729. doi: 10.1016/j.conbuildmat.2007.05.012
19. Handoo SK, Agarwal S, Agarwal SK (2002) Physicochemical, mineralogical, and morphological characteristics of concrete exposed to elevated temperatures. Cement and Concrete Research 32(7): 1009–1018. doi: 10.1016/S0008-8846(01)00736-0
20. Xuan DX, Shui ZH (2011) Rehydration activity of hydrated cement paste exposed to high temperature. Fire Mater. 35(7): 481–490. doi: 10.1002/fam.1067
21. Zhang L, Ji Y, Li J et al. (2019) Effect of retarders on the early hydration and mechanical properties of reactivated cementitious material. Construction and Building Materials 212: 192–201
22. Florea MV, Brouwers HJ (2013) The influence of crushing method on recycled concrete properties. In: Proceedings of the international conference on advances in cement and concrete technology in Africa, Johannesburg (South Africa), pp 1041–1050
23. Bordy A, Younsi A, Aggoun S et al. (2017) Cement substitution by a recycled cement paste fine: Role of the residual anhydrous clinker. Construction and Building Materials 132: 1–8. doi: 10.1016/j.conbuildmat.2016.11.080
24. Carriço A, Bogas JA, Guedes M (2020) Thermoactivated cementitious materials – A review. Construction and Building Materials 250: 118873. doi: 10.1016/j.conbuildmat.2020.118873
25. Ohemeng EA, Ekolu SO (2020) A review on the reactivation of hardened cement paste and treatment of recycled aggregates. Magazine of Concrete Research 72(10): 526–539. doi: 10.1680/jmacr.18.00452
26. Lim S, Mondal P (2014) Micro- and Nano-scale Characterization to Study the Thermal Degradation of Cement-based Materials. Materials Characterization 92: 15. doi: 10.1016/j.matchar.2014.02.010
27. Huixia Wu, Jianguang Xu, Dingyi Yang et al. (2021) Utilizing thermal activation treatment to improve the properties of waste cementitious powder and its newmade cementitious materials. Journal of Cleaner Production 322: 129074. doi: 10.1016/j.jclepro.2021.129074
28. Zhiming Ma, Jiaxin Shen, Huixia Wu et al. (2022) Properties and activation modification of eco-friendly cementitious materials incorporating high-volume hydrated cement powder from construction waste. Construction and Building Materials 316: 125788. doi: 10.1016/j.conbuildmat.2021.125788
29. Sui Y, Ou C, Liu S et al. (2020) Study on Properties of Waste Concrete Powder by Thermal Treatment and Application in Mortar. Applied Sciences 10(3): 998. doi: 10.3390/app10030998
30. Kalinowska-Wichrowska K, Kosior-Kazberuk M, Pawluczuk E (2019) The Properties of Composites with Recycled Cement Mortar Used as a Supplementary Cementitious Material. Materials (Basel, Switzerland) 13(1). doi: 10.3390/ma13010064
31. Zhou J, Lu D, Yang Y et al. (2020) Physical and Mechanical Properties of HighStrength Concrete Modified with Supplementary Cementitious Materials after Exposure to Elevated Temperature up to 1000 °C. Materials (Basel, Switzerland) 13(3). doi: 10.3390/ma13030532
32. Ali MH, Dinkha YZ, Haido JH (2017) Mechanical properties and spalling at elevated temperature of high performance concrete made with reactive and waste inert powders. Engineering Science and Technology, an International Journal 20(2): 536–541. doi: 10.1016/j.jestch.2016.12.004

33. Abed M, Brito J de (2020) Evaluation of high-performance self-compacting concrete using alternative materials and exposed to elevated temperatures by non-destructive testing. Journal of Building Engineering 32: 101720. doi: 10.1016/j.jobe.2020.101720
34. Dossena MH, Bevilaqua D, Silva LL et al. (2019) Evaluation of Mechanical Properties of Sealing Mortar with Partial Replacement of Portland Cement by Stone Crusher Waste. Mat. Res. 22(suppl 1). doi: 10.1590/1980-5373-mr-2018-0868
35. Pereira MC, Soares A, Flores-Colen I et al. (2020) Influence of Exposure to Elevated Temperatures on the Physical and Mechanical Properties of Cementitious Thermal Mortars. Applied Sciences 10(6): 2200. doi: 10.3390/app10062200
36. Ripani M, Xargay H, Iriarte I et al. (2020) Thermal Action on Normal and High Strength Cement Mortars. Applied Sciences 10(18): 6455. doi: 10.3390/app10186455
37. He Z, Zhu X, Wang J et al. (2019) Comparison of CO2 emissions from OPC and recycled cement production. Construction and Building Materials 211: 965–973. doi: 10.1016/j.conbuildmat.2019.03.289
38. Wang W, Wu H, Ma Z et al. (2020) Using Eco-Friendly Recycled Powder from CDW to Prepare Strain Hardening Cementitious Composites (SHCC) and Properties Determination. Materials (Basel, Switzerland) 13(5). doi: 10.3390/ma13051143
39. Kaliyavaradhan SK, Ling T-C, Mo KH (2020) Valorization of waste powders from cement-concrete life cycle: A pathway to circular future. Journal of Cleaner Production 268: 122358. doi: 10.1016/j.jclepro.2020.122358
40. Zhang Q, Ye G (2011) Microstructure Analysis of Heated Portland Cement Paste. Procedia Engineering 14: 830–836. doi: 10.1016/j.proeng.2011.07.105
41. Locher FW (2006) Cement: principles of production and use. Verlag Bau+ Technik GmbH, Düsseldorf
42. Lea FM, Desch CH (1956) The Chemistry of Cement and Concrete. Revised Edition, by FM Lea. Edward Arnold
43. Kurdowski W (2014) Cement and concrete chemistry. Springer Science & Business, New York
44. Hewlett P, Liska M (2019) Lea's chemistry of cement and concrete. Butterworth-Heinemann
45. Chatterjee AK (2018) Cement Production Technology. Principles and Practice. Taylor & Francis Group
46. Bye G (2011) Portland Cement, 3rd. ICE Publishing, London
47. Taylor HFW (1997) Cement Chemistry, 2nd. Thomas Telford, London
48. B.Kohlhaas (1983) Cement Engineers' Handbook, 4th. Bauverlag GmbH, Berlin
49. Li Z (2011) Advanced concrete technology. John Wiley & Sons, Hoboken N.J.
50. Aïtcin PC, Flatt RJ (2016) Science and Technology of Concrete Admixtures. Woodhead Publishing
51. Ghosh SN (2003) Advances in cement technology: chemistry, manufacture and testing. 81883050
52. Brunauer S, Le Copeland (1964) The chemistry of concrete. Scientific American 210(4): 80–93
53. MacLaren DC, White MA (2003) Cement: Its chemistry and properties. Journal of Chemical Education 80(6): 623
54. van Oss HG, Padovani AC (2002) Cement manufacture and the environment: part I: chemistry and technology. Journal of Industrial Ecology 6(1): 89–105
55. Bapat JD (2012) Mineral admixtures in cement and concrete. CRC Press
56. Ludwig H-M, Zhang W (2015) Research review of cement clinker chemistry. Cement and Concrete Research 78: 24–37

57. Ghosh SN (1991) Cement and concrete science and technology. Thomas Telford
58. Gan MS (1997) Cement and concrete. CRC Press
59. Sorrentino F (2011) Chemistry and engineering of the production process: State of the art. Cement and Concrete Research 41(7): 616–623
60. Herfort D, Moir GK, Johansen V et al. (2010) The chemistry of Portland cement clinker. Advances in Cement Research 22(4): 187–194
61. Aragaw TA (2018) Concise Introduction to Cement Chemistry and Manufacturing. Morgan & Claypool, San Rafael, California (USA)
62. Duggal SK (2008) Building Materials, 3rd. New Age International (P) Ltd.
63. Pöllmann H (2017) Cementitious Materials Composition, Properties, Application. Walter de Gruyter GmbH, Berlin, Boston
64. Brouwers HJH (2004) The work of Powers and Brownyard revisited: Part 1. Cement and Concrete Research 34(9): 1697–1716
65. Bensted J, Barnes P (2002) Structure and Performance of Cements, 2nd. CRC Press
66. Stark J, Bollmann K (2000) Delayed ettringite formation in concrete. NORDIC CONCRETE RESEARCH-PUBLICATIONS- 23: 4–28
67. Odler I, Wonnemann R (1983) Effect of alkalies on portland cement hydration II. Alkalies present in form of sulphates. Cement and Concrete Research 13(6): 771–777
68. Williams PT (1983) Proceedings of the seventh international congress on the chemistry of cement, paris 1980, vols. i and iv: Published by Editions Septima, 14 rue Falguière, 75015, Paris, France
69. Odler I, Abdul-Maula S (1987) Investigations on the relationship between porosity structure and strength of hydrated portland cement pastes III. Effect of clinker composition and gypsum addition. Cement and Concrete Research 17(1): 22–30
70. Beaudoin JJ, Ramachandran VS (1992) A new perspective on the hydration characteristics of cement phases. Cement and Concrete Research 22(4): 689–694
71. Tazawa E, Miyazawa S (1995) Influence of cement and admixture on autogenous shrinkage of cement paste. Cement and Concrete Research 25(2): 281–287
72. Bentz DP, Garboczi EJ, Haecker CJ et al. (1999) Effects of cement particle size distribution on performance properties of Portland cement-based materials. Cement and Concrete Research 29(10): 1663–1671
73. Odler I (1991) Strength of cement. Mater Struct 24(2): 143–157
74. Jons ES, Osbaeck B (1982) The effect of cement composition on strength described by a strength-porosity model. Cement and Concrete Research 12(2): 167–178
75. Jawed I, Skalny J (1978) Alkalies in cement: a review: II. Effects of alkalies on hydration and performance of Portland cement. Cement and Concrete Research 8(1): 37–51
76. Richartz W (1986) Einfluß des K2O-Gehalts und des Sulfatisierungsgrads auf Erstarren und Erhärten des Zements. ZKG international 39(12): 678–687
77. Abdul-Maula S, Odler I (1982) Effect of oxidic composition on hydration and strength development of laboratory-made Portland cements. World Cement 13: 216
78. Osbaeck B (1979) Influence of alkalis on the strength of portland cement. Zem.-Kalk-Gips 32(2): 72–77
79. Soroka I, Abayneh M (1986) Effect of gypsum on properties and internal structure of PC paste. Cement and Concrete Research 16(4): 495–504
80. Myrdal R (2007) Accelerating admixtures for concrete. State of the art. 82536098
81. Gartner EM, Young JF, Da Damidot et al. (2002) Hydration of Portland cement. Structure and performance of cements 2: 57–113
82. Kubens S (2010) Interaction of cement and admixtures and its influence on rheological properties. Cuvillier Verlag

83. Skripkiunas G, Yakovlev G, Karpova E et al. (2019) Hydration process and physical properties of cement systems modified by calcium chloride and multi-walled carbon nanotubes. Revista Romana de Materiale 49(1): 58–67
84. Li Q (2015) Chemical composition and microstructure of hydration products of hardened white portland cement pastes containing admixtures. Journal of Wuhan University of Technology-Mater. Sci. Ed. 30(4): 758–767
85. Dorn T, Blask O, Stephan D (2022) Acceleration of cement hydration–A review of the working mechanisms, effects on setting time, and compressive strength development of accelerating admixtures. Construction and Building Materials 323: 126554
86. Bertola F, Gastaldi D, Irico S et al. (2022) Influence of the amount of calcium sulfate on physical/mineralogical properties and carbonation resistance of CSA-based cements. Cement and Concrete Research 151: 106634
87. Neto, José da Silva Andrade, Angeles G, Kirchheim AP (2021) Effects of sulfates on the hydration of Portland cement–A review. Construction and Building Materials 279: 122428
88. Weeks C, Hand RJ, Sharp JH (2008) Retardation of cement hydration caused by heavy metals present in ISF slag used as aggregate. Cement and Concrete Composites 30(10): 970–978
89. Cheung J, Jeknavorian A, Roberts L et al. (2011) Impact of admixtures on the hydration kinetics of Portland cement. Cement and Concrete Research 41(12): 1289–1309
90. Olmo IF, Chacon E, Irabien A (2001) Influence of lead, zinc, iron (III) and chromium (III) oxides on the setting time and strength development of Portland cement. Cement and Concrete Research 31(8): 1213–1219
91. Tamas FD (1966) Acceleration and retardation of Portland cement hydration by additives. REt EIVED: 392
92. Nochaiya T, Sekine Y, Choopun S et al. (2015) Microstructure, characterizations, functionality and compressive strength of cement-based materials using zinc oxide nanoparticles as an additive. Journal of Alloys and Compounds 630: 1–10
93. Aggoun S, Cheikh-Zouaoui M, Chikh N et al. (2008) Effect of some admixtures on the setting time and strength evolution of cement pastes at early ages. Construction and Building Materials 22(2): 106–110
94. Young JF (1972) A review of the mechanisms of set-retardation in Portland cement pastes containing organic admixtures. Cement and Concrete Research 2(4): 415–433
95. Arliguie G, Ollivier JP, Grandet J (1982) Study on the retarding effect of zinc on the hydration of portland-cement paste. Cement and Concrete Research 12(1): 79–86
96. Thomas NL, Jameson DA, Double DD (1981) The effect of lead nitrate on the early hydration of Portland cement. Cement and Concrete Research 11(1): 143–153
97. Mehdipour I, Khayat KH (2017) Effect of particle-size distribution and specific surface area of different binder systems on packing density and flow characteristics of cement paste. Cement and Concrete Composites 78: 120–131
98. Zhang YM, Napier-Munn TJ (1995) Effects of particle size distribution, surface area and chemical composition on Portland cement strength. Powder Technology 83(3): 245–252
99. Hu J, Ge Z, Wang K (2014) Influence of cement fineness and water-to-cement ratio on mortar early-age heat of hydration and set times. Construction and Building Materials 50: 657–663. doi: 10.1016/j.conbuildmat.2013.10.011
100. Ke X, Hou H, Zhou M et al. (2015) Effect of particle gradation on properties of fresh and hardened cemented paste backfill. Construction and Building Materials 96: 378–382
101. Ritzmann H (1968) On the Relation between the Particle Size Distribution and the Strength of Portland Cement. Zement-Kalk-Gips

102. Zhu BL, Huang X, Guo Y Influence of Cement Particle Size Distribution on Strength of Cement Paste. In: Advanced Materials Research. Trans Tech Publ, pp 1007–1011
103. Celik IB (2009) The effects of particle size distribution and surface area upon cement strength development. Powder Technology 188(3): 272–276
104. Wong HH, Kwan AKH (2008) Rheology of cement paste: role of excess water to solid surface area ratio. J. Mater. Civ. Eng. 20(2): 189–197
105. Wyrzykowski M, McDonald PJ, Scrivener KL et al. (2017) Water redistribution within the microstructure of cementitious materials due to temperature changes studied with 1H NMR. J. Phys. Chem. C 121(50): 27950–27962
106. Zheng S, Liu T, Jiang G et al. (2021) Effects of Water-to-Cement Ratio on Pore Structure Evolution and Strength Development of Cement Slurry Based on HYMOSTRUC3D and Micro-CT. Applied Sciences 11(7): 3063
107. Jennings HM, Bullard JW, Thomas JJ et al. (2008) Characterization and modeling of pores and surfaces in cement paste: correlations to processing and properties. ACT 6(1): 5–29
108. Jantasuto O, Wiwattanachang N, Youngsukasem N (2021) Relationship between Porosity & Compressive Strength of Concrete with Variable W/C Ratio. UTK RESEARCH JOURNAL 15(1): 74–82
109. Bede A, Ardelean I Revealing the influence of water-cement ratio on the pore size distribution in hydrated cement paste by using cyclohexane. In: AIP conference proceedings. AIP Publishing LLC, p 40002
110. Tracz T (2016) Open porosity of cement pastes and their gas permeability. Bulletin of the Polish Academy of Sciences: Technical Sciences 64(4)
111. Singh SB, Munjal P, Thammishetti N (2015) Role of water/cement ratio on strength development of cement mortar. Journal of Building Engineering 4: 94–100
112. Zhutovsky S, Kovler K Effect of water to cement ratio and degree of hydration on chemical shrinkage of cement pastes. In: 2nd International RILEM Workshop on Concrete Durability and Service Life Planning, ConcreteLife'09, pp 47–54
113. Sideris KK, Konsta-Gdoutos M (1996) Influence of the water to cement ratio W/C on the compressive strength of concrete—An application of the cement hydration equation to concrete. Applied Composite Materials 3(5): 335–343
114. Hranice C (2002) The effect of water ratio on microstructre and composition of the hydration products of Portland cement pastes. Ceramics− Silikáty 46(4): 152–158
115. Lothenbach B, Winnefeld F, Alder C et al. (2007) Effect of temperature on the pore solution, microstructure and hydration products of Portland cement pastes. Cement and Concrete Research 37(4): 483–491
116. Lu B, Drissi S, Liu J et al. (2022) Effect of temperature on CO2 curing, compressive strength and microstructure of cement paste. Cement and Concrete Research 157: 106827
117. Gallucci E, Zhang X, Scrivener KL (2013) Effect of temperature on the microstructure of calcium silicate hydrate (CSH). Cement and Concrete Research 53: 185–195
118. Kjellsen KO, Detwiler RJ, Gjørv OE (1991) Development of microstructures in plain cement pastes hydrated at different temperatures. Cement and Concrete Research 21(1): 179–189
119. Murray SJ, Subramani VJ, Selvam RP et al. (2010) Molecular Dynamics to Understand the Mechanical Behavior of Cement Paste. Transportation Research Record 2142(1): 75–82. doi: 10.3141/2142-11
120. Pellenq RJ-M, van Damme H (2004) Why does concrete set?: The nature of cohesion forces in hardened cement-based materials. Mrs Bulletin 29(5): 319–323

121. Yang M, Jennings HM (1995) Influences of mixing methods on the microstructure and rheological behavior of cement paste. Advanced cement based materials 2(2): 70–78
122. Jiang SP, Mutin JC, Nonat A (1995) Studies on mechanism and physico-chemical parameters at the origin of the cement setting. I. The fundamental processes involved during the cement setting. Cement and Concrete Research 25(4): 779–789
123. Barbara Lothenbach, André Nonat (2015) Calcium silicate hydrates: Solid and liquid phase composition. Cement and Concrete Research 78: 57–70. doi: 10.1016/j.cemconres.2015.03.019
124. Gauffinet-Garrault S (2012) The rheology of cement during setting. In: Nicolas Roussel (ed) Understanding the Rheology of Concrete. Woodhead Publishing, pp 96–113
125. Gartner E, Maruyama I, Chen J (2017) A new model for the C-S-H phase formed during the hydration of Portland cements. Cement and Concrete Research 97: 95–106. doi: 10.1016/j.cemconres.2017.03.001
126. Stark J (2011) Recent advances in the field of cement hydration and microstructure analysis. Cement and Concrete Research 41(7): 666–678. doi: 10.1016/j.cemconres.2011.03.028
127. Scrivener K, Ouzia A, Juilland P et al. (2019) Advances in understanding cement hydration mechanisms. Cement and Concrete Research 124: 105823. doi: 10.1016/j.cemconres.2019.105823
128. Pinson MB, Masoero E, Bonnaud PA et al. (2015) Hysteresis from multiscale porosity: modeling water sorption and shrinkage in cement paste. Physical Review Applied 3(6): 64009
129. Powers TC (1958) Structure and physical properties of hardened Portland cement paste. J Am Ceram Soc 41(1): 1–6
130. Hansen TC (1986) Physical structure of hardened cement paste. A classical approach. Mater Struct 19(6): 423–436
131. Hansen TC, Radjy F, Sellevold EJ (1973) Cement Paste and Concrete. Annual Review of Management Science 3
132. Jambor J (1990) Pore structure and strength development of cement composites. Cement and Concrete Research 20(6): 948–954. doi: 10.1016/0008-8846(90)90058-6
133. Jambor J Influence of water–cement ratio on the structure and strength of hardened cement pastes. In: Proceedings of a conference held at university of sheffield (1976), pp 8–9
134. Taylor HFW (1977) Discussion of the paper “Microstructure and strength of hydrated cements”. Cem. Concr. Res. 7. doi: 10.1016/0008-8846(77)90077-1
135. Mindess S (1970) Relation between the compressive strength and porosity of autoclaved calcium silicate hydrates. J Am Ceram Soc 53(11): 621–624
136. Mindess S (1984) Relationships between strength and microstructure for cement-based materials: an overview. MRS Online Proceedings Library (OPL) 42
137. Jambor, J., ‘Pore structure and strengths of hardened cement pastes’, in Proceedings of 8th ICCC, Rio de Janeiro, 1986, Vol. III, pp. 363–368
138. Odler I, Rößler M (1985) Investigations on the relationship between porosity, structure and strength of hydrated Portland cement pastes. II. Effect of pore structure and of degree of hydration. Cement and Concrete Research 15(3): 401–410
139. Beaudoin JJ, Feldman RF, Tumidajski PJ (1994) Pore structure of hardened Portland cement pastes and its influence on properties. Advanced cement based materials 1(5): 224–236
140. Jambor J (ed) (1973) Pore Structure and Properties of Materials, vol 2

141. Takahashi T, Yamamoto M, Ioku K et al. (1997) Relationship between compressive strength and pore structure of hardened cement pastes. Advances in Cement Research 9(33): 25–30
142. Jin S, Zhao X, Tai Y et al. (2022) Multiscale model for the scale effect of tensile strength of hardened cement paste based on pore size distribution. Construction and Building Materials 325
143. Nadeau JS, Mindess S, Hay JM (1974) Slow crack growth in cement paste. J Am Ceram Soc 57(2): 51–54
144. Baldie KD, Pratt PL (1985) Crack growth in hardened cement paste. MRS Online Proceedings Library (OPL) 64
145. Brown JH (1972) Measuring the fracture toughness of cement paste and mortar. Magazine of Concrete Research 24(81): 185–196
146. Cotterell B, Mai Y-W (1987) Crack growth resistance curve and size effect in the fracture of cement paste. J Mater Sci 22(8): 2734–2738
147. Struble LJ, Stutzman PE, Fuller Jr ER (1989) Microstructural aspects of the fracture of hardened cement paste. J Am Ceram Soc 72(12): 2295–2299
148. Ahmed A, Struble L (1994) Effects of Microstructure on Fracture Behavior of Hardened Cement Paste. MRS Online Proceedings Library (OPL) 370
149. Pavlík Z, Trník A, Kulovaná T et al. (2016) DSC and TG Analysis of a Blended Binder Based on Waste Ceramic Powder and Portland Cement. Int J Thermophys 37(3): 32. doi: 10.1007/s10765-016-2043-3
150. Zhou Q, Glasser FP (2001) Thermal stability and decomposition mechanisms of ettringite at< 120 C. Cement and Concrete Research 31(9): 1333–1339
151. Gabrovšek R, Vuk T, Kaučič V (2006) Evaluation of the hydration of Portland cement containing various carbonates by means of thermal analysis. Acta Chim. Slov 53(2): 159–165
152. Shimada Y, Young JF (2001) Structural changes during thermal dehydration of ettringite. Advances in Cement Research 13(2): 77–81
153. Kaufmann J, Winnefeld F, Lothenbach B (2016) Stability of ettringite in CSA cement at elevated temperatures. Advances in Cement Research 28(4): 251–261. doi: 10.1680/jadcr.15.00029
154. Perraki M, Perraki T, Kolovos K et al. (2002) Secondary raw materials in cement industry. J Therm Anal Calorim 70(1): 143–150
155. Han J, Wang K, Shi J et al. (2015) Mechanism of triethanolamine on Portland cement hydration process and microstructure characteristics. Construction and Building Materials 93: 457–462
156. Zhang Z, Du J, Shi M (2022) Quantitative Analysis of the Calcium Hydroxide Content of EVA-Modified Cement Paste Based on TG-DSC in a Dual Atmosphere. Materials (Basel, Switzerland) 15(7): 2660
157. Sha W, Pereira GB (2001) Differential scanning calorimetry study of ordinary Portland cement paste containing metakaolin and theoretical approach of metakaolin activity. Cement and Concrete Composites 23(6): 455–461
158. Vogler N, Drabetzki P, Lindemann M et al. (2022) Description of the concrete carbonation process with adjusted depth-resolved thermogravimetric analysis. J Therm Anal Calorim 147(11): 6167–6180
159. Zhang Q, Ye G (2012) Dehydration kinetics of Portland cement paste at high temperature. J Therm Anal Calorim 110(1): 153–158. doi: 10.1007/s10973-012-2303-9
160. Tantawy MA (2017) Effect of High Temperatures on the Microstructure of Cement Paste. MSCE 05(11): 33–48. doi: 10.4236/msce.2017.511004

161. Almeida AEFdS, Sichieri EP (2006) Thermogravimetric analyses and mineralogical study of polymer modified mortar with silica fume. Mat. Res. 9: 321–326
162. Gad EAA, Habib AO, Mousa MM (2018) Understanding the mechanism of decomposition reactions of neat and superplasticized ordinary Portland cement pastes using thermal analysis. Epitoanyag-Journal of Silicate Based & Composite Materials 70(3)
163. Jia F, Yao Y, Wang J (2021) Influence and Mechanism Research of Hydration Heat Inhibitor on Low-Heat Portland Cement. Frontiers in Materials: 187
164. Pacewska B, Wilińska I (2020) Usage of supplementary cementitious materials: advantages and limitations. J Therm Anal Calorim 142(1): 371–393
165. Amer AA, El-Hoseny SM (2017) Hydration Kinetics and Fire Resistance of Recycled Low Grade Alumino-Silicate Refractory Bricks Waste-Metakaolin Composite Cement Pastes. micron 12(13.60): 12–80
166. Boualleg S (2021) The Study of Slag Cement's Microstructural Properties
167. Real S, Carriço A, Bogas JA et al. (2020) Influence of the Treatment Temperature on the Microstructure and Hydration Behavior of Thermoactivated Recycled Cement. Materials (Basel, Switzerland) 13(18): 3937. doi: 10.3390/ma13183937
168. Araújo Jr. AG de, Da Silva LJ, Panzera TH et al. (2016) Hydration and Dehydration of High Initial Strength Portland Cement Type CP V - ARI. MSF 869: 106–111. doi: 10.4028/www.scientific.net/MSF.869.106
169. Peng G-F, Huang Z-S (2008) Change in microstructure of hardened cement paste subjected to elevated temperatures. Construction and Building Materials 22(4): 593–599. doi: 10.1016/j.conbuildmat.2006.11.002
170. Zhang Q, Ye G (2013) Quantitative analysis of phase transition of heated Portland cement paste. J Therm Anal Calorim 112(2): 629–636
171. Ouyang SX (1986) Study on a series of characteristics of C–S–H system. Ph. D. Thesis, School of Material Science and Engineering, Wuhan University …
172. Sun T, Shui ZH, Huo T (2011) Rehydration performance of binary binders made with dehydrated cement paste and phosphogypsum. Key Engineering Materials: 1238–1242
173. Bogas JA, Carriço A, Pereira MF (2019) Mechanical characterization of thermal activated low-carbon recycled cement mortars. Journal of Cleaner Production 218: 377–389
174. Vyšvařil M, Bayer P, Chromá M et al. (2014) Physico-mechanical and microstructural properties of rehydrated blended cement pastes. Construction and Building Materials 54: 413–420. doi: 10.1016/j.conbuildmat.2013.12.021
175. Splittgerber F, Mueller A (2003) Inversion of the cement hydration as a new method for identification and/or recycling. International congress on the chemistry of cement: 1282–1290
176. Li Y, Luo Y, Du H et al. (2022) Evolution of Microstructural Characteristics of Carbonated Cement Pastes Subjected to High Temperatures Evaluated by MIP and SEM. Materials (Basel, Switzerland) 15(17): 6037
177. Heikal M, Ali AI, Ismail MN et al. (2014) Behavior of composite cement pastes containing silica nano-particles at elevated temperature. Construction and Building Materials 70: 339–350. doi: 10.1016/j.conbuildmat.2014.07.078
178. Heikal M (2000) Effect of temperature on the physico-mechanical and mineralogical properties of Homra pozzolanic cement pastes. Cement and Concrete Research 30(11): 1835–1839
179. Heikal M (2008) Effect of elevated temperature on the physico-mechanical and microstructural properties of blended cement pastes. Building Research Journal 56(2): 157–172

180. Wang W, Liu X, Guo L et al. (2019) Evaluation of Properties and Microstructure of Cement Paste Blended with Metakaolin Subjected to High Temperatures. Materials (Basel, Switzerland) 12(6). doi: 10.3390/ma12060941
181. Heikal M, Al-Duaij OK, Ibrahim NS (2015) Microstructure of composite cements containing blast-furnace slag and silica nano-particles subjected to elevated thermally treatment temperature. Construction and Building Materials 93: 1067–1077
182. El-Gamal SM, Abo-El-Enein SA, El-Hosiny FI et al. (2018) Thermal resistance, microstructure and mechanical properties of type I Portland cement pastes containing low-cost nanoparticles. J Therm Anal Calorim 131(2): 949–968
183. Lin R-S, Han Y, Wang X-Y (2021) Macro–meso–micro experimental studies of calcined clay limestone cement (LC3) paste subjected to elevated temperature. Cement and Concrete Composites 116: 103871
184. Weerdt K de, Haha MB, Le Saout G et al. (2011) Hydration mechanisms of ternary Portland cements containing limestone powder and fly ash. Cement and Concrete Research 41(3): 279–291
185. Memon SA, Shah SFA, Khushnood RA et al. (2019) Durability of sustainable concrete subjected to elevated temperature–A review. Construction and Building Materials 199: 435–455
186. Wang D, Noguchi T, Nozaki T et al. (2021) Investigation on the fast carbon dioxide sequestration speed of cement-based materials at 300° C–700° C. Construction and Building Materials 291: 123392
187. Jia Z, Chen C, Shi J et al. (2019) The microstructural change of CSH at elevated temperature in Portland cement/GGBFS blended system. Cement and Concrete Research 123: 105773
188. Beuvier T, Bardeau J-F, Calvignac B et al. (2013) Phase transformations in CaCO3/iron oxide composite induced by thermal treatment and laser irradiation. Journal of Raman Spectroscopy 44(3): 489–495
189. Seifert S, Liesch A-L, Thome V et al. (2018) Application of recycled waste material for the production of autoclaved aerated concrete. ce/papers 2(4): 495–502
190. Pacheco-Torgal F, Ding Y (2013) Handbook of recycled concrete and demolition waste. Elsevier
191. Ong KG, Akbarnezhad A (2014) Microwave-assisted concrete technology: production, demolition and recycling. CRC Press
192. American Concrete Pavement Association (2009) Recycling concrete pavements. ACPA
193. Hoffmann Sampaio C, Cazacliu BG, Ambrós WM et al. (2020) Demolished concretes recycling by the use of pneumatic jigs. Waste Management & Research 38(4): 392–399
194. Makul N, Fediuk R, Amran M et al. (2021) Design strategy for recycled aggregate concrete: A review of status and future perspectives. Crystals 11(6): 695
195. Everaert M, Stein R, Michaux S et al. (2019) Microwave radiation as a pre-treatment for standard and innovative fragmentation techniques in concrete recycling. Materials (Basel, Switzerland) 12(3): 488
196. Silva RV, Brito J de, Dhir RK (2014) Properties and composition of recycled aggregates from construction and demolition waste suitable for concrete production. Construction and Building Materials 65: 201–217
197. van de Wouw PM, Florea MV, Brouwers HJ Quantification of concrete aggregate liberation through abrasion comminution. In: 9th International Symposium on Cement and Concrete (ISCC 2017), 31 October-3 November 2017, Wuhan, China, pp 1–8

198. Aytekin B, Mardani-Aghabaglou A (2022) Sustainable Materials: A Review of Recycled Concrete Aggregate Utilization as Pavement Material. Transportation Research Record 2676(3): 468–491
199. Shima H, Tateyashiki H, Matsuhashi R et al. (2005) An advanced concrete recycling technology and its applicability assessment through input-output analysis. ACT 3(1): 53–67
200. Xing W (2004) Quality improvement of granular secondary raw building materials by separation and cleansing techniques. PhD Dissertation, Technical University of Delft, Netherlands
201. Alexandru T, Marinela B, Laura D et al. (2019) Mechanical and Environmental Performances of Concrete Using Recycled Materials. Procedia Manufacturing 32: 253–258. doi: 10.1016/j.promfg.2019.02.211
202. Gebremariam AT, Di Maio F, Vahidi A et al. (2020) Innovative technologies for recycling End-of-Life concrete waste in the built environment. Resources, Conservation and Recycling 163: 104911. doi: 10.1016/j.resconrec.2020.104911
203. Nikmehr B, Al-Ameri R (2022) A State-of-the-Art Review on the Incorporation of Recycled Concrete Aggregates in Geopolymer Concrete. Recycling 7(4): 51. doi: 10.3390/recycling7040051
204. Schenk KJ (2011) Patent No. WO 2011 142663
205. Seifert S, Thome V, Karlstetter C (2014) Elektrodynamische Fragmentierung. Eine Technologie zur effektiven Aufbereitung von Abfallströmen. Recycling und Rohstoffe 7: 431–438
206. Noguchi T (2010) Toward sustainable resource recycling in concrete society. In: Proceedings of the 2nd International Conference on Sustainable Construction Materials and Technologies, pp 321–334
207. Mindess S, Young JF, Darwin D (2003) Concrete, 2nd Edition. New Jersey , Pearson Education
208. Tam VWY, Tam CM, Le KN (2007) Removal of cement mortar remains from recycled aggregate using pre-soaking approaches. Resources, Conservation and Recycling 50(1): 82–101
209. Akbarnezhad A, Ong KC, Zhang MH et al. (2013) Acid treatment technique for determining the mortar content of recycled concrete aggregates. ASTM International
210. Akbarnezhad A, Ong KC, Zhang MH et al. (2011) Microwave-assisted beneficiation of recycled concrete aggregates. Construction and Building Materials 25(8): 3469–3479
211. Brouwer P (2006) Theory of XRF. Almelo, Netherlands: PANalytical BV
212. Scientific TF (2020) XRF technology
213. Scrivener K, Snellings R, Lothenbach B (2016) A practical guide to microstructural analysis of cementitious materials, vol 540. Crc Press Boca Raton, FL, USA
214. Speakman SA (2011) Basics of X-ray powder diffraction. Massachusetts-USA, 2011a. Disponível em:< http://prism. mit. edu/xray/Basics% 20of% 20X-Ray% 20Powder% 20Diffraction. pdf
215. Giesche H (2006) Mercury Porosimetry: A General (Practical) Overview. Part. Part. Syst. Charact. 23(1): 9–19. doi: 10.1002/ppsc.200601009
216. Abell, Willis, Lange (1999) Mercury Intrusion Porosimetry and Image Analysis of Cement-Based Materials. Journal of colloid and interface science 211(1): 39–44. doi: 10.1006/jcis.1998.5986
217. Berodier E, Bizzozero J, Muller ACA (2016) Mercury intrusion porosimetry. A practical guide to microstructural analysis of cementitious materials 419

218. Ma H (2014) Mercury intrusion porosimetry in concrete technology: tips in measurement, pore structure parameter acquisition and application. J Porous Mater 21(2): 207–215. doi: 10.1007/s10934-013-9765-4
219. Guimarães D, Oliveira VA, Leão VA (2016) Kinetic and thermal decomposition of ettringite synthesized from aqueous solutions. J Therm Anal Calorim 124(3): 1679–1689. doi: 10.1007/s10973-016-5259-3
220. Jiang C, Fang J, Chen J-Y et al. (2020) Modeling the instantaneous phase composition of cement pastes under elevated temperatures. Cement and Concrete Research 130: 105987. doi: 10.1016/j.cemconres.2020.105987
221. Mtarfi NH, Rais Z, Taleb M (2017) Effect of clinker free lime and cement fineness on the cement physicochemical properties. J. Mater. Environ. Sci 8(7): 2541–2548
222. Nawaz A, Julnipitawong P, Krammart P et al. (2016) Effect and limitation of free lime content in cement-fly ash mixtures. Construction and Building Materials 102: 515–530
223. Ji X, Ji D, Yang Z et al. (2021) Study on the phase composition and structure of hardened cement paste during heat treatment. Construction and Building Materials 310: 125–267
224. Maddalena R, Hall C, Hamilton A (2019) Effect of silica particle size on the formation of calcium silicate hydrate [C-S-H] using thermal analysis. Thermochimica Acta 672: 142–149. doi: 10.1016/j.tca.2018.09.003
225. Alexandre Bogas J, Carriço A, Real S (2021) Thermoactivated Recycled Cement. In: Sustainable Concrete [Working Title]. IntechOpen
226. Sabeur H, Saillio M, Vincent J (2019) Thermal stability and microstructural changes in 5 years aged cement paste subjected to high temperature plateaus up to 1000 °C as studied by thermal analysis and X-ray diffraction. Heat Mass Transfer 55(9): 2483–2501. doi: 10.1007/s00231-019-02599-w
227. Periyasamy M, Sain S, Mukhopadhyay S et al. (2022) An Investigation into the Influence of α–β Quartz Phase Transition on Banded Iron Ore Comminution. JOM 74(1): 222–233
228. Johnson SE, Song WJ, Cook AC et al. (2021) The quartz α↔ β phase transition: Does it drive damage and reaction in continental crust? Earth and Planetary Science Letters 553: 116622
229. Carl E-R, Liermann H-P, Ehm L et al. (2018) Phase transitions of α-quartz at elevated temperatures under dynamic compression using a membrane-driven diamond anvil cell: Clues to impact cratering? Meteoritics & Planetary Science 53(8): 1687–1695
230. He J, Jusnes KF, Tangstad M (2021) Phase transformation in quartz at elevated temperatures. 2578-0255
231. Shen Y, Hou X, Yuan J et al. (2020) Thermal cracking characteristics of high-temperature granite suffering from different cooling shocks. International Journal of Fracture 225: 153–168
232. Zobnin NN, Torgovets AK, Pikalova IA et al. (2018) Influence of thermal stability of quartz and the particle size distribution of burden materials on the process of electrothermal smelting of metallurgical silicon. Oriental Journal of Chemistry 34(2): 1120
233. Cai Y, Ke H, Dong J et al. (2011) Effects of nano-SiO2 on morphology, thermal energy storage, thermal stability, and combustion properties of electrospun lauric acid/PET ultrafine composite fibers as form-stable phase change materials. Applied Energy 88(6): 2106–2112
234. Wang L, Wang Z, Yang H et al. (1999) The study of thermal stability of the SiO2 powders with high specific surface area. Materials chemistry and physics 57(3): 260–263
235. Davenport P, Ma Z, Nation W et al. (2020) Thermal stability of silica for application in thermal energy storage. AIP Conference Proceedings(1): 160003

236. Gallyamova R, Galyshev S, Musin F et al. (2019) Thermal stability of the carbon fibers with SiO2 coating. MATEC Web of Conferences: 90
237. Tahiri N, Khouchaf L, Elaatmani M et al. (2014) Study of the thermal treatment of SiO2 aggregate. IOP Conference Series(1): 12002
238. Bonne M, Pronier S, Batonneau Y et al. (2010) Surface properties and thermal stability of SiO 2-crystalline TiO 2 nano-composites. Journal of Materials Chemistry 20(41): 9205–9214
239. Wang KY, Liu RX, Zhang L et al. (2019) Preparation and thermal stability of quartz fiber reinforced silicon doped aluminum aerogel composites. IOP Conference Series(1): 12076
240. Patil DS, Anadinni SB, Shivapur AV (2022) Evaporation, Degree Of Hydration, Porosity And Gel/Space Ratio Of Self-Curing Polymer PEG 400 Modified Ordinary Portland Cement Paste. Journal of Applied Science and Engineering 26(3): 303–311
241. Tracz T, Zdeb T (2019) Effect of Hydration and Carbonation Progress on the Porosity and Permeability of Cement Pastes. Materials (Basel, Switzerland) 12(1). doi: 10.3390/ma12010192
242. Latifee ER, Sen D, Kabir MR (2016) Effect of water to cement ratio and age on portland composite cement mortar porosity, strength and evaporation rate. American Journal of Engineering Research,(8): 120–127
243. Gabriel-Wettey FKN, Appiadu-Boakye K, Anewuoh F (2021) Impact of Curing Methods on the Porosity and Compressive Strength of Concrete. Journal of Engineering Research and Reports 20(9): 18–30
244. Chen X, Wu S, Zhou J (2013) Influence of porosity on compressive and tensile strength of cement mortar. Construction and Building Materials 40: 869–874. doi: 10.1016/j.conbuildmat.2012.11.072
245. Prochoń P, Piotrowski T (2016) Bound water content measurement in cement pastes by stoichiometric and gravimetric analyses. Journal of Building Chemistry 1: 18–25

Appendix

Appendix 1. Additional results for the reactivation of hydrated cement powder through thermal treatment.

1.1. XRD phase contents (wt. %) of DhCeP for the hold times of 3h, 5h, and 10h.

Phase	DhCeP 200_3	DhCeP 400_3	DhCeP 600_3	DhCeP 800_3	DhCeP 1000_3	DhCeP 200_5	DhCeP 400_5	DhCeP 600_5	DhCeP 800_5	DhCeP 1000_5	DhCeP 200_10	DhCeP 400_10	DhCeP 600_10	DhCeP 800_10	DhCeP 1000_10
Ettringite $[Ca_6Al_2(SO_4)_3(OH)_{12}\cdot 26H_2O]$															
Portlandite $[Ca(OH)_2]$	23.0%	13.0%	2.0%	0.2%	0.3%	29.0%	17.0%	2.5%	1.0%	0.2%	26.5%	21.0%	2.5%	1.0%	0.1%
Dicalcium Silicate $[Ca_2SiO_4]$	11.0%	26.0%	24.5%	14.5%	64.0%	12.5%	19.0%	31.5%	17.0%	72.0%	14.0%	29.0%	33.0%	38.0%	70.0%
Dicalcium Silicate - Alpha	6.0%	10.0%	65.5%	67.0%	4.5%	2.5%	6.0%	56.0%	60.0%	3.0%	1.0%	1.5%	57.0%	42.5%	8.0%
Hatrurite $[Ca_3SiO_5]$	3.0%	2.0%	6.5%	2.0%		4.0%	2.0%	9.0%	3.0%		2.5%	3.5%	7.0%	2.0%	
Brownmillerite $[Ca_2(Al,Fe)_2O_5]$	0.4%		1.0%	1.0%	3.0%	1.0%	3.5%		2.5%	2.0%			0.2%		2.0%
Tricalcium Aluminate $[Ca_3Al_2O_6]$					0.5%										
Tobermorite (C-S-H) $[Ca_5Si_6O_{16}(OH)_2]$	56.5%	46.0%				50.0%	48.0%				54.5%	42.0%			
Calcite $[CaCO_3]$	0.1%	3.0%	0.4%			1.0%	4.5%	1.0%			1.5%	3.0%	0.3%		
Silicocarnotite $[Ca_5Si_2SO_{12}]$					12.5%										
Calcium Silicide $[CaSi_2]$				0.4%					0.5%	1.0%				0.2%	0.2%
Lime [CaO]				15.0%	15.0%				16.1%	17.0%				16.0%	16.5%
Orthoenstatite $[Mg_2Si_2O_6]$										5.0%					3.0%

1.2. Comparison of XRD patterns of DhCeP resulting from different hold times (1h, 3h, 5h, and 10h) at maximum temperatures for the same dehydration temperatures.

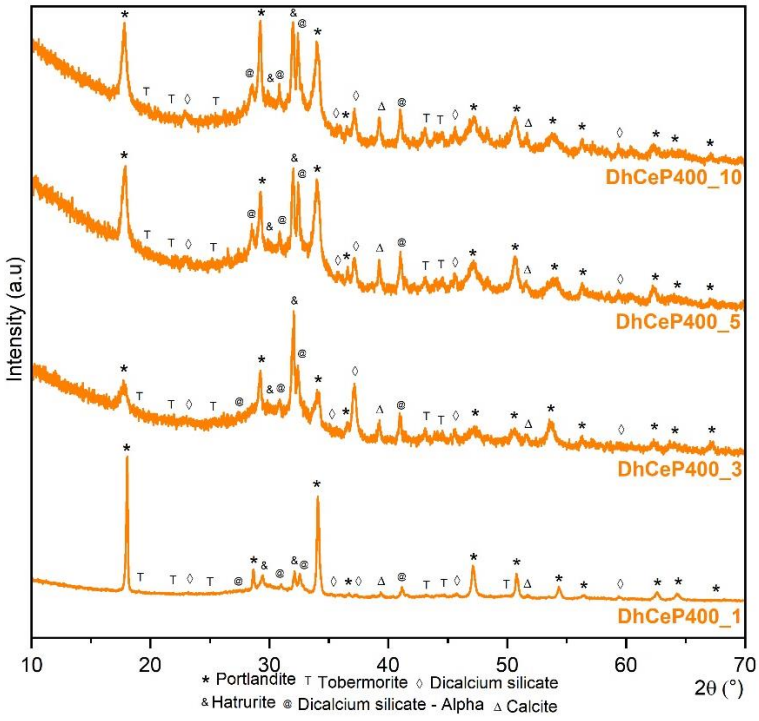

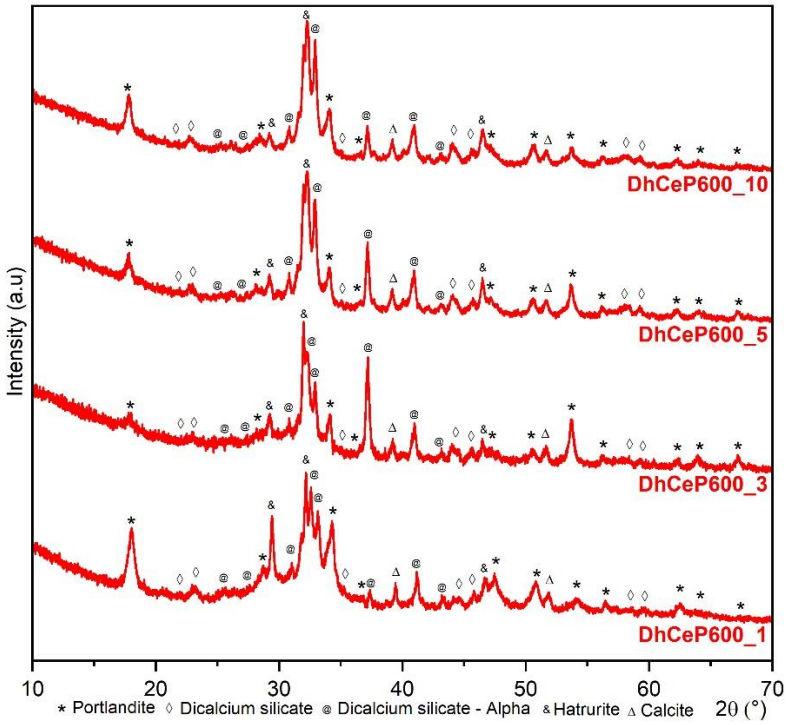

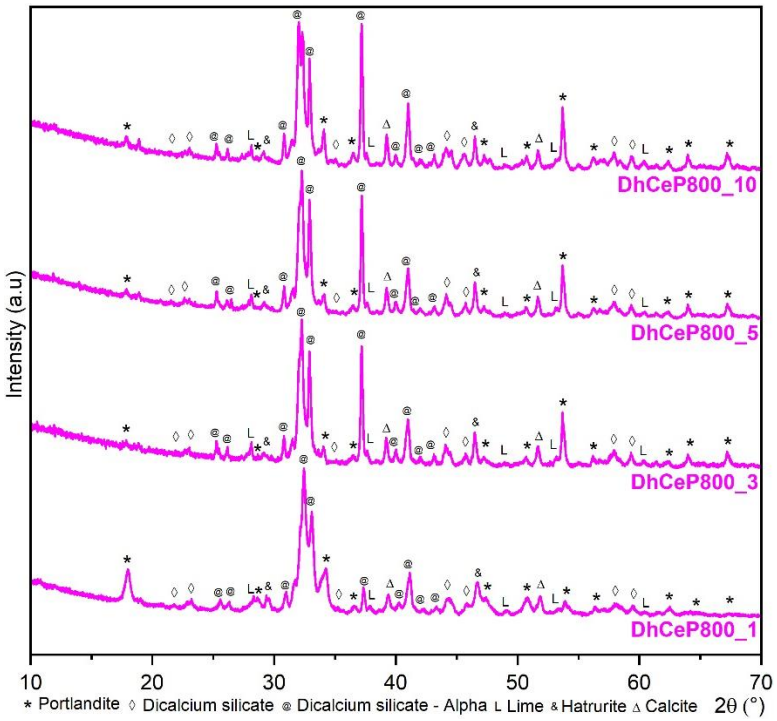

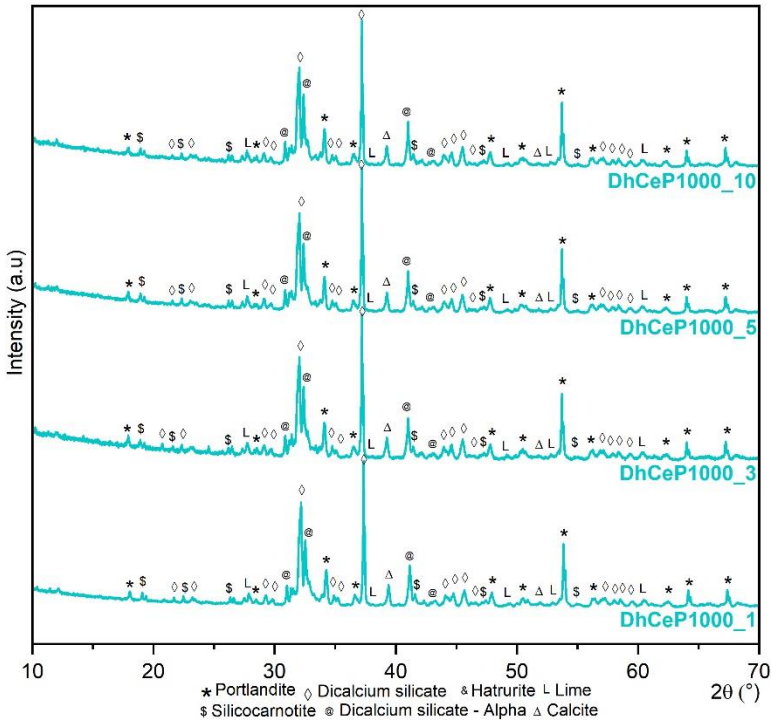

1.3. Comparisons of DSC (mW/mg) and TG (% mass loss) curves of HCeP and DhCeP (D200 to D1000) for the hold times of 3h, 5h, and 10h.

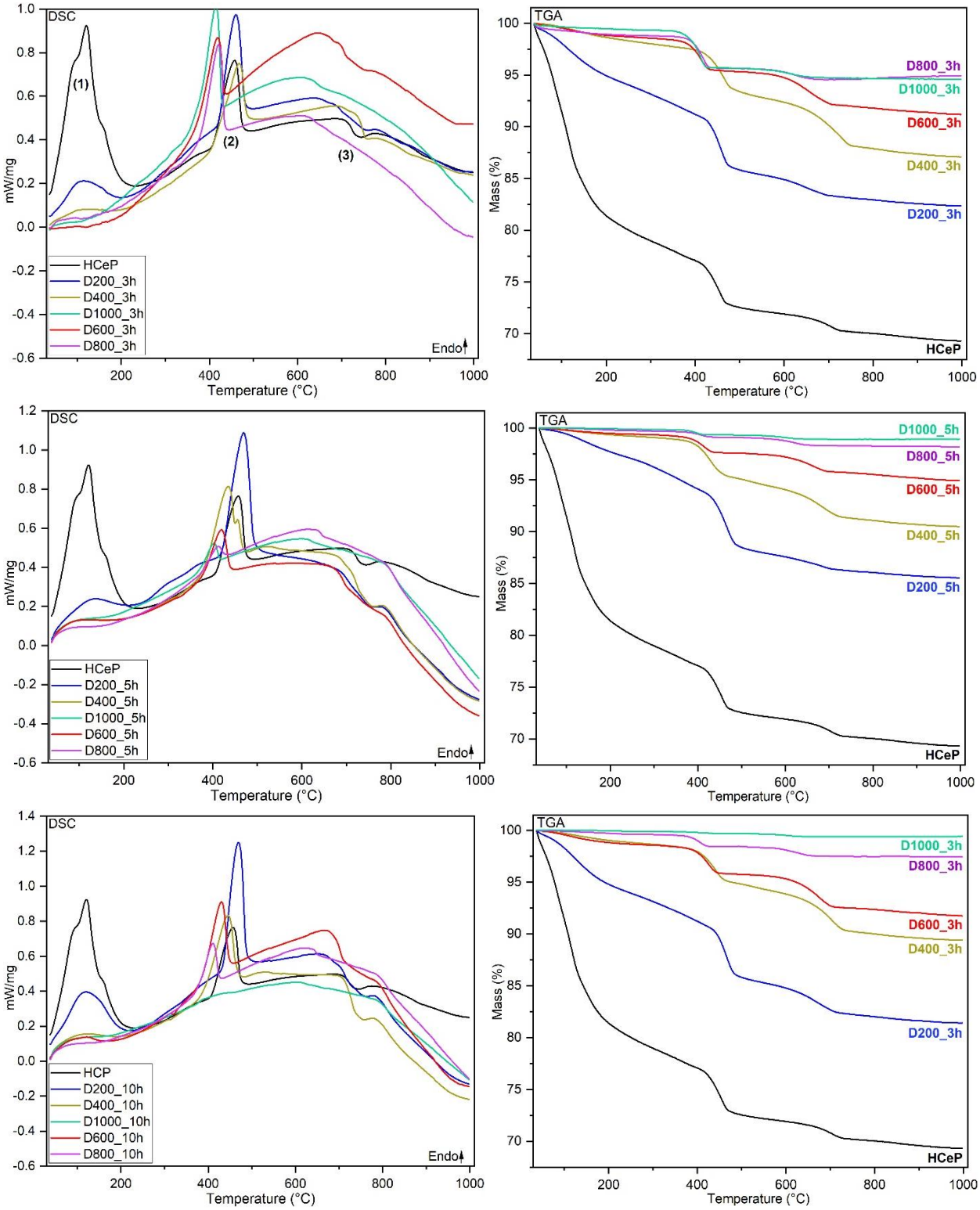

1.4. The DSC - TG peaks and mass loss analyses for the DhCeP for the hold times of 3h, 5h, and 10h.

Sample type	Identified peaks	Peak temperature (± 3°C)	Mass loss section (± 5°C)	Mass loss percentage (± 0.3%)
D200_3h	Peak 1 (C-S-H; Ettringite)	115 °C	85 °C – 150 °C	2.5%
	Peak 2 ($Ca(OH)_2$)	460 °C	445 °C – 475 °C	3.0%
	Peak 3 ($CaCO_3$)	650 °C	625 °C – 675 °C	1.0%
D400_3h	Peak 1 (non-identified)			
	Peak 2	465 °C	445 °C – 480 °C	2.5%
	Peak 3	725 °C	705 °C – 745 °C	2.0%
D600_3h	Peak 1 (non-identified)			
	Peak 2*	418 °C	405 °C – 425 °C	1.5%
	Peak 3	650 °C	620 °C – 685 °C	1.7%
D800_3h	Peak 1 (non-identified)			
	Peak 2*	420 °C	405 °C – 430 °C	2.0%
	Peak 3	620 °C	580 °C – 660 °C	1.0%
D1000_3h	Peak 1 (non-identified)			
	Peak 2*	415 °C	400 °C – 425 °C	2.2%
	Peak 3	610 °C	585 °C – 630 °C	0.5%
D200_5h	Peak 1 (C-S-H; Ettringite)	135 °C	105 °C – 165 °C	1.2%
	Peak 2 ($Ca(OH)_2$)	470 °C	450 °C – 485 °C	3.5%
	Peak 3 ($CaCO_3$)	685 °C	670 °C – 700 °C	0.4%
D400_5h	Peak 1 (non-identified)			
	Peak 2	435 °C	415 °C – 450 °C	1.8%
	Peak 3	680 °C	650 °C – 715 °C	1.7%
D600_5h	Peak 1 (non-identified)			
	Peak 2*	420 °C	400 °C – 435 °C	1.0%
	Peak 3	665 °C	640 °C – 685 °C	1.0%
D800_5h	Peak 1 (non-identified)			
	Peak 2*	412 °C	390 °C – 430 °C	0.4%
	Peak 3	620 °C	595 °C – 640 °C	0.5%
D1000_5h	Peak 1 (non-identified)			
	Peak 2*	403 °C	390 °C – 410 °C	0.3%
	Peak 3	605 °C	565 °C – 645 °C	0.3%
D200_10h	Peak 1 (C-S-H; Ettringite)	120 °C	90 °C – 155 °C	2.8%
	Peak 2 ($Ca(OH)_2$)	467 °C	445 °C – 485 °C	3.8%
	Peak 3 ($CaCO_3$)	665 °C	640 °C – 695 °C	1.2%
D400_10h	Peak 1 (non-identified)			
	Peak 2	443 °C	425 °C – 460 °C	2.0%
	Peak 3	700 °C	680 °C – 725 °C	1.8%
D600_10h	Peak 1 (non-identified)			
	Peak 2*	430 °C	415 °C – 445 °C	1.5%
	Peak 3	675 °C	650 °C – 700 °C	1.5%
D800_10h	Peak 1 (non-identified)			
	Peak 2*	410 °C	395 °C – 420 °C	0.5%
	Peak 3	630 °C	590 °C – 660 °C	0.5%
D1000_10h	Peak 1 (non-identified)			
	Peak 2* (negligible)			
	Peak 3 (negligible)			

1.5. Details on the calculation of the specific surface areas of the VCe and the DhCeP for a hold time of 1h at maximum temperature

Material	Density	Porosity	Mass	Time (t)				Air Viscosity	Specific surface area	e^3	√e3	1-e	√t
	r	e	m1	t1	t2	t3	t(average)	√0.1η					
	[g/cm³]		[g]	[1/10s]	[1/10s]	[1/10s]	[1/10s]	[Pa*s]	[cm²/g]				[1/10s]
VCe	3.1	0.5	108.8	207.0	206.0	206.3	206.43333	0.001353	4018.479993	0.125	0.3535534	0.5	14.367788
D20	2.0325	0.5	71.3	165.1	164.3	164.4	164.6	0.001358	5452.754934	0.125	0.3535534	0.5	12.829653
D200_1h	2.1154	0.5	74.2	264.5	263.0	263.4	263.63333	0.001356	6640.172459	0.125	0.3535534	0.5	16.23679
D400_1h	2.141	0.5	75.1	157.2	157.2	156.9	157.1	0.001356	5064.576365	0.125	0.3535534	0.5	12.533954
D600_1h	2.4489	0.5	85.9	138.9	137.9	138.0	138.26667	0.001358	4147.814386	0.125	0.3535534	0.5	11.758685
D800_1h	2.9016	0.5	101.8	186.6	186.3	186.4	186.43333	0.001359	4061.964946	0.125	0.3535534	0.5	13.654059
D1000_1h	3.113	0.5	109.2	64.2	63.8	63.8	63.933333	0.001354	2225.344626	0.125	0.3535534	0.5	7.9958322

Appendix 2. Additional results for the reactivation of Recycled concrete powder through thermal treatment.

2.1. XRD phase contents (wt. %) of DhCoP obtained by Smart Crushing (SC) for the hold times of 3h, 5h, and 10h.

Phase	SC400_3	SC600_3	SC800_3	SC1000_3	SC400_5	SC600_5	SC800_5	SC1000_5	SC400_10	SC600_10	SC800_10	SC1000_10
Quartz [SiO_2]	66.5%	69.5%	59.5%	48.0%	66.5%	71.5%	58.5%	45.0%	64.5%	68.5%	59.0%	39.5%
Coesite [SiO_2]	2.5%	3.0%		8.0%	3.0%	0.5%	0.1%	4.5%	4.0%	6.0%		0.4%
Calcite [$CaCO_3$]	13.0%	16.5%			14.5%	10.5%	0.1%	0.5%	12.5%	10.0%	1.0%	
Vaterite [$CaCO_3$]	10.5%	0.2%		2.0%	11.0%			2.5%	12.5%			3.5%
Dicalcium Silicate [Ca_2SiO_4]	0.5%	4.0%	10.5%	1.0%	0.5%	13.0%	9.0%		0.5%	13.0%	8.0%	
Dicalcium Silicate - Alpha			24.0%	2.0%			22.5%			0.5%	21.0%	
Hatrurite [Ca_3SiO_5]	0.5%	1.0%		1.5%	1.0%	0.1%	0.5%	0.2%	0.5%	0.5%		
Tobermorite (C-S-H) [$Ca_5Si_6O_{16}(OH)_2 \cdot 4H_2O$]	2.5%	3.0%			0.5%	2.5%			2.0%	1.0%		
Brownmillerite [$Ca_2(Al,Fe)_2O_5$]							0.1%			0.5%	0.1%	
Orthoenstatite [$Mg_2Si_2O_6$]	4.0%	2.5%	2.0%	7.0%	3.0%	2.0%		6.0%	3.0%		3.0%	7.0%
Akermanite [$Ca_2MgSi_2O_7$]			3.5%	30.5%			7.0%	30.0%			8.0%	27.0%
Lime [CaO]			0.3%				0.1%				0.1%	
Clinoenstatite [$Mg_2Si_2O_6$]							2.0%	2.5%				8.5%
Wollastonite [$CaSiO_3$]								8.5%				14.0%
Zeolite [SiO_2]									0.3%			

2.2. XRD phase contents (wt. %) of DhCoP obtained by Electrodynamic Fragmentation (EF) for the hold times of 3h, 5h, and 10h.

Phase	EF400_3	EF600_3	EF800_3	EF1000_3	EF400_5	EF600_5	EF800_5	EF1000_5	EF400_10	EF600_10	EF800_10	EF1000_10
Quartz [SiO_2]	74.5%	75.0%	77.0%	70.0%	76.5%	76.5%	77.5%	58.0%	74.5%	85.0%	72.5%	68.5%
Coesite [SiO_2]	3.0%	0.5%	0.1%		4.5%	5.5%		1.0%	3.0%	1.5%		1.5%
Calcite [$CaCO_3$]	8.5%	9.5%	0.5%	0.5%	7.5%	2.5%	0.2%		8.0%	1.5%	0.3%	
Vaterite [$CaCO_3$]				0.3%						0.5%		
Dicalcium Silicate [Ca_2SiO_4]		4.0%	4.5%	13.0%		1.5%	18.0%	17.0%		1.5%	19.5%	11.0%
Dicalcium Silicate - Alpha		0.5%	14.0%	2.0%		1.0%	0.3%	1.0%		1.0%	1.5%	1.5%
Hatrurite [Ca_3SiO_5]	1.0%	1.0%			1.0%	2.5%		0.5%	0.5%	1.0%		
Tobermorite (C-S-H) [$Ca_5Si_6O_{16}(OH)_2{\cdot}4H_2O$]		2.0%				1.5%	2.5%	2.5%	3.0%			2.5%
Brownmillerite [Ca2(Al,Fe)2O5]												
Orthoenstatite [$Mg_2Si_2O_6$]	9.0%	7.5%	0.5%	2.0%	9.5%	9.0%	0.5%		9.5%	8.0%	5.5%	
Akermanite [$Ca_2MgSi_2O_7$]			1.0%	5.0%				1.5%			0.1%	7.5%
Lime [CaO]			2.0%									
Clinoenstatite [$Mg_2Si_2O_6$]	1.5%		0.2%	7.0%	1.0%		1.0%	18.5%	1.5%		0.5%	7.5%
Wollastonite [$CaSiO_3$]												
Zeolite [SiO_2]	2.5%				0.3%				0.2%			

2.3. Comparison of XRD patterns of DhCoP obtained by Smart Crushing (SC) resulting from different hold times (1h, 3h, 5h, and 10h) at maximum temperatures for the same dehydration temperatures.

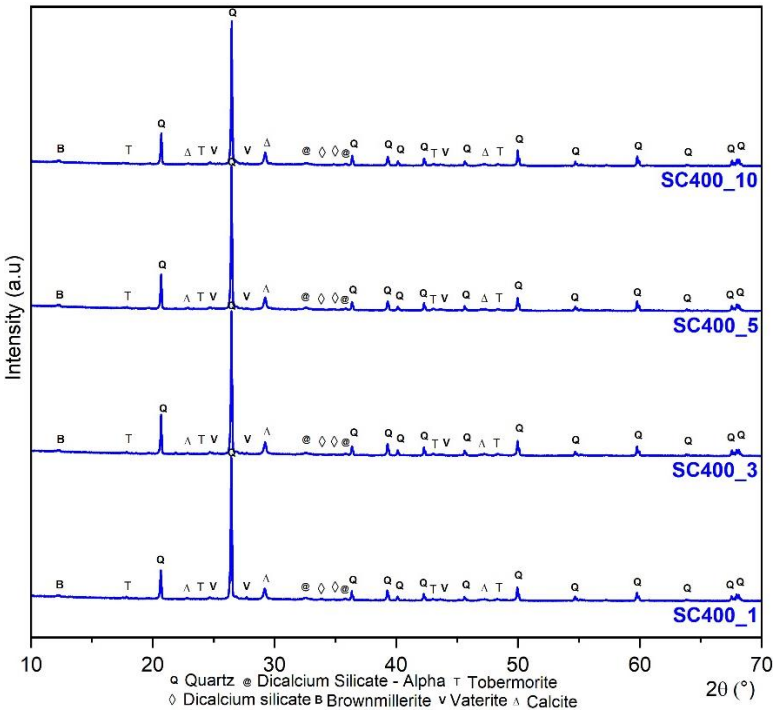

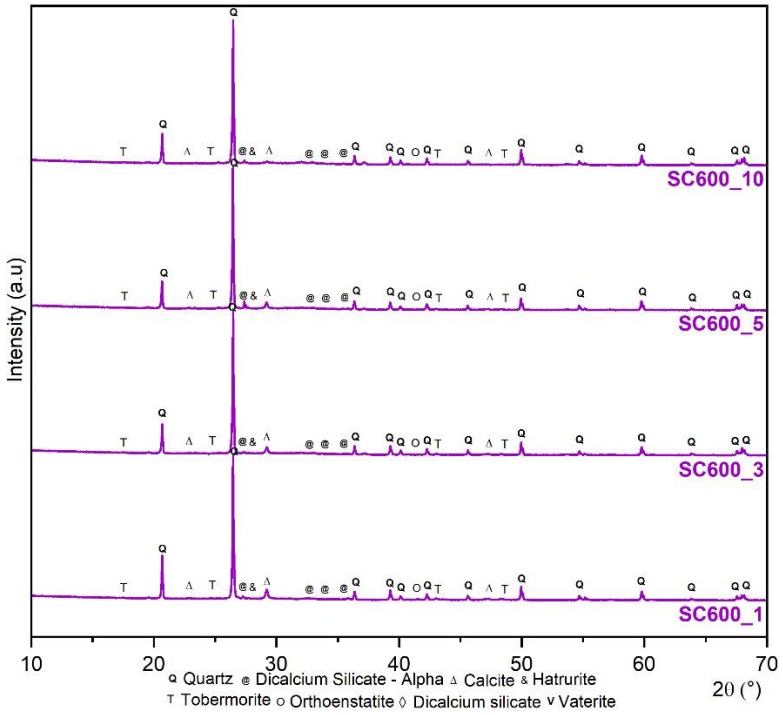

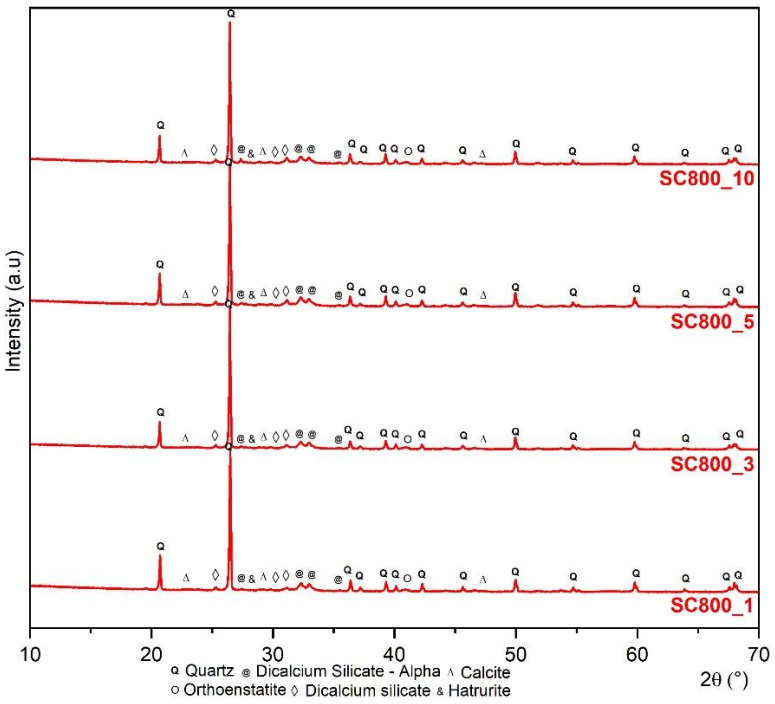

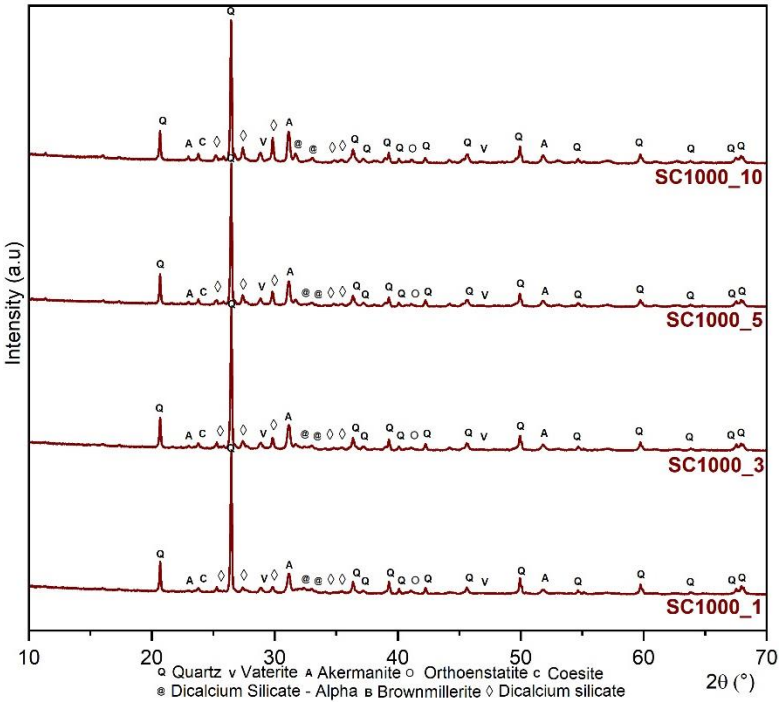

2.4. Comparison of XRD patterns of DhCoP obtained by Electrodynamic Fragmentation (EF) resulting from different hold times (1h, 3h, 5h, and 10h) at maximum temperatures for the same dehydration temperatures.

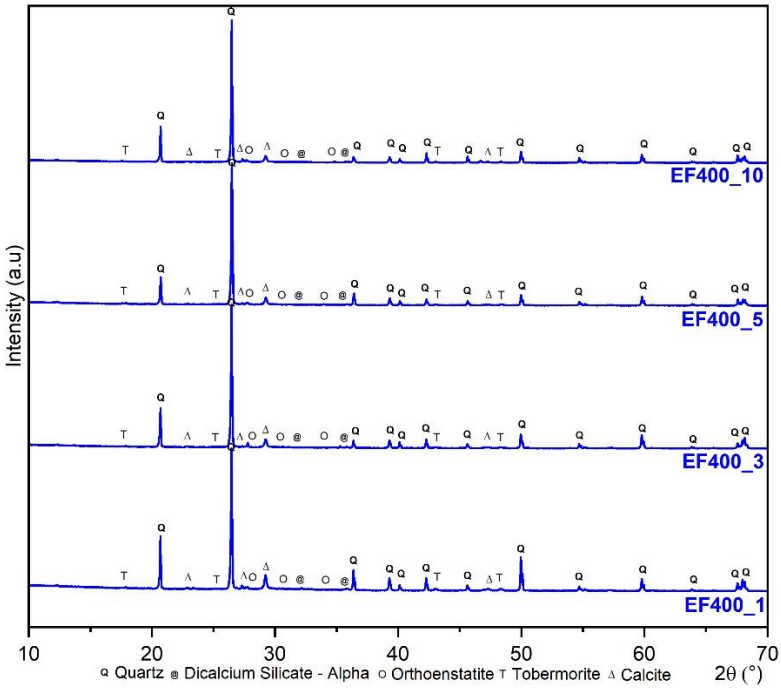

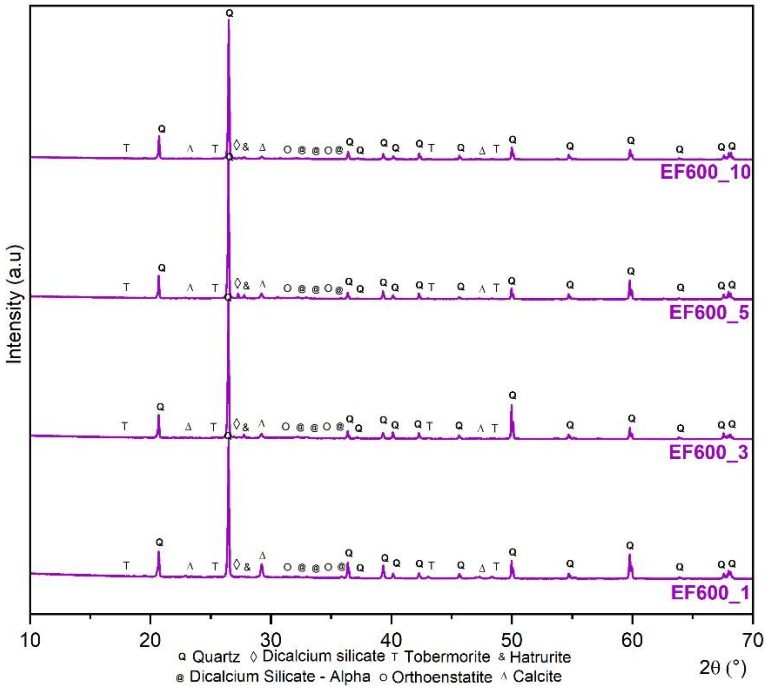

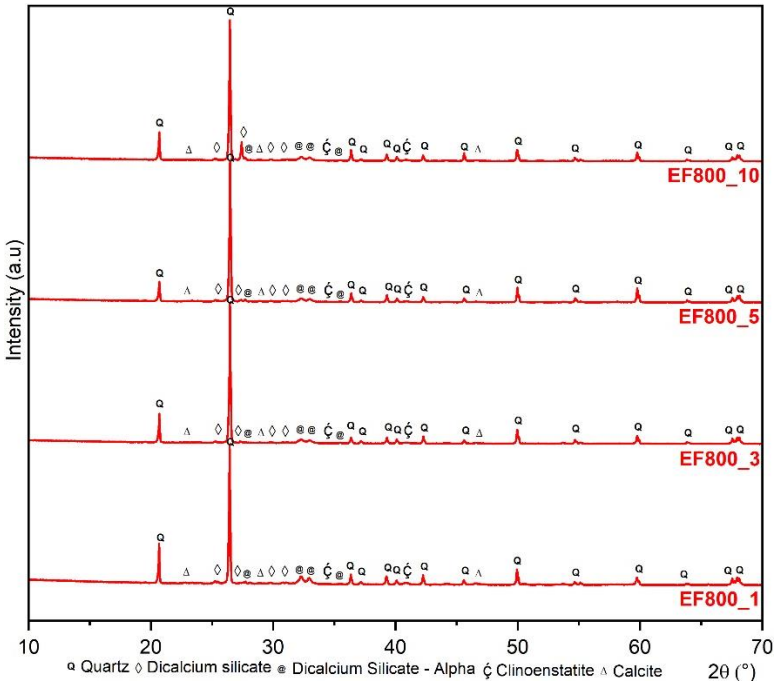

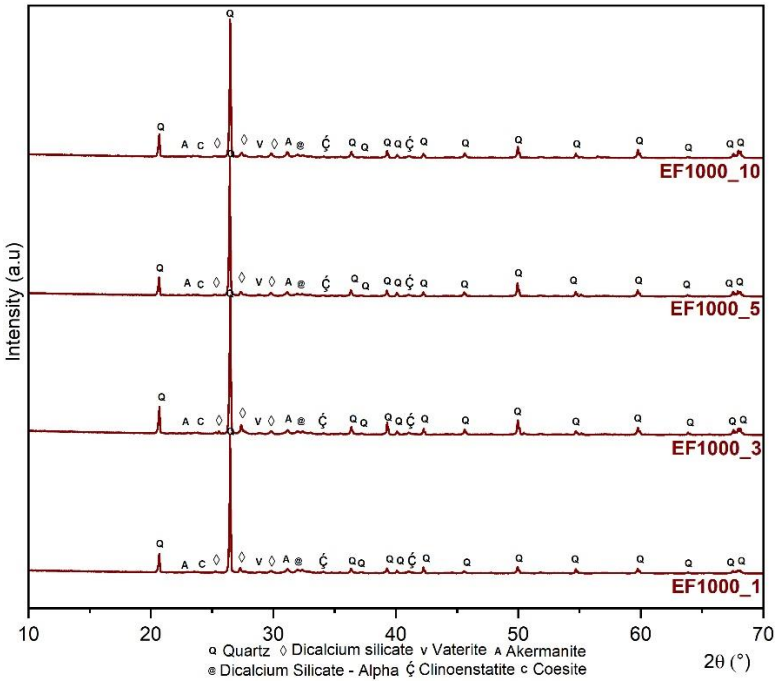

2.5. Comparisons of DSC (mW/mg) and TG (% mass loss) curves of DhCoP (SC200 to SC1000) obtained by Smart Crushing (SC) for the hold times of 3h, 5h, and 10h.

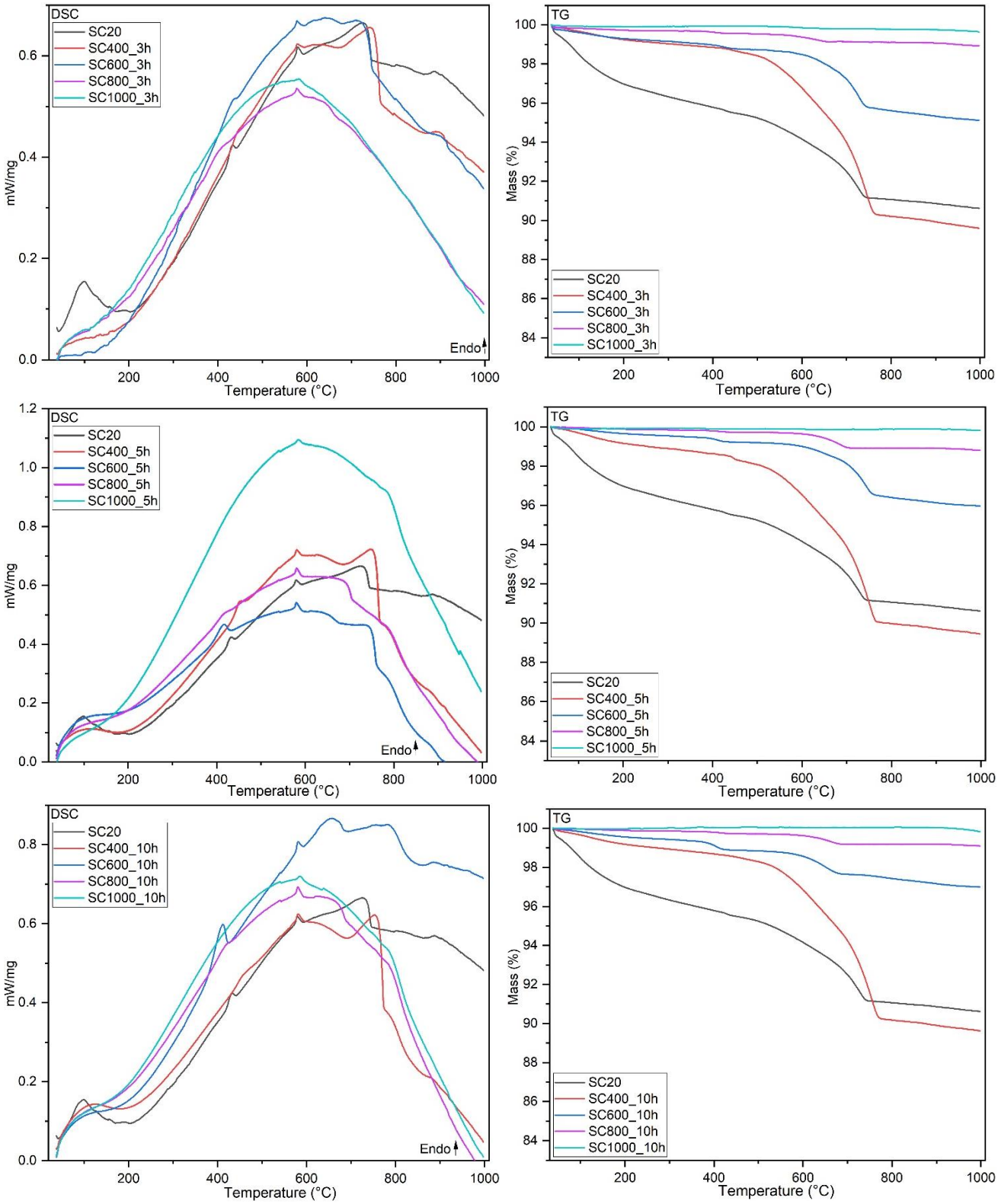

2.6. Comparisons of DSC (mW/mg) and TG (% mass loss) curves of DhCoP (EF200 to EF1000) obtained by Electrodynamic Fragmentation (EF) for the hold times of 3h, 5h, and 10h.

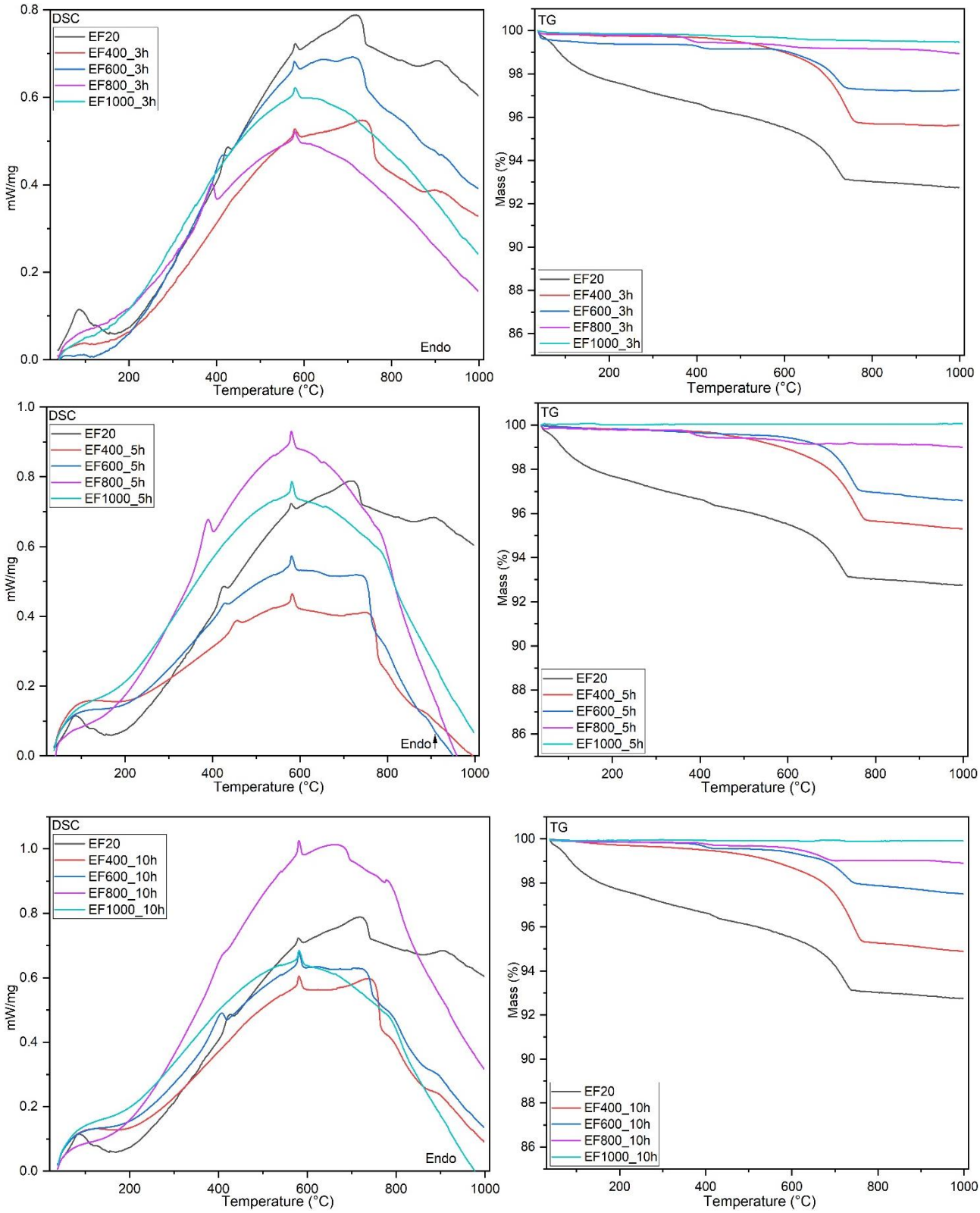

2.7. DSC - TG peaks and mass loss analyses for the DhCoP obtained by Smart Crushing (SC) for the hold times of 3h, 5h, and 10h.

Sample type	Identified peaks	Peak temperature (± 3°C)	Mass loss percentage (± 0.3%)
SC400_3h	Peak 1 (non-identified)		
	Peak 2	450 °C	negligible
	Peak 3	578 °C	-
	Peak 4	742 °C	8.0%
SC600_3h	Peak 1 (non-identified)		
	Peak 2	438 °C	negligible
	Peak 3	578 °C	-
	Peak 4	718 °C	2.8%
SC800_3h	Peak 1 (non-identified)		
	Peak 2	410 °C	negligible
	Peak 3	578 °C	-
	Peak 4 (negligible)		
SC1000_3h	Peak 1 (non-identified)		
	Peak 2 (non-identified)		
	Peak 3	580 °C	-
	Peak 4 (non-identified)		
SC400_5h	Peak 1 (negligible)		
	Peak 2	455 °C	negligible
	Peak 3	580 °C	-
	Peak 4	750 °C	8.0%
SC600_5h	Peak 1 (negligible)		
	Peak 2	417 °C	negligible
	Peak 3	581 °C	-
	Peak 4	742 °C	2.6%
SC800_5h	Peak 1 (negligible)		
	Peak 2	418 °C	negligible
	Peak 3	581 °C	-
	Peak 4 (negligible)		
SC1000_5h	Peak 1 (negligible)		
	Peak 2 (non-identified)		
	Peak 3	582 °C	-
	Peak 4	785 °C	negligible
SC400_10h	Peak 1 (negligible)		
	Peak 2	455 °C	negligible
	Peak 3	580 °C	-
	Peak 4	753 °C	7.9%
SC600_10h	Peak 1 (negligible)		
	Peak 2	410 °C	negligible
	Peak 3	581 °C	-
	Peak 4	658 °C	1.1%
SC800_10h	Peak 1 (negligible)		
	Peak 2	420 °C	negligible
	Peak 3	580 °C	-
	Peak 4	665 °C	negligible
SC1000_10h	Peak 1 (negligible)		
	Peak 2 (non-identified)		
	Peak 3	582 °C	-
	Peak 4	785 °C	negligible

2.8. DSC - TG peaks and mass loss analyses for the DhCoP obtained by Electrodynamic Fragmentation (EF) for the hold times of 3h, 5h, and 10h.

Sample type	Identified peaks	Peak temperature (± 3°C)	Mass loss percentage (± 0.3%)
EF400_3h	Peak 1 (non-identified)		
	Peak 2	440 °C	negligible
	Peak 3	578 °C	-
	Peak 4	740 °C	3.2%
EF600_3h	Peak 1 (non-identified)		
	Peak 2	415 °C	negligible
	Peak 3	578 °C	-
	Peak 4	718 °C	1.4%
EF800_3h	Peak 1 (non-identified)		
	Peak 2	390 °C	negligible
	Peak 3	578 °C	-
	Peak 4 (negligible)		
EF1000_3h	Peak 1 (non-identified)		
	Peak 2 (non-identified)		
	Peak 3	578 °C	-
	Peak 4 (non-identified)		
EF400_5h	Peak 1 (negligible)		
	Peak 2	455 °C	negligible
	Peak 3	580 °C	-
	Peak 4	755 °C	3.5%
EF600_5h	Peak 1 (negligible)		
	Peak 2	427 °C	negligible
	Peak 3	579 °C	-
	Peak 4	745 °C	2.3%
EF800_5h	Peak 1 (negligible)		
	Peak 2	390 °C	negligible
	Peak 3	578 °C	-
	Peak 4	781 °C	negligible
EF1000_5h	Peak 1 (negligible)		
	Peak 2 (non-identified)		
	Peak 3	579 °C	-
	Peak 4	782 °C	negligible
EF400_10h	Peak 1 (negligible)		
	Peak 2 (non-identified)		
	Peak 3	580 °C	-
	Peak 4	745 °C	3.1%
EF600_10h	Peak 1 (negligible)		
	Peak 2	407 °C	negligible
	Peak 3	579 °C	-
	Peak 4	725 °C	1.5%
EF800_10h	Peak 1 (negligible)		
	Peak 2	410 °C	negligible
	Peak 3	580 °C	-
	Peak 4	670 °C	0.7%
EF1000_10h	Peak 1 (negligible)		
	Peak 2 (non-identified)		
	Peak 3	580 °C	-
	Peak 4	782 °C	negligible

Appendix 3. The measured and the inaccessible porosity (%) for standard-size specimens after curing for 7 and 28 days, as shown by the Mercury Intrusion Porosimetry (MIP) results.

3.1. Measured and inaccessible porosity (%) of the specimens cured for 7 days.

Report date:04-03-21

Probe Zement CEM I 52,5 HCS 7d

ThermoFisher SCIENTIFIC

SAMPLE RESULTS

Inc / Dec - Probe Zement CEM I 52,5 HCS 7d

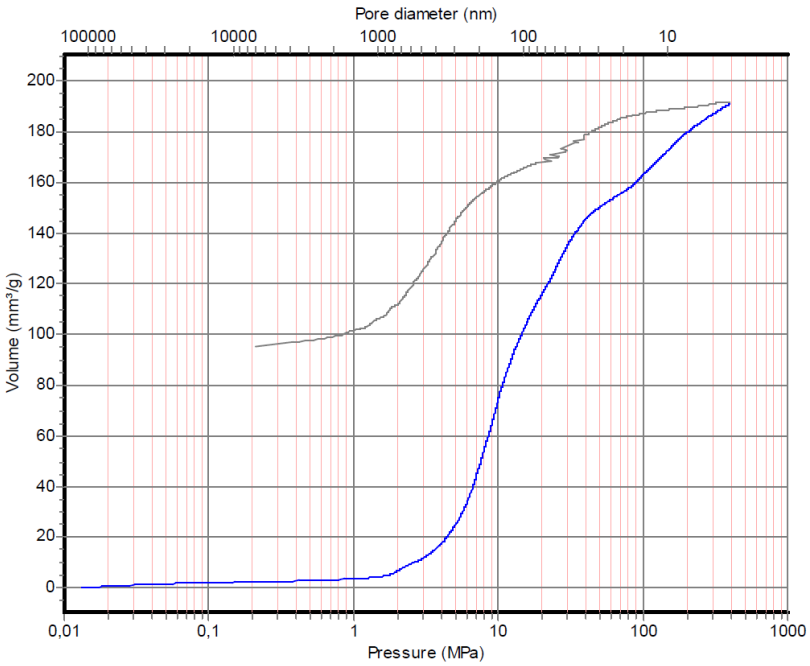

RESULTS WITHOUT COMPRESSIBILITY CORRECTION

Total intruded volume (mm³)	290,42		
Total intruded volume (mm³/g):	191,24	at pressure of MPa:	401,0070
Spec. Vol. by skeleton dens. (mm³/g) Vd:	413,82		
Bulk density (g/cm³):	1,0146		
Envelope density (g/cm³):	1,0147	at pressure of MPa:	0,013 Diam.(nm) 112018,7
Apparent density (g/cm³):	1,2589	at pressure of MPa:	401,007 Diam.(nm) 3,7
Porosity by skeleton density (%):	41,99	Calculated by skeleton density of	1,749 g/cm³
Porosity by Hg intrusion (%):	19,40		
Inaccessible porosity (%):	22,58		

Conform to ISO 15901-1

Page 2/6

Report date:08-03-21

Probe Zement 200°C 7d

ThermoFisher SCIENTIFIC

SAMPLE RESULTS

Inc / Dec - Probe Zement 200°C 7d

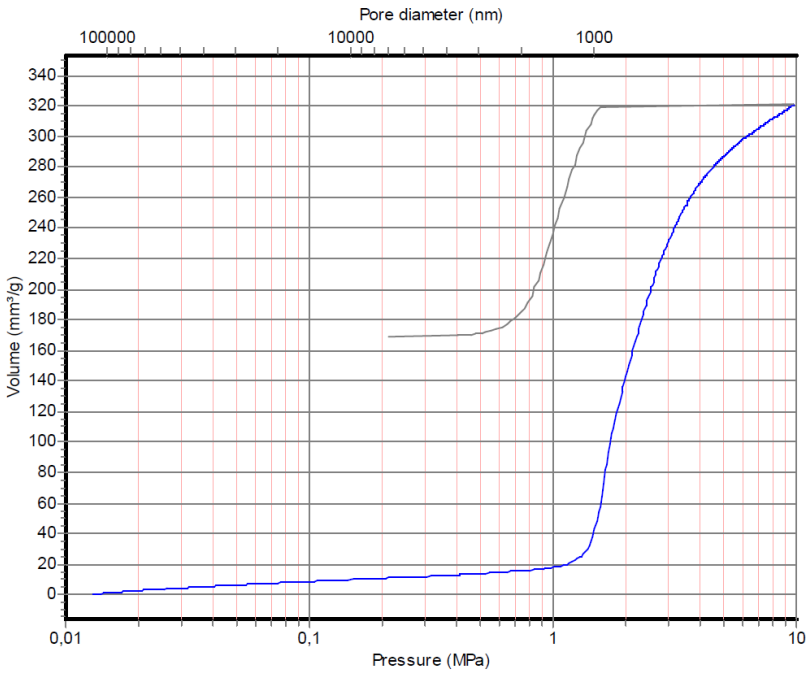

RESULTS WITHOUT COMPRESSIBILITY CORRECTION

Total intruded volume (mm³)	329,94		
Total intruded volume (mm³/g):	320,80	at pressure of MPa:	9,7167
Spec. Vol. by skeleton dens. (mm³/g) Vd:	712,57		
Bulk density (g/cm³):	0,7038		
Envelope density (g/cm³):	0,7040	at pressure of MPa:	0,013 Diam.(nm) 113927,6
Apparent density (g/cm³):	0,9091	at pressure of MPa:	9,7167 Diam.(nm) 151,4
Porosity by skeleton density (%):	50,15	Calculated by skeleton density of	1,412 g/cm³
Porosity by Hg intrusion (%):	22,58		
Inaccessible porosity (%):	27,57		

Report date:09-03-21

Probe Zement 400°C 7d

ThermoFisher SCIENTIFIC

SAMPLE RESULTS

Inc / Dec - Probe Zement 400°C 7d

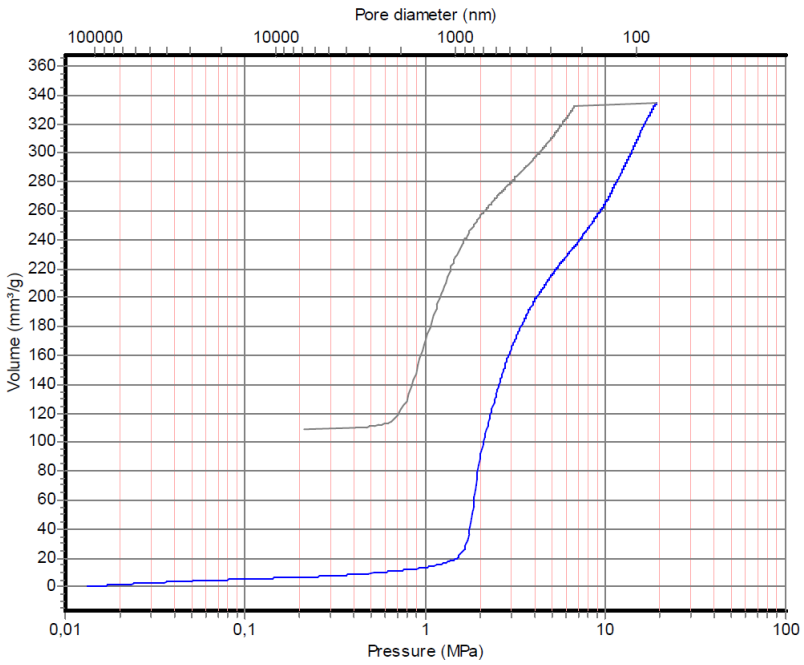

RESULTS WITHOUT COMPRESSIBILITY CORRECTION

Total intruded volume (mm³)	340,06		
Total intruded volume (mm³/g):	333,98	at pressure of MPa:	18,9664
Spec. Vol. by skeleton dens. (mm³/g) Vd:	787,09		
Bulk density (g/cm³):	0,6974		
Envelope density (g/cm³):	0,6975	at pressure of MPa:	0,013 Diam.(nm) 112104,1
Apparent density (g/cm³):	0,9091	at pressure of MPa:	18,9664 Diam.(nm) 77,5
Porosity by skeleton density (%):	54,89	Calculated by skeleton density of	1,546 g/cm³
Porosity by Hg intrusion (%):	23,29		
Inaccessible porosity (%):	31,60		

Report date:09-03-21

Probe Zement 600°C 7d

ThermoFisher SCIENTIFIC

SAMPLE RESULTS

Inc / Dec - Probe Zement 600°C 7d

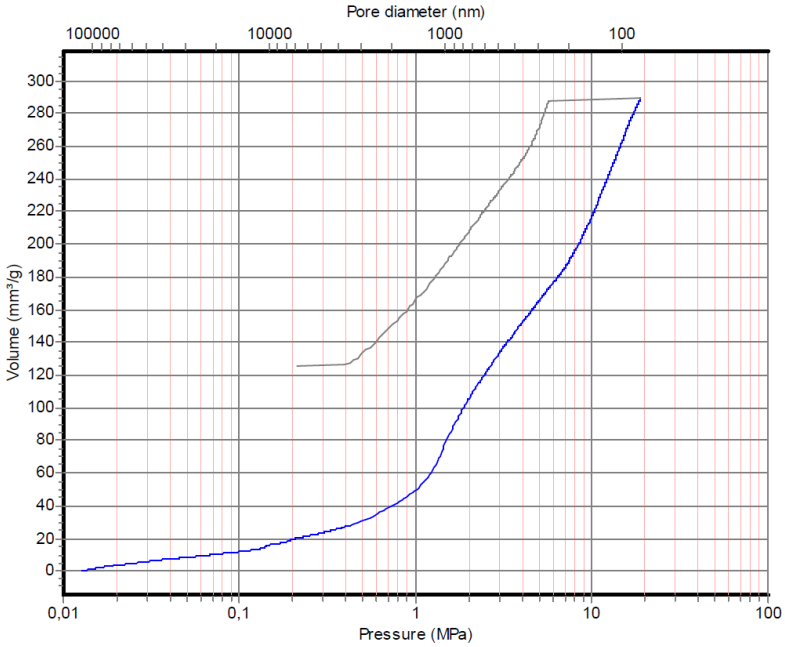

RESULTS WITHOUT COMPRESSIBILITY CORRECTION

Total intruded volume (mm³)	331,31		
Total intruded volume (mm³/g):	289,15	at pressure of MPa:	18,8270
Spec. Vol. by skeleton dens. (mm³/g) Vd:	617,76		
Bulk density (g/cm³):	0,7799		
Envelope density (g/cm³):	0,7800	at pressure of MPa:	0,013 Diam.(nm) 115266,9
Apparent density (g/cm³):	1,0070	at pressure of MPa:	18,827 Diam.(nm) 78,1
Porosity by skeleton density (%):	48,18	Calculated by skeleton density of	1,505 g/cm³
Porosity by Hg intrusion (%):	22,55		
Inaccessible porosity (%):	25,63		

Conform to ISO 15901-1

Page 2/28

Report date:09-03-21

Probe Zement 800°C 7d

ThermoFisher SCIENTIFIC

SAMPLE RESULTS

Inc / Dec - Probe Zement 800°C 7d

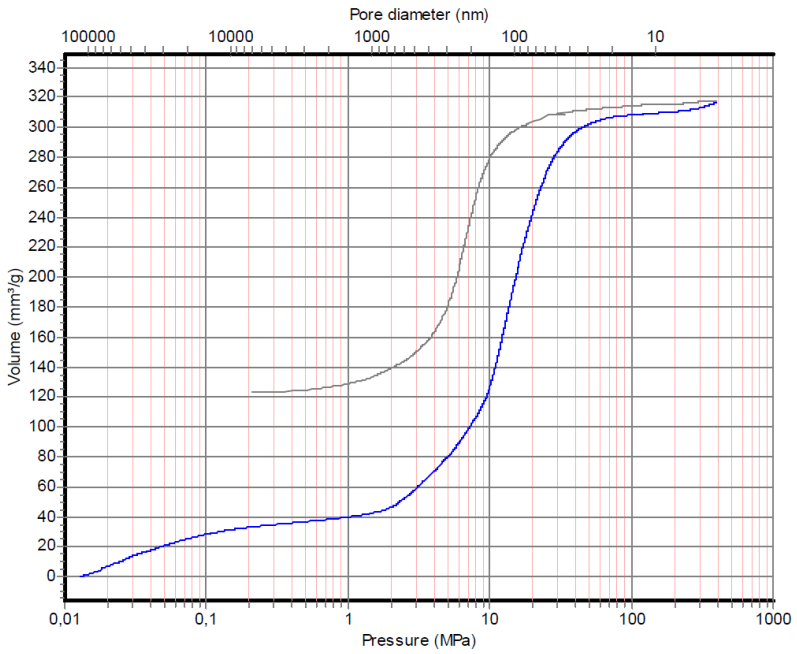

RESULTS WITHOUT COMPRESSIBILITY CORRECTION

Total intruded volume (mm³)	283,72		
Total intruded volume (mm³/g):	316,93	at pressure of MPa:	401,0077
Spec. Vol. by skeleton dens. (mm³/g) Vd:	786,89		
Bulk density (g/cm³):	0,6169		
Envelope density (g/cm³):	0,6170	at pressure of MPa:	0,013 Diam.(nm) 115902,7
Apparent density (g/cm³):	0,7669	at pressure of MPa:	401,0077 Diam.(nm) 3,7
Porosity by skeleton density (%):	48,55	Calculated by skeleton density of	1,199 g/cm³
Porosity by Hg intrusion (%):	19,55		
Inaccessible porosity (%):	28,99		

Conform to ISO 15901-1

Page 2/6

Report date:09-03-21

Probe Zement 1000°C 7d

ThermoFisher SCIENTIFIC

SAMPLE RESULTS

Inc / Dec - Probe Zement 1000°C 7d

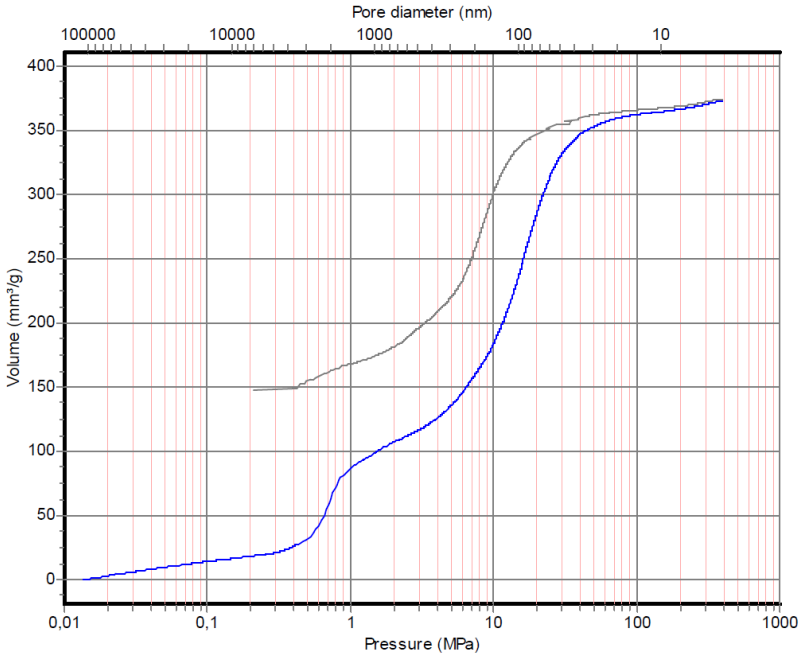

RESULTS WITHOUT COMPRESSIBILITY CORRECTION

Total intruded volume (mm³)	298,89		
Total intruded volume (mm³/g):	373,57	at pressure of MPa:	400,9072
Spec. Vol. by skeleton dens. (mm³/g) Vd:	1119,18		
Bulk density (g/cm³):	0,5543		
Envelope density (g/cm³):	0,5543	at pressure of MPa:	0,013 Diam.(nm) 109925,7
Apparent density (g/cm³):	0,6990	at pressure of MPa:	400,9072 Diam.(nm) 3,7
Porosity by skeleton density (%):	62,03	Calculated by skeleton density of	1,46 g/cm³
Porosity by Hg intrusion (%):	20,71		
Inaccessible porosity (%):	41,33		

Conform to ISO 15901-1

Page 2/6

3.2. Measured and inaccessible porosity (%) of the specimens cured for 28 days.

ThermoFisher SCIENTIFIC
SAMPLE RESULTS

Probe Zement 20°C
UDEMAT Materialwissenschaft

Report date:28-01-20

Inc / Dec - Probe Zement 20°C

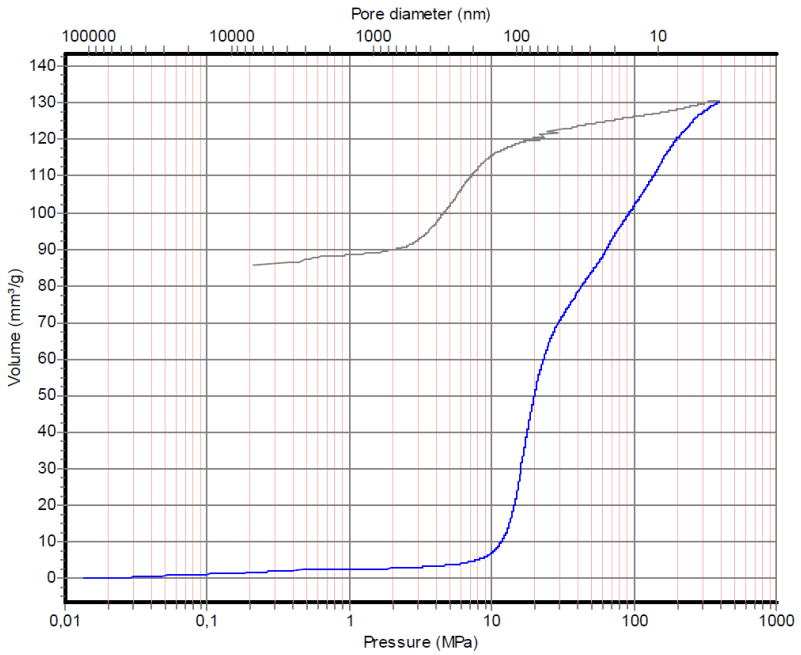

RESULTS WITHOUT COMPRESSIBILITY CORRECTION

Total intruded volume (mm³)	210,88		
Total intruded volume (mm³/g):	130,39	at pressure of MPa:	400,8081
Spec. Vol. by skeleton dens. (mm³/g) Vd:	87,31		
Bulk density (g/cm³):	1,7532		
Envelope density (g/cm³):	1,7532	at pressure of MPa:	0,014 Diam.(nm) 108867,9
Apparent density (g/cm³):	2,2727	at pressure of MPa:	400,8081 Diam.(nm) 3,7
Porosity by skeleton density (%):	15,31	Calculated by skeleton density of 2,07 g/cm³	
Porosity by Hg intrusion (%):	22,86		
Inaccessible porosity (%):	-7,55		

Conform to ISO 15901-1

Page 2/50

ThermoFisher SCIENTIFIC
SAMPLE RESULTS

Probe Zement 200°C 2.Messung
UDEMAT Materialwissenschaft

Report date:28-01-20

Inc / Dec - Probe Zement 200°C 2.Messung

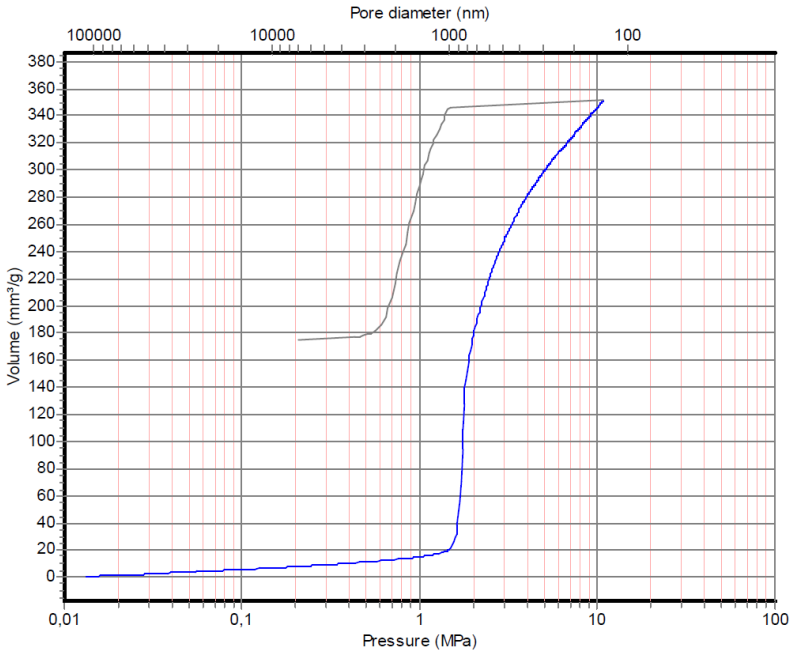

RESULTS WITHOUT COMPRESSIBILITY CORRECTION

Total intruded volume (mm³)	380,57		
Total intruded volume (mm³/g):	351,27	at pressure of MPa:	10,7254
Spec. Vol. by skeleton dens. (mm³/g) Vd:	289,56		
Bulk density (g/cm³):	1,2257		
Envelope density (g/cm³):	1,2260	at pressure of MPa:	0,013 Diam.(nm) 111678,5
Apparent density (g/cm³):	2,1524	at pressure of MPa:	10,7254 Diam.(nm) 137,1
Porosity by skeleton density (%):	35,49	Calculated by skeleton density of	1,9 g/cm³
Porosity by Hg intrusion (%):	43,06		
Inaccessible porosity (%):	-7,56		

Conform to ISO 15901-1

Page 2/17

ThermoFisher SCIENTIFIC
SAMPLE RESULTS

Probe Zement 400°C 28d
UDEMAT Materialwissenschaft

Report date:28-01-20

Inc / Dec - Probe Zement 400°C 28d

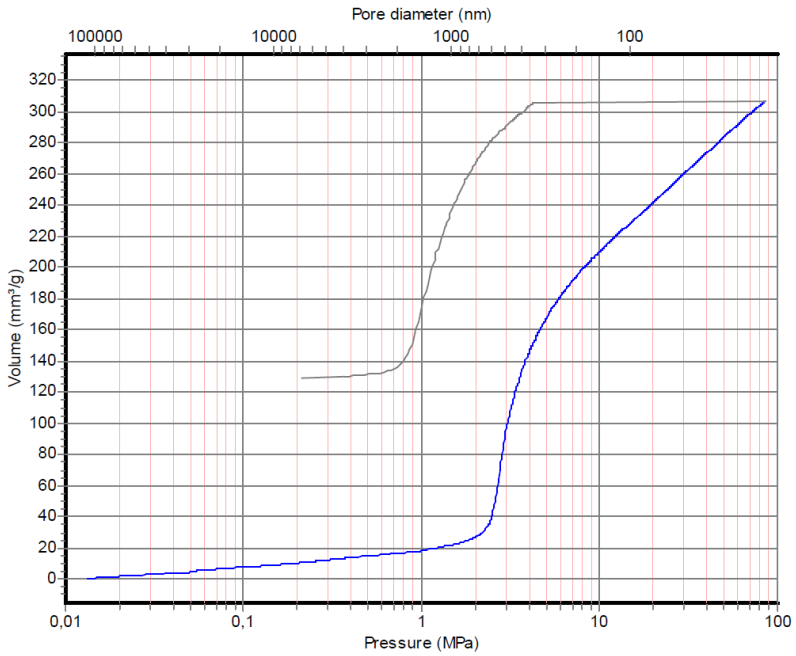

RESULTS WITHOUT COMPRESSIBILITY CORRECTION

Total intruded volume (mm³)	356,97		
Total intruded volume (mm³/g):	306,33	at pressure of MPa:	84,4659
Spec. Vol. by skeleton dens. (mm³/g) Vd:	231,20		
Bulk density (g/cm³):	1,3104		
Envelope density (g/cm³):	1,3111	at pressure of MPa:	0,013 Diam.(nm) 110753,4
Apparent density (g/cm³):	2,1892	at pressure of MPa:	84,4659 Diam.(nm) 17,4
Porosity by skeleton density (%):	30,30	Calculated by skeleton density of	1,88 g/cm³
Porosity by Hg intrusion (%):	40,14		
Inaccessible porosity (%):	-9,85		

ThermoFisher SCIENTIFIC
SAMPLE RESULTS

Probe Zement 600°C 28d
UDEMAT Materialwissenschaft

Report date:28-01-20

Inc / Dec - Probe Zement 600°C 28d

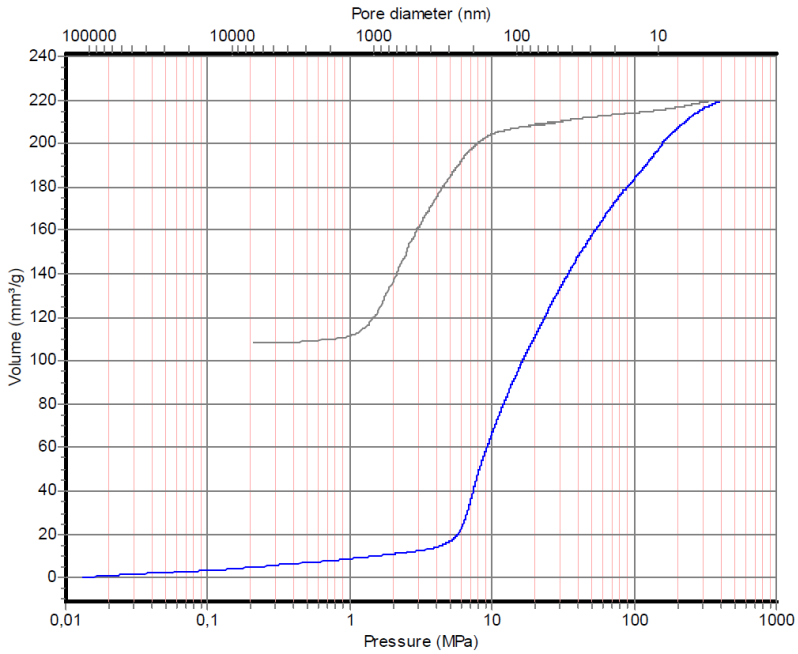

RESULTS WITHOUT COMPRESSIBILITY CORRECTION

Total intruded volume (mm³)	334,31		
Total intruded volume (mm³/g):	219,38	at pressure of MPa:	400,8059
Spec. Vol. by skeleton dens. (mm³/g) Vd:	127,10		
Bulk density (g/cm³):	1,6638		
Envelope density (g/cm³):	1,6642	at pressure of MPa:	0,013 Diam.(nm) 111593,7
Apparent density (g/cm³):	2,6202	at pressure of MPa:	400,8059 Diam.(nm) 3,7
Porosity by skeleton density (%):	21,15	Calculated by skeleton density of 2,11 g/cm³	
Porosity by Hg intrusion (%):	36,50		
Inaccessible porosity (%):	-15,35		

Conform to ISO 15901-1

Page 2/7

ThermoFisher SCIENTIFIC
SAMPLE RESULTS

Probe Zement 800°C 28d 2.Messung
UDEMAT Materialwissenschaft

Report date:28-01-20

Inc / Dec - Probe Zement 800°C 28d 2.Messung

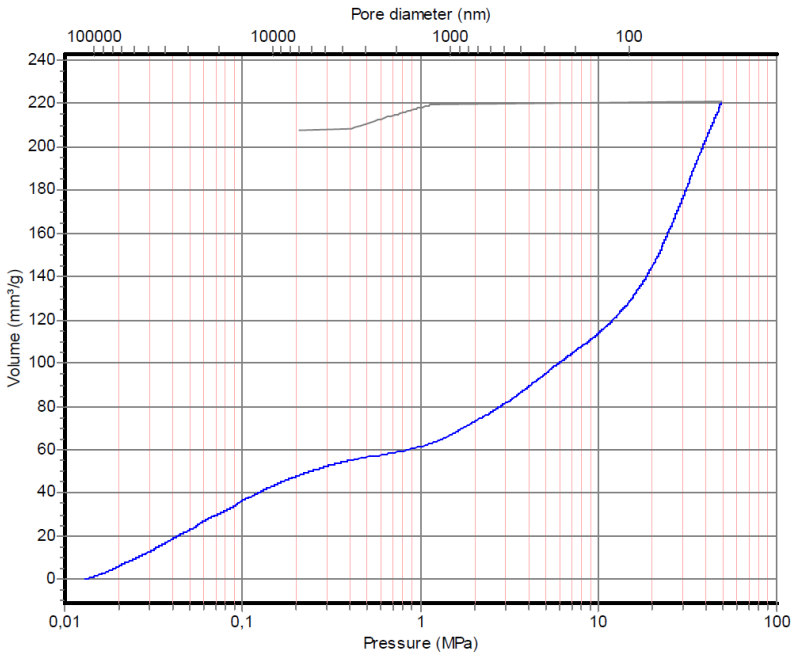

RESULTS WITHOUT COMPRESSIBILITY CORRECTION

Total intruded volume (mm³)	353,97		
Total intruded volume (mm³/g):	220,71	at pressure of MPa:	49,0072
Spec. Vol. by skeleton dens. (mm³/g) Vd:	79,42		
Bulk density (g/cm³):	1,7407		
Envelope density (g/cm³):	1,7408	at pressure of MPa:	0,013 Diam.(nm) 114638,0
Apparent density (g/cm³):	2,8268	at pressure of MPa:	49,0072 Diam.(nm) 30,0
Porosity by skeleton density (%):	13,83	Calculated by skeleton density of	2,02 g/cm³
Porosity by Hg intrusion (%):	38,42		
Inaccessible porosity (%):	-24,60		

Conform to ISO 15901-1

Page 2/7

ThermoFisher SCIENTIFIC
SAMPLE RESULTS

Probe Zement 1000°C 28d
UDEMAT Materialwissenschaft

Report date:28-01-20

Inc / Dec - Probe Zement 1000°C 28d

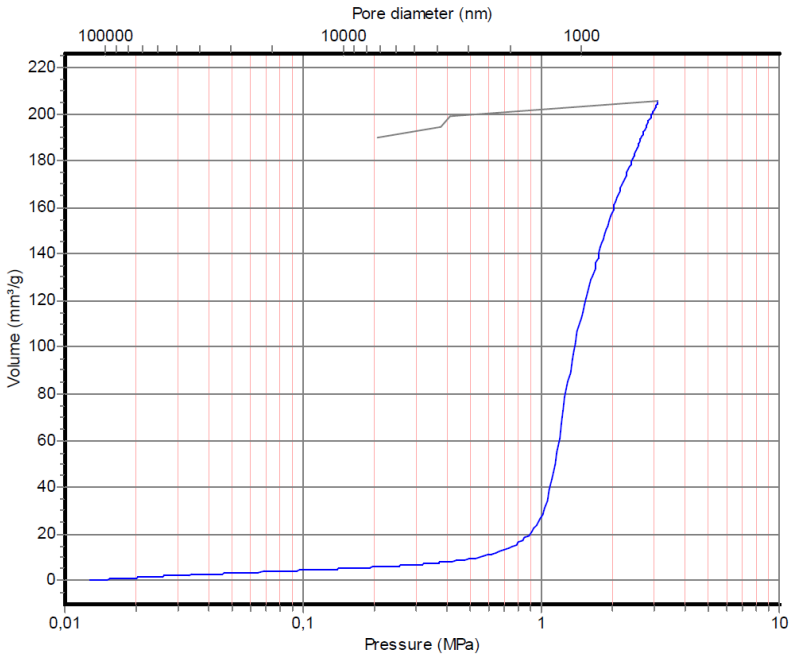

RESULTS WITHOUT COMPRESSIBILITY CORRECTION

Total intruded volume (mm³)	355,19		
Total intruded volume (mm³/g):	205,37	at pressure of MPa:	3,0859
Spec. Vol. by skeleton dens. (mm³/g) Vd:	167,54		
Bulk density (g/cm³):	1,8590		
Envelope density (g/cm³):	1,8591	at pressure of MPa:	0,013 Diam.(nm) 116085,7
Apparent density (g/cm³):	3,0071	at pressure of MPa:	3,0859 Diam.(nm) 476,6
Porosity by skeleton density (%):	31,15	Calculated by skeleton density of	2,7 g/cm³
Porosity by Hg intrusion (%):	38,18		
Inaccessible porosity (%):	-7,03		